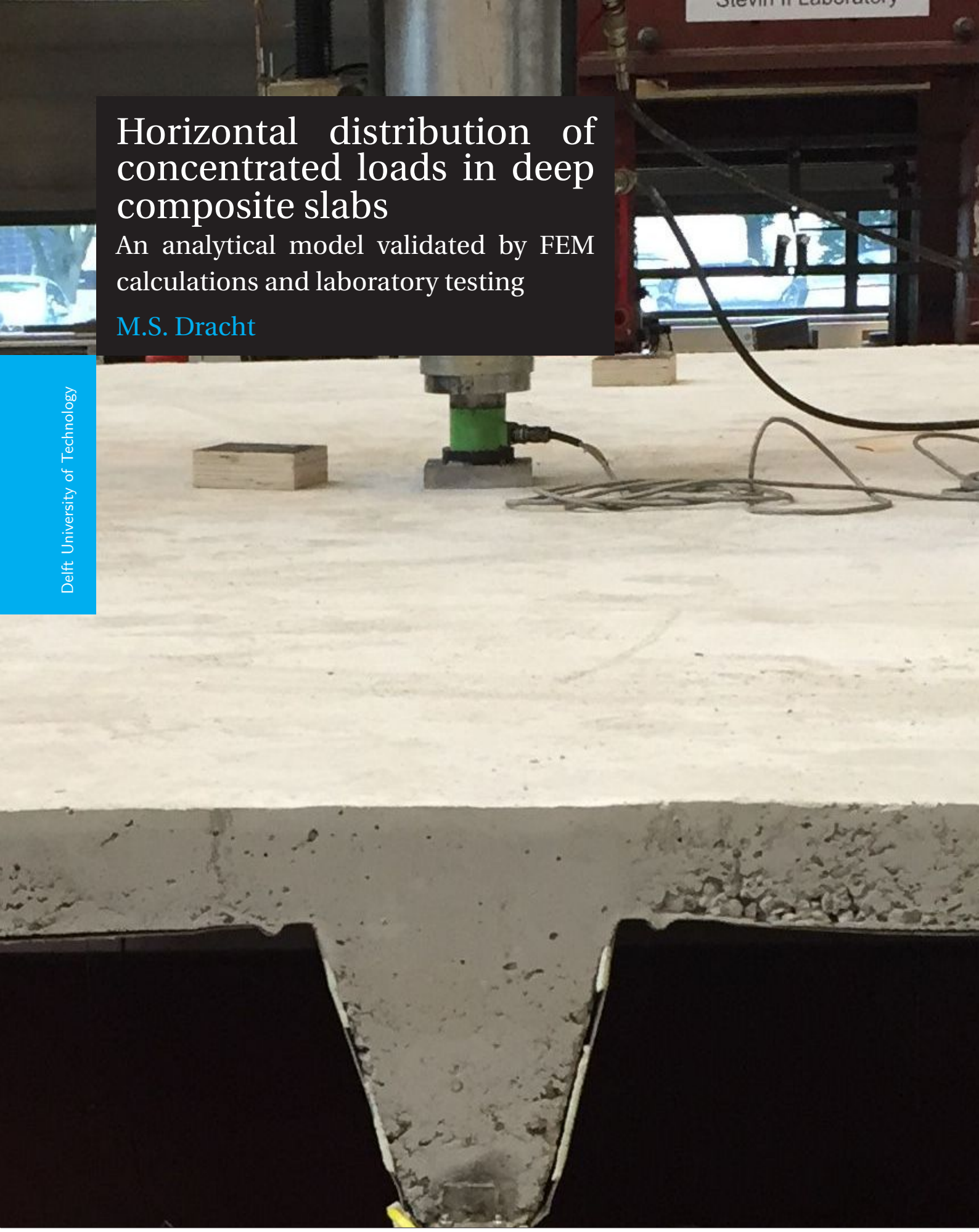

Horizontal distribution of concentrated loads in deep composite slabs

An analytical model validated by FEM calculations and laboratory testing

M.S. Dracht

Delft University of Technology

TU Delft Delft University of Technology

Challenge the future

HORIZONTAL DISTRIBUTION OF CONCENTRATED LOADS IN DEEP COMPOSITE SLABS

AN ANALYTICAL MODEL VALIDATED BY FEM CALCULATIONS AND LABORATORY TESTING

by

Matthijs Sebastiaan Dracht

in partial fulfilment of the requirements for the degree of

Master of Science
in Civil Engineering

at the Delft University of Technology,
Faculty of Civil Engineering and Geosciences,
Tuesday 25th August, 2015

Supervisor:	Prof. ir. F. S. K. Bijlaard,	TU Delft, supervisor
Thesis committee:	ir. R. Abspoel,	TU Delft
	Dr. ir. M. A. N. Hendriks,	TU Delft
	ir. H. Prins,	Dutch Engineering raadgevend ingenieurs B.V.
	Em. Prof. ir. J.W.B. Stark,	Emiritus Professor TU Delft

TU Delft Delft University of Technology

PREFACE

This thesis was written in partial fulfilment of the degree of master of science in civil engineering. The report consists of four distinct parts: an initial research into existing literature on the subject, a theoretical part, a finite element part and the last part about laboratory experiments performed in the Stevin II laboratory of the Technical University in Delft, the Netherlands.

The subject of this thesis was conceived in cooperation with Dutch Engineering in Zoeterwoude and its execution would not have been possible without their academic and financial support. I would therefore like to thank Dutch Engineering and the people who helped prepare the test specimens for the laboratory experiments.

I would also like to thank the people in the Stevin II laboratory of the Technical University Delft, who worked tirelessly in order to make sure that the experiments could be executed in a manner as smooth and correct as possible. And I would like to give special thanks to Arjen van Rhijn who made it possible through hard work to perform the experiments in a timely and orderly fashion.

Then I would also like to give many thanks to Maarten Rikken who assisted me greatly by taking on the organisation, execution and analysis of the materials testing which was done on the materials that were used in the construction of the test specimens of the laboratory experiments.

Finally I would like to thank all members of my thesis committee who provided me with valuable feedback and comments during the process of writing this thesis and who made its completion possible.

Matthijs Sebastiaan Dracht
Delft, July 2015

CONTENTS

SUMMARY

Composite steel-concrete floor slabs are a type of flooring that consists of a steel profiled deck, cast in-place concrete and steel reinforcement meshes in the concrete and steel reinforcement bars in the profiled ribs of the steel deck. Composite floors can roughly be separated into two types, those that use: shallow steel decks and deep steel decks. The deep profiled deck ComFlor210 is installed by hand and is then used as a work floor and as permanent form work for the casting of the concrete. The use of deep composite steel-concrete floor slabs is advantageous if aspects such as low self-weight, construction speed and floor height are important. The ComFlor210 composite floor is constructed by default with one reinforcement mesh, but if a large concentrated force is expected in the design than a second reinforcement mesh is added. However the effect that this added mesh has on the distribution of that concentrated force is not exactly known. The design of deep composite slabs also falls outside of the scope of Eurocode 4, design of composite structure, which leads to conservative assumptions and inefficient usage of materials. These factors lead to a need for more insight into the behaviour of composite slabs loaded by a concentrated load and in what manner this is effected by the addition of a second reinforcement mesh.

An analytical was created in order to predict the horizontal distribution. In the analytical model it was chosen to only model a two dimensional strip over the width of the composite slab. Any three dimensional aspects occurring in the slab were then incorporated into the two dimensional model. This was achieved by assuming the ribs of the composite slab as zero dimensional points which were supported by translation springs. The translation springs were modelling the ribs deflection and stiffness behaviour. The top part of the composite slab was modelled as a continuous beam spanning the entire width of the model. In order to incorporate the rotation resistance of the ribs, rotation springs were used to connect the ribs to the translation springs. For the analytical model accuracy, ease of use and a basis in mechanical behaviour were the aims.
A finite element model was also created in order to validate the analytical model and to analyse the behaviour of the composite slabs. Only a quarter of the slab was modelled by making use of the symmetry and only the areas of the steel deck effective in bending were included in the model. Finally laboratory experiments were also performed on life-sized test specimens. Three test specimens: one with two reinforcement meshes, one with one mesh and one without a mesh were tested. A concentrated load was applied in a non-destructive test at a quarter of the span length and a destructive test was performed at half the span length. The results of these tests were compared with the analytical and finite element model.

The result of the comparison was that the accuracy goal of the analytical model could not be reached. This was because the translation springs in the model included both the distribution at the point of loading and the redistribution between that point and the supports. Therefore the distribution cannot be accurately estimated without further research and experimentation. The analytical model should therefore be revised in order to more easily assess its parameters. The stiffness of the supports is another aspect that was not taken into account into the model that could be included. The finite element model also did not have sufficient accuracy in order to use as a validation method, possibly due to the use of only the effective steel profile. Adding the whole steel deck might improve the accuracy. The experiment results yielded the conclusion that the second reinforcement mesh increases the distribution of the load in the horizontal direction significantly while loaded at mid span. The slab without mesh also could be loaded until high loads of 100 kN, but its load was far more concentrated than in the other slabs. Although initially at 10 kN all slabs had very similar distributions and until a load 60 kN the maximum difference in the middle rib was only 10% of the total applied load. It was also concluded that the steel deck was active in the transverse direction after the chemical steel-concrete bonding was lost, but the size of contribution depended on the number of reinforcement meshes.
Suggestions for future research that were not included in this thesis include the horizontal and vertical shear capacity of the composite deck, the crack propagation in the slabs and the behaviour of the steel-concrete chemical bond.

List of Figures

List of Tables

LIST OF SYMBOLS

Latin upper case letters

A_a	Total steel area of a single rib of the deep composite steel profiled deck.
A_{as}	Total effective area of the longitudinal reinforcement bar in a rib of the deep composite steel profiled deck.
A_{bot}	Total effective area of the bottom flange of the effective steel profile.
A_{eff}	Total effective area in bending of a single rib of the deep composite steel profiled deck.
A_{rebar}	Total effective area of the longitudinal reinforcement bar in a rib of the deep composite steel profiled deck.
B_{dis}	The distributive width used to determine the bending stiffness of the top slab which is used in the analytical model.
B_{rib}	The width of the widest part of a rib in the deep composite steel profiled deck.
$B_{rib,bot}$	The width of the bottom of a rib in the deep composite steel profiled deck.
$B_{rib,eff}$	The average width of a rib in the deep composite steel profiled deck.
B_{tot}	The centre-to-centre distance of ribs in deep composite steel profiled deck.
$C_{Rk,c}$	A factor used in the calculation of the punching shear resistance of a reinforced concrete slab.
E_a	The characteristic value of the Young's modulus of steel.
E_c	The characteristic value of the Young's modulus of concrete.
E_{cm}	The mean value of the Young's modulus of concrete.
E_{sup}	The the Young's modulus of the 'support' elements used in the finite element model.
EI	General: the bending stiffness of a material.
$EI_{rib,cr}$	The bending stiffness of the cracked ribs in the deep composite slab.
$EI_{rib,uc}$	The bending stiffness of the uncracked ribs in the deep composite slab.
EI_{TS}	The bending stiffness of the top slab of the deep composite slab in the transverse direction.
$EI_{TS,long}$	The bending stiffness of the top slab of the deep composite slab in the longitudinal direction.
$EI_{TS,neg}$	The bending stiffness of the top slab of the deep composite slab in the negative direction.
$EI_{TS,pos}$	The bending stiffness of the top slab of the deep composite slab in the positive direction.
F	General: a concentrated load.
F_r	The force in the translation springs in the analytical model.
G	General: the shear modulus of a material.
G_c	The compressive fracture energy of concrete used in the finite element model.
G_F	The fracture energy of concrete used in the finite element model.
$I_{a,eff}$	The second moment of inertia of the effective area of the steel profiled deck.
I_{conc}	The second moment of inertia of the uncracked concrete in the ribs of the deep composite slab.
J	General: the moment of inertia.
K	An load amplification factor for the load in a two-way concrete ribbed bridge deck.
L	General: A length.
L_{bar}	The length of the infinitely stiff bar in type 1 of the analytical model.
L_{dis}	The distributive length used to determine the bending stiffness of the top slab which is used in the analytical model.
L_{rib}	The total length of the ribs of the composite slab examined in the analytical model.

L_o	Length of the composite slab continuing past the support in the test set-up for the determination of the partial shear capacity of a composite slab according to Eurocode 4 annex B.3.6 [1].
L_s	Length of the load to the closest support in the test set-up for the determination of the partial shear capacity of a composite slab according to Eurocode 4 annex B.3.6 [1].
L_{span}	The span length of the ribs in the deep composite slab.
M_e	The elastic bending moment capacitys.
$M_{rib,cr}$	The bending moment at which the concrete in the ribs of the deep composite slab will begin to crack.
$M_{rib,kc}$	The remaining bending moment capacity of a rib in the composite slab after it has been reduced by the bending moment applied by the self-weight.
M_s	The bending moment in the rotation springs in the type 1 analytical model.
M_{SW}	The bending moment applied to the ribs by the acting self-weight of the composite slab.
N_{cf}	Total concrete compression force in the test set-up for the determination of the partial shear capacity of a composite slab according to Eurocode 4 annex B.3.6 [1].
N_{conc}	The total force in the compressive zone of the concrete.
Q_k	General: a characteristic concentrated load.
T	General: A torsion moment.
V	General: A shear force.
V_{Ek}	General: A characteristic shear force.

Latin lower case letters

a	General: distance of an applied load to the closest support.
b_{tot}	The centre-to-centre distance between ribs in the composite slab.
d_s	General: length of the uncracked cross-section in a loaded beam element.
d	General: height from the top of a reinforced concrete beam to the effective tensile reinforcement.
d_p	The effective depth of the tensile reinforcement from the top in a composite deck punching shear calculation.
f_{ck}	General: characteristic concrete compressive strength.
f_{cm}	The mean concrete compressive strength.
f_{ctm}	The mean concrete tensile strength.
f_{yk}	The characteristic yield stress of the steel deck.
f_y	The mean yield stress of the steel deck.
$f_{y,rebar}$	The mean yield stress of the steel reinforcement.
f_{ysk}	The characteristic yield strength of the reinforcement steel.
h_a	Height of the deep steel profiled deck.
h_c	Height of the concrete of the top slab.
h_{eq}	The effective height of elements in the finite element model.
$h_{s,ab}$	Height at which the longitudinal reinforcement in the rib is located measured from the bottom of the steel profile.
h_{rebar}	Height at which the longitudinal reinforcement in the rib is located measured from the bottom of the steel profile.
h_{sl1}	Height at which the longitudinal reinforcement of the top mesh is located measured from the top side of the slab.
h_{sl2}	Height at which the longitudinal reinforcement of the bottom mesh is located measured from the top side of the slab.
h_{st1}	Height at which the transverse reinforcement of the top mesh is located measured from the top side of the slab.

h_{st2}	Height at which the transverse reinforcement of the bottom mesh is located measured from the top side of the slab.
h_{tot}	Total height of the composite slab.
k	Coefficient used for the determination of the horizontal shear capacity in the m-k method from Eurocode 4 annex B.3 [1] *or* coefficient used in the determination of the vertical shear resistance capacity of a reinforced concrete element according to Eurocode 2 section 6.2.2 [2].
k_r	The stiffness coefficient of the translation spring modelling the deflection behaviour of the ribs in the analytical model.
k_{rib}	The stiffness coefficient of the translation spring modelling the deflection behaviour of the ribs in the analytical model.
k_{rt}	The torsion stiffness coefficient of the rotation spring modelling the rotation stiffness behaviour of the ribs in the analytical model.
k_s	The rotation stiffness coefficient of the rotation springs in the type 1 analytical model.
k_{sd}	The rotation stiffness coefficient of the rotation springs in the type 1 analytical model in the downwards direction.
k_{su}	The rotation stiffness coefficient of the rotation springs in the type 1 analytical model in the upwards direction.
m	Coefficient used for the determination of the horizontal shear capacity in the m-k method from Eurocode 4 annex B.3 [1].
n	The ratio of the positive and negative bending stiffnesses of the top slab of the deep composite slab.
q_k	General: a characteristic line load.
q_{rib}	The self-weight of a rib per unit of rib length.
t	The width of a steel profile section.
u_1	Perimeter length at which the punching shear should be checked according to Eurocode 2 [2].
v_{Ek}	The characteristic applied shear stress on the concrete in the punching shear calculation.
v_{min}	The minimal shear capacity of unreinforced concrete according to Eurocode 4 [1].
$v_{Rk,c}$	The minimal shear capacity of reinforced concrete according to Eurocode 4 [1].
w	General: the deflection.
x_e	Height of the compressive zone of the concrete in an serviceability limit state check.
x_u	Height of the compressive zone of the concrete in an ultimate limit state check.
z_c	General: The height of the neutral axis.
z_{cp}	The height of the neutral axis of the steel deck to the top flange.

Greek lower case letters

β	Coefficient used in determining the acting punching shear load according to Eurocode 2 [2] *or* a factor used to determine the moment of inertia of a rectangular shape.
δ_r	The deflection of the translation springs in the analytical model.
δ_{a-g}	The deflection of the ribs A-G respectively in the analytical model.
ϵ	General: the strain of a material.
ϵ_c	The strain of concrete.
η	coefficient used for the determination of the partial shear capacity of a composite slab according to Eurocode 4 annex B.3.6 [1].
θ	General: a rotation.
θ_{bar}	The rotation of the infinitely stiff bars in the type 1 analytical model.
θ_s	The rotation of the rotation springs in the type 1 analytical model.
κ	General: the rotation of a cross-section due to a bending moment.
λ	The characteristic length of differential equation used to solve the elastic foundation problem.

ν_c	The Poisson ratio of concrete.
ν_s	The Poisson ratio of steel.
ρ_l	Effective reinforcement ratio used for the determination of the punching shear resistance capacity according to Eurocode 2 [2].
ρ_{lx}	Reinforcement ratio in the x-direction for the determination of the punching shear resistance capacity according to Eurocode 2 [2].
ρ_{ly}	Reinforcement ratio in the y-direction for the determination of the punching shear resistance capacity according to Eurocode 2 [2].
τ_u	The partial shear strength according to Eurocode 4 annex B.3.6 [1].

ABBREVIATIONS

TU Delft	Technical University of Delft, the Netherlands
TNO	De Nederlandse Organisatie voor toegepast-natuurwetenschappelijk onderzoek [Dutch] (The Dutch Organisation for applied natural scientific research)
LVDT	Linear Variable Differential Transformer
DIANA	Displacement method Analyser

1

INTRODUCTION

Before any research or advancing work can be done in a scientific manner, it is always prudent to know what other progress has been made in the field in question. Knowing this may help to define one's own research to a more definite subject and it can also prevent any efforts being put in subjects that others may already have researched. Therefore, before the proposed subject of this thesis is presented, a short overview of composite decks and the research that has already been done will be given.
But first of all an overview of the different components in this thesis report will be given. This overview is illustrated in figure 1.1.

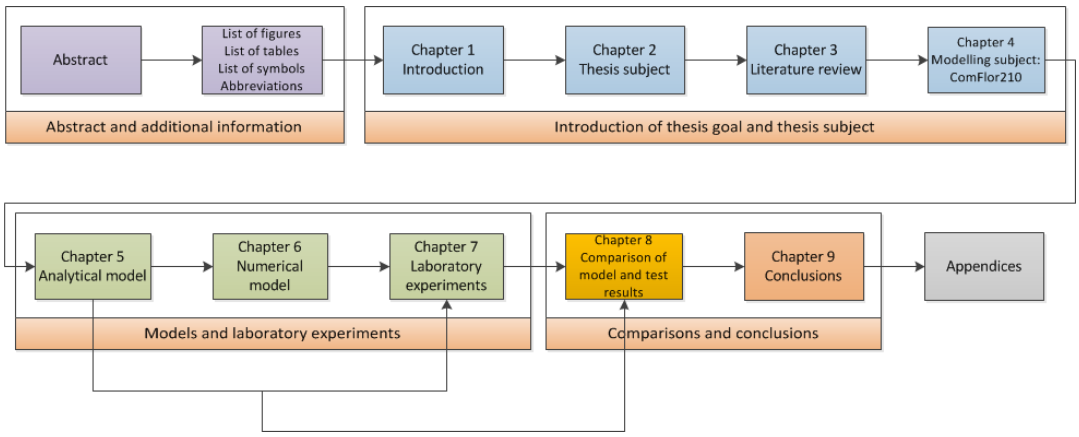

Figure 1.1: The overview above shows the components of which this thesis report is made up.

1.1. STRUCTURAL COMPOSITE MEMBERS

Composite structural materials make use of two materials by combining them into a single product, which has improved properties. This is generally done to supplement the undesirable aspects of one material with the other; to create a new product with improved behaviour and the desired characteristics. Materials that are used to construct composites for civil engineering purposes include: concrete, steel and wood. These materials are combined together to complement each other in aspects such as:

- stiffness
- strength
- stability
- fire resistance
- weight

- ductility
- corrosion and weathering resistance

Composite materials are used in many applications and fields and they also prove to be useful for application in construction, but as of yet most of them are executed in steel and concrete. Traditionally steel and concrete have been used in the same constructions for a longer time already, so combining them into a single structural element by means of shear connections is a natural evolution. This thesis will also focus on steel-concrete composite structural members and any reference to composite materials made will actually refer to steel-concrete composite members.
At the moment steel and concrete are the materials that are most widely used to create composite constructions. In essence an application like reinforced concrete, either poured or prefabricated, is also a composite, where the brittleness and the limited ability of concrete to resist tension stresses is supplemented by the addition of steel reinforcement. This provides ductility and tension resistance to the final product, resulting in an acceptable construction material, where concrete on its own would otherwise not provide enough resistance against tensions stresses or enough ductility to be used as a safe construction material. The difference between reinforced concrete and composite applications is that in the former the applied steel reinforcement does not have any bearing capacity or bending stiffness on its own while in the later it does. According to Shobaki [3], Crisinel [4], Stark [5] and Stark & Abspoel [6]), another way to combine steel and concrete together is not by using steel reinforcement but by using steel beams or steel profiled plates to act in conjunction with a concrete slab. Hereby the steel is acting effectively as external reinforcement. By using steel beams and concrete slabs composite beams can be made and by using a steel profiled plate to act as permanent form-work for a concrete slab a composite slab is created, an example can be seen in figure 1.2. Reinforced concrete, especially prefabricated concrete elements, and composite members fill a similar niche. This means that the composite slab competes with the reinforced concrete slab and prefabricated concrete. Composite beams and slabs are thus an alternative for traditional reinforced concrete and the more recent prefabricated concrete. The choice for either one of them depends on several factors according to Shobaki [3]. Costs are always an important aspect when choosing which material to use, but in reality the total costs of reinforced concrete and composite structural elements do not differ greatly. Instead what determines the choice between either one of them are:

- Stiffness
- Self-weight
- Response to vibrations
- Erection speed
- Material availability
- Aesthetics

As a start: composite structures make for slender and light structures, this can make them favourable when a slender or light-weight building is preferred. Another aspect of this characteristic is that slender floor systems mean that a building will have a decreased height for any number of floors, thus saving in façade costs or enabling the construction of an additional floor. They are also useful for high-rise construction due to their low self-weight. This eases the load exerted per floor and decreases the load on the foundation, thus saving costs and material in that area as well.
Other advantages of composite structures are the ability to create special shapes, such as cantilever beams and long spans, that are difficult to realize in form-work for poured concrete due to weight issues. It is also rather easy to create gaps and openings in the slab, simply by placing shapes made of wooden form-work or polystyrene of the desired forms on the steel plates. The construction process of composite slabs is also relatively easy. The steel decks can be transported in stacked batches and can then be hoisted with one movement of the crane to the floor currently under construction. This means that less use of the crane is needed and also the number of trucks coming to and from the construction site is reduced. The space needed for storage of the steel deck is also rather small and if timed well they can be lifted directly from the arriving transport trucks to the floor under construction, where they can be laid out by hand.
An important point of attention in composite structures is the shear connection between the two materials that are used. When shear connectors are used to connect the steel beam/steel deck and the concrete floor

slab a composite system is created; possible shear connectors that can be used to achieve this are shown in figure 1.3. Of the connectors shown there the stud connector the most widely used type. This connection combines the good stability and ability to bear compression stresses of the concrete with the steels ability to bear tension stresses into a whole, thereby reducing the weight and the overall height of the system. But if, on the other hand, composite members are not sufficiently connected by shear connectors it may cause incompatibility between the concrete and steel. This can result in horizontal slip at the interface or vertical uplift. Shear connectors that are used to accomplish a good shear connections are e.g. shear studs, welded to the steel beams and for slabs embossments and deck geometry are used. To improve understanding of how these shear connectors behave research to this end was done by Remco Schuurman [7].

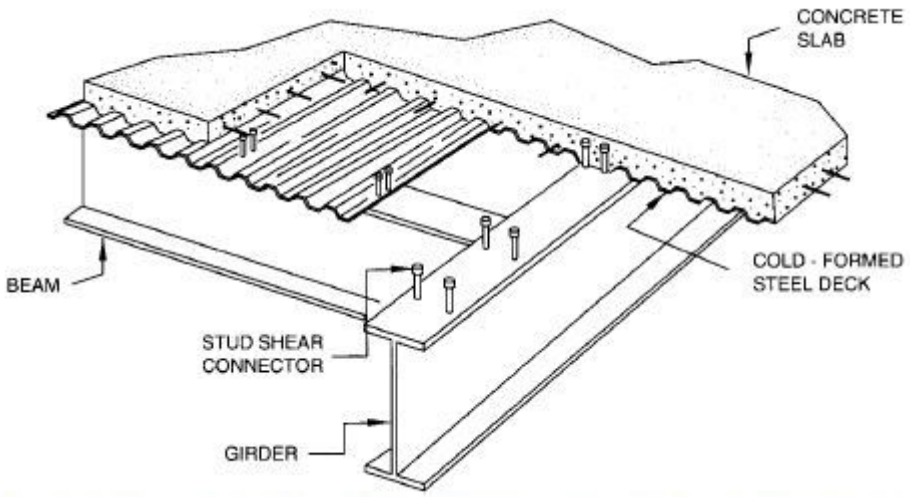

Figure 1.2: Schematic representation of a composite beam and composite slab

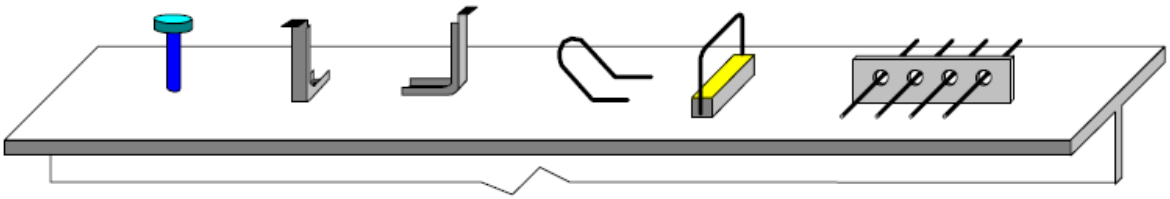

Figure 1.3: Different types of shear connectors that can be used, of these the stud connector is used by far the most widely.

1.2. COMPOSITE SLABS AND PROFILED DECKS

A composite slab consists of a cold-formed profiled steel sheet covered with concrete and possibly including steel reinforcement (Crisinel [4]). Nowadays the sheeting fulfils a number of roles during its lifetime: during the construction the sheeting is laid out by hand on top of the buildings frame work and the sheeting then functions as a work floor for the construction workers and their equipment. It is even possible to store construction materials on the floor to a certain extend. During the casting of the concrete the steel deck functions as form-work and after the concrete has hardened the steel sheeting acts as external reinforcement for the composite slab.

The idea of composite slabs is still relatively new. It was first developed during the 30's of the 20th century, at which time the steel decks were used as permanent form-work, and has been used in buildings because of the reduction in weight that it introduced. Since the 1950s the concept was used in the United States and thereafter the idea was carried over to Europe. Initially only pure chemical bonding forces between steel and concrete were used as a means to connect the two materials, but later through the development of new geometries of the steel sheet such as dovetails and re-entrant profiles (figure 1.4 and figure 1.5) and then embossments the connection of the elements was improved. Over the course of the following decades the

principle of composite slabs was further developed and improved. And the concept as it is known today has been in use, mainly in the United Kingdom, starting in the 1980's, but also in other European countries (Shobaki [3]).

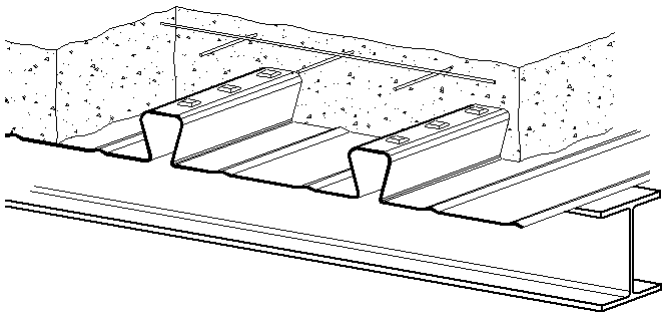

Figure 1.4: Example of a dovetail or re-entrant profile

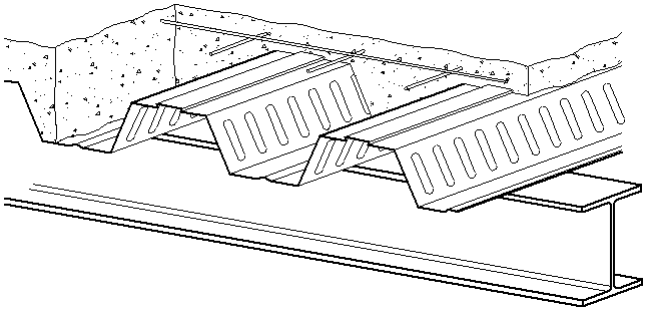

Figure 1.5: Example of a trapezoidal profile

The profiled steel sheets that are used can be between 0.75 mm – 1.50 mm thick, but usually they are between 0.75 – 1.25 mm thick. They are practically always treated with a hot-dip galvanization treatment on both sides, to protect the steel sheets against the effects of corrosion. This adds another approximate 40 micrometres to the thickness of the profiled steel deck (20 μm per side of the steel profiled deck) and this translates to approximately 275 g/m^2. The decks come in many shapes and forms. A general division is made between shallow decks and deep decks by dividing them by height (Stark & Stark [6]). Shallow decks are usually between 16 – 100 mm in height and deep decks have heights greater than 200 mm. Because the steel sheeting is so thin, it can be cold formed into the desired shapes during the process of rolling the profiled decks. The shapes that are most widely used are the re-entrant, or 'Dove-tail', and the trapezoidal profiles (figure 1.4 and figure 1.5 respectively), although it is also possible to create hybrid profiles with the aspects of both types of sheeting included (figure 1.6). The aim of these profiles is to increase the interlock between the concrete and the steel through the geometry of the decking. This mechanical interlock can be further increased by producing decks with embossments, or small indentations in the steel decking, pressed into them. Because the steel decks are so thin, the embossments can be pressed into the decking during the production stage, although the height of the embossments is limited to about 4.0 mm. In practice they are usually between 1 and 2 mm deep. It is possible to create these embossments on all the flat surfaces of the steel profiles and they can be pressed into several different shapes (figure 1.7).
Using a composite slab as a structural member provides several advantages over other methods of construction, according to Shobaki [3] and Stark & Stark [6]. These advantages are derived from either the concrete part of the structure or the steel elements. So is it possible to construct relatively slender construction elements due to the effective use of the materials involved. This can be done through either the construction of composite floor slabs which are a part of the underlying composite beam or through the construction of an integrated floor slab, which is supported on the bottom flanges of the steel beams (see figure 1.8). Apart from possible aesthetic values this results in, it also decreases the material usage. The steel profiled decks are light in weight and are transported in large batches to the construction site, where they can be moved up to the desired floor with only one or a few movements of the crane. Then they can be installed by hand, after which they serve as work floors for the construction workers and protect those below them, although

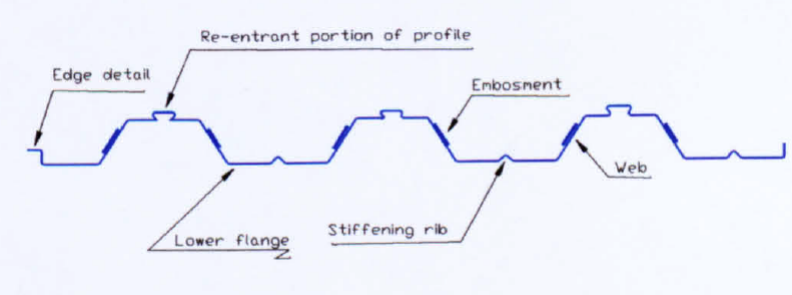

Figure 1.6: Schematic representation of a hybrid steel profile

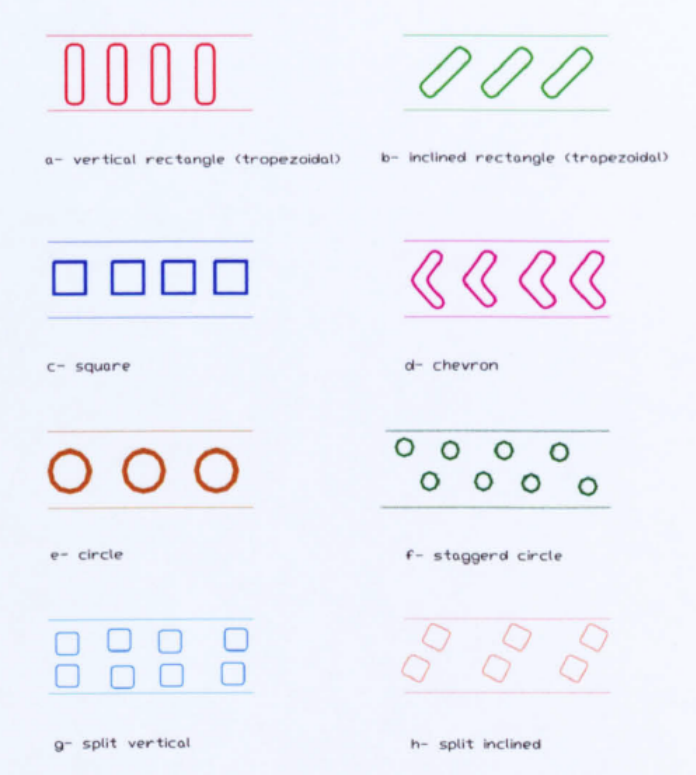

Figure 1.7: Schematic examples of possible embossment types

prior to the installation safety measures like a safety-net or safety-line remain necessary. The profiled decks serve as form-work for the concrete during the casting, thereby negating the need for specialised form-work that has to be placed and removed. If the steel decks are not propped then high construction speeds can be reached with this method. By propping it is meant that the steel beam or steel profiled deck is supported by one or multiple temporary supports to prevent excessive deflection due to the dead load or weight of the wet concrete during the construction phase, before the concrete has hardened. Propping allows for greater spans to be reached with composite construction systems but increases the costs of construction and also decreases the construction speed greatly. This is because the props can only be removed after the concrete of the supported floor has hardened sufficiently and only then can construction of the next floor begin.
After construction the composite floor could possibly add to the stability of the entire structure through diaphragm-action, (Stark & Stark [6]). Even before the composite phase the steel deck could theoretically add to the stability of the building but in practice this takes a considerable amount of effort to realize. Because of the shape of the steel decks it is also possible to fit electrical installations, wiring, piping, ducts and other utility services to them, through the use of specialised attachments. Due to their relatively light weight and low construction height per floor they are very suitable for high-rise buildings where they reduce the overall weight and height of the building or allow for extra floors to be added. Buildings where the weight is a critical factor also profit from composite construction methods. One more use for composite floors is found in the

Figure 1.8: A rendering of an integrated composite floor system

renovation of old structures. If extra capacity is need but no extra structural height can be found, composite elements are a good solution.

1.3. DEEP COMPOSITE DECKS

As mentioned before an approximate division can be made in the type of profiled steel deck that is used for the construction of composite slabs. Profiled decks with a height of around 200 mm or more can be called deep decks. These deep decks can span greater lengths than the shallow decks due to the increased height of the steel deck, unpropped they can span up to approximately 5.5 meters. This is due to the increased stiffness of the steel deck. Their shape is also different (figure 1.9). They resemble ribbed concrete floors more so than shallow decks. A deep composite deck complete with cast and hardened concrete can be seen in figure 1.10

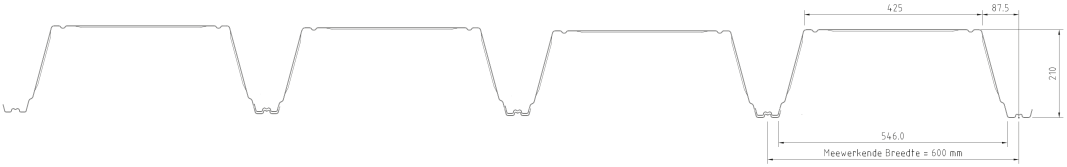

Figure 1.9: Schematic example of a deep deck profile

Figure 1.10: A picture of a completed composite slab with a deep profiled steel deck

The composite slabs can be fitted with reinforcing steel. This can be placed both in the ribs along the length of the slab and in the top slab part, where it is possible to use reinforcement meshes. An example of a reinforcement bar which is placed in a rib with the help of a spacer can be seen in figure 1.11a and a picture of reinforcement meshes suspended in the top slab ready for the casting of concrete can be seen in figure 1.11b.

In practise this type of composite slab is always constructed with a minimum of one reinforcement mesh in the top part. However, if large concentrated loads come into play then sometimes a second reinforcement mesh is added to the composite slab. A problem that occurs though is that the precise impact that the second reinforcement mesh has on the redistribution of loads is unclear. This makes it hard to design efficiently.

(a) A picture of a reinforcement bar placed in the rib of a deep steel deck

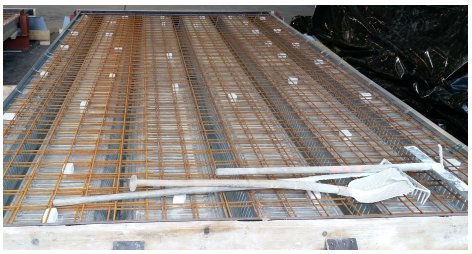

(b) A picture of reinforcement meshes suspended in place ready for the concrete to be cast

Figure 1.11: Two pictures of the reinforcement placed in a rib and of the reinforcement meshes in the top mesh respectively

An issue with deep decks, however, is that they fall outside of the scope of the Eurocode 1994-1-1 (Stark & Stark [5]). Meaning that when using deep decks the designer has to rely on conservative estimations, calculations and design methods or has to provide for his own calculations with an equal safety. Another aspect of the problem is that shear forces and shear failure become more critical (Brekelmans, Daniels, Van Hove, & Koukkari [8])) than they are for shallow decks. Both vertical shear and horizontal shear forces play a large role in transferring the external loads to the load-bearing parts of the structure. This is also true when redistributing the stress resulting from a concentrated load (Bode [9]). More knowledge about the way in which these loads are distributed over the structural element is necessary, if one wants to produce an effective design dealing with large concentrated loads.
Deep decks nevertheless represent an advantage over shallow steel decks because of the greater span length that is possible. It is therefore imperative that more is found out about their behaviour and about which loads will be most critical for them.

2

THESIS SUBJECT

Composite slabs are becoming more popular as structural design solutions in cases where characteristics are wanted that cannot be delivered by in-situ cast concrete or prefabricated concrete elements. And although research has been done to study their behaviour, as of yet not enough is known to use them effectively. This is especially true for the distribution of concentrated loads over the ribs of the composite slabs in the horizontal direction. Also the influence of adding or subtracting reinforcement from the composite slab has an influence that is not yet accurately quantifiable.

2.1. THESIS GOAL

This thesis will focus on gaining more insight on the behaviour of deep composite slabs, in particular the way in which concentrated loads act on them and are distributed throughout the structural components. The way in which the stresses caused by concentrated loads are spread over the nearby ribs and how much load each rib will have to bear is very important when designing the slab. If one then has to use very conservative rules and estimations, this will lead to an inefficient design. With the horizontal distribution of a concentrated load it is meant to find out what percentage of the load is borne by which ribs of the slab, as is shown in figure 2.1 which shows a top view of a deep composite slab with a concentrated load acting at a quarter of the span length.

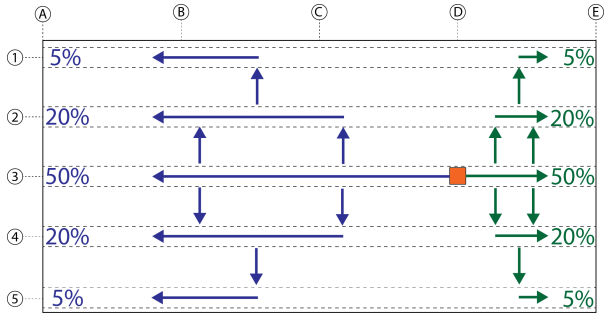

Figure 2.1: A schematic figure showing a top view of a deep composite slab with a concentrated load applied at a quarter of the span length and the force distribution shown with arrows. The percentages indicate how much of the total load at each support is borne per rib.

Considering all this, the following thesis subject was adopted: to set up an analytical mechanical model for evaluating the distribution of forces due to a concentrated load. This model should be validated through numerical modelling and testing, in order to gain insight in the failure mechanisms of deep composite slabs and in what way they can be influenced. A final evaluation of the resulting model will be done in the form of testing life-sized samples in a laboratory and comparing the model to the experimental results.
In short the subject of this thesis is: An analytical model of the horizontal distribution of concentrated loads

in deep composite slabs which is validated by FEM calculations and laboratory testing

2.2. THESIS OBJECTIVE

The objective of this thesis is therefore to produce an accurate analytical model for the evaluation of the distribution of forces over the ribs in the transverse direction, due to loading by concentrated loads in deep composite slabs and and the way in which this distribution is affected by the presence different numbers of reinforcement meshes and validate this model by doing finite element modelling and laboratory tests.

2.3. THESIS OUTLINE

This thesis has a total of nine chapters of which chapter 1 and 2 introduce the thesis subject and the goal of the thesis.
Chapter 3 examines the information and literature that is already available concerning composite slabs. Methods of determining the vertical and horizontal shear resistance of composite slabs and parallels of distribution of concentrated loads in concrete ribbed slabs are highlighted.
Chapter 4 describes the deep composite slab that will be used while constructing the analytical model. Also the loads and resulting load cases that will be considered are described here.
In chapter 5 the analytical model of the composite slab is described. First of all the composite slab which is examined and the acting load are outlined. Then the two-dimensional models used to describe the situation are explained. These models are expanded with additional features in a step by step manner. Then the resulting final model is subjected to a parameter study, showing the sensitivity of the involved parameters.
Then in chapter 6 a finite element model is set up which will be used to validate and improve the previously acquired analytical model.
Chapter 7 describes how the laboratory tests were designed and then executed. The following results and conclusions that can be tied to them are explained in this chapter as well.
The comparison between the results from the analytical model and the empirical results from the laboratory tests is made in chapter 8.
Finally in chapter 9 conclusions about the analytical model are drawn and evaluated. Also some suggestions for further research possibilities are made.

3

LITERATURE REVIEW

This chapter gives an overview of the research that has been done into methods of determining the horizontal distribution in composite slabs. More information concerning deep composite slabs will also be given. At the moment of writing there is still little information available about the horizontal distribution of concentrated loads in composite slabs. Therefore a comparison between deep composite slabs and ribbed concrete slabs is also made to see if anything useful can be learned from concrete slabs that could also be applied in composite slabs.

3.1. LOAD DISTRIBUTION OF CONCENTRATED LOADS

In composite slabs constructed with deep steel decks, as opposed to shallow steel decks, the vertical shear force becomes the critical issue more often (Bode & Däuwel [9]). Due to this fact it is vital to know more about the vertical shear force behaviour of the deep composite slabs. The vertical shear forces are mainly resisted by the ribs of the slab and these forces are transported through the top part of the slab to these ribs. But when a load is placed on top of a slab, being either a line load or a concentrated load, it is not clear how much of the imposed load is borne by how many of the slabs ribs.
In this thesis only concentrated loads will be considered and line loads are therefore not included in the rest of the report. When considering a concentrated load, it is meant to be a concentrated load according to Eurocode 1 [10]. In Eurocode 1 the important loads given are 7 kN on a 50x50 mm^2 area for buildings and 10 kN or higher on a 200x200 mm^2 area for car parks, although the concentrated loads that can be borne by the deep composite slab are much higher. When a concentrated load is placed on a slab, above a rib, how much of that load is carried by the rib directly below it and how much is transferred away through the top of the slab? This is as of yet not well very well known. Some research has been done on this subject, which this section will elaborate on. The similarity in geometry between deep composite slabs and concrete slabs with ribs also justifies a look into what research has been done into the spreading of concentrated loads on concrete slabs.

3.1.1. THE BEHAVIOUR OF THE SPREADING OF STRESS DUE TO CONCENTRATED LOADS ON COMPOSITE DECKS

Research and experiments on the distribution of loads in deep decks (COMFLOR210) has also already been performed by Bode & Däuwel [9], from which it followed that having a concentrated load between two ribs was not critical when considering the punching shear resistance of composite slabs with a concrete height of 75 mm or more and a concrete strength of C20/25 or more. Furthermore a test was done to analyse the behaviour of concentrated loads and line loads on composite decks and how their load would be spread through the composite slab (figure 3.1). It was also shown that punching shear was not critical, but rather that the vertical shear capacity of the slab and specifically the thin parts of the slab became critical for the COMFLOR210 deep decks. Concerning the vertical shear capacity of the deck, it was also found that the shear capacity of the deck could be added to the shear capacity of the concrete slab to give an accurate prediction of the total capacity.
Similar results were obtained by Stark & Stark [5] for the COMFLOR60 as mentioned earlier. The obtained results showed that the load, independent of the load value, 50% of the load was carried by the central rib di-

rectly under the load and 25% was transferred to the neighbouring ribs on either side. While the concentrated load was increased this pattern remained constant until the thinner top slab of the composite slab failed under the load it was transferring to the neighbouring ribs. At that moment the full load is carried solely by the centre rib until that too fails.

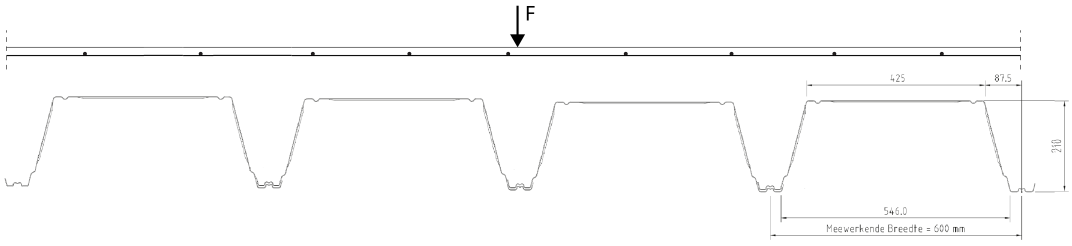

Figure 3.1: Schematic cross-section of a deep composite slab loaded by a concentrated load

3.1.2. THE SPREADING OF CONCENTRATED LOADS IN RIBBED CONCRETE SLABS

Because the geometry of concrete ribbed slabs is so similar to that of the composite deep slabs, it is worthwhile to observe what is known in this area about the spreading of the load when a concentrated load is acting on the slab. A concrete slab is designed for concentrated loads by using the effective-width theory (Eurocode 2 [2]). This is also done in the Dutch (NEN 6725 [11]) code. The load is categorised into line loads and concentrated loads of the three cases that can be seen in table 3.1.

Table 3.1: Load categories used in NEN6725 for line loads and concentrated loads

Case	**Line load q_k [kN/m]**	**Concentrated load Q_k [kN]**
Case 1	<3	<3
Case 2	3 - 6	3 - 6
Case 3	>6	>6

For case one loads the loads are to be considered as equally distributed loads. For load case two the effective width method is used according to figure 3.2 and for load case three the strip method is used according to 7.5.4. of (NEN 6720 [12] (withdrawn)). This means that the load is carried by a hypothetical strip in the concrete slab. The width of this strip depends on the size of the concentrated load, the distance to the sides of the slab and the eccentricity of the load.

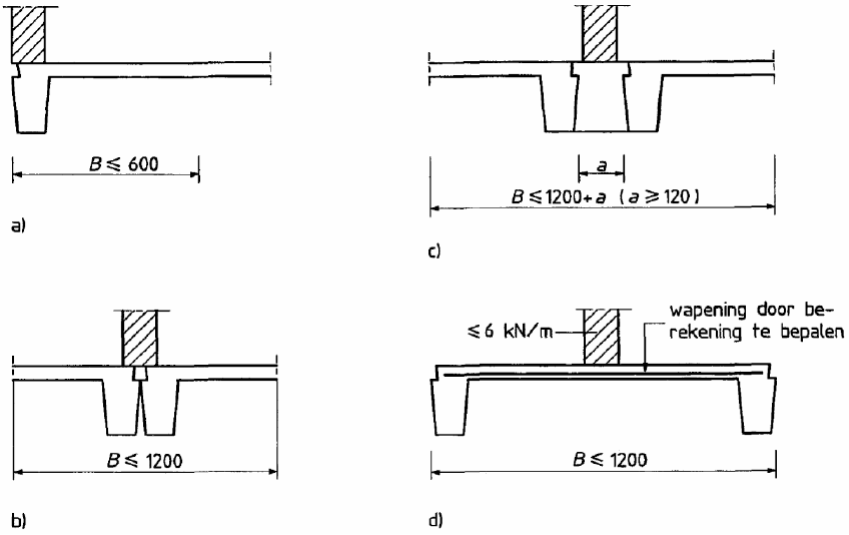

Figure 3.2: The effective widths used according to NEN6725

A set of loads is also implemented on the thin parts of the ribbed concrete slab to make sure they can resist the transverse loads. These rules, however do not incorporate any physical behaviour of the slabs and the ribs and the cooperation that might exist between these two elements. That a similar load dispersion relationship exists for ribbed concrete slabs as for deep composite slabs is suggested by the results of the tests done by Arrajarusit & Gamble [13], which give a similar result as Bode & Däuwel [9], indicating that when the concentrated load is placed on the centre rib of a one-way spanning slab the two ribs on either sides bear approximately half of the load. The report concerns testing on one-way and two-way spanning slabs with concentrated loads on the centre ribs and edge ribs (for the one-way slabs). The aim was to find out more about the moment, shear and torsional behaviour of the slabs.
The example above illustrates a concrete slab with ribs, but the ribs are still spaced apart quite significantly. An article by Hofman and Van der Vlugt which summarizes methods from other sources, provides a method of calculating the distribution of concentrated loads in concrete bridges with both longitudinal and transverse rib stiffeners, see figure 3.3.

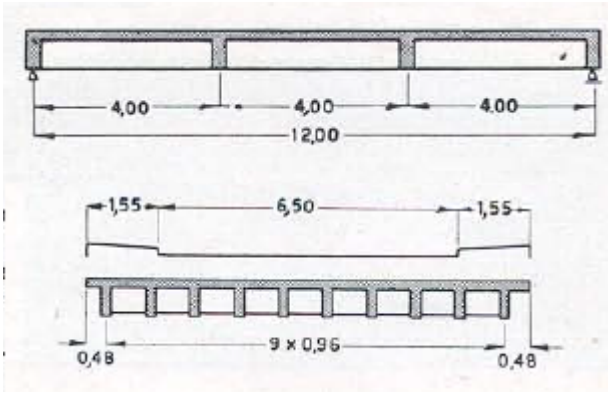

Figure 3.3: A side view and front view of a concrete bridge with longitudinal and transverse rib stiffeners

This method calculates the moments occurring in each of the longitudinal and transverse ribs caused by a point load applied at a random position on the concrete bridge. This is achieved by first calculating the deflection in each of the ribs, along the width of the slab, as if the load was a distributed load to gain the average deflection. And then to multiply this deflection by a factor K to obtain the deflection of the specific rib that one is analysing. The point load is estimated through a Fourrier-function in order to make it easier to calculate the resulting moments in the slab from the deflections. Since the occurring moments in the slab are more important in this analysis than the precise deflections, or so it is stated.
The factor K is then calculated and tabulated according to the position of the rib that is to be analysed and the position of the load on the bridge deck. The torsion resistance of the separate ribs can also be taken into account or not be taken into account according to the wishes of the designer. The result of these calculations are graphs and tables such as can be seen in figures 3.4 and 3.5 respectively. In these graphs the bending stiffness of the main spanning beams is set along the x-axis and the value for the factor K of that rib on the y-axis. There are several lines representing the different loading positions that are possible. For each of the ribs considered a new graph such as this one has to be drawn.
The method described above was originally created for reinforced concrete bridge decks with stiffeners in both directions. It might be worthwhile to examine the possible use for deep composite slabs though, since the geometric properties are quite similar. The results from such a calculation could be compared to the analytical model created in this thesis in order to improve or enhance it. On the other hand the analysis of each rib requires another graph to be calculated and drawn, but from a designer point of view only the critical rib is important, but if the location of this critical rib is already know this does not have to be a downside.

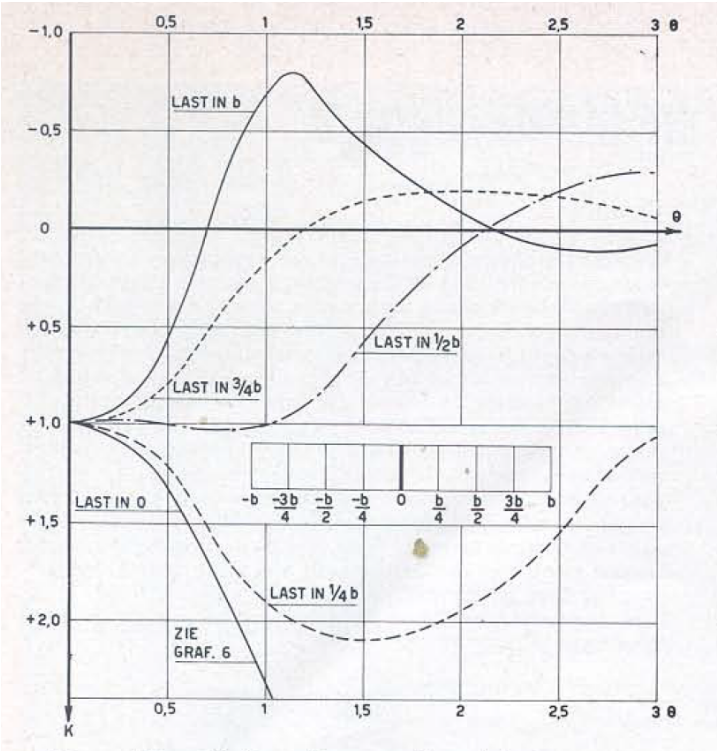

Figure 3.4: A graph depicting the size of the factor K for each location of the load, stiffness of the beams.

PLAATS VAN DE LIGGER	PLAATS VAN DE LAST									Σ K
	− b	− ¾ b	− ½ b	− ¼ b	0	¼ b	½ b	¾ b	b	
0	0,52	0,76	1,01	1,25	1,37	1,25	1,01	0,76	0,52	7,93
¼ b	-0,05	0,28	0,62	0,97	1,24	1,42	1,42	1,38	1,33	7,97
½ b	-0,53	-0,18	0,22	0,62	1,01	1,45	1,82	2,07	2,28	7,89
¾ b	-0,94	-0,52	-0,18	0,29	0,76	1,38	2,08	2,85	3,70	8,04
b	-1,38	-0,92	-0,54	-0,05	0,50	1,32	2,28	3,70	4,90	8,05

Figure 3.5: A side view and front view of a concrete bridge with longitudinal and transverse rib stiffeners

4

MODELLING SUBJECT AND APPLIED LOADS

4.1. MODELLING SUBJECT: THE STEEL PROFILED DECK AND THE COMPOSITE SLAB

The subject of the analytical model will be a composite slab, consisting of a deep profiled steel deck, steel reinforcement and a concrete top layer. An example of a deep steel profiled deck for a composite slab has already been given in section 1.3, figure 1.9. The cross-section of the steel profiled deck is shown in figure 4.1. The steel profiled deck type that is used for modelling purposes in this thesis. The figure shows a single steel deck plate, which consists of two halves of a rib and an intermediate part. Joining two or more of these parts together will form the desired ribbed slab shape.

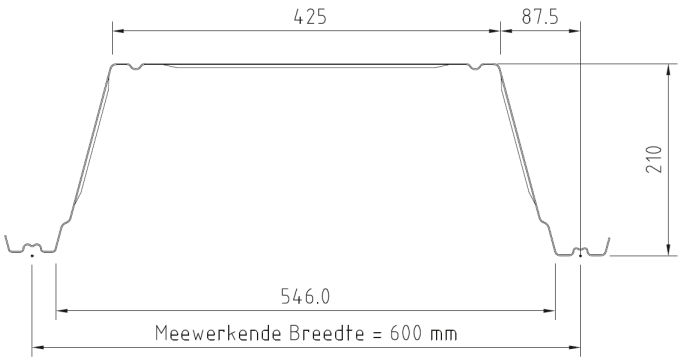

Figure 4.1: A cross-section of the actual steel profiled deck

For the ease of modelling, however, a more generic steel profile will be assumed. The steel profiled deck that is assumed can be seen in figure 4.2, where instead of two halve ribs a single rib is depicted. Because the model will be analytical, the exact dimensions of the modelled slab are not relevant yet at this stage. These dimensions will be parameters in the model and can be adapted to suit any type of steel deck at a later stage. But because the goal is to make comparisons with numerical models and laboratory tests dimensions are eventually needed. It is therefore chosen to use the dimensions shown in this section.
The bottom flange of the steel rib has twice the thickness of the other parts of the steel profile, this is due to the overlapping of the individual steel plates when they are installed. The width of the slab that should be modelled depends on the amount of ribs that is taken into account and the distribution of the force of the concentrated load.

4.1.1. COMPOSITE SLAB DIMENSIONS

The centre-to-centre distance between ribs is 600 mm, so the width of the composite slab that will be modelled should a multiple of that number. The total span length of the slab will be taken at 5.4 meters. Furthermore there is a longitudinal reinforcement bar of variable diameter embedded at a height of 56 mm above the

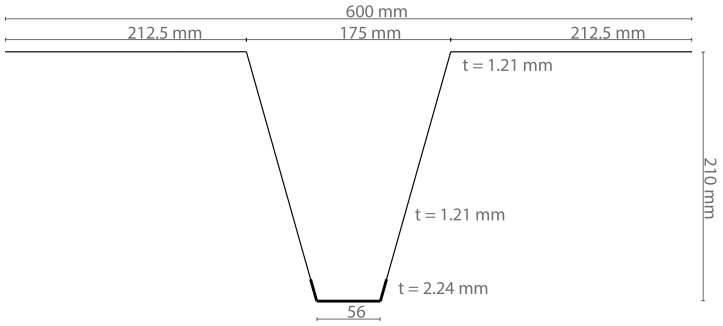

Figure 4.2: The simplified steel profile of a single rib and two halves of the intermediate slab that is used in the analytical model

bottom flange of the steel deck and there are two possible locations for reinforcement meshes in the top part of the composite slab consisting of 8Ø-150 reinforcement meshes. The longitudinal reinforcement bars are located at 27 mm and 48 mm height from the top of the slab respectively and the transverse reinforcement is located at 19 mm and 56 mm respectively from the top. The top concrete slab itself has a height of 70 mm. All of these dimensions can be found in figure 4.3.

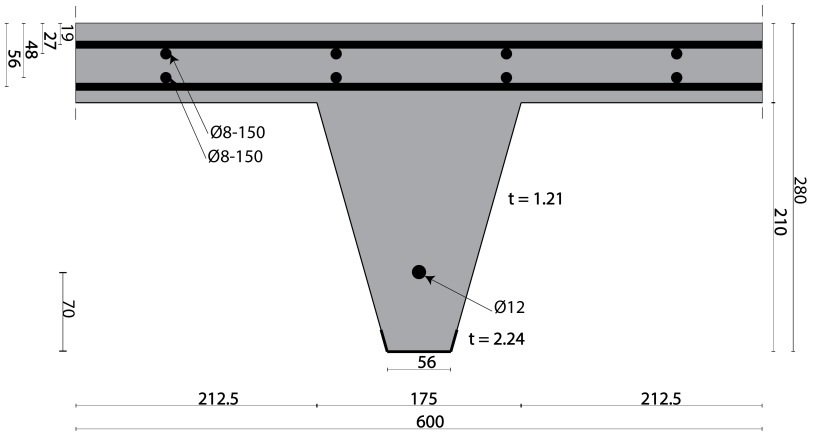

Figure 4.3: The cross-section of a unit width of the composite slab that is to be modelled

4.1.2. EFFECTIVE STEEL PROFILE

The steel profile has embossments pressed into the walls to increase the bond between the concrete and the steel, thus increasing the composite action. The embossments can be observed in the 3D rendering in figure 4.4. The disadvantage of these embossments is that when the slab is loaded by a bending moment, the areas that have been embossed are weakened in the longitudinal direction and do not contribute to the bending capacity.

This results in an effective steel profile that has to be used when bending is considered. This effective profile is shown in figure 4.5 and finally all the symbols associated with the cross-section are shown in figure 4.6.

Figure 4.4: A 3D rendering of a COMFLOR210 deep composite slab

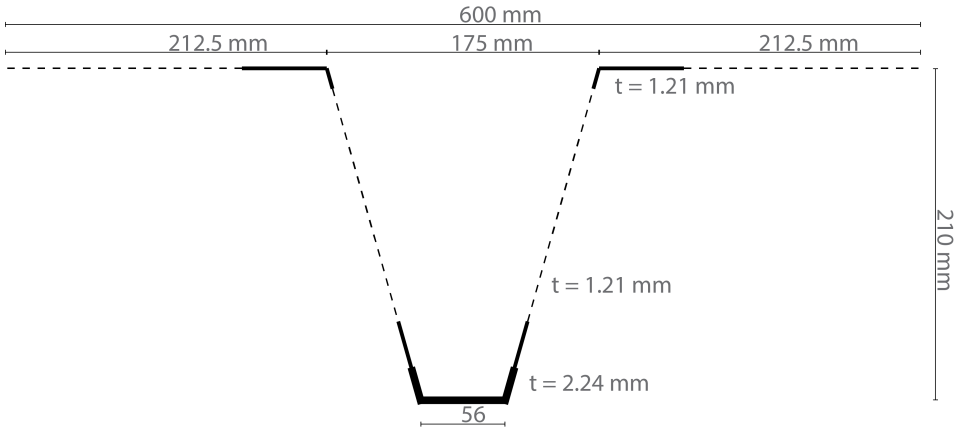

Figure 4.5: The effective cross-section of the steel profile

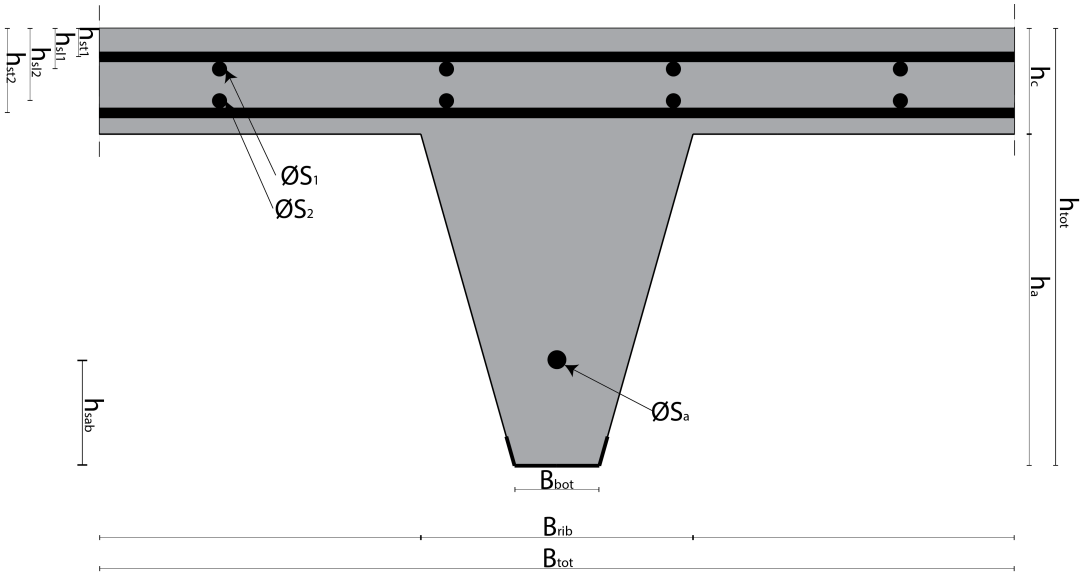

Figure 4.6: The cross-section with the associated symbols

4.2. MATERIAL PROPERTIES

The material properties that will be used in the analytical model are as shown in table 4.1.

Parameters	Symbol	Value	Unit
Concrete class	-	C20/25	-
Characteristic concrete strength	f_{ck}	20	N/mm^2
Concrete Young's modulus	E_c	30000	N/mm^2
Characteristic steel yield strength	f_{yk}	350	N/mm^2
Steel reinforcement yield strength	f_{ysk}	500	N/mm^2
Steel Young's modulus	E_c	210000	N/mm^2
Effective steel profile area	$A_{a,eff}$	572.1	mm^2
Effective steel profile second moment of inertia	$I_{a,eff}$	4.20×10^6	mm^4
Height of neutral axis from top flange	z_{cp}	103.9	mm

Table 4.1: The values of the material properties used in the analytical model.

4.3. BOUNDARY CONDITIONS

In this thesis it will be assumed that the composite slab is simply supported at both sides of the longitudinal span length and the transverse ends are not supported. See also the the top view in figure 4.7. The span length is 5400 mm, the over length of 100 mm on each side and the total length is 5600 mm. The width is 2575 mm.

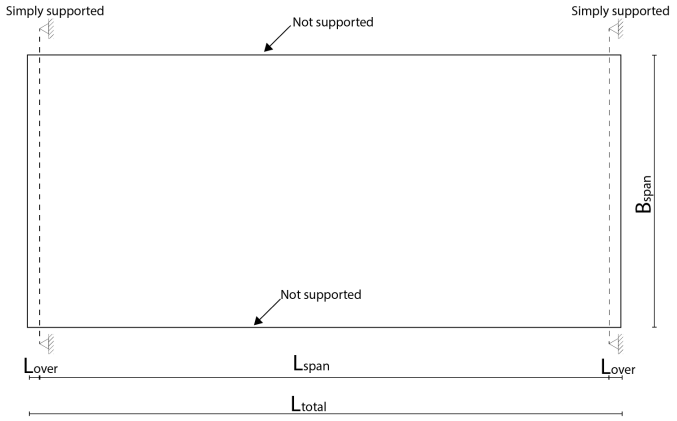

Figure 4.7: The possible locations where the concentrated load F could be placed

However, it is good to note that in practise the composite slab is often integrated into a composite beam by placing it on the bottom flange of a steel beam. Or otherwise it will be fastened on top of a composite beam. In both cases this means that the composite slab is not actually simply supported, since the ribs are cast into the rest of the structure. However, it is chosen to neglect all of these effects mentioned above in this thesis. It is chosen to analyse the simply supported situation first and if that can be modelled correctly, it might be possible to add other boundary conditions.

4.4. THE CONCENTRATED LOAD F AND LOAD-CASES

The concentrated load F will be applied on top of the slab in one or multiple locations. The location of the load can be varied along the longitudinal and/or the transverse axis of the slab. The longitudinal placement of

the load F will be discussed later, since it does affect the distribution but not the type of load case itself and so the transverse placement remains. With regards to the placement of the loads, two load cases are considered in this thesis. They are shown below.

Load-cases

1. Above a rib (in the centre of the rib)
2. Between the ribs

This is illustrated in figure 4.8. These load-cases in turn result into several critical cross-sections (figure 4.9), namely

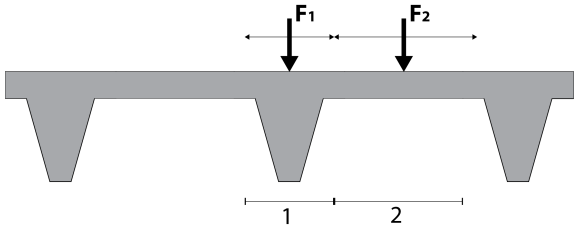

Figure 4.8: The possible locations where the concentrated load F could be placed

Critical cross-sections

1. The rib due to vertical shear or bending moment.
2. The vertical interface between the ribs and the top slab due to vertical shear.
3. The middle of the intermediate top slab due to punching shear.

The research that is done in this thesis only consider the load case in which the load is placed on top of a rib. If one assumes or calculates that the punching shear strength of the top slab is sufficient to bear the load, then load case two will never be critical, since the load will be immediately divided over two ribs. While in load case one the load is concentrated on the single rib in the centre.

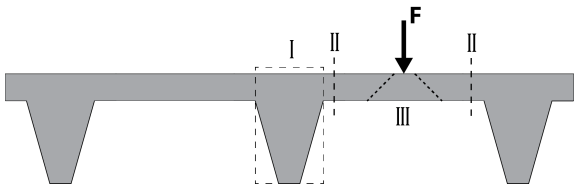

Figure 4.9: The three critical cross-sections are illustrated. Where in I the rib fails in vertical shear or bending, in II the top slab fails in vertical shear and in III the top slab fails in punching shear.

The concentrated load F will be applied on a certain surface depending on the size of the load. This is done in accordance with Eurocode 1 [10], see table 4.2.

Table 4.2: The internal forces in the beam acquired through the equilibrium equations

Load F [kN]	Area of application
≤ 7	50 mm x 50 mm
>10	200mm x 200 mm

It has to be noted though that the 200x200 mm application area of the larger loads are wider than a single rib. It is therefore possible that for the laboratory experiments it will be chosen to use a slightly smaller area of application, such as 150x150 mm.

4.4.1. BENDING MOMENT RESISTANCE OF THE RIB

The bending moment resistance of the ribs is calculated according to Eurocode 4 [1]. The cross-section of the rib consists of several components: the concrete in the compression zone, the top flange of the steel deck, the reinforcement bar in the rib and the bottom flange of the steel deck. First of all the cracking moment is calculated by assuming that only the concrete is active and the reinforcement and steel do not yet participate. By calculating the equilibrium in the section according to figure ???, the respective strains of each of the components can be found. Solving that equilibrium also provides the height of the compressive zone of the concrete. By assuming yielding in the reinforcing steel and the steel profiled deck and then computing the equilibrium the bending resistance of the rib can be obtained. The rib cross-section is assumed to be as is shown in figure 4.6 and also the effective steel profile (figure 4.5) will be used for the following calculations. The values used are shown in table 4.3. By assuming yielding in the steel profiled deck and the reinforcement bar in the rib and computing the horizontal force equilibrium as in equation **??**, the height of the compression zone can be obtained.

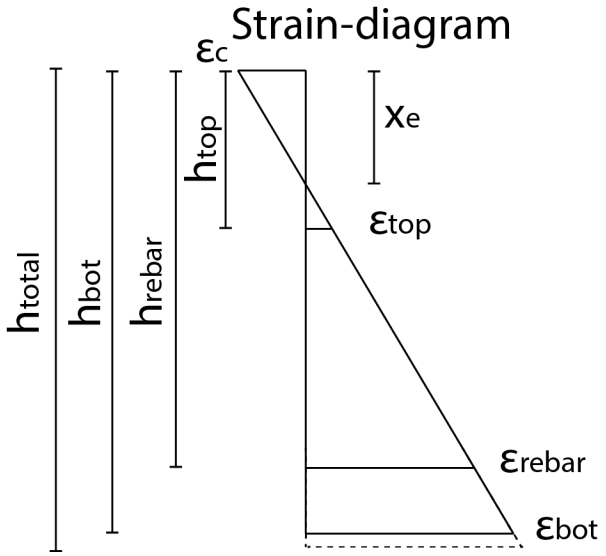

Figure 4.10: A schematic representation of the strains in the cross-section of the rib just after the concrete has cracked.

All parameters that are used in this section are shown in table 4.3. As mentioned before the equilibrium of the section where the concrete just cracked has to be calculated first. The cracking moment of the concrete is calculated in equation 4.1. There the moment of inertia of the concrete consists of the contributions of the top part of the cross-section and the contribution of the concrete in the rib. Again the mean concrete tension strength is taken instead of the characteristic value. Now the equilibrium after the concrete cracks can be determined. This is done with the help of figure 4.10 and the equations for congruent triangles, the horizontal equilibrium and the moment equilibrium. These equations are shown in 4.2, 4.3, 4.4, 4.5 and 4.6 respectively. In these equations x_e is the height of the compressive zone, which is the parameter that is needed.

$$M_{rib,cr} = \frac{f_{ctm} \times I_{conc}}{h_{tot}} = \frac{2.8 \times 1.69 \times 10^8}{270} = 2.44 \times 10^6 Nmm \tag{4.1}$$

Solving the equilibrium equations for the height of the compressive zone provides the value $x_e = 53.45\ mm$. Now the compressive height is know, the following step is to assume that the steel in the rib is yielding and then calculate the moment resistance of the rib's cross-section. The assumption is that the steel of the bottom flange of the steel deck and the rib reinforcement bar are yielding, but not the top flange of the steel deck. When the reinforcement bar just starts yielding at a strain of 1.9×10^{-3}, then through the use of equation 4.7 the strain in the top flange can be found to be 6.02×10^{-4}.

$$\frac{\epsilon_c}{\epsilon_{top}} = \frac{x_e}{h_{top} - x_e} \tag{4.2}$$

$$\frac{\epsilon_c}{\epsilon_{rebar}} = \frac{x_e}{h_{rebar} - x_e} \tag{4.3}$$

$$\frac{\epsilon_c}{\epsilon_{bot}} = \frac{x_e}{h_{bot} - x_e} \tag{4.4}$$

$$\frac{1}{2} b_{tot} x_e \epsilon_c E_{cm} = \epsilon_{top} A_{top} E_a + \epsilon_{rebar} A_{rebar} E_a + \epsilon_{bot} A_{bot} E_a \tag{4.5}$$

$$M_{rib,cr} = \epsilon_{top} A_{top} E_a h_{top} + \epsilon_{rebar} A_{rebar} E_a h_{rebar} + \epsilon_{bot} A_{bot} E_a h_{bot} - \frac{1}{2} \frac{b_{tot} x_e^2 \epsilon_c E_{cm}}{3} \tag{4.6}$$

$$\frac{\epsilon_{top}}{\epsilon_{rebar}} = \frac{h_{top}}{h_{rebar}} \tag{4.7}$$

The first step is to check whether or not the total tension force in the steel does not exceed the compressive force that the concrete in the compression zone can provide. This check is done in equations 4.8 and 4.9. As can be seen the concrete can provide a much higher force than the steel and this check is therefore passed.

$$\begin{gathered} N_{steel} = A_{rebar} \times f_{y,rebar} + f_y \times (A_{top} + A_{bot}) = \\ 314.16 \times 540 + 400 \times (169.40 + 314.60) = 316.91 \times 10^3 N \end{gathered} \tag{4.8}$$

$$N_{conc} = 0.75 \times x_e \times b_{tot} \times f_{cm} = 0.75 \times 600 \times 28 = 673.47 \times 10^3 N \tag{4.9}$$

Now the moment resistance of the rib can be calculated according to equation 4.10.

$$\begin{gathered} M_{rib,k} = A_{top} \times \epsilon_{top} \times E_a \times h_{top} + A_{rebar} \times f_{y,rebar} \times h_{rebar} + A_{bot} \times f_y \times h_{bot} - \frac{N_{steel} \times x_e}{3} = \\ 169.40 \times 2.1 \times 10^5 \times 71.35 + 314.16 \times 540 \times 224 + 314.60 \times 400 \times 262.76 - \frac{316.91 \times 10^3 \times 53.45}{3} = 66.95 \times 10^6 Nmm \end{gathered} \tag{4.10}$$

Of course each rib has to carry its self-weight as well. This load decreases the actual moment capacity $M_{rib,kc}$ of a rib by a certain amount. The bending moment caused by the self-weight of the ribs is calculated in equation 4.11 and the actual moment capacity of the ribs is determined in equation 4.12 and with this the moment capacity of each rib is known.

$$M_{SW} = \frac{1}{8} \times q_{rib} \times L_{span} = \frac{1}{8} \times 1.83 \times 5400 = 6.67 \times 10^6 Nmm \tag{4.11}$$

$$M_{rib,kc} = M_{rib,k} - M_{SW} = 66.95 \times 10^6 - 6.67 \times 10^6 = 60.28 \times 10^6 Nmm \tag{4.12}$$

Table 4.3: The values used to compute the vertical shear resistance of the top slab

Parameter	Symbol	Value	Unit
Mean concrete compressive strength	f_{cm}	28	N/mm^2
Total width of the rib	b_{tot}	600	mm
Height of the reinforcement bar	h_{rebar}	224	mm
Total height of the cross-section	h_{tot}	270	mm
Height of the top flange of the steel deck	h_{top}	71.35	mm
Height of the bottom flange of the steel deck	h_{bot}	262.76	mm
Surface area of the top flange of the steel deck	A_{top}	169.40	mm^2
Surface area of the bottom flange of the steel deck	A_{bot}	314.16	mm^2
Surface area of the reinforcement bar	A_{rebar}	314.16	mm
The moment of inertia of the concrete in the cross-section	I_{conc}	1.69×10^8	mm^4
The mean tensile strength of the concrete	f_{ctm}	2.8	N/mm^2
The Young's modulus of the concrete	E_{cm}	30000	N/mm^2
The Young's modulus of the steel	E_a	2.1×10^5	N/mm^2
The yield strength of the steel deck	f_y	400	N/mm^2
The yield stength of the reinforcement steel	$f_{y,rebar}$	540	N/mm^2
The self-weight of a rib	q_{rib}	1.83	kN/m
The rib span length	L_{span}	5400	mm

5

ANALYTICAL MODELLING

In this chapter the analytical model of a deep composite slab will be presented. The aim of the model is to give an expression for the way in which a concentrated load will be distributed over the width of the deep composite deck. This means that the goal is to find the part of the concentrated load that is carried by each rib. When the concentrated load is placed on the centre rib, the centre rib is likely to carry the largest part of the load e.q. 50% as was the case in the experiment conducted by Bode [14]. The neighbouring ribs will subsequently have lesser parts of the load to carry. The analytical model aims to find how the load is distributed across the ribs of the slab. To achieve this the composite slab will be examined further and then two different preliminary models will be presented. And finally, one or both model will be further expanded into a definite model, which will be validated by a numerical analysis and laboratory testing.
It is chosen to develop two-dimensional models first. This two-dimensional model will span the width of the deep composite slab. After the model in two dimensions is set up the three-dimensional behaviour of the composite plate will be added into the two-dimensional model. The overview of the chapter's components is shown in figure 5.1.

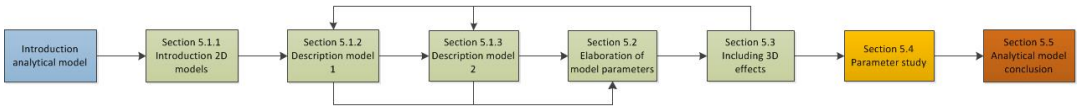

Figure 5.1: The overview above shows the components of which chapter five is made up. If chapters often refer to other components this is also indicated as an arrow.

5.1. DIFFERENT TYPES OF ANALYTICAL TWO-DIMENSIONAL MODELS

Now that it is clear what is to be modelled a choice has to be made in what way is the structure (figure 5.2) going to be represented. Before the three dimensional aspects of the slab will be included into the model a two dimensional model will be constructed. This model can then be expanded to include the three dimensional aspects in a later stage. The models will be based on the thought that the concentrated load will cause the centre rib to deflect. The ribs right next to the centre rib are connected with centre rib through the top slab. Because the neighbouring ribs will lag behind the centre ribs deflection, the top slab will start deforming and through this deformation a part of the force is transferred to the outer ribs, see figure 5.3. Two types of models were considered to model the real shape:

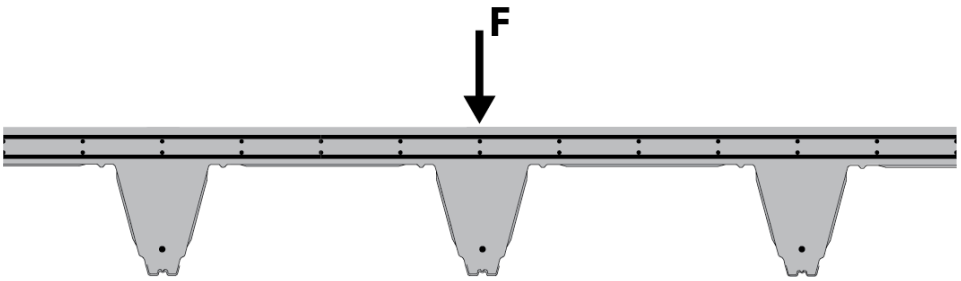

Figure 5.2: A cross-section of the composite slab with three ribs and a load placed on the centre rib.

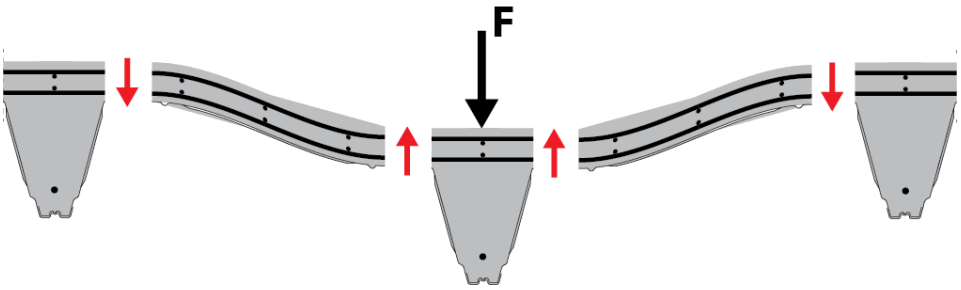

Figure 5.3: A cross-section of the composite slab with three ribs and a load placed on the centre rib. The centre rib has deflected due to the load deforming the top slab in the process which transfers part of the force to the neighbouring ribs.

Analytical models

1. Model with translation springs, rotation springs and stiff bars (figure 5.6)
2. Model with a continuous beam supported by vertical translation springs (figure 5.5)

The first assumption on which the initial models are based is that the ribs function as vertical translation springs, which support the top slab. The distribution of the concentrated force has to take place through the to slab which covers the entire width of the composite slab. Thus the model will focus on modelling the behaviour of the top slab.
In order to further develop the model the composite slab is now thought of as a reinforced concrete slab which is supported by composite ribs. In the two-dimensional model the width of the ribs will be neglected and only the width of the top slab which is not supported by ribs will be used. When the ribs are then thought of as separate simply-supported beams on which the top part of cross-section is supported it becomes possible to give a force-deflection relation to these fictional beams and then they effectively become vertical translation springs. How the stiffness of these vertical translation springs is determined will be discussed in a later section. The result of the assumptions above are shown in figure 5.4.

The next issue is the way in which the top part of the cross-section should be modelled. The concrete of the top part of the slab could be seen as a fictional continuous beam, with a length equal to the width of the composite slab, supported by the rib-springs as depicted in 5.5. This would result in a model of a beam that is loaded by concentrated loads and loads resulting from upwards reaction forces of the ribs. The top part of the composite slab will react much like a beam. This means that the part of the top slab directly above the ribs will be taken into account twice. Once for evaluating the stiffness of the ribs and once for evaluating the stiffness of the top slab. This is not a problem, however, because both stiffnesses work in directions perpendicular to each other. The beam in this model will be supported by the translation springs through hinges. So the beam is free to deform in any shape without being restricted apart from in the vertical direction.
Another option is to model the ribs and intermediate spans between the ribs as separate elements. Then it is possible to include the entire rib as a single rigid element and the intermediate spans both as separate elements. The bars modelling the top slab are assumed as infinitely stiff. The elements have to be connected somehow. Connecting them by rotational springs with a certain stiffness seems the best option, because then the rotation springs can be used to simulate the resistance behaviour of the top slab. The rigid rib elements can only move vertically and are restricted in all other directions. The stiffness of the rotation springs will

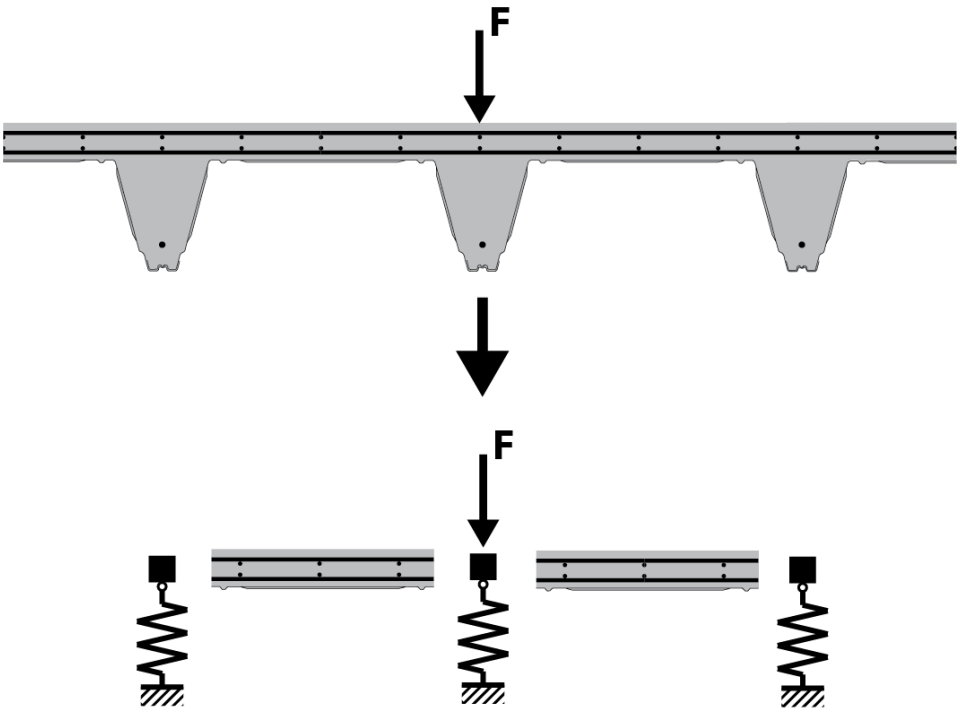

Figure 5.4: The first step in the creation of the two-dimensional model from the cross-section of the composite slab.

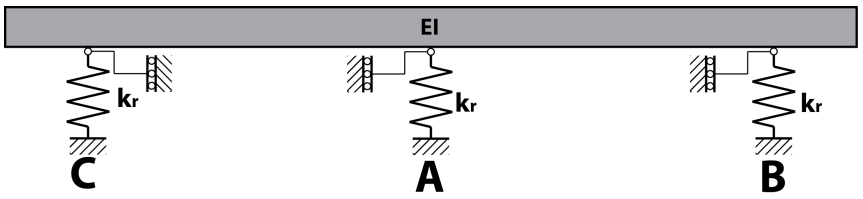

Figure 5.5: Model type 2b: a continuous transverse spanning beam supported by a single translation spring at each rib location

be derived from the deflection-moment relation of a rigidly supported beam that is subjected to support settlement, see figure 5.7. This is meant to model the effect that the top slab will have on the ribs, when a difference in deflection occurs. This model type is shown in figure 5.6.

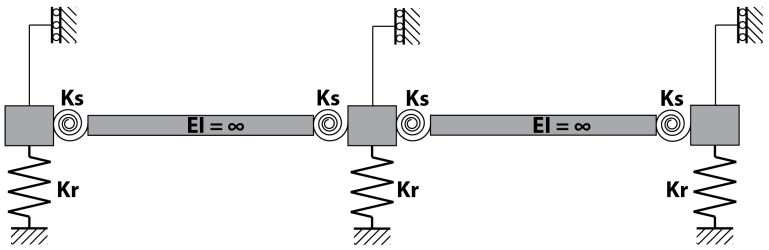

Figure 5.6: Model type 1: a system of rigid elements supported by a translation springs, representing the ribs, connected by bar-elements representing the connecting top-slab

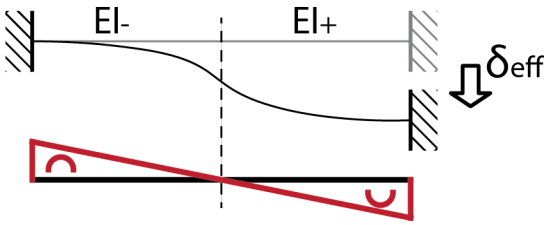

Figure 5.7: Rigidly supported beam subjected to support settlement and the shape of the resulting moment diagram

5.1.1. ASSUMPTIONS AND BOUNDARY CONDITIONS

Before the models can further developed, however, it is imperative that the initial assumptions and boundary conditions of these models are established.

INITIAL ASSUMPTIONS

1. The steel and concrete are complete bonded, thus providing a complete composite cross-section.
2. Concrete does not have any tensile stress capacity.
3. To determine the rib-stiffness the effective steel cross-section has to be used.
4. The bending stiffness of the ribs is initially assumed to be constant over the length of the rib.
5. The load F is positioned on the centre of the middle rib.
6. If the load F is equal to or smaller than 7 kN the load is applied on a 50 mm x 50mm square. If the load is 10 kN or larger it is applied on a 200mm x 200mm square.
7. The self-weight of the construction is initially neglected

BOUNDARY CONDITIONS

1. The ribs are simply supported on either end, allowing for rotation and horizontal translation but restricting vertical translation
2. The slab is supported by two supports, at $x = 0$ and $x = L_{rib}$, but transversely the slab is not supported in any way.

5.1.2. MODEL 1: A SPRING-BAR SYSTEM

In this model the transfer of the load F acting on the system happens trough the rotation of the rotation-springs connecting the bar-elements with the stiff rib-elements, which are in turn supported by the translation-springs. The bar elements are also assumed to be infinitely stiff, since their resistance and rotation capacity is included by the addition of the rotation spring. When the middle rib deflects under the load F and the ribs on either side do not deflect as much a difference in deflection will cause the rotation springs and bar elements to rotate, thus causing a resulting moment in the rotation-springs (figure 5.8). The goal of this model type is to create a model that is easier to solve than by using differential equations to model every intermediate beam.

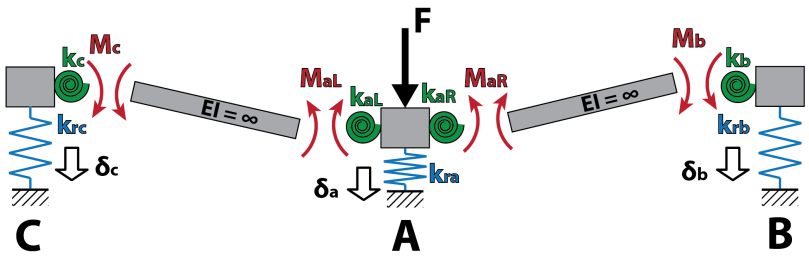

Figure 5.8: Model type 1: showing the resulting moments caused by unequal deflection of the system

Looking at the system the first thing that can be said is that the rotation of the springs on either side of a bar is equal (z-angles). The rotation springs and translation springs are governed by the spring equations 5.1 and 5.2 respectively.

$$M_s = k_s \times \theta_s \tag{5.1}$$

$$F_r = k_r \times \delta_r \tag{5.2}$$

Where: θ_s is the rotation of the bar-elements and δ_r is the deflection of a rib. The system is governed by these two equations. The system does not have any rigid supports and is thus a mechanism. Its equilibrium is derived from the spring stiffnesses. If we examine a rotational-spring closer (figure 5.9) the equilibrium equation can be stated as is done in equation 5.3.

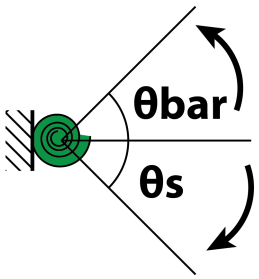

Figure 5.9: A close-up of a rotational-spring with θ_{bar} the rotation caused by the unequal deflection of the ribs and θ_s the rotation caused by the spring reaction.

$$\theta_{bar} - \theta_s = 0 \tag{5.3}$$

Where: the index s denominates variables related to the rotation spring and index r denominates variables related to the translation spring. θ_{bar} is the rotation caused by unequal deflection of the ribs and θ_s is the rotation caused by the reaction in the spring. Because the rotation springs and the bars are connected $Theta_s$ and $Theta_{bar}$ have of course to be equal to each other.
The contribution to the rotation due to bending of the intermediate bars will be neglected because these bars are assumed to be infinitely stiff. This is done because the bars have a width/height ratio of approximately $\frac{1}{6}$ and are therefore very stiff. The rotation θ_{bar} can then be related to the deflection of the ribs according to equation 5.4 (see figure 5.10) and θ_s can be rewritten by using equation 5.1 into equation 5.5.

$$\theta_{bar,ab} = \frac{(\delta_a - \delta_b)}{L_{bar}} \tag{5.4}$$

$$\theta_s = \frac{M_s}{k_s} \tag{5.5}$$

The deflection δ is then expressed into a resultant of the internal shear forces by using figure 5.11, resulting into equations 5.6 and 5.7. The equations state that the deflection must be equal to the net internal force that is exerted on the translation springs.

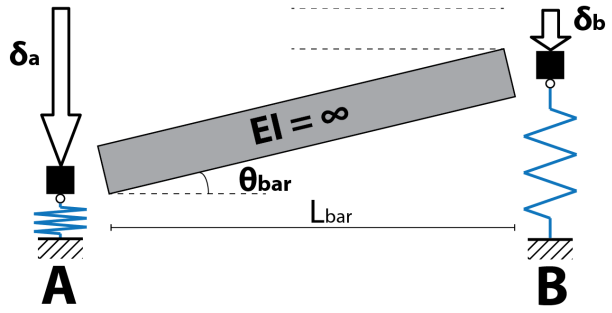

Figure 5.10: A schematic representation of the stiff bar rotating due to a difference in deflection between the central rib A and the outer rib B.

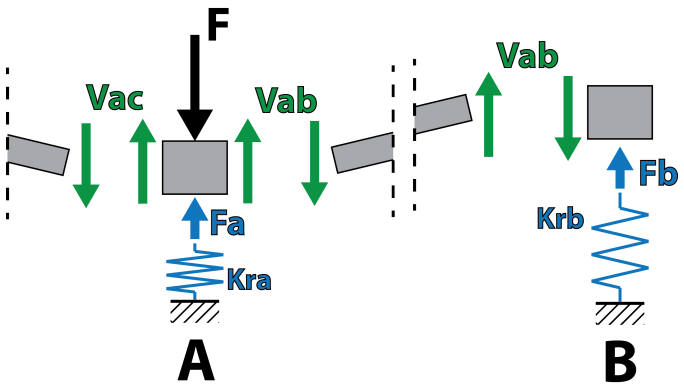

Figure 5.11: The internal shear forces due to the moments caused by the springs and directly caused by the translational-springs

$$\delta_a = \frac{F - V_{ab} - V_{ac}}{k_{ra}} \tag{5.6}$$

$$\delta_b = \frac{V_{ab}}{k_{rb}} \tag{5.7}$$

Because there is no additional load on the intermediate bars apart from the moments on either end, the shear force in the bars must be constant and equal to the value in equation 5.8 (see again figure 5.8).

$$V_{ab} = \frac{M_{aR} + M_b}{L_{ab}} \tag{5.8}$$

Where: V_{ab} is the shear force in the bar, M_{aR} and M_b are the moments acting on both ends of the bar caused by the rotational-springs and L_{ab} is the length of the bar. These moments are caused by the resistance in the rotational-springs due to the rotation of the intermediate bar. Because the rotation of the bar (equation 5.5) is equal on both sides the moments on both ends can be related by equating the rotation at the left-hand side of the bar to the rotation on the right-hand side of the bar according to equation 5.9.

$$\frac{M_{aR}}{k_{aR}} = \frac{M_b}{k_b} \tag{5.9}$$

Now it is possible to insert equations 5.4, 5.5, 5.6, 5.7, 5.8 and 5.9 into equation 5.3 to obtain the spring equilibrium 5.10 equation for the right side of the mechanism. This equation states that the total rotation in the rotation spring M_{aR} due to the movement of the mechanism θ_{bar} must be equal to the resistance in the rotation spring θ_s due to the moment being enacted on it.

$$\theta_{bar,ab} - \theta_{aR} = 0 \rightarrow \frac{(\delta_a - \delta_b)}{L_{bar}} - \frac{M_{aR}}{k_{ar}} = 0 \rightarrow \frac{\frac{F - \frac{M_{aR}(1+\frac{k_b}{k_{aR}})}{L_{ab}} - \frac{M_{aL}(1+\frac{k_c}{k_{aL}})}{L_{ac}}}{k_{ra}} - \frac{\frac{M_{aR}(1+\frac{k_b}{k_{aR}})}{L_{ab}}}{k_{rb}}}{L_{ab}} - \frac{M_{aR}}{k_{aR}} = 0 \tag{5.10}$$

The same equation can be composed for the left-hand side of the mechanism as can be seen in equation 5.11.

$$\theta_{bar,ac} - \theta_{aL} = 0 \rightarrow \frac{(\delta_a - \delta_c)}{L_{bar}} - \frac{M_{aL}}{k_{aL}} = 0 \rightarrow \frac{F - \frac{M_{aR}(1+\frac{k_b}{k_{aR}})}{L_{ab}} - \frac{M_{aL}(1+\frac{k_c}{k_{aL}})}{L_{ac}}}{k_{ra}} - \frac{\frac{M_{aL}(1+\frac{k_c}{k_{aL}})}{L_{ac}}}{k_{rc}} - \frac{M_{aL}}{k_{aL}} = 0 \tag{5.11}$$

These two equations now describe the behaviour of the mechanism. They relate the internal forces that occur to the deflection and to the force that is applied at the central rib. The resistances of the rotation springs k_{aR} and K_{aL} will be determined at a later stage. So that means that there are only two unknowns: M_{aR} and M_{aL}, since the force is known and so is the length of the span. The unknown internal moments that are left can be solved with these two equations (5.10 and 5.11).
Up until now the rotational stiffnesses for all rotation-springs were assumed to be different from each other. But this is not the case, since they are all derived from the same top plate spanning the width of the slab. If it is assumed that only the direction in which the mechanism rotates makes a difference to the rotational-stiffness (just as the stiffness of a beam is different when loaded by a hogging moment or a sagging moment) then all rotational-stiffnesses can be replaced by a upwards stiffness K_{su} and a downwards stiffness K_{sd}. Equations 5.11 and 5.10 then simplify to 5.12 and 5.13.

$$\frac{F - \frac{M_{aR}(1+\frac{k_{sd}}{k_{su}})}{L_{ab}} - \frac{M_{aL}(1+\frac{k_{sd}}{k_{su}})}{L_{ac}}}{k_{ra}} - \frac{\frac{M_{aR}(1+\frac{k_{sd}}{k_{su}})}{L_{ab}}}{k_{rb}} - \frac{M_{aR}}{k_{su}} = 0 \tag{5.12}$$

$$\frac{F - \frac{M_{aR}(1+\frac{k_{sd}}{k_{su}})}{L_{ab}} - \frac{M_{aL}(1+\frac{k_{sd}}{k_{su}})}{L_{ac}}}{k_{ra}} - \frac{\frac{M_{aL}(1+\frac{k_{sd}}{k_{su}})}{L_{ac}}}{k_{rc}} - \frac{M_{aL}}{k_{su}} = 0 \tag{5.13}$$

The acquired system of equations describes a system of three ribs and a single force F acting on the middle rib. By solving it all the unknown internal forces can be found. By using the same methods as done in this section the set of equations can be expanded to include more ribs on either side and more forces acting on any of the ribs, the way in which this was done for five ribs is shown in appendix C. Furthermore is it important to mention that in this approach until now the ribs are assumed to be rigid elements only translating vertically and the connecting bars too are assumed to be rigid elements with an infinite bending stiffness only rotating due to the unequal deflection of the ribs. This will result in a discrete deflection diagram, concentrated in the ribs of which an example is shown in figure 5.12.

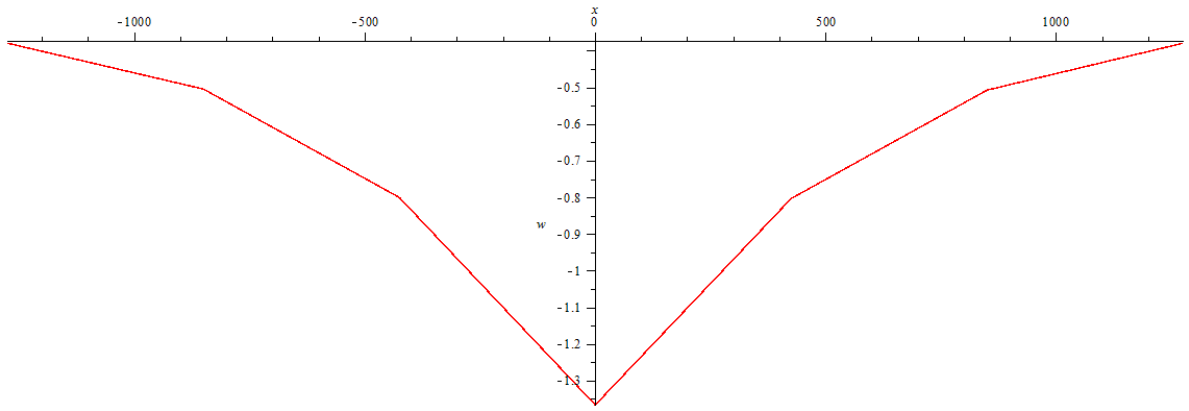

Figure 5.12: An example of the deflection of the composite slab, with five ribs, while being loaded by a concentrated load on the centre rib. Each kink in the deflection diagram indicates the location of a rib

INCLUDING ADDITIONAL FEATURES IN THE MODEL

Up until now the model has only included the vertical translation of the ribs and it was assumed that the bending stiffness of the intermediate beams was constant. This allows for the modelling of a single intermediate beam, as is done in section 5.2.2. The coefficients k_{su} and k_{sd} can be determined by modelling the

intermediate beams with a differential equation. The moments at both ends of the beam can be expressed as functions difference in deflection between two neighbouring ribs.
A problem arises, however, when torsion resistance of the ribs is introduced. When the assumption that the ribs cannot rotate is abandoned, the ribs will rotate due to an effective moment, the difference between the moment acting on the left side and the right side of the rib, that is acting over it. This means that, if one wants to include the effect of the torsional resistance of the ribs, a model se-up that has been used up until now is no longer possible. The internal forces in the ribs and intermediate beams are influenced by internal forces elsewhere in the composite slab and thus a model using differential equations and boundary conditions is more suited to describing this, than one where the moments and deflections are concentrated in single points.
Practically this means that the approach used for model type 1 is no longer possible when including torsion effects. If the torsion stiffness of the ribs is so high, that their rotation can be neglected then this model can still be used. This will result in a deflection diagram similar to figure 5.13. It can be seen that the ribs do not rotate and thus the intermediate beams act as though they have clamped supports, see figure 5.7.

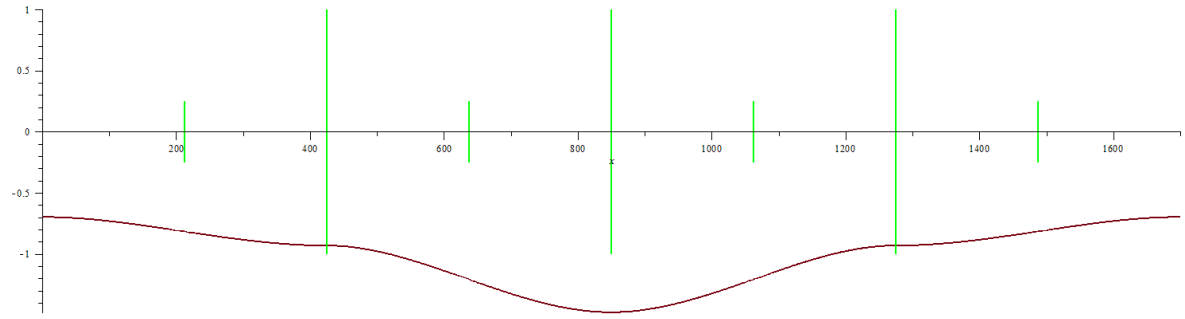

Figure 5.13: An example of the deflection of the composite slab with infinite rib torsion stiffness and with five ribs, while being loaded by a concentrated load on the centre rib. The long vertical green lines indicate the position of the ribs and the short vertical green lines indicate the transition from positive to negative bending moment and vice versa.

CONCLUSION ON MODEL TYPE 1

The goal of this model type was to create a set of equations that is easier to solve than by solving it through differential equations. In the end, however, it is only possible to include rotation of the rib-components when using the differential equation approach. Model type 1 will therefore eventually result in the same modelling type as type 2. The distinction between both of them is thus no longer necessary.

5.1.3. MODEL 2: CONTINUOUS BEAM SUPPORTED BY VERTICAL TRANSLATION-SPRINGS

A second way in which the horizontal spread of the force of the concentrated load could be modelled is by modelling the top concrete part of the cross-section as a single continuous beam supported by the same vertical translation-springs modelling the ribs as seen in the previous section. The deflection of the beam will be characterized by the differential equation for bending in an Euler-bernoulli beam as seen in equation 5.14 (the distributed force q is equal to zero).

$$EI\frac{d^4w}{dx^4} = 0 \tag{5.14}$$

This equation can be integrated to acquire, in turn, expressions for the shear force, moment, cross-section rotation and finally the deflection as seen in equation 5.15.

$$w(x) = \frac{1}{6}C_1x^3 + \frac{1}{2}C_2x^2 + C_3x + C_4 \tag{5.15}$$

Where: w is the deflection of the beam and C_i are the integration constants. This equation is true for every separately appointed field of the beam. Since the differential equation cannot handle any discreet forces or changes, the continuous beam has to be divided into multiple elements, for all of which this equation holds true. Combined with the spring coefficients k_r this makes it possible to calculate how much of the load goes to each rib. The continuous beam has thus been split into two fields, as shown in figure 5.14, from point C to A and from point A to B respectively. All of the ribs could be loaded by a concentrated load and the translation springs also exact a force at the bottom of the slab. The length between each rib is equal to L. Now that the

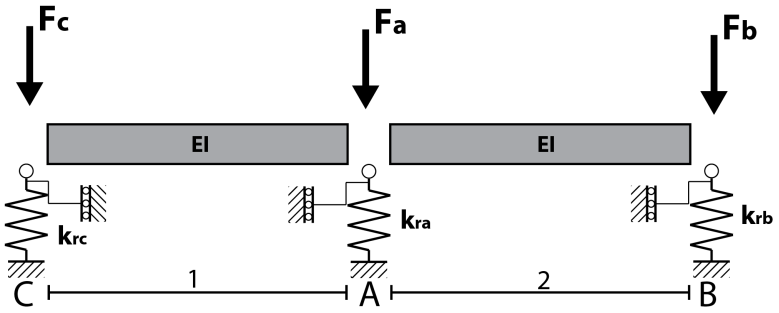

Figure 5.14: A subdivision of the continuous top slab into two separate fields for the application of the differential equation for bending. Each field has a length L

expression for the deflection and the fields to which it has to be applied are known, the next step is to state the boundary conditions and the the interface between two fields the interface conditions. The boundary conditions are stated in table 5.1 and the interface conditions can be found in table 5.2.

Table 5.1: The boundary conditions applied to the differential equations of the continuous beam

Boundary conditions	
$x = 0$	$x = 2L$
$M_1 = 0$	$M_2 = 0$
$V_1 = k_{rc}\,w(0) - F_c$	$V_2 = -k_{rc}\,w(2L) + F_b$

Table 5.2: The interface conditions applied to the differential equations of the continuous beam

Interface conditions
$x = L$
$M_1 = M_2$
$V_1 + V_2 + k_{ra}\,w(L) = F_a$
$\varphi_1 = \varphi_2$
$w_1 = w_2$

These eight equations and the eight unknowns from the expressions for the deflection in both fields result in a solvable system of linear equations, as seen below in equation 5.16. When solved one has acquired the expression for the deflection of the continuous beam and through derivation the cross-section rotation, moment and shear acting in the beam can also be obtained. This system describes only three ribs supporting the top slab, but this method could of course be applied to a slab supported by any number of ribs. One only needs to state the system of equations governing the model, which consist of the same boundary conditions and the interface conditions repeated as many times as there are interfaces between separate fields. A system of five ribs is described in detail in appendix C.

$$\begin{bmatrix} 0 & -1 & 0 & 0 & 0 & 0 & 0 & 0 \\ 1 & 0 & 0 & \frac{k_c}{EI} & 0 & 0 & 0 & 0 \\ -L & -1 & 0 & 0 & L & 0 & 0 & 0 \\ -\frac{L^2}{2EI} & -\frac{L}{EI} & -\frac{1}{EI} & 0 & \frac{L^2}{2EI} & \frac{L}{EI} & \frac{1}{EI} & 0 \\ -\frac{L^3}{6EI} & -\frac{L^2}{2EI} & -\frac{L}{EI} & -\frac{1}{EI} & \frac{L^3}{6EI} & \frac{L^2}{2EI} & \frac{L}{EI} & \frac{1}{EI} \\ 0 & 0 & 0 & 0 & -2L & -1 & 0 & 0 \\ 0 & 0 & 0 & 0 & \frac{k_b(2L)^3}{6EI} - 1 & \frac{k_b(2L)^2}{EI} & \frac{k_b 2L}{EI} & \frac{k_b}{EI} \\ \frac{k_a L^3}{6EI} - 1 & \frac{k_a L^2}{EI} & \frac{k_a 2L}{EI} & \frac{k_a}{EI} & 1 & 0 & 0 & 0 \end{bmatrix} \times \begin{bmatrix} C_1 \\ C_2 \\ C_3 \\ C_4 \\ D_1 \\ D_2 \\ D_3 \\ D_4 \end{bmatrix} = \begin{bmatrix} 0 \\ F_c \\ 0 \\ 0 \\ 0 \\ 0 \\ F_b \\ F_a \end{bmatrix} \tag{5.16}$$

INCLUDING ADDITIONAL FEATURES IN THE MODEL

The base model has now been established. It is, however, not complete yet. The behaviour that it exhibits now is not modelling reality as close as is desirable. In order to accomplish that improvements will now be made. This is done by adding additional features to the existing model and expanding its matrix until a sufficiently accurate model is acquired.

Varying bending stiffness

The system above models a composite slab where the intermediate parts have a constant bending stiffness. This is not a good approximation of reality though, since the top part of the slab has a different bending stiffness depending on the direction of the bending moment. Thus parts of the intermediate slab under a positive bending moment will act stiffer or less stiff than parts under a negative bending moment. This problem can be solved by dividing the intermediate slab into two separate fields, each with its own differential equation. By doing that different bending stiffnesses can be introduced. The result of this extra step can be seen in equation 5.17.

Even now the intermediate slabs have been subdivided into two parts, they are not entirely accurate yet. The bending stiffness of these parts of the slab vary with the direction of the bending moment, but they also vary due to cracking of the concrete. When a certain bending moment is reached, the concrete in the intermediate slabs will start to crack. At this point the bending moment stiffness of these cracked parts will decrease, thus resulting in more variation of the bending stiffness. This can be modelled by dividing the top slabs into yet more fields on which the differential equation is applied. The intermediate slabs are now divided into four separate fields for positive and negative bending moments and for cracked and uncracked sections for each. The result of this addition is a repetition of the steps taken previously, thus the results are not shown here but can be found in appendix C. The model has now been adapted by adding varying bending stiffnesses, the improved model can now be seen in figure 5.15.

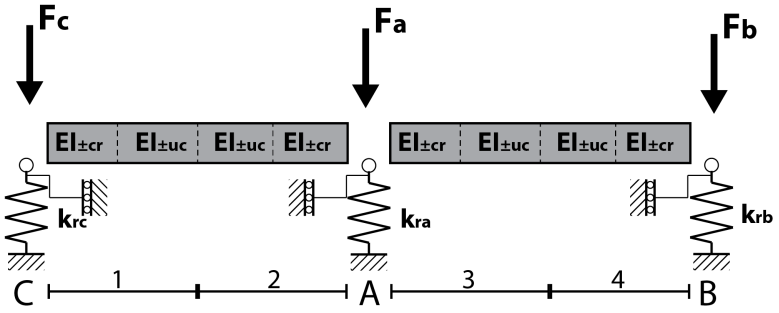

Figure 5.15: Model type 2 has been adapted to allow for varying bending stiffnesses along the length of the top slabs. Each bending stiffness has its own fields with accompanying bending stiffness.

Rotation resistance of the rib components

Modelling the slab in this manner still underestimates the stiffness. Because the slab is connected to the translation springs through freely rotating hinges. This leaves the cross-section of the top slab free to rotate even above the ribs. But in reality the ribs will give some resistance to this rotation because of their torsional stiffness. Again the paragraph about torsion resistance in section 5.2.2 can be used to add this aspect to the model matrix. Doing so will result in the set of equations shown in 5.17. In these equations a_{ac} and a_{ab} are the locations of the interface between two differential equations. These locations can be placed anywhere on the span of an intermediate beam. Thus making it possible to vary the stiffness of the beams according to the directions that are obtained from drawing the moment diagram.

$$
\begin{bmatrix}
\frac{1}{k_{rc}} & 0 & 0 & \frac{1}{EI_-} & 0 & 0 & 0 & 0 & 0 & 0 & 0 & 0 & 0 & 0 & 0 & 0 \\
0 & \frac{1}{k_{rt}} & -\frac{1}{EI_-} & 0 & 0 & 0 & 0 & 0 & 0 & 0 & 0 & 0 & 0 & 0 & 0 & 0 \\
-a_{ac} & -1 & 0 & 0 & a_{ac} & 1 & 0 & 0 & 0 & 0 & 0 & 0 & 0 & 0 & 0 & 0 \\
-\frac{a_{ac}^2}{2EI_-} & -\frac{a_{ac}}{EI_-} & -\frac{1}{EI_-} & 0 & \frac{a_{ac}^2}{2EI_+} & \frac{a_{ac}}{EI_+} & \frac{1}{EI_+} & 0 & 0 & 0 & 0 & 0 & 0 & 0 & 0 & 0 \\
\frac{a_{ac}^3}{6EI_-} & \frac{a_{ac}^2}{2EI_-} & \frac{a_{ac}}{EI_-} & \frac{1}{EI_-} & -\frac{a_{ac}^3}{6EI_+} & -\frac{a_{ac}^2}{2EI_+} & -\frac{a_{ac}}{EI_+} & -\frac{1}{EI_+} & 0 & 0 & 0 & 0 & 0 & 0 & 0 & 0 \\
0 & 0 & 0 & 0 & \frac{k_a L^3}{6EI_+} - 1 & \frac{k_a L^2}{2EI_+} & \frac{k_a L}{EI_+} & \frac{k_a}{EI_+} & 1 & 0 & 0 & 0 & 0 & 0 & 0 & 0 \\
0 & 0 & 0 & 0 & -L & -1 & 0 & L & 1 & 0 & 0 & 0 & 0 & 0 & 0 & 0 \\
0 & 0 & 0 & 0 & -\frac{(L)^2}{2EI_+} - \frac{L}{EI_+} & -\frac{L}{EI_+} - \frac{1}{k_{rt}} & -\frac{L}{EI_+} & 0 & \frac{(L)^2}{2EI_+} + \frac{L}{k_{rt}} & -\frac{L^3}{6EI_+} & \frac{L}{EI_+} + \frac{1}{k_{rt}} & -\frac{L^2}{2EI_+} & \frac{1}{EI_+} & -\frac{L}{EI_+} & -\frac{1}{EI_+} & 0 \\
0 & 0 & 0 & 0 & \frac{L^3}{6EI_+} & \frac{L^2}{2EI_+} & \frac{L}{EI_+} & \frac{1}{EI_+} & -\frac{L^3}{6EI_+} & 0 & 0 & 0 & 0 & 1 & 0 & 0 \\
0 & 0 & 0 & 0 & 0 & 0 & 0 & -1 & 0 & -1 & 0 & 0 & 0 & 0 & 1 & a_{ab} \\
0 & 0 & 0 & 0 & 0 & 0 & 0 & -a_{ab} & -1 & 0 & -\frac{a_{ab}}{EI_+} & 0 & -\frac{1}{EI_+} & 0 & 0 & 0 \\
0 & 0 & 0 & 0 & 0 & 0 & 0 & 0 & -\frac{a_{ab}^2}{2EI_+} & \frac{a_{ab}^3}{6EI_+} & \frac{a_{ab}^2}{2EI_+} & \frac{a_{ab}}{EI_+} & \frac{1}{EI_+} & -\frac{a_{ab}^2}{2EI_-} & -\frac{a_{ab}^3}{6EI_-} & -\frac{a_{ab}}{EI_-} - \frac{1}{EI_-} \\
0 & 0 & 0 & 0 & 0 & 0 & 0 & 0 & \frac{k_b(3L)^3}{6EI} - 1 & \frac{k_b(3L)^2}{2EI} & \frac{k_b(3L)}{EI} & \frac{k_b}{EI} & 1 & 0 & 0 & 0 \\
0 & 0 & 0 & 0 & 0 & 0 & 0 & 0 & 0 & 0 & 0 & 0 & -\frac{(2L)^2}{2EI_-} - \frac{2L}{k_{rt}} & \frac{2L}{EI_-} - \frac{1}{k_{rt}} & \frac{1}{EI_-} & 0 \\
0 & 0 & 0 & 0 & 0 & 0 & 0 & 0 & 0 & 0 & 0 & 0 & -\frac{(2L)^3}{6EI_-} - \frac{1}{k_{rb}} & \frac{(2L)^2}{2EI_-} & \frac{2L}{EI_-} & \frac{1}{EI_-}
\end{bmatrix}
\times
\begin{bmatrix} A_1 \\ A_2 \\ A_3 \\ A_4 \\ B_1 \\ B_2 \\ B_3 \\ B_4 \\ C_1 \\ C_2 \\ C_3 \\ C_4 \\ D_1 \\ D_2 \\ D_3 \\ D_4 \end{bmatrix}
=
\begin{bmatrix} \frac{F_c}{k_{rc}} \\ 0 \\ 0 \\ 0 \\ 0 \\ 0 \\ 0 \\ F_a \\ 0 \\ 0 \\ 0 \\ 0 \\ 0 \\ 0 \\ 0 \\ \frac{F_b}{k_{rb}} \end{bmatrix}
\tag{5.17}
$$

Line load

The model has now been adapted to deal with features like varying bending stiffness and rotation resistance of the ribs. This is good for the load case of concentrated loads on the ribs. It is also possible to add a line load to the model. This will not be part of the laboratory testing but it is a likely load case nonetheless if the model is to be applied to other design situations. Adding a line load can be done by adding a distributed load q to the differential equations used at all separate fields. For this purpose equations 5.14 and 5.15 are modified into equations 5.18 and 5.19 respectively. The line load is then applied over the full width of the model. The results of this adaptation are not shown here and can be viewed in appendix C.

$$
EI\frac{d^4w}{dx^4} = q \tag{5.18}
$$

$$w(x) = \frac{1}{EI}\left(\frac{1}{24}qx^4 + \frac{1}{6}C_1x^3 + \frac{1}{2}C_2x^2 + C_3x + C_4\right) \tag{5.19}$$

CONCLUSION ON MODEL TYPE 2

This model began as a continuous beam with a constant bending stiffness supported by three translation springs and connected by hinges. This was a somewhat unrealistic modelling of reality, so varying bending stiffnesses and rotation resistance by the ribs have been added. A line load can now also be applied to the entire width of the composite slab. It is also possible to expand the model with as many ribs on either side as is wanted and all of them can be loaded by a concentrated force. The deflection, rotation and internal forces are then obtained by through solving the set of linear equations. Expanding the model with more ribs on either side just enlarges the matrix shown above, but does not increase the difficulty of the model. The stiffnesses of the beams, springs and ribs can be adjusted to suit different types of deep steel profiled deck as well. The resulting deflection diagram is a continuous representation instead of a discrete one. Since this approach gives a more accurate model and is not more difficult to solve or adapt it is a definite improvement over model type 1. Therefore from now on only model type 2 will be continued.
A schematic representation of the definite model that will be used is shown in figure 5.16. Here it must be noted that the length fields which have the bending stiffness of the cracked top slab $EI_{\pm cr}$ can be equal to zero. This happens when the bending moment acting in the intermediate slabs never reaches the cracking moment of the top slab cross-section.

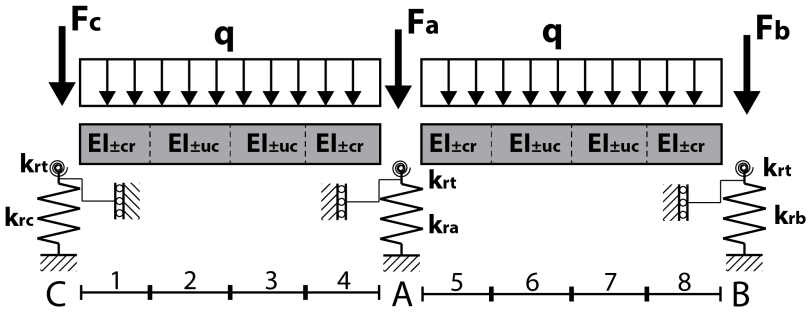

Figure 5.16: The schematic representation of the final version of the model that will be used to study the distribution of a concentrated load acting on a composite slab. The translation springs can only move vertically and are connected to the beam by rotation springs. Each rib can be loaded by a concentrated load if desirable.

5.2. DETERMINING MODEL PARAMETERS

Now that both models have been established, the next step is to determine the constants and parameters that are used in both models. These are the stiffnesses of the rotation-spring and translation-spring and the bending stiffness of the top slab. The top-slab's stiffness and the rotational-spring stiffness can be determined right away because they are both effects that work in the two dimensional plane. The stiffness of the ribs, however, can not be determined yet because this stiffness can vary over the length of the rib. This depends on the degree of loading and whether or not the concrete in the ribs is cracked, not cracked or partially cracked. This will be further explained in section 5.3.1.
One three dimensional aspect that does effect the other two parameters is the distributive length over which the stresses due to the concentrated load F are being distributed. In other words: what length of the top slab is contributing to the transverse distribution of the stress? What is the distributive length L_{dis}? See also figure 5.17. In several sections a value of 200 mm may be assumed for this parameter, but this is as of yet still only an assumption. This topic will be discussed later on.

5.2.1. TOP SLAB STIFFNESS EI_{ts}

The cross-section of the top slab consists of several components similar to the cross-section of the entire slab. A figure of the cross-section of the slab spanning the length between each rib is given in figure 5.18. The bending stiffness of this cross-section can be calculated by adding the contribution of the separate components:

1. the concrete
2. the top mesh (transverse only)

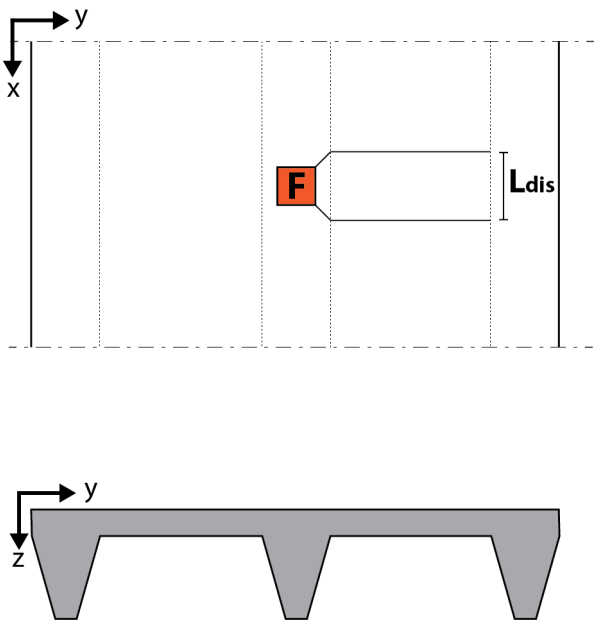

Figure 5.17: A top view of the composite slab loaded by a concentrated load F. The load is distributed to the ribs on both side of the centre rib, but what length of the top slab is contributing to this distribution? This question needs to be answered.

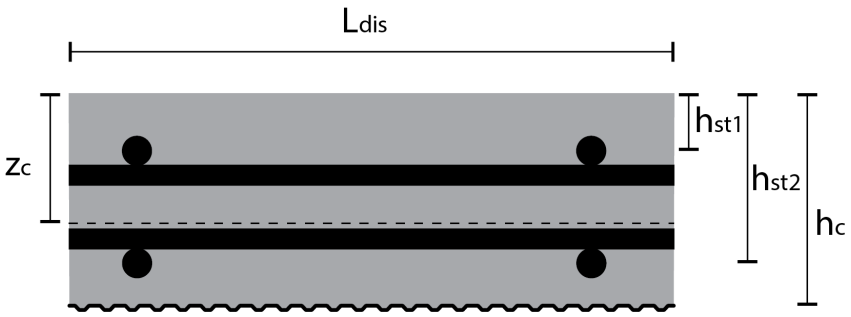

Figure 5.18: A cross-section of a part of the top slab that spans the length between each rib, with a certain distributive length. The parameter z_c indicates the height of the neutral axis in the cross-section.

3. the top mesh (transverse only)

The contribution of the steel profiled deck is neglected because, due to the embossments, the profiled deck will not be able to contribute much. The deck is not sufficiently anchored in the length to assume that the deck will contribute. Also, because the meshes being optional, the bending stiffness depends slightly on whether or not reinforcement meshes are present. When the meshes are not present the effective height of the cross-section from the concrete compression zone to the active reinforcement will change and this greatly influences the the bending stiffness.
Since the top slab can also be loaded by a negative bending moment, the bending stiffness in the negative direction is also of importance. This is especially true when only one of the reinforcement meshes (e.g. the top mesh) is present, since then the arm between the concrete compression zone and the effective tensile reinforcement becomes very small, resulting in a low effective bending stiffness. The different bending stiffnesses for both positive and negative moments and with two meshes, only the top mesh and no meshes are all shown in table 5.3 and all different situations are illustrated in figure 5.19. A detailed description of this computation is written in appendix D.

Table 5.3: The different bending moment stiffnesses of the intermediate slab, depending on the reinforcement meshes and with a distributive length of 200 mm.

Effective bending stiffness $EI_{ts}[Nmm^2]$ $(L_{dis} = 200mm)$		
	Positive moment	Negative moment
both reinforcement meshes	1.52×10^{11}	1.26×10^{11}
Only top reinforcement mesh	4.91×10^{10}	1.58×10^{11}
No reinforcement mesh	$1.72 * 10^{11}$	$1.72 * 10^{11}$

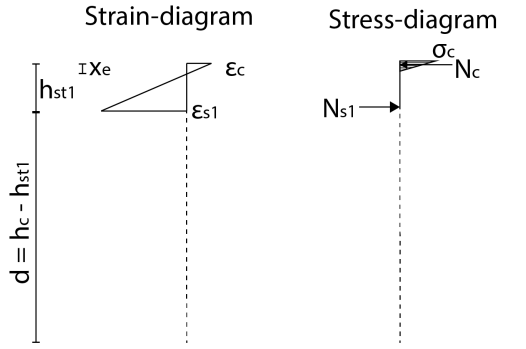

(a) The stress and strain diagram resulting from a positive bending moment on a cross-section with only the top reinforcement mesh.

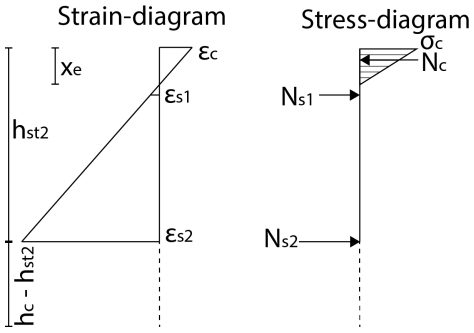

(b) The stress and strain diagram resulting from a positive bending moment on a cross-section with both the top and the bottom reinforcement meshes.

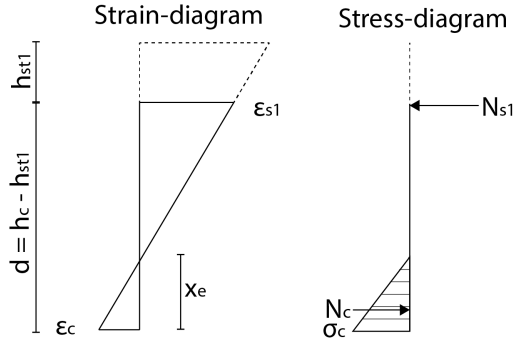

(c) The stress and strain diagram resulting from a negative bending moment on a cross-section with only the top reinforcement mesh.

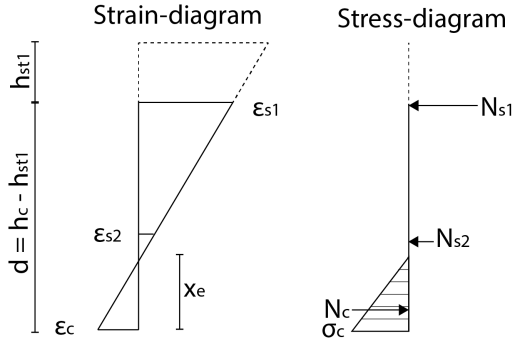

(d) The stress and strain diagram resulting from a negative bending moment on a cross-section with both the top and the bottom reinforcement meshes.

Figure 5.19: Both stress and strain diagrams resulting from a positive and negative bending moments acting on the cross-section of the top part of the composite slab.

PLASTIC BEHAVIOUR OF THE TOP SLAB

Now the bending stiffness of the top slab in the transverse direction is known it can be used in the analytical model. But now another question arises: how does the top slab behave when is no longer in the linear elastic zone? Here it will be assumed that the top slabs have a M-κ relation as shown in figure 5.20. This means that after reaching the plastic limit of the top slab, the point at which the reinforcement steel starts yielding, the moment cannot further increase despite the rotation of the cross-section increasing.

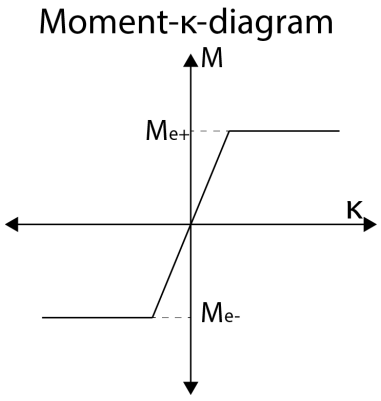

Figure 5.20: The assumed rotation-moment relation of the top slabs.

When this is combined with the relation between the bending moment and the rotation of a cross-section which is shown equation 5.20, the bending stiffness of the top slab in the plastic zone can be obtained. The increasing rotation in the cross-section and the constant bending moment mean that the bending stiffness of the top slab has to decrease continuously after the plastic phase is reached. This continues until a certain rotation value is reached where failure will occur. Failure will likely occur because the increasing rotation will become too much for the concrete in the compressive zone and that concrete will be crushed. Only the concept of this calculation is discussed here. The precise values that will be used are calculated and shown in appendix D.

$$M = EI \times \kappa \tag{5.20}$$

5.2.2. ROTATION-SPRING k_s STIFFNESS AND INTERMEDIATE SLAB STIFFNESS

This variable is important for both model type 1 and type 2. The rotation spring coefficient k_s determines the traverse distribution of the load of model type 1 in a large manner and the bending stiffness of the top slab functions in the same manner for model type 2. It is therefore important that this parameter is examined carefully. First it has to be established where the rotation resistance comes from.

CLAMPED INTERMEDIATE TOP SLAB

The intermediate parts of the top slab are considered as clamped beams that under go a certain support settlement at one side as shown in figure 5.21. They are considered clamped because they are connected to the ribs, which will resist rotation. The top slab is modelled in this way because it is rigidly connected to the ribs and the difference in deflection between the middle rib and a rib next to it can be combined into a single effective deflection δ_{eff}. When the beam depicted is subjected to the support settlement the bending

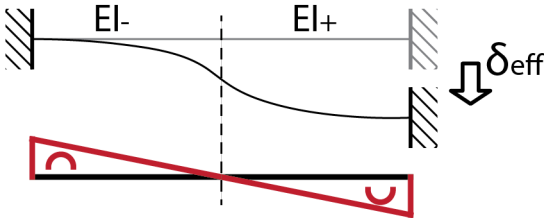

Figure 5.21: A rigidly supported beam subjected to support settlement and the resulting shape of the moment diagram

stiffness of the beam will resist this reflection. If this beam is then analysed through the differential equation

for bending it is possible to obtain a relation between the deflection and the moments at both ends of the beam. This relation is the rotation stiffness coefficient of parameter k_s and thus the goal of this section.

One complication, however, arises when the bending stiffness of the beam is observed. If the bending stiffness of the deflecting beam is constant over its length the moments at both ends will be equal to one and another. But it has to be kept in mind that the intermediate top slab has a different bending stiffness when it is loaded by negative bending moment. So instead of a constant bending stiffness over the beam length, a beam with two different stiffnesses has to be examined. This can still be done by using the differential equation but the beam has to be divided into two fields. Because of the difference in stiffness the moments at both ends of the beam will not be equal and thus the distance at which the moment changes signs (from positive to negative and vice versa) is not known and has to be found as well. Thus the beam in figure 5.22 is examined. Since there are again two differential equations, this problem can as before be stated in a set of linear

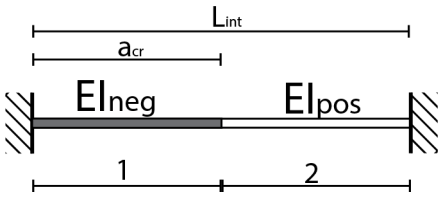

Figure 5.22: The rigidly supported beam divided into two fields with the unknown distance a_{cr} the distance of the start of the negative bending zone to the closest support

equations through the use of boundary conditions. The boundary and interface conditions used are shown in table 5.4 and the distance a acts effectively as an additional unknown and can be expressed as is done in equation 5.21. To solve this new unknown one extra boundary condition is needed, therefore there are 9 in total.

Table 5.4: The boundary conditions applied to the differential equations of the deflected beam

Boundary conditions	
$x = 0$	$x = L$
$w_1 = 0$	$w_2 = \delta_{eff}$
$\varphi_1 = 0$	$\varphi_2 = 0$
Interface conditions	
$x = a$	
$V_1 = V_2$	
$M_1 = 0$	
$M_2 = 0$	
$\varphi_1 = \varphi_2$	
$w_1 = w_2$	

$$a = M_1 \frac{L_{int} - a}{M_2} = \frac{M_1 L}{M_1 + M_2} \tag{5.21}$$

The set of linear equations that is obtained by stating these boundary conditions by means of the integration constants of the differential equations is shown in equation 5.22. While solving this set, equation 5.23 will come up and from this equation, when neglecting the trivial and negative solution, a can be solved. The

equation for a is given in 5.24.

$$\begin{bmatrix} 0 & 0 & 0 & 1 & 0 & 0 & 0 & 0 \\ 0 & 0 & 1 & 0 & 0 & 0 & 0 & 0 \\ -1 & 0 & 0 & 0 & 1 & 0 & 0 & 0 \\ -a & -1 & 0 & 0 & 0 & 0 & 0 & 0 \\ 0 & 0 & 0 & 0 & -a & -1 & 0 & 0 \\ -\frac{a^2}{2EI_-} & -\frac{a}{EI_-} & -\frac{1}{EI_-} & 0 & \frac{a^2}{2EI_+} & \frac{a}{EI_+} & \frac{1}{EI_+} & 0 \\ \frac{a^3}{6EI_-} & \frac{a^2}{2EI_-} & \frac{a}{EI_-} & \frac{1}{EI_-} & -\frac{a^3}{6EI_+} & -\frac{a^2}{2EI_+} & -\frac{a}{EI_+} & -\frac{1}{EI_+} \\ 0 & 0 & 0 & 0 & -\frac{L^2}{2EI_+} & -\frac{L}{EI_+} & -\frac{1}{EI_+} & 0 \\ 0 & 0 & 0 & 0 & \frac{L^3}{6EI_+} & \frac{L^2}{2EI_+} & \frac{L}{EI_+} & \frac{1}{EI_+} \end{bmatrix} \times \begin{bmatrix} C_1 \\ C_2 \\ C_3 \\ C_4 \\ D_1 \\ D_2 \\ D_3 \\ D_4 \end{bmatrix} = \begin{bmatrix} 0 \\ 0 \\ 0 \\ 0 \\ 0 \\ 0 \\ 0 \\ \delta_{eff} \end{bmatrix} \tag{5.22}$$

$$D_1 \left[\frac{1}{2} a^2 (n-1) + aL - \frac{L_{int}^2}{2} \right] = 0 \tag{5.23}$$

$$a = \frac{-L_{int} + \sqrt{nL_{int^2}}}{n-1} \tag{5.24}$$

In which n is the ratio between the positive bending stiffness and the negative bending stiffness of the top slab $n = EI_+/EI_-$, C_i and D_i are the integration constants and a is the distance of the beam over which a negative moment is acting. With this expression for the distance a and the set of linear equations stated above, the moments at both ends of the beam can be expressed as a coefficient times the rotation of the intermediate slab between the ribs. These coefficients are the values for the rotation spring stiffness that are needed for model 1.

ROTATING INTERMEDIATE BEAM SUPPORTS

While the supports of the intermediate beam were considered clamped, this is of course not entirely true. The ribs will resist rotation of the intermediate beams, but they cannot resist this rotation completely and the supports are thus now the supports will be modelled as being rotation springs instead. The stiffness of this spring is provided by the torsion resistance of the ribs.

Torsional moment resistance coefficient of the ribs

The ribs will undergo a rotation due to the deflection caused by the acting load. This rotation will in turn cause a resisting torsion moment. The rotation in an element due to a torsional moment is determined through equation 5.25.

$$\theta = \frac{TL}{JG} \tag{5.25}$$

Where T is the torsional moment, L is the length of the beam, G is the shear modulus and J is the moment of inertia of the beam. The shear modulus of concrete is calculated according to equation 5.26, with a poisson-ratio ν_c for concrete of 0.2. The moment of inertia of a rectangular beam is estimated through the usage of the formula shown in 5.27.

$$G_c = \frac{E_c}{2(1+\nu_c)} = \frac{30000}{2(1+0.2)} = 12500 N/mm^2 \tag{5.26}$$

$$J = \beta a b^3 \tag{5.27}$$

Where J is the moment of inertia, a is the length of the long side of the rectangle and b is the short side of the rectangle and β is a coefficient that can be determined with table 5.5. Using the information above, the rib is then approximated by two rectangles, one representing the top part of the slab with the dimensions $B \times L$ of 270×70 and the other representing the actual rib itself with the dimensions of 115.5×210. Then, by combining equations 5.25, 5.26 and 5.27, the torsion stiffness coefficient of the rib can be computed as is done in 5.28. The value is multiplied by two,because the torsional moment is applied in the middle of the rib span and thus both sides of the composite slab resist half of the applied moment.

$$k_{rt} = 2 \times \frac{JG}{L} = 2 \times \frac{(0.278 \times 270 \times 70^3 + 0.213 \times 210 \times 115.5^3) \times 12500}{5400} = 8.77 \times 10^8 Nmm \tag{5.28}$$

Table 5.5: A table with approximations for the value of $beta$

a/b	β
1.0	0.141
1.5	0.196
2.0	0.229
2.5	0.249
3.0	0.263
4.0	0.281
5.0	0.291
6.0	0.299
10.0	0.312
∞	0.333

Rotating support modelling for the intermediate slab

Having calculated the torsion stiffness coefficient of the ribs, the reaction of the intermediate slab can be determined again, but now including the rotation stiffness at the supports instead of a clamped support. The boundary conditions are almost the same, save for the rotation conditions, as can be seen in table 5.6. These

Table 5.6: The boundary conditions applied to the differential equations of the deflected beam including the rotation at the supports

Boundary conditions	
$x = 0$	$x = L$
$w_1 = 0$	$w_2 = \delta_{eff}$
$\varphi_1 = \varphi_0$	$\varphi_2 = \varphi_L$
Interface conditions	
$x = a$	
$V_1 = V_2$	
$M_1 = 0$	
$M_2 = 0$	
$\varphi_1 = \varphi_2$	
$w_1 = w_2$	

boundary conditions then result in the set of equations as shown in 5.29, the changes in the matrix compared to the clamped intermediate beam have been highlighted.

$$\begin{bmatrix} 0 & 0 & 0 & 1 & 0 & 0 & 0 & 0 \\ 0 & \frac{\mathbf{1}}{\mathbf{k_{rt}}} & -\frac{1}{EI_-} & 0 & 0 & 0 & 0 & 0 \\ -1 & 0 & 0 & 0 & 1 & 0 & 0 & 0 \\ -a & -1 & 0 & 0 & 0 & 0 & 0 & 0 \\ 0 & 0 & 0 & 0 & -a & -1 & 0 & 0 \\ -\frac{a^2}{2EI_-} & -\frac{a}{EI_-} & -\frac{1}{EI_-} & 0 & \frac{a^2}{2EI_+} & \frac{a}{EI_+} & \frac{1}{EI_+} & 0 \\ \frac{a^3}{6EI_-} & \frac{a^2}{2EI_-} & \frac{a}{EI_-} & \frac{1}{EI_-} & -\frac{a^3}{6EI_+} & -\frac{a^2}{2EI_+} & -\frac{a}{EI_+} & -\frac{1}{EI_+} \\ 0 & 0 & 0 & 0 & -\frac{L^2}{2EI_+} - \frac{\mathbf{L}}{\mathbf{k_{rt}}} & -\frac{L}{EI_+} - \frac{\mathbf{1}}{\mathbf{k_{rt}}} & -\frac{1}{EI_+} & 0 \\ 0 & 0 & 0 & 0 & \frac{L^3}{6EI_+} & \frac{L^2}{2EI_+} & \frac{L}{EI_+} & \frac{1}{EI_+} \end{bmatrix} \times \begin{bmatrix} C_1 \\ C_2 \\ C_3 \\ C_4 \\ D_1 \\ D_2 \\ D_3 \\ D_4 \end{bmatrix} = \begin{bmatrix} 0 \\ 0 \\ 0 \\ 0 \\ 0 \\ 0 \\ 0 \\ \delta_{eff} \end{bmatrix} \tag{5.29}$$

Solving the set of equations above results in the following expression for the distance a. With n again being the ratio of the different bending stiffnesses $n = EI+/EI-$.

$$a = \frac{-L - \frac{2EI_+}{k_{rt}} + \sqrt{nL^2 + \frac{2EI_+}{k_{rt}}(1 + n + \frac{2EI_+}{Lk_{rt}})}}{n-1} \tag{5.30}$$

The expression above is similar to that of the one found before and indeed when $k_{rt} = \infty$ is used, the previous expression for a is again obtained. There is, however, another major difference between the result just obtained and the previous modelling with clamped supports. The initial rotation of ribs is dependant on the moment at both sides of the rib that are exerted on it. This means that the modelling of the intermediate beam cannot simply be used to obtain coefficients relating the moment at the beam ends to the deflection any more. Since the moments in other intermediate beams are also influencing the moments in this intermediate beam. The only option is therefore to integrate the modelling of this intermediate beam into a single model as it is done for model type 2.

CRACKING OF THE INTERMEDIATE SLABS

Differences of the bending stiffness in the intermediate slabs have now been introduced by dividing them into multiple fields each with its own differential equation and bending stiffness. The bending moment stiffness, however, does not only vary due with the direction of the acting bending moment. It is also influenced by whether the intermediate slabs are cracked or not.

5.2.3. RIB BENDING STIFFNESS EI_r

The bending stiffness of the rib component is not constant throughout the loading of the slab. After a certain threshold of the applied bending moment is reached the concrete in the rib, apart from that in the compressive zone, will start to crack. It is assumed that the now cracked concrete has a lowered Young's modulus. The entire cross-section will get a decreased bending stiffness as a result of the cracking of the concrete. It is now assumed that only the concrete in the troughs of the profiled steel deck cracks and that the concrete layer on top serves as the compression zone. Another assumption is that the cracked concrete has a Young's modulus equal to a third of the uncracked concrete or 10000 N/mm^2 in this particular case.
With these assumptions the bending stiffness for the uncracked rib cross-section $EI_{rib,uc}$ and the bending stiffness for the cracked rib cross-section $EI_{rib,cr}$ can both be calculated by using figure 5.23. The results of this process are shown in table 5.7 for easy comparison and a detailed description of this computation is given in appendix D.

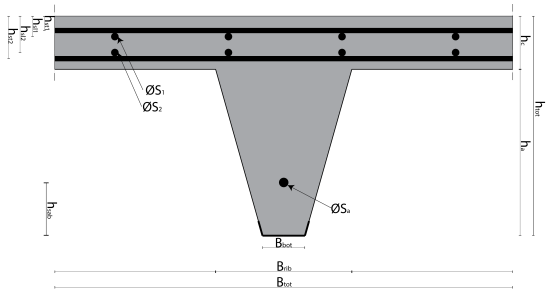

Figure 5.23: The cross-section of a rib

Table 5.7: This table displays an overview of the bending stiffness of the cracked ribs with or without the presence of the reinforcement meshes in the top part of the cross-section.

Situation	**Uncracked bending stiffness** $EI_{rib,uc}$ $[Nmm^2]$	**Cracked bending stiffness** $EI_{rib,cr}$ $[Nmm^2]$	$\frac{EI_{rib,cr}}{EI_{rib,uc}} \times 100$ **[%]**
Both top and bottom reinforcement mesh	1.337×10^{13}	8.688×10^{12}	64.98
Only top reinforcement mesh	1.331×10^{13}	8.688×10^{12}	65.15
No top or bottom mesh	1.315×10^{13}	8.688×10^{12}	65.40

5.2.4. ASSUMPTIONS MADE IN THE TWO-DIMENSIONAL MODEL

Here all the assumptions made in this section are summarized to give a clear overview of them.

- Concrete does not have any tensile stress capacity.
- To determine the rib-stiffness the effective steel cross-section has to be used.
- The load F is only located on the centres of a rib.
- If the load F is equal to or smaller than 7 kN the load is applied on a 50 mm x 50mm square. If the load is 10 kN or larger it is applied on a 200mm x 200mm square.
- After cracking of the concrete in the ribs occurs, it is assumed that only the concrete in the steel troughs is cracked.
- It is assumed that the cracked concrete has a Young's modulus equal to $^1/_3$ of the uncracked Young's modulus. This equals to a stiffness of 10000 N/mm^2 for C20/25 concrete.
- The steel deck does not contribute to the transverse bending stiffness of the top slab.
- The bars connecting the ribs in model 1 are infinitely stiff.
- The steel deck profile is reduced to the effective profile when loaded by a bending moment.

5.3. EXPANDING THE MODEL TO INCLUDE THREE-DIMENSIONAL EFFECTS

Now that the two dimensional models have been established the next step is to discuss three dimensional effects into the models. The effects that will be discussed are:

- The varying bending stiffness EI of the rib.
  - Due to cracking of concrete
  - Due to differences in support stiffness or settlement
- The distributive length L_{dis} over which the concentrated load is distributed transversely.
- The position of the concentrated load F with regards to the distance to the supports.

5.3.1. THE TRANSLATION-SPRING STIFFNESS k_r AND DISTANCE OF LOAD F TO THE SUPPORTS

The translation-spring with a stiffness K_r has already been mentioned in the previous section. It plays a prominent role in both model 1 and model 2, because the ribs support the top slab. The ribs could be seen as fictional beams supporting the slab on top. For these fictional beams a relation between the deflection and the force applied can be found by using the differential equation for bending. This differential equation assumes, however, an uniform bending stiffness over the length of the beam and this is not true for the ribs. The concrete in the ribs will start to crack after a certain load threshold is reached and then their bending stiffness will decrease. The rib will then consist of partially uncracked and a partially cracked sections.

Another aspect that exerts its influence when expanding the models to include to include three dimensional effects is the location of the concentrated load F. Since when the load F is placed closer to the supports of the slab, the slab will be stiffer than when it is placed at the center of the span. Because this issue is closely related to the determination of k_r, they will be examined together.

CONSTANT STIFFNESS

First the case where the bending stiffness EI_{rib} of the rib is uniform is assumed, see figure 5.24. The rib is modelled as a simply supported beam loaded by a concentrated load F at a distance a from support A and b is the distance from the load to support B. Where a always is the shortest distance of a and b. This results in the moment diagram of figure 5.25. The beam has a constant bending stiffness EI_{uc} and a length : L_{rib}. From

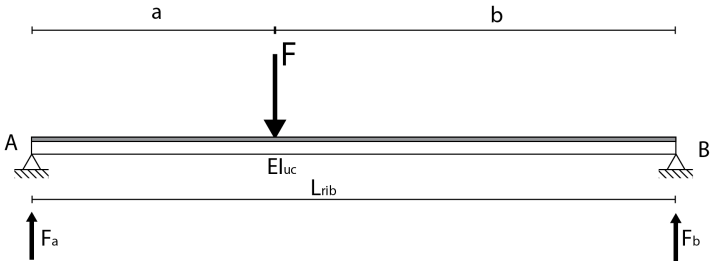

Figure 5.24: The longitudinal cross-section of a rib

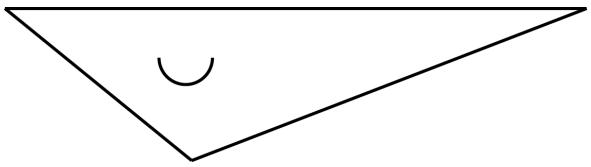

Figure 5.25: The moment diagram of a rib loaded by a concentrated load at distance a

the equilibrium equations the support forces F_a, F_b and the moment at the location of the load M_c can now be obtained; they are displayed in table 5.8. The beam has to be divided into two parts, because the moment

Table 5.8: The internal forces in the beam acquired through the equilibrium equations

Forces	Epressions
Support force F_a	$\frac{Fb}{a+b}$
Support force F_b	$\frac{Fa}{a+b}$
Moment M_c	$\frac{Fab}{a+b}$

diagram contains a kink so it cannot be covered by a single differential equation. The left side of the moment diagram can be expressed according to equation 5.31 and when the moment is equated to the second order differential of the deflection 5.33 is obtained. This can then be integrated to obtain equations 5.34 and 5.31.

$$M(x) = \frac{Fb}{a+b}x \tag{5.31}$$

$$EI\frac{d^2w}{dx^2} = -M(x) = -\frac{Fb}{a+b}x \tag{5.32}$$

$$EI\frac{dw}{dx} = -EI\varphi(x) = -\frac{1}{2}\frac{Fb}{a+b}x^2 + C_1 \tag{5.33}$$

$$EIw(x) = -\frac{1}{6}\frac{Fb}{a+b}x^3 + C_1x + C_2 \tag{5.34}$$

The next step is to apply the boundary conditions shown in table 5.9, the resulting values for the integration constants are also shown. The deflection $w(x)$ can then be written as done in 5.35, by simplifying and replacing b by $(L_{rib} - a)$ equation 5.36 is acquired. Because the deflection will be the largest at $x = a$, this value is assumed for x and thus equation 5.37 is obtained.

Table 5.9: The boundary conditions applied to the differential equations of the simply supported beam

Boundary	$x = 0$	$x = a$
Condition	$w(x) = 0$	$\varphi(x) = 0$
Result	$C_2 = 0$	$C_1 = \frac{1}{2}\frac{Fba^2}{a+b}$

$$w(x) = \frac{1}{EI}\left(-\frac{1}{6}\frac{Fb}{a+b}x^3 + \frac{1}{2}\frac{Fba^2}{a+b}x\right) \tag{5.35}$$

$$w(x) = \frac{F(L_{rib} - a)}{6EIL_{rib}}\left(-x^3 + 3a^2x\right) \tag{5.36}$$

$$w(a) = \frac{Fa^3(L_{rib} - a)}{3EIL_{rib}} \tag{5.37}$$

If this formula is now rewritten to fit the format of a spring $F = k * u$, then the spring-coefficient k_{rib} for the translation spring is now obtained, see 5.38. When this formula is checked by taking $a = \frac{1}{2}L_{rib}$ it is obtained that $k_{rib} = \frac{48EI}{L_{rib}^3}$, which is indeed the stiffness coefficient of a simply supported beam loaded by a concentrated load at mid span.

$$k_{rib} = \frac{3EIL_{rib}}{a^3(L_{rib} - a)} \tag{5.38}$$

VARYING STIFFNESS IN STEPS

Now that the spring coefficient is obtained for a rib with an uniform bending stiffness, it is time to look at a rib with a non-uniform bending stiffness. It is assumed that there are now two bending stiffnesses in the rib: a bending stiffness for the uncracked parts of the rib EI_{uc} and a bending stiffness for the cracked parts of the rib EI_{cr}. The load F is still applied at a distance a from support A. It is assumed that the rib cross-section will crack after a certain threshold moment M_{cr} is reached. The length of the uncracked zone on the shorter side of the rib is now called d. In figure 5.37 the newly modelled rib is displayed and in figure 5.37 the moment diagram belonging to the rib is shown. For the length a of the rib two differential equations have to be posed

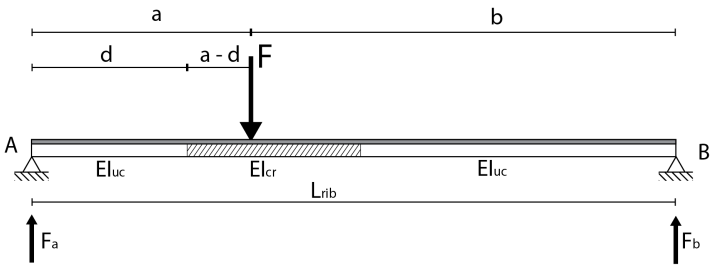

Figure 5.26: The longitudinal cross-section of a rib with a cracked zone and two uncracked zones

because the bending stiffness differs between the two newly created zones. So in order to have two fields with a constant bending stiffness field one with a deflection $w_1(x)$ is taken from $x = 0$ to $x = d$ and field two with a deflection $w_2(x)$ is taken from $x = d$ to $x = a$. Where d is related to M_{cr}, F and a according to equation 5.39 and d should be taken as 5.40.

$$d = \frac{M_{cr}}{F}\frac{a+b}{b} = \frac{M_{cr}}{F}\frac{L_{rib}}{L_{rib} - a} \tag{5.39}$$

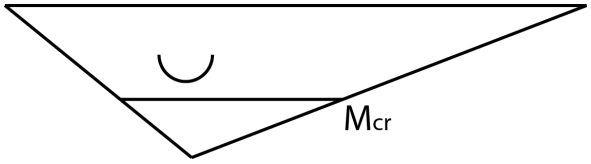

Figure 5.27: The moment diagram belonging to the cracked rib

$$d = \begin{cases} \frac{M_{cr}}{F}\frac{L_{rib}}{L_{rib}-a} & \text{if } 0 \leq \text{d} \leq \text{a} \\ a & \text{if d} \geq \text{a} \end{cases} \tag{5.40}$$

Now the same differential equations can be posed and integrated for both fields as done for the rib with a constant bending stiffness. This is done in equations 5.41, 5.42, 5.43, 5.44, 5.45 and 5.46.

$$EI_{uc}\frac{d^2w_1}{dx^2} = -M_1(x) = -\frac{Fb}{a+b}x \tag{5.41}$$

$$EI_{uc}\frac{dw_1}{dx} = -EI\varphi_1(x) = -\frac{1}{2}\frac{Fb}{a+b}x^2 + C_1 \tag{5.42}$$

$$EI_{uc}w_1(x) = -\frac{1}{6}\frac{Fb}{a+b}x^3 + C_1x + C_2 \tag{5.43}$$

$$EI_{cr}\frac{d^2w}{dx^2} = -M_2(x) = -\frac{Fb}{a+b}x \tag{5.44}$$

$$EI_{cr}\frac{dw_2}{dx} = -EI\varphi_2(x) = -\frac{1}{2}\frac{Fb}{a+b}x^2 + D_1 \tag{5.45}$$

$$EI_{cr}w_2(x) = -\frac{1}{6}\frac{Fb}{a+b}x^3 + D_1x + D_2 \tag{5.46}$$

Again the boundary conditions of the previous section can be applied as seen in table 5.10. But because there

Table 5.10: The boundary conditions applied to the differential equations of the simply supported beam

Boundary	$x = 0$	$x = a$
Condition	$w_1(x) = 0$	$\varphi_2(x) = 0$
Result	$C_2 = 0$	$D_1 = \frac{1}{2}\frac{Fba^2}{a+b}$

are now two fields another set of two interface conditions are needed to ensure that they represent one beam with continuous deflection and rotation. The interface conditions at $x = d$ are as shown in table 5.11. The

Table 5.11: The boundary conditions applied to the differential equations of the simply supported beam

Interface	$x = d$
Condition 1	$\varphi_1(d) = \varphi_2(d)$
Condition 2	$w_1(d) = w_1(d)$

continuation of the moment has already been secured by using the same slope for the moment diagram in both functions. The result from interface condition 1 is that C_1 is now known, this is shown in equation 5.47 and the result from interface condition 2 (by inserting C_1)is the value for D_2 as shown in equation 5.48.

$$C_1 = \frac{1}{2}\frac{Fbd^2}{a+b}\left(1 - \frac{EI_{uc}}{EI_{cr}} + \frac{EI_{uc}}{EI_{cr}}\frac{a^2}{d^2}\right) \tag{5.47}$$

$$D_2 = \frac{1}{6}\frac{Fbd^3}{a+b}\left(1 - \frac{EI_{cr}}{EI_{uc}}\right) + \frac{1}{2}\frac{Fbd^3}{a+b}\left(\frac{EI_{cr}}{EI_{uc}} - 1 + \frac{a^2}{d^2}\right) - \frac{1}{2}\frac{Fba^2d}{a+b} \tag{5.48}$$

At this point it becomes convenient to introduce the constant $n = \frac{EI_{uc}}{EI_{cr}}$, while noting that for this constant $n \geq 1$ should hold true. The found constants C_1 and D_2 can now be rewritten to equations 5.49 and 5.50.

$$C_1 = \frac{1}{2}\frac{Fbd^2}{a+b}\left(1-n+n\frac{a^2}{d^2}\right) \tag{5.49}$$

$$D_2 = \frac{1}{6}\frac{Fbd^3}{a+b}\left(3\frac{a^2}{d^2}+\frac{2}{n}-2\right)-\frac{1}{2}\frac{Fba^2d}{a+b} \tag{5.50}$$

By introducing these found expressions into the expression for the deflection, equations 5.51 and 5.52 are obtained.

$$w_1(x) = \frac{Fb}{6EI_{uc}(a+b)}\left[-x^3+3d^2\left(1+n\left[\frac{a^2}{d^2}-1\right]\right)\right] \tag{5.51}$$

$$w_2(x) = \frac{Fb}{6EI_{cr}(a+b)}\left[-x^3+3a^2(x-d)+d^3\left(3\frac{a^2}{d^2}+\frac{2}{n}-2\right)\right] \tag{5.52}$$

Again we are only interested in the deflection at a, so we put $x = a$ and $b = (L_{rib} - a)$ into the expression for the deflection w_2 and then through a small simplification equation 5.53 is acquired. This formula can be checked by using $n = 1$ and $d = a$ and when these values are used equation 5.37 is indeed found. The spring coefficient k_{rib} when parts of the rib are cracked is thus found to be equal to equation 5.54.

$$w_2(a) = \frac{F(L_{rib}-a)}{6EI_{cr}L_{rib}}\left[2a^3-d^3\left(2-\frac{2}{n}\right)\right] \tag{5.53}$$

$$k_{rib} = \frac{6EI_{cr}L_{rib}}{(2a^3-d^3\left(2-\frac{2}{n}\right))(L_{rib}-a)} \tag{5.54}$$

COMPOSITE SLAB SELF-WEIGHT

Up until now only the concentrated load has been included into the model. A line load can be applied to the top slab, but the self-weight of the composite slab has not yet been included. The self-weight of the composite slab will be applied to the ribs as a line load, since it affects the moment distribution in the ribs and thus the size of the area of the ribs where the concrete is cracked. It also affects the deflection and the load capacity of the ribs.

The self-weight of the composite slab exercises a bending moment on the ribs as does the concentrated load. The shape of the bending moment is parabolic and both bending moment diagrams can be added to each other. The formula for the bending moment can then be expressed as is done in equation 5.55. When equating the expression for the bending moment in the ribs with the cracking moment calculated for the ribs M_{cr} the value for which the cracking moment is reached d can again be found. This is shown in equation 5.56. This equation is parabolic and the solution is shown in equations 5.57 and 5.58.

$$M(x) = \frac{1}{2}qx^2 - \frac{Fbx}{L_{rib}} - \frac{1}{2}qL_{rib}x \tag{5.55}$$

$$M(x) = \frac{1}{2}qx^2 - \frac{Fbx}{L_{rib}} - \frac{1}{2}qL_{rib}x = -M_{cr} \tag{5.56}$$

$$d_{1,2} = \frac{L_{rib}^2q+2F(L_{rib}-a)+\sqrt{L_{rib}^4q^2+4FL_{rib}^2(L_{rib}-a)q+aF^2(L_{rib}-a)^2-8qL_{rib}^2M_{cr}}}{2qL_{rib}} \tag{5.57}$$

$$d_{1,2} = \frac{L_{rib}^2q+2F(L_{rib}-a)-\sqrt{L_{rib}^4q^2+4FL_{rib}^2(L_{rib}-a)q+aF^2(L_{rib}-a)^2-8qL_{rib}^2M_{cr}}}{2qL_{rib}} \tag{5.58}$$

Of the two answers found d_2 is the answer that was desired and that gives the distance at which the concrete in the ribs will be cracked when loaded by a concentrated load and a distributed load. Using the expression d_2 to find the rib translation stiffness coefficient as stated in the previous paragraph includes the effect of the self-weight of the composite slab into the model.

Of course the self-weight also induces some deflection in the composite slab and has to be resisted and thus takes up some bending moment capacity. When both of these aspects examined when predicting the behaviour of the experiment the effect the self-weight has needs to be kept in mind.

5.3.2. THE DISTRIBUTIVE LENGTH L_{dis}

The distributive length has been named before in previous sections. This variable is not an actual material or geometrical variable, but stems from the type of modelling that was chosen, see figure 5.28 and 5.29. It was chosen to approach the modelling the three-dimensional composite slab by composing a two-dimensional model first for the width of the composite slab and to incorporate three-dimensional aspects that are relevant into that model. These two-dimensional models can span the entire width of the composite slab. But the length of the two-dimensional model along the rib is not easily determined.

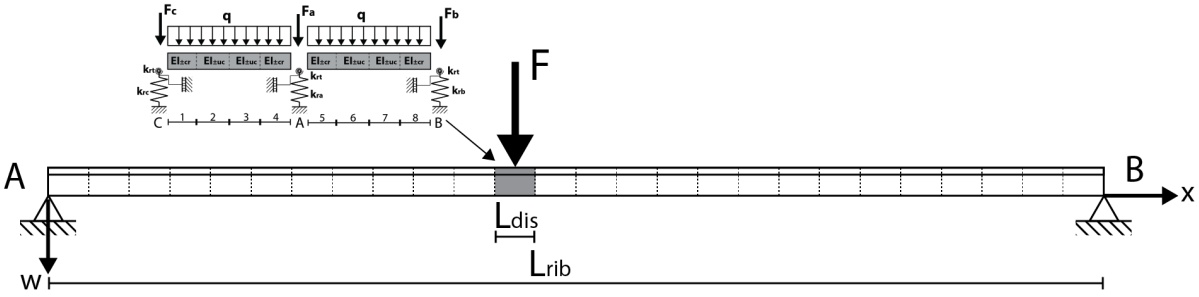

Figure 5.28: The ribs are divided longitudinally into discrete elements. Each one of these elements is modelled using the two-dimensional model that was developed. The element coloured grey is analysed here with regard to the distribution of the force F.

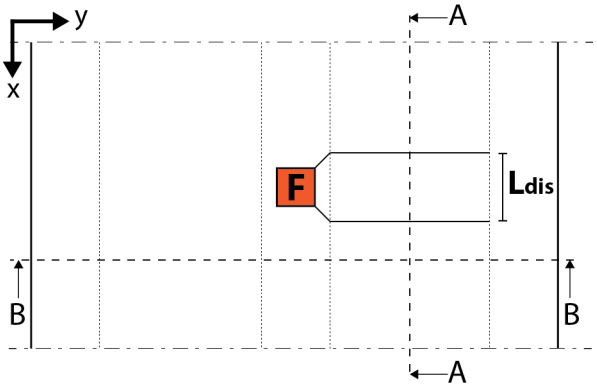

(a) A top view of a composite slab consisting of three ribs, with the concentrated load F placed on the central rib.

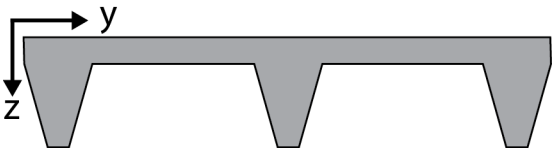

(b) Cross-section B-B of the composite slab, showing a schematic picture of the three ribs and the top slab of the composite slab.

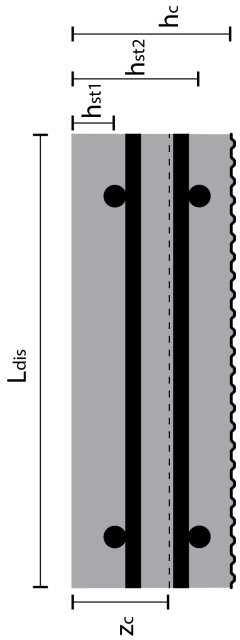

(c) Cross-section A-A of the composite slab, showing the top slab with the transverse reinforcement over the distributive length but not the reinforcement or the steel deck.

Figure 5.29: The top view of the composite slab and two details, showing the effective length.

The distributive length is a factor when determining the bending stiffness of the top part of the composite slab and thus effects the distribution of the concentrated load over the width of the composite slab indirectly. A smaller distributive length will result in a less stiff top slab and thus a smaller distribution of the concentrated load. Vice versa this is also true: longer distributive lengths result in a stiffer top slab in the model and thus a greater spread of the load. This raises the question: how large should the distributive length L_{dis} be chosen? It is not a physical property of the materials used or a geometrical property of the composite slab. This distributive length is an imaginary factor introduced into the model to cope with the fact that a two-dimensional model is used to make predictions about a three-dimensional composite slab. The influence on

the distribution along the width is quite large thus it will not satisfy to just guess a value for the distributive length. This section describes the manner in which the distributive length is estimated.

DISTRIBUTIVE WIDTH AND DISTRIBUTIVE LENGTH

The size of the distributive length that is chosen does not affect the distribution along the length of the rib. But it certainly affects the horizontal distribution. This is due to the fact that the distributive length influences the bending stiffness of the top slab (the larger the distributive length, the higher the bending stiffness of the top slab in the model becomes). And the ratio of the bending stiffness and the stiffness of the translation springs determine in what way the load is distributed. This effect will be discussed further in section 5.4.
In order to acquire an estimation of the distributive length the following approach will be used:

1. Assume a number for the distributive length L_{dis} (e.g. 200 mm).
2. Calculate the distribution of the concentrated force over the ribs using the analytical model.
3. Using the distribution from the model (in percentages per rib) compute a representative distributive width B_{dis}
4. Use the distributive width in a new model to determine the distribution of a force over the length of a rib to determine the distributive length L_{dis}.
5. Repeat steps 1 through 4 until a stable solution has been reached.

Distributive width B_{dis}

By distributive width B_{dis} it is meant that the output of the analytical model as a percentage of the concentrated load per rib will be converted in a width measurement of the composite slab that is supposed to contributed towards the bearing of the load. A similar problem is tackled with concrete ribbed slabs in Eurocode 2 [2], see the extract from Eurocode 2 in figure 5.30. But whereas the Eurocode rules are empirical, in this case the model output provides some support. The question is though: how to define an distributive width.
The stresses in the top slab will be largest at the location of loading in the rib and will slowly decay when moving away from the loading location. This will have a shape similar to figure 5.30. However, since it is hard to calculate with different or varying stress levels. It is easier to assume the stress to be equally distributed over an distributive length.

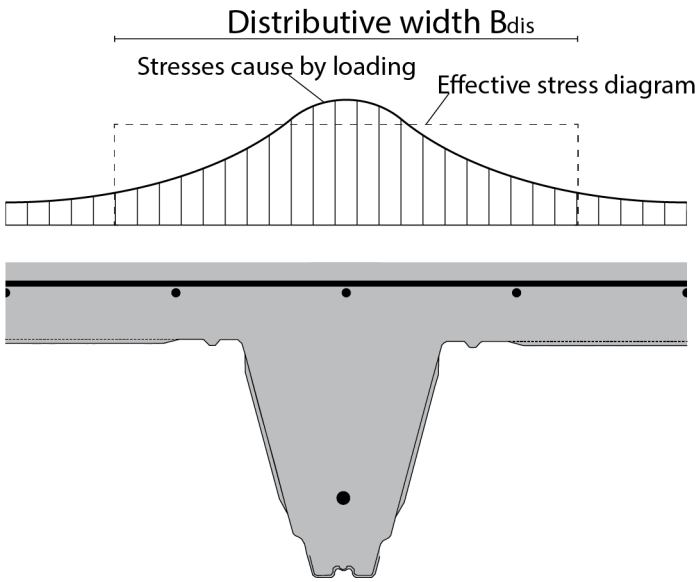

Figure 5.30: A schematic representation of the stress diagram caused by an acting concentrated load and the block of equal stress with a length of the distributive width representing the same load.

The shape of the stress diagram is not clear yet though. The model output gives the percentage of the concentrated load that is borne per rib. If one assumes that the ribs all are a point on the stress diagram of the

transverse stresses in the composite slab. And if one then looks at the percentage that is borne in the centre, neighbouring and outer ribs then three points on the stress diagram are known. Plotting an S-curve through these points will give an approximation of the stress diagram. The basic formula used to construct this S-curve is shown as in equation 5.59.

$$S-curve(x) = A + \frac{B}{C + e^{Dx+E}} \tag{5.59}$$

Where A,B,C,D and E are constants that can be adjusted to suit the output of the analytical model. The result is a family of S-curves as shown in figure 5.32. Converting the curves into a block with width B_{eff} and an equal stress requires certain assumptions. The assumptions made about the stress block are as follows.

1. The integral of the stress block and the S-curve are equal
2. The height of the stress block is equal to 80 % of the maximum stress of the curve.
3. When the load percentage in the centre rib exceeds 80% it is chosen to take the stress block height as 85% off the centre rib percentage.

It is chosen to use a slightly higher stress block when the load is more concentrated on the centre rib. This is done in order to avoid using stresses that are much lower than the actual occurring peak stresses in a rib. Using the three assumptions above the width of the stress block can be calculated and those blocks are also shown in the figure along with the curves. In table 5.12 the variables used for the examples displayed in the figure 5.32 are shown. With that the distributive width correlating with the output of the two dimensional model is known. The exact manner of calculation of the distributive width B_{eff} is shown in equation 5.60. When the loading percentage of the centre rib exceeds 80%, equation 5.61 is used instead.
Whenever the distributive width increases, eventually the width will increase to encompass more than one rib. The analytical model delivers the percentage of the total load that is carried by each rib. The stress distribution in between the ribs is not known. In order to still make an estimation about the distributive width with the S-curve, it is assumed that the stresses follow the S-curve along with width of the composite slab with the output of the analytical model being points on the curve, see figure 5.31. This method overestimates the stresses that are carried by the parts between the ribs and thus overestimates the distributive width. This fact needs to be kept in mind, since it does influence the final results.

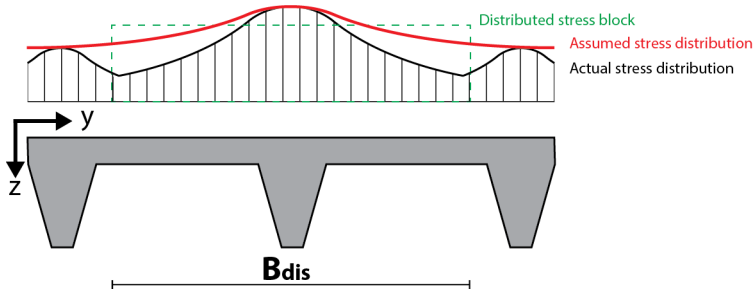

Figure 5.31: A schematic representation of the stress diagram caused by an acting concentrated load on three ribs and the block of equal stress with a length of the distributive width representing the same load.

$$B_{dis} = 2 \times \frac{\int_{Rib_3}^{Rib_1} S-curve(x)}{0.80 \times Rib_{1,\%}} \tag{5.60}$$

$$B_{dis} = 2 \times \frac{\int_{Rib_3}^{Rib_1} S-curve(x)}{0.85 \times Rib_{1,\%}} \tag{5.61}$$

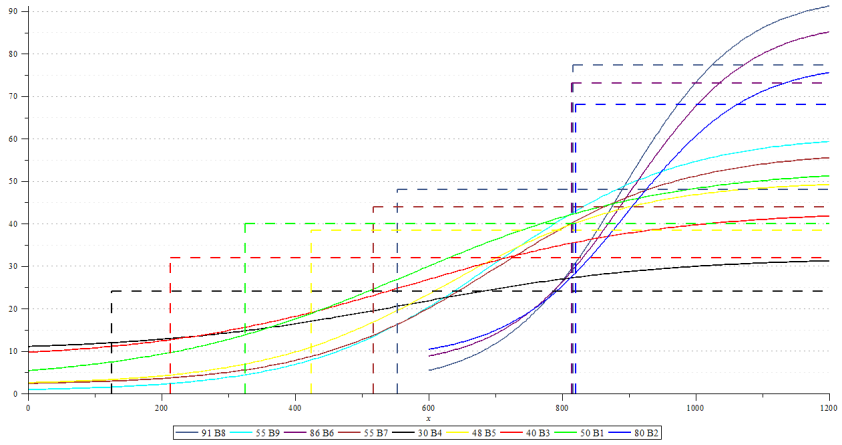

Figure 5.32: A schematic representation of half of the stress diagram caused by an acting concentrated load and the block of equal stress with a length of the distributive width representing the same load.

Table 5.12: The values of the parameters used to construct the S-curves representing .

Curve name	Rib 1 [%]	Rib 2 [%]	Rib 3 [%]	A	B	C	D	E
B1 50	50	30	6	3	50	1	$-\frac{1}{190}$	3
B2 80	50	30	6	8	70	1	$-\frac{1}{90}$	10
B3 40	50	30	6	8	35	1	$-\frac{1}{190}$	3
B4 30	50	30	6	10	33	1	$-\frac{1}{190}$	3
B5 48	50	30	6	2	82	1	$-\frac{1}{140}$	4.5
B6 86	50	30	6	6	55	1	$-\frac{1}{90}$	10
B7 55	50	30	6	2	92	1	$-\frac{1}{140}$	5
B8 91	50	30	6	2	60.5	1	$-\frac{1}{89}$	10
B9 60	50	30	6	0.5	2	1	$-\frac{1}{140}$	5

Distributive length

The output of the two dimensional model which results in the calculation of the distributive width depends on the distributive length, which is shown in figure 5.29. Because of their mutual dependence the best way to find a reasonable solution is to choose a starting value and calculate and recalculate both values until a stable solution is obtained. Thus the distributive width depends on the distributive length which was assumed at a certain value at the start. Determining the size of the distributive length will be done as follows.

The top slab is now considered in the y-direction, instead of the x-direction as was done before. The top slab is assumed to be a beam supported by an elastic foundation. This is depicted in figure 5.33. The ribs of the composite slab form this elastic foundation and the top slab will be modelled as a beam supported by the rib-foundation. The bending stiffness of this beam depends on the positioning of the longitudinal reinforcement meshes in the top slab and the distributive width that was calculated previously.

The model that is now obtained can be worked out. The goal is to find the deflection of the beam and how this deflection is influenced by the respective stiffness of the beam and the foundation. To work out the solution for this problem the euler-bernoulli differential equation will be applied onto the beam. Because the beam is supported by the elastic foundation the differential equation is as shown in equation 5.62.

$$EI_{ts,long}\frac{d^4w}{dx^4} + k_{rib}w = q \tag{5.62}$$

Where w is the deflection of the beam. Because there is no distributed load the factor q is equal to zero. There is of course the self-weight of the top slab, but this weight is left out of the analysis. Now after substituting $w = e^{mx}$ into equation 5.62 gives the characteristic equation 5.63

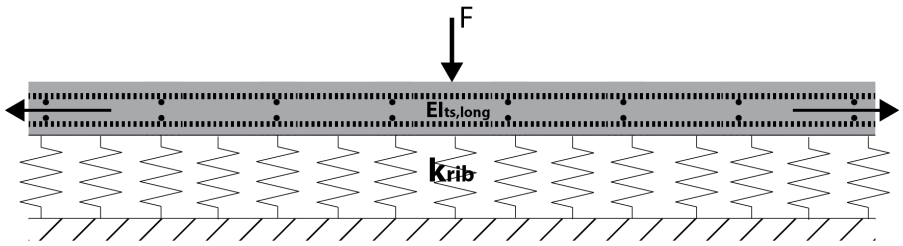

Figure 5.33: A schematic representation of half of the stress diagram caused by an acting concentrated load and the block of equal stress with a length of the distributive width representing the same load.

$$m^4 + \frac{k_{rib}}{EI_{ts,long}} = 0 \tag{5.63}$$

The roots of this equation are:

$$m_1 = -m_3 = \lambda(1+i), \quad m_2 = -m_4 = \lambda(-1+i) \tag{5.64}$$

With

$$\lambda^4 = \frac{k_{rib}}{4EI_{ts,long}} \tag{5.65}$$

The factor λ is the characteristic value of the solution and has a dimension $length^{-1}$. The general solution of the differential equation then becomes as is depicted in equation 5.66.

$$w = \sum_{i}^{1,4} A_i e^{m_i x} \tag{5.66}$$

This can be rewritten into equation 5.68 using the two equations from 5.67.

$$e^{i\lambda x} = \cos(\lambda x) + i\sin(\lambda x), \quad e^{-i\lambda x} = \cos(\lambda x) - i\sin(\lambda x) \tag{5.67}$$

$$w(x) = e^{\lambda x}\left[C_1\cos(\lambda x) + C_2\sin(\lambda x)\right] + e^{-\lambda x}\left[C_3\cos(\lambda x) + C_4\sin(\lambda x)\right] \tag{5.68}$$

The constants are related to constants A_i through the following relations.

$$C_1 = A_1 + A_2, \quad C_2 = i(A_1 - A_4), \quad C_3 = A_2 + A_3, \quad C_4 = i(A_2 - A_3) \tag{5.69}$$

The constants can be determined by applying the boundary conditions on the general solution. The beam is assumed to be infinitely long so the deflection must be equal to zero at an infinite distance. This results in constants C_1 and C_2 being zero because e^{λ} has to be zeroed out. The other two constants can be found by applying the concentrated load F at $x = 0$ and because of symmetry the rotation of the beam $\frac{dw}{dx}$ has to be equal to zero at $x = 0$ as well. Both of these conditions result in the other two constants being $C_3 = C_4 = F\lambda/k_{rib}$. Now all the constants are known the solution for the problem that was considered is as shown in equation 5.70.

$$w(x) = \frac{F\lambda}{k_{rib}} e^{-\lambda x}\left[\cos(\lambda x) + \sin(\lambda x)\right] \tag{5.70}$$

The equation above generates half of a shape that will be used to describe the distribution of the concentrated load along the longitudinal axis of the composite slab, which is along the rib. Equation 5.70 is applied from $x = 0$ to $x = \infty$ and this curve is then mirrored along the w axis to create the desired shape of the deflection. In this formula the load F determines only the amplitude of the deflection diagram and not the shape. The shape of the deflection diagram when plotted looks as displayed in figure 5.34.
The curve above has a nice clock shape but does not level out by converging on the x-axis. Instead it crosses the x-axis once and then converges back towards the x-axis. The second part of the curve is not useful for modelling the distribution and thus will not be analysed any further. Converting the clock-shaped part of

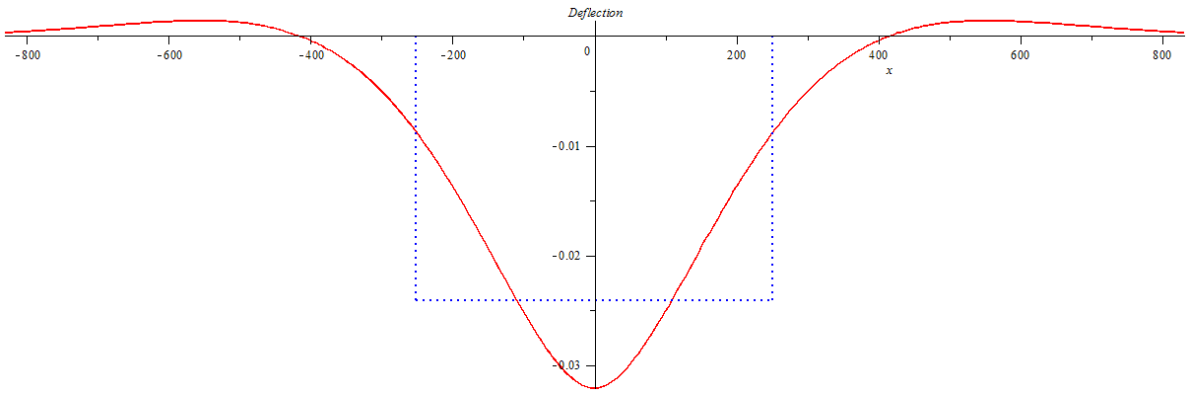

Figure 5.34: The shape of the deflection diagram of a beam on an elastic foundation, which is used to model the distribution of the concentrated load along the axis of the ribs. The stress block with the same area as the graph from centre until it crosses the x-axis is also displayed.

this graph into an distributive length is done in the same manner as it was done for the distributive width. The area underneath the deflection curve between the two root values is calculated. This area is then divided by 75% of the maximum deflection of the curve. From this calculation the distributive length L_{eff} follows. The deflection curve cuts the x-axis at a value of $x = \pi/1.35\lambda$ The exact formulation is shown in equation 5.71. It has to be noted that in case the distributive width spans more than a single rib, the stiffness of the elastic foundation should be increased. This is because the top slab is then carried not by a single rib any more, but several.

$$L_{dis} = 2 \times \frac{\int_{-\frac{\pi}{1.35\lambda}}^{0} w(x)}{0.75 \times w_0} \tag{5.71}$$

With the equation from above it is possible to determine the distributive length of the top slab when the distributive width is already known.

Obtaining a solution

Now that calculation methods for both the distributive length and the distributive width have been established, a final solution for both parameters can be reached. The path that has to be followed was already described at the start of this section. First a value for the distributive length has to be assumed. Then the distribution of the concentrated load can be determined using the analytical model from which the value for the distributive width can be calculated. Using this value a new value of the distributive length can be calculated. This value can then be used to go through the entire process again, resulting in another distributive length value. These steps have to be repeated until the value of the distributive length will not vary to a significant degree any more. A solution for both distributive parameters is then acquired and a square area of the composite slab that contributes towards resisting the concentrated load that is applied, see figure 5.35.

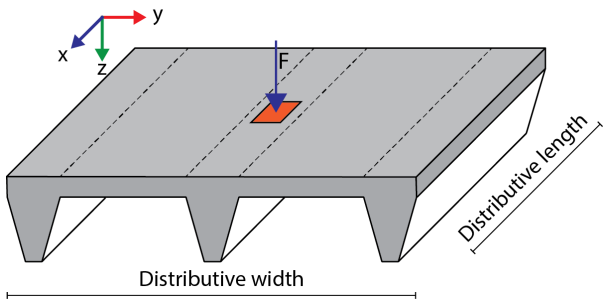

Figure 5.35: A schematic .

5.3.3. ASSUMPTIONS MADE IN THE THREE-DIMENSIONAL MODEL

This section sums up the assumptions that where made during the inclusion of three-dimensional aspects into the two dimensional model. Keeping a clear overview of the assumptions made is of importance because the assumptions could be incorrect or oversimplifications that are just too large, which in turn effect the behaviour of the model. The assumptions made are as follows.

1. The ribs act as simply supported beams acted upon by a concentrated load.
2. The bending stiffness of the ribs varies in steps. It has either a cracked or an uncracked bending stiffness.
3. The output of the two-dimensional model in percentages per rib was converted into a continuous stress curve.
4. The continuous stress curve was converted into an distributive width, by assuming a block of equal stress with the same area as the curve.
5. The distributive length is modelled by assuming the top slab to be a beam on an elastic foundation.
6. The distributive width is overestimated because of the S-curve that is used over multiple ribs.

5.4. THE INFLUENCE OF THE PARAMETERS USED IN THE MODEL

The model has now been completely worked out. The next step is to examine what the magnitude of the influence is of the different parameters that are being used in the model. This is valuable information to know, since it will tell in what manner the model will react to a change in its parameters and thus also in what way the modelled slab can be influenced by making these changes. Needless to say the influence of the parameters on the distribution of the concentrated force is the main interest in this section. The examples put up in this section are all loaded by the same load and have the same dimensions unless specified otherwise. The parameters that are used by default are shown in table 5.13. The examples in this section are meant to highlight the influence of all different parameters. It should also be mentioned that the distribution of the load can be observed by looking at the deflection of the beam at the location of a rib. Since the more a rib's translation spring deflects, the more shear force is acting on this particular rib. Per parameter a comparison of influence will be made by increasing the parameter by 25% and checking by what percentage the deflection increases. Additionally, extreme values of the parameter in question can be used to find out which types of mechanism to the model will tend to. This means that raising or decreasing a variable by a factor 10 might yield additional insight or confirmation of a found trend.

Table 5.13: The parameters used in the model by default to make a comparison of the parameter influence.

Parameter	Symbol	Value	Unit
Uncracked top slab bending stiffness	$EI_{ts,uc}$	4.29×10^{11}	Nmm^2
Negative cracked top slab bending stiffness	$EI_{ts,cr,neg}$	1.90×10^{11}	Nmm^2
Positive cracked top slab bending stiffness	$EI_{ts,cr,pos}$	1.85×10^{11}	Nmm^2
Inter-rib top slab length	L	425	mm
Rib torsion resistance	$k_{t,rib}$	6.38×10^{8}	Nmm/rad
Concentrated load (rib A)	F_a	30	kN
Translation spring stiffness (A-G)	$k_{rib,A-G}$	2649	N/mm
Distributed load	q_k	0	kN/m^2
Effective length	L_{dis}	500	mm
Effective width	B_{dis}	2150	mm

The model that will be used is a five rib model with varying top slab stiffness and rib rotation resistance, see figure 5.36. Each time a parameter is studied, the model will be used several times. This is because the assigned bending stiffness of the top slab has to reflect the moment diagram resulting from the load. This

division of bending stiffness has to be found by running the model repeatedly until a stable solution has been found. The same applies for the distributive length and distributive width. The values for both parameters given in the table above are the values found for the default parameters that are used in this section.

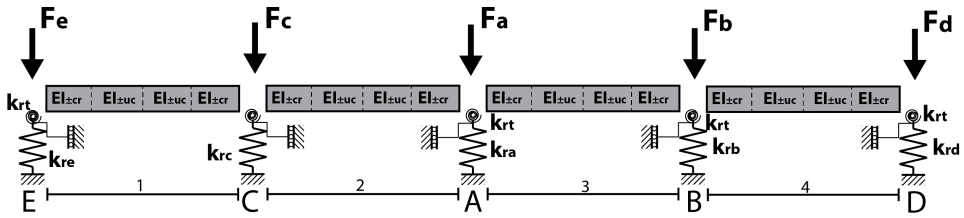

Figure 5.36: The five model rib model that is used for the parameter analysis.

The parameters that will be analysed in this section are the following.

- Vertical translation spring stiffness k_{rib}
- Positive top slab bending stiffness $EI_{ts,pos}$
- Negative top slab bending stiffness $EI_{ts,neg}$
- Rotation spring stiffness $k_{t,rib}$
- Inter-rib span length L
- The rib span length L_{rib}

All these input parameters can be varied according to the users desire. The other parameters such as the distributive length, distributive width and the cracking moment of the top slab are results of these main parameters. The span length of the ribs is not a direct model parameter but the vertical translation spring stiffness is directly influenced by the rib span length. The span length is in practise a very important parameter and knowing the influence it has on the behaviour exhibited by the composite plate is vital. The diagram that will be used to compare the results of the variables mentioned above is that of the deflection of the top slab. The deflection diagram resulting out of the default variables is shown in figure 5.37. In this graph the green vertical lines represent the location of a transition between two areas of varying bending stiffness. The blue vertical lines indicate the location of a rib.

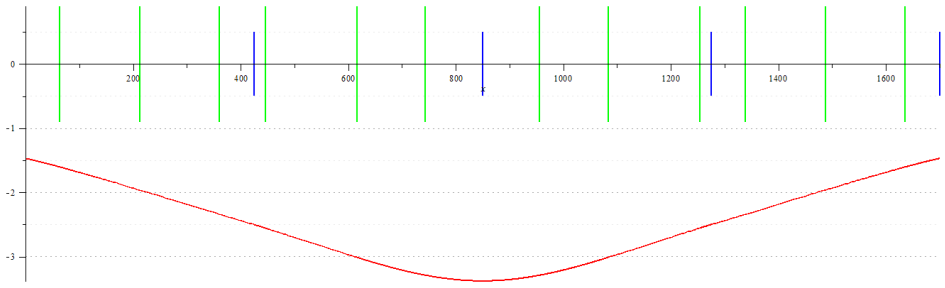

Figure 5.37: The deflection curve given by the model when the default variables are used as input. The green lines represent the boundaries between varying bending stiffness fields and the blue lines the locations of a rib.

The comparison will be made by examining the deflection of the curve at the location of the central rib. The relative change of deflection will give an indication of the size of the influence a parameter has on the distribution across the rib. The percentage of the load that is carried per rib will also be given. The results of the default variables are shown in table 5.14.

Table 5.14: The output from the model when the default values of the variables are used..

		Load per rib [kN (%)]				
	Deflection at rib A [mm]	**Rib E**	**Rib C**	**Rib A**	**Rib B**	**Rib D**
Default values	3.38	3.89 (12.98%)	6.63 (22.09%)	8.96 (29.85%)	6.63 (22.09%)	3.89 (12.98%)
Values with changed variable	-	-	-	-	-	-
Change	-	-	-	-	-	-

5.4.1. THE VERTICAL TRANSLATION SPING STIFFNESS

The translation spring stiffness coefficient is directly derived from the bending stiffness of the ribs and the composite slab span length. The spring stiffness could be increased by reducing the slab span length or by increasing the bending stiffness of the ribs. Doing the opposite will of course lower the spring stiffness instead.

Increased translation spring stiffness

It is expected that if the translation spring coefficient is increased, the load will distribute less when compared to the default case. The stiffness of the top slab with respect to the translation springs will tend more towards the scenario of an infinitely stiff beam supported on springs. When the spring stiffness is increased by 25% the deflection diagram resulting from the model will look as depicted in figure 5.38. The raised value of the translation spring stiffness k_{rib} is now taken as $3311.25 N/mm$.

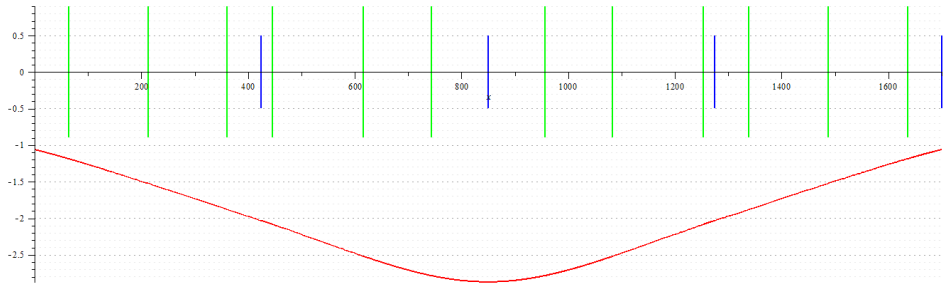

Figure 5.38: The deflection curve given by the model when the translation spring stiffness value is raised by 25% and used as input.

The corresponding values are shown in table 5.15.

Table 5.15: The output from the model when the increased values of the translation spring stiffness are used.

k_{rib} = 3311.25 [125%]		**Load per rib [kN (%)]**				
	Deflection at rib A [mm]	**Rib E**	**Rib C**	**Rib A**	**Rib B**	**Rib D**
Default values	3.38	3.89 (12.98%)	6.63 (22.09%)	8.96 (29.85%)	6.63 (22.09%)	3.89 (12.98%)
Values with changed variable	2.87	3.51 (11.71)	6.73 (22.43)	9.51 (31.70)	6.73 (22.43)	3.51 (11.71)
Change	-0.51 (-15.1)	-0.38 (-1.27)	0.10 (0.34)	0.56 (1.85)	0.10 (0.34)	-0.38 (-1.27)

The shape of the deflection curve does not change visibly, but the deflection along the entire curve decreases somewhat due to the increased spring stiffness. Also the load is concentrated slightly more in the central three ribs. If the spring stiffness is now raised to ten times its normal value, the curve in figures 5.39 is found.

Table 5.16 confirms the expectation that the stress from the concentrated load is further concentrated to the middle of the slab and less distributed. The overall deflection also decreases drastically due to the increased stiffness of the springs.

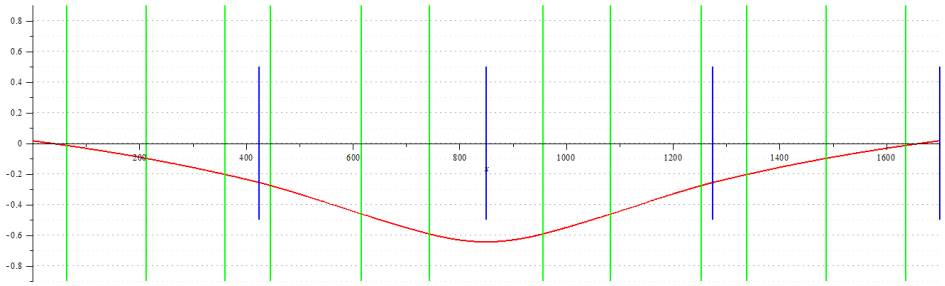

Figure 5.39: The deflection curve given by the model when the translation spring stiffness coefficient is multiplied by ten.

Table 5.16: The output from the model when strongly increased values of the translation spring stiffness are used.

$\mathbf{k_{rib}}$ **= 26490 [1000%]**		**Load per rib [kN (%)]**				
	Deflection at rib A [mm]	**Rib E**	**Rib C**	**Rib A**	**Rib B**	**Rib D**
Default values	3.38	3.89 (12.98%)	6.63 (22.09%)	8.96 (29.85%)	6.63 (22.09%)	3.89 (12.98%)
Values with changed variable	0.65	-0.38 (-1.27)	6.83 (22.77)	17.10 (56.99)	6.83 (22.77)	-0.38 (-1.27)
Change	-2.73 (-80.8)	-4.28 (-14.25)	0.20 (0.68)	8.14 (27.14)	0.20 (0.68)	-4.28 (-14.25)

Decreased translation spring stiffness

Now the translation spring stiffness is lowered by 25% instead. It is the expectation that conversely to the increased load concentration that was found when increasing the stiffness, the load will distribute more over the width of the model. The model will tend towards a relatively strong beam supported by weaker springs which is able to distribute the force better than when the beam is relatively weak. The deflection curve in figure 5.40 and the corresponding results table 5.17 are found.

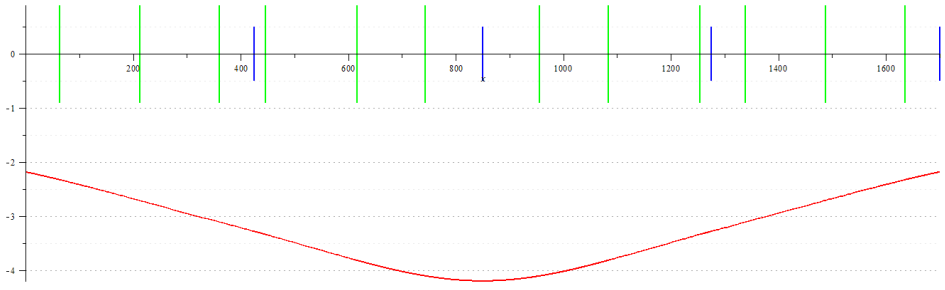

Figure 5.40: The deflection curve given by the model when the translation spring stiffness coefficient is reduced by 25%.

The concentrated load is indeed distributed more evenly over the ribs in the model than was the case in the default configuration. The deflection also increases because of the overal stiffness reduction of the translation springs. The shape of the deflection curve still remains the same at a glance as the default curve. Now the effect of lowering the spring coefficient to 10% of its original value will be observed. The deflection will obviously increase greatly, but the main point of interest is the shape of the deflection curve. It is expected

Table 5.17: The output from the model when the reduced values of the translation spring stiffness are used.

k_{rib} = 1986.75 [75%]		Load per rib [kN (%)]				
	Deflection at rib A [mm]	**Rib E**	**Rib C**	**Rib A**	**Rib B**	**Rib D**
Default values	3.38	3.89 (12.98%)	6.63 (22.09%)	8.96 (29.85%)	6.63 (22.09%)	3.89 (12.98%)
Values with changed variable	4.19	4.36 (14.43)	6.51 (21.69)	8.33 (27.76)	6.51 (21.69)	4.36 (14.43)
Change	0.81 (24.0)	0.47 (1.55)	-0.12 (-0.40)	-0.63 (-2.09)	-0.12 (-0.40)	0.47 (1.55)

the that the beam will behave more stiffly and distribute the load even more evenly across all the ribs. The results are shown in figure 5.41 and table 5.18.

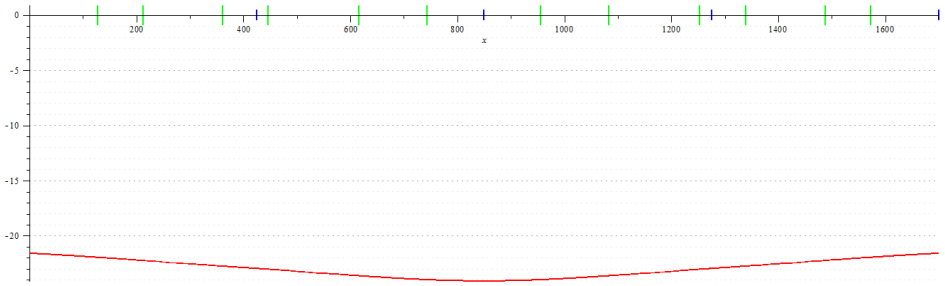

Figure 5.41: The deflection curve given by the model when the translation spring stiffness coefficient is reduced by 90%.

Table 5.18: The output from the model when the strongly decreased values of the translation spring stiffness are used.

k_{rib} = 246.9 [10%]		Load per rib [kN (%)]				
	Deflection at rib A [mm]	**Rib E**	**Rib C**	**Rib A**	**Rib B**	**Rib D**
Default values	3.38	3.89 (12.98%)	6.63 (22.09%)	8.96 (29.85%)	6.63 (22.09%)	3.89 (12.98%)
Values with changed variable	24.10	5.72 (19.07)	6.09 (20.29)	6.39 (21.29)	6.09 (20.29)	5.72 (19.07)
Change	20.72 (613.0)	1.83 (6.09)	-0.54 (-1.80)	-2.57 (-8.56)	-0.54 (-1.80)	1.83 (6.09)

As expected the deflection is increased greatly, but apart from that the beam also distributes the load very evenly over the width of the model now. It is almost as if the beam is infinitely stiff and is distributing the load evenly across all ribs.

5.4.2. THE POSITIVE TOP SLAB BENDING STIFFNESS

The positive bending stiffness of the top slab is the next parameter to be analysed. This parameter is important to the model because the addition or removal of the bottom reinforcement mesh in the top slab greatly affects the positive bending stiffness of the top slab. This is while assuming that the top flange of the steel profiled deck does not contribute to the bending stiffness. Removing the bottom mesh will then reduce the positive bending stiffness of the top slab. Therefore finding the size of the influence of this parameter is certainly important.

Increased positive top slab bending stiffness

First the positive bending stiffness is raised by 25% and 900% respectively. It is expected that the higher stiffness will result in greater spread of the load along the width of the model. The results are shown in figures 5.42 and 5.43 and in tables 5.19 and 5.19 respectively.

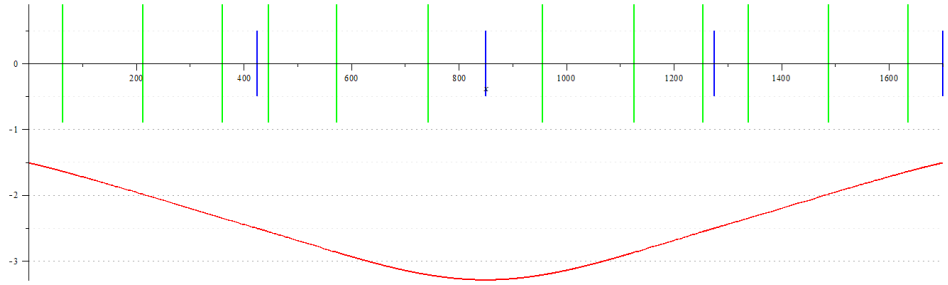

Figure 5.42: The deflection curve given by the model when the top slab positive bending stiffness coefficient is raised by 25%.

Table 5.19: The output from the model when the increased values of the positive top slab bending stiffness are used.

$EI_{TS,pos} = 2.31 \times 10^{11}$ [125%]		Load per rib [kN (%)]				
	Deflection at rib A [mm]	**Rib E**	**Rib C**	**Rib A**	**Rib B**	**Rib D**
Default values	3.38	3.89 (12.98%)	6.63 (22.09%)	8.96 (29.85%)	6.63 (22.09%)	3.89 (12.98%)
Values with changed variable	3.21	4.00 (13.34)	6.64 (22.13)	8.72 (29.06)	6.64 (22.13)	4.00 (13.34)
Change	-0.17 (-5.0)	0.11 (0.36)	0.01 (0.04)	-0.24 (-0.79)	0.01 (0.04)	0.11 (0.36)

It is indeed observed that the load is distributed somewhat more than is the case with the default values. The effect is less pronounced however than when the translation spring stiffness was adjusted. This might be because the bending stiffness of only those parts of the top slab that are loaded by a positive bending moment larger than the cracking moment are affected. When the translation spring stiffness is adjusted, the relative bending stiffness of the entire top slab is affected by this, instead of only parts of it.

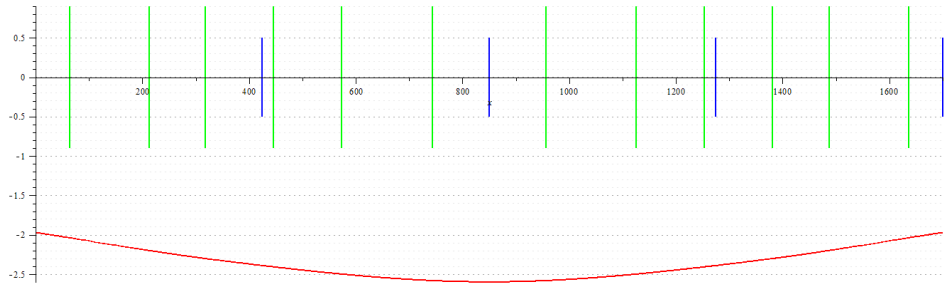

Figure 5.43: The deflection curve given by the model when the top slab positive bending stiffness coefficient is raised by 900%.

With the extreme value of the top slab positive bending stiffness the load is distributed even more along the width of the model. Also a larger part of the slab is now affected because the stiffer top slab parts attract more moment and cause the adjacent top slab parts also to be acted upon by a positive bending moment. But still the changes in the model output are not as large as those when the translation spring stiffness was increased.

Table 5.20: The output from the model when the strongly increased values of the positive top slab bending stiffness are used.

$EI_{TS,pos} = 1.85 \times 10^{12}$ [1000%]		Load per rib [kN (%)]				
	Deflection at rib A [mm]	**Rib E**	**Rib C**	**Rib A**	**Rib B**	**Rib D**
Default values	3.38	3.89 (12.98%)	6.63 (22.09%)	8.96 (29.85%)	6.63 (22.09%)	3.89 (12.98%)
Values with changed variable	2.60	5.23 (17.42)	6.33 (21.11)	6.80 (22.65)	6.33 (21.11)	5.23 (17.42)
Change	-0.78 (-23.1)	1.33 (4.44)	-0.29 (-0.98)	-2.16 (-7.20)	-0.29 (-0.98)	1.33 (4.44)

decreased positive top slab bending stiffness

Now the top slab positive bending stiffness lowered by 25% and 90% respectively. Contrary to when the bending stiffness was increased, the expectation is now that the load is concentrated more than with the default values. The results are shown in figures 5.44 and 5.44 and in tables 5.22 and 5.22 respectively.

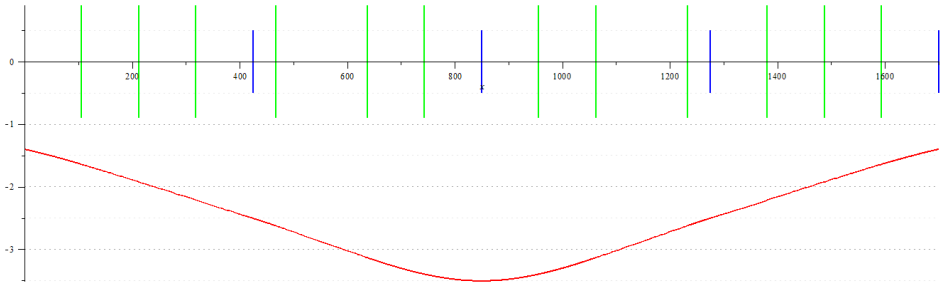

Figure 5.44: The deflection curve given by the model when the top slab positive bending stiffness coefficient is decreased by 25%.

Table 5.21: The output from the model when the decreased values of the positive top slab bending stiffness are used.

$EI_{TS,pos} = 1.39 \times 10^{11}$ [75%]		Load per rib [kN (%)]				
	Deflection at rib A [mm]	**Rib E**	**Rib C**	**Rib A**	**Rib B**	**Rib D**
Default values	3.38	3.89 (12.98%)	6.63 (22.09%)	8.96 (29.85%)	6.63 (22.09%)	3.89 (12.98%)
Values with changed variable	3.51	3.71 (12.38)	6.64 (22.13)	9.29 (30.97)	6.64 (22.13)	3.71 (12.38)
Change	0.13 (3.8)	-0.18 (-0.60)	0.01 (0.04)	0.34 (1.12)	0.01 (0.04)	-0.18 (-0.60)

When the positive bending stiffness is lowered by 25%, the load indeed concentrates somewhat more on the centre of the model.

The extremely low value of the positive bending stiffness further concentrates the load to the central three ribs. The sections of the top slab that are being acted upon by a positive bending moment are smaller and solely concentrated around the centre rib. This means that the weakened positive bending is acting as a type of plastic hinge, thus producing this deflection curve.

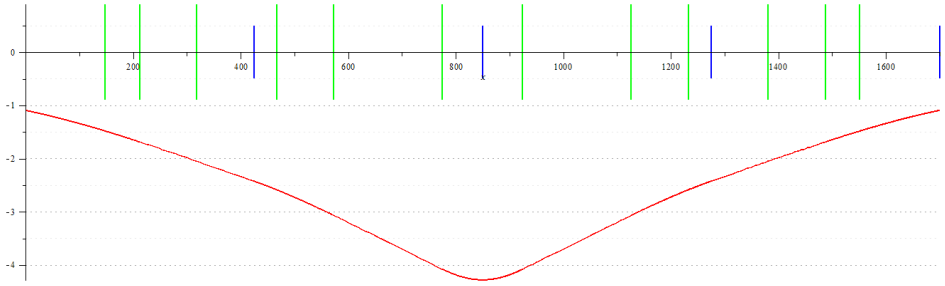

Figure 5.45: The deflection curve given by the model when the top slab positive bending stiffness coefficient is decreased by 90%.

Table 5.22: The output from the model when the strongly decreased values of the positive top slab bending stiffness are used.

$EI_{TS,pos} = 1.85 \times 10^{10}$ [10%]		Load per rib [kN (%)]				
	Deflection at rib A [mm]	**Rib E**	**Rib C**	**Rib A**	**Rib B**	**Rib D**
Default values	3.38	3.89 (12.98%)	6.63 (22.09%)	8.96 (29.85%)	6.63 (22.09%)	3.89 (12.98%)
Values with changed variable	4.28	2.90 (9.67)	6.43 (21.43)	11.35 (7.82)	6.43 (21.43)	2.90 (9.67)
Change	0.90 (26.6)	-0.99 (-3.31)	-0.20 (-0.66)	2.39 (7.97)	-0.20 (-0.66)	-0.99 (-3.31)

5.4.3. THE NEGATIVE TOP SLAB BENDING STIFFNESS

The negative bending stiffness of the top slab is not influenced in the same amount by the addition or removal of the bottom reinforcement mesh. The top reinforcement mesh contributes 40 times more to the negative bending stiffness than the bottom mesh. The top mesh is in practice always present, but for the sake of completion and curiosity its influence will be analysed regardless.

Increased negative top slab bending stiffness

First of all the negative bending stiffness of the top slab will be raised by 25% and 900% respectively to 2.38×10^{11} and 1.9×10^{12}. The parts of the top slab that are acting under a negative bending moment will become stiffer and attract more forces. Therefore it is expected that the load distribution will again improve, but this is only true for the parts of the top slab that are in negative bending. So the effect should be smaller again than was the case for the translation spring coefficient. The effect may be also be smaller than it was for the change of the positive bending stiffness, because a smaller part of the top slab is acting in negative bending than positive bending. The results of the two increases in value are shown in figures 5.46 and 5.47 and in tables 5.23 and 5.24 respectively.

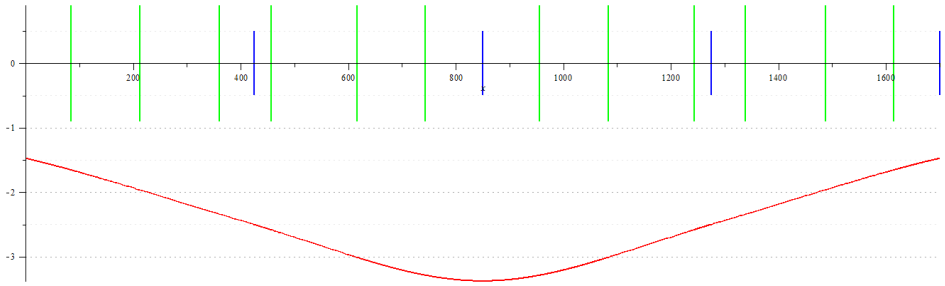

Figure 5.46: The deflection curve given by the model when the top slab negative bending stiffness coefficient is increased by 25%.

There is a very slight change in the distribution of the concentrated load, but the change is almost insignificant. The total deflection of the curve is also not affected.

Table 5.23: The output from the model when the increased values of the negative top slab bending stiffness are used.

$EI_{TS,neg} = 2.38 \times 10^{11}$ [125%]		Load per rib [kN (%)]				
	Deflection at rib A [mm]	**Rib E**	**Rib C**	**Rib A**	**Rib B**	**Rib D**
Default values	3.38	3.89 (12.98%)	6.63 (22.09%)	8.96 (29.85%)	6.63 (22.09%)	3.89 (12.98%)
Values with changed variable	3.38	3.90 (13.01)	6.62 (22.08)	8.94 (29.81)	6.62 (22.08)	3.90 (13.01)
Change	0.0 (0.0)	0.01 (0.03)	0.00 (-0.00)	-0.01 (-0.04)	0.00 (-0.00)	0.01 (0.03)

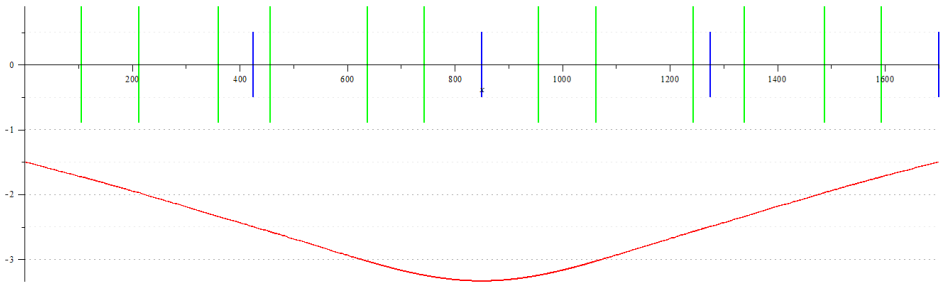

Figure 5.47: The deflection curve given by the model when the top slab negative bending stiffness coefficient is increased by 900%.

When the negative bending stiffness is increased by a factor ten, the effect becomes more noticeable, but the effect is still very small compared to the parameters considered previously.

Table 5.24: The output from the model when the strongly increased values of the negative top slab bending stiffness are used.

$EI_{TS,neg} = 1.85 \times 10^{12}$ [1000%]		Load per rib [kN (%)]				
	Deflection at rib A [mm]	**Rib E**	**Rib C**	**Rib A**	**Rib B**	**Rib D**
Default values	3.38	3.89 (12.98%)	6.63 (22.09%)	8.96 (29.85%)	6.63 (22.09%)	3.89 (12.98%)
Values with changed variable	3.34	(13.22)	(22.47)	(29.45)	(22.47)	(13.22)
Change	-0.04 (-1.2)	0.07 (0.24)	0.11 (0.38)	-0.12 (-0.40)	0.11 (0.38)	0.07 (0.24)

Decreased negative top slab bending stiffness

Now the negative bending stiffness of the top slab is reduced by 25% and 90% respectively. The load will be concentrated more towards the centre. But since the effect was so small when the values were increased, it is expected that decreasing them will have an effect with a similar size. The results of the two decreases in value are shown in figures 5.48 and 5.49 and in tables 5.25 and 5.26 respectively.

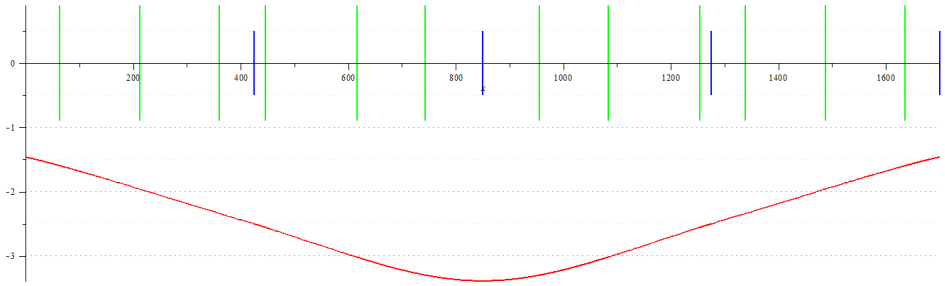

Figure 5.48: The deflection curve given by the model when the top slab negative bending stiffness coefficient is decreased by 25%.

Table 5.25: The output from the model when the decreased values of the negative top slab bending stiffness are used.

$EI_{TS,neg} = 1.43 \times 10^{11}$ [75%]		Load per rib [kN (%)]				
	Deflection at rib A [mm]	**Rib E**	**Rib C**	**Rib A**	**Rib B**	**Rib D**
Default values	3.38	3.89 (12.98%)	6.63 (22.09%)	8.96 (29.85%)	6.63 (22.09%)	3.89 (12.98%)
Values with changed variable	3.39	3.88 (12.93)	6.63 (22.10)	8.90 (29.95)	6.63 (22.10)	3.88 (12.93)
Change	0.01 (0.3)	-0.02 (-0.05)	0.00 (0.00)	-0.06 (0.20)	0.00 (0.00)	-0.02 (-0.05)

The effect is slightly larger when the negative bending stiffness value is lowered by 25% than when it was raised. This might by due to the fact that the relative change of the value form 100% to 75% is larger than it was from 100% to 125%. But nonetheless it is still an almost negligible change of the output.

When the negative bending stiffness is lowered to 10% of its original value the parts of the top slab that are acting with a negative cracked bending stiffness become very small. Reducing the values even more would result in this parts of the slab starting to act as plastic hinges. The deflection is increased a little and the load is concentrated more towards the centre of the model, as was already the case when the stiffness was only slightly reduced, but now the effect is more pronounced.

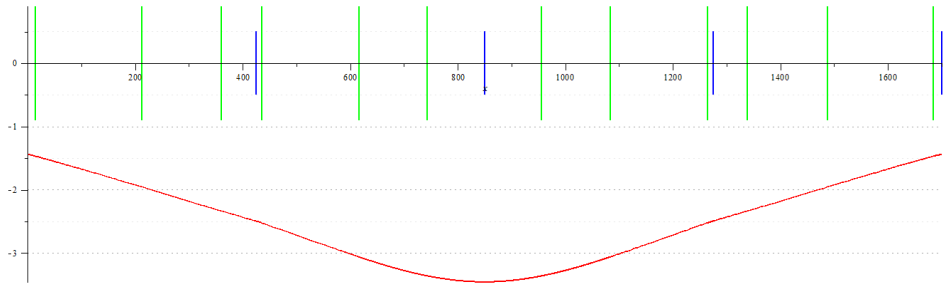

Figure 5.49: The deflection curve given by the model when the top slab negative bending stiffness coefficient is decreased by 90%.

Table 5.26: The output from the model when the strongly decreased values of the negative top slab bending stiffness are used.

$EI_{TS,neg} = 1.85 \times 10^{10}$ [10%]		Load per rib [kN (%)]				
	Deflection at rib A [mm]	**Rib E**	**Rib C**	**Rib A**	**Rib B**	**Rib D**
Default values	3.38	3.89 (12.98%)	6.63 (22.09%)	8.96 (29.85%)	6.63 (22.09%)	3.89 (12.98%)
Values with changed variable	3.46	3.82 (12.72)	6.61 (22.02)	9.16 (30.52)	6.61 (22.02)	3.82 (12.72)
Change	0.08 (2.4)	-0.08 (-0.26)	-0.02 (-0.07)	0.20 (0.67)	-0.02 (-0.07)	-0.08 (-0.26)

5.4.4. THE ROTATION SPRING STIFFNESS

The next parameter to be analysed is the rotation spring stiffness. This coefficient determines how strong the torsion resistance of the ribs is in the model. Since it is still unclear whether or not the torsion resistance of the ribs is actually contributing to the distribution of the load in any way, it is vital that this parameter is analysed as well. Then a better understanding of the model output when this parameter is changed will be obtained.

Increased rotation spring stiffness

First of all the rotation spring stiffness of the top slab will be raised by 25% and 900% respectively to 7.98×10^8 and 6.38×10^9. This stiffness coefficient increase move the model closer towards the end situation where the model could be represented by separate clamped beams connected to one and another. In this situation the beam would behave stiffly and thus the distribution should improve when the rotation stiffness is increased. The results of the two increases in value are shown in figures 5.50 and 5.51 and in tables 5.27 and 5.28 respectively.

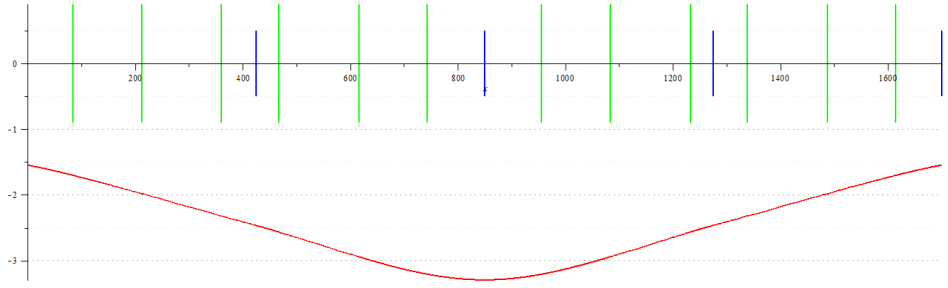

Figure 5.50: The deflection curve given by the model when the rotation spring coefficient is increased by 25%.

Indeed as expected the load is distributed more evenly over the with of the beam, although the effect is not quite as strong as with the translation spring coefficient it is still stronger than if the bending stiffnesses of the top slab are increased or decreased.

Table 5.27: The output from the model when the increased values of the rotation spring coefficient are used.

$k_{rt} = 7.98 \times 10^8$ [125%]		Load per rib [kN (%)]				
	Deflection at rib A [mm]	**Rib E**	**Rib C**	**Rib A**	**Rib B**	**Rib D**
Default values	3.38	3.89 (12.98%)	6.63 (22.09%)	8.96 (29.85%)	6.63 (22.09%)	3.89 (12.98%)
Values with changed variable	3.30	4.10 (13.67)	6.53 (21.78)	8.73 (29.10)	6.53 (21.78)	4.10 (13.67)
Change	-0.08 (-2.4)	0.21 (0.69)	-0.09 (-0.31)	-0.23 (-0.75)	-0.09 (-0.31)	0.21 (0.69)

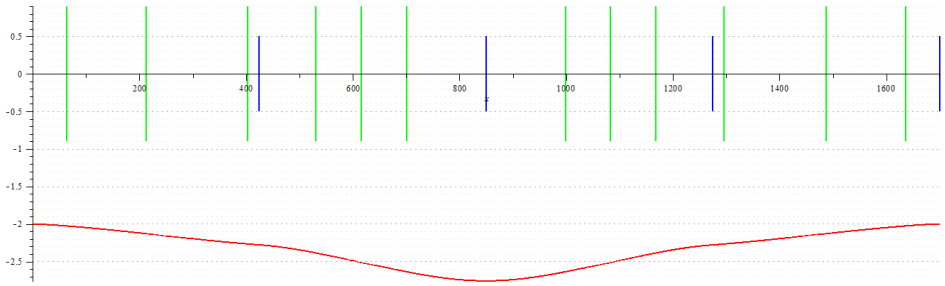

Figure 5.51: The deflection curve given by the model when the rotation spring coefficient is increased by 25%.

With the tenfold increase of the rotation stiffness coefficient of the ribs a clear change in the deflection curve is now visible. At the locations of the ribs the deflection curve straightens out a little, as if the top slab was clamped in that location. This can be found as well in the distribution of the load. The load is distributed much more evenly across the width of the model.

Table 5.28: The output from the model when the strongly increased values of the rotation spring coefficient are used.

$k_{rt} = 6.38 \times 10^9$ [1000%]		Load per rib [kN (%)]				
	Deflection at rib A [mm]	**Rib E**	**Rib C**	**Rib A**	**Rib B**	**Rib D**
Default values	3.38	3.89 (12.98%)	6.63 (22.09%)	8.96 (29.85%)	6.63 (22.09%)	3.89 (12.98%)
Values with changed variable	2.76	5.30 (17.68)	6.04 (20.13)	7.31 (24.37)	6.04 (20.13)	5.30 (17.68)
Change	-0.62 (-18.3)	1.41 (4.70)	-0.59 (-1.96)	-1.64 (-5.48)	-0.59 (-1.96)	1.41 (4.70)

Decreased rotation spring stiffness

Now the rotation stiffness coefficient is reduced by 25% and 90% respectively to 4.79×10^8 and 6.38×10^7. Instead of acting more like clamped beams, the reduction of the rotation stiffness will make the top slab act more like a continuous beam without restrictions at the locations of the ribs. The load should therefore distribute less towards the sides of the model. The results of the two decreases in value are shown in figures 5.52 and 5.53 and in tables 5.29 and 5.30 respectively.

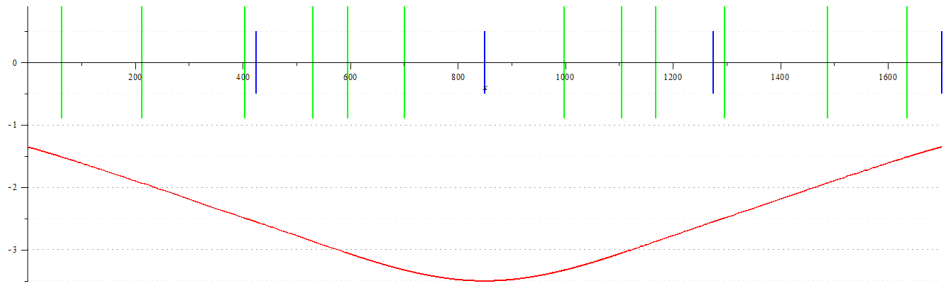

Figure 5.52: The deflection curve given by the model when the rotation spring coefficient is decreased by 25%.

Table 5.29: The output from the model when the decreased values of the rotation spring coefficient are used.

$k_{rt} = 4.79 \times 10^8$ [75%]		Load per rib [kN (%)]				
	Deflection at rib A [mm]	**Rib E**	**Rib C**	**Rib A**	**Rib B**	**Rib D**
Default values	3.38	3.89 (12.98%)	6.63 (22.09%)	8.96 (29.85%)	6.63 (22.09%)	3.89 (12.98%)
Values with changed variable	3.50	3.59 (11.96)	6.77 (22.57)	9.28 (30.94)	6.77 (22.57)	3.59 (11.96)
Change	0.12 (3.6)	-0.31 (-1.02)	0.14 (0.48)	0.33 (1.09)	0.14 (0.48)	-0.31 (-1.02)

Reducing the rotation stiffness coefficient has the effect of concentrating the load more towards the centre of the model. The deflection is also slightly increased.

After decreasing the rotation stiffness of the ribs even further it appears as though the top slab is now acting as a continuous beam. The ribs hardly resist rotation anymore and a larger part of the top slab is subject to a positive bending moment instead of a negative one. The top slab deflects a significant amount more as well and the load is now almost completely restricted to the central three ribs.

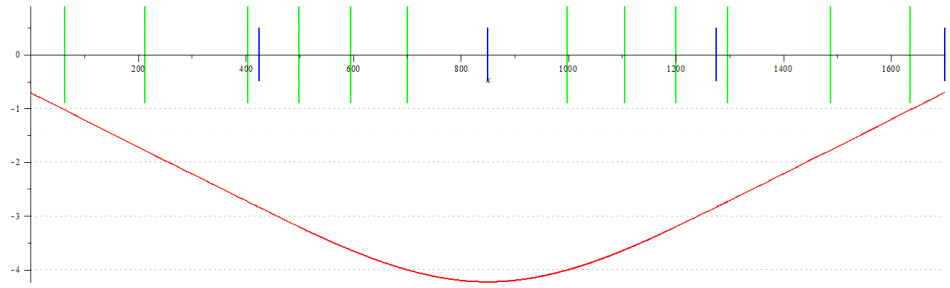

Figure 5.53: The deflection curve given by the model when the rotation spring coefficient is decreased by 90%.

Table 5.30: The output from the model when the strongly decreased values of the rotation spring coefficient are used.

$\mathbf{k_{rt} = 6.38 \times 10^7}$ [10%]		Load per rib [kN (%)]				
	Deflection at rib A [mm]	**Rib E**	**Rib C**	**Rib A**	**Rib B**	**Rib D**
Default values	3.38	3.89 (12.98%)	6.63 (22.09%)	8.96 (29.85%)	6.63 (22.09%)	3.89 (12.98%)
Values with changed variable	4.23	1.88 (6.25)	7.52 (25.07)	11.21 (37.36)	7.52 (25.07)	1.88 (6.25)
Change	0.85 (25.10)	-2.02 (-6.73)	0.89 (2.98)	2.25 (7.51)	0.89 (2.98)	-2.02 (-6.73)

5.4.5. THE LENGTH OF THE INTER-RIB TOP SLAB SECTIONS

The final parameter that will be analysed in this section is the length of the intermediate parts of the top slab that are located between the ribs. This parameter is unlikely to change because it cannot be influenced by adding or removing reinforcement or using different concrete classes, but is instead a global dimension of the steel profiled deck plate. It is still useful to know its influence though. Because this will tell what the benefits or draw backs would be when a different steel deck type is selected where the ribs have a different spacing.

Increased inter-rib top slab length

First of all the inter-rib length of the top slab will be increased by 25% and 900% respectively to 531.25 and 4250. Increasing the length of the top slab in between the ribs will effectively make the top slab less stiff, so it is expected to see a similar result as when the bending stiffness of the top slab was lowered, but since the entire top slab is now affected the effect might be larger. The results of the two increases in value are shown in figures 5.54 and 5.55 and in tables 5.31 and 5.32 respectively.

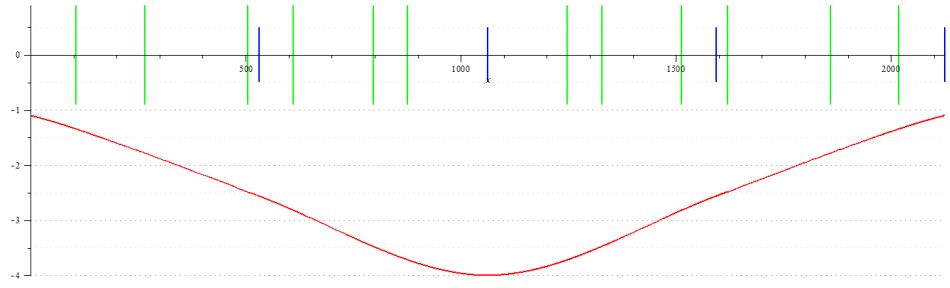

Figure 5.54: The deflection curve given by the model when the inter-rib top slab length is increased by 25%.

The effect of increasing the length between the ribs is rather large compared to the influence the other parameters have and comparable with the effect that the translation spring coefficient has. This can be explained through the fact that in the model calculation the length between the ribs is always present when to the power two or three or even four. Thus even small changes in this values will quickly add up to large changes in the

Table 5.31: The output from the model when the increased values of the inter-rib top slab length are used.

L = 538.25 [125%]		**Load per rib [kN (%)]**				
	Deflection at rib A [mm]	**Rib E**	**Rib C**	**Rib A**	**Rib B**	**Rib D**
Default values	3.38	3.89 (12.98%)	6.63 (22.09%)	8.96 (29.85%)	6.63 (22.09%)	3.89 (12.98%)
Values with changed variable	4.00	2.92 (9.72)	6.79 (22.62)	10.60 (35.32)	6.79 (22.62)	2.92 (9.72)
Change	0.62 (18.3)	-0.98 (-3.26)	0.16 (0.53)	1.64 (5.47)	0.16 (0.53)	-0.98 (-3.26)

model output.

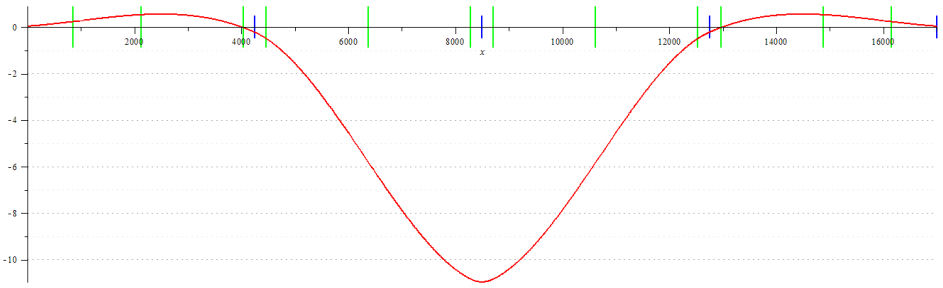

Figure 5.55: The deflection curve given by the model when the inter-rib top slab length is increased by 900%.

Table 5.32: The output from the model when the strongly increased values of the inter-rib top slab length are used.

L = 4250 [1000%]		**Load per rib [kN (%)]**				
	Deflection at rib A [mm]	**Rib E**	**Rib C**	**Rib A**	**Rib B**	**Rib D**
Default values	3.38	3.89 (12.98%)	6.63 (22.09%)	8.96 (29.85%)	6.63 (22.09%)	3.89 (12.98%)
Values with changed variable	10.96	-0.10 (-0.34)	0.58 (1.94)	29.04 (96.80)	0.58 (1.94)	-0.10 (-0.34)
Change	7.58 (224.3)	-4.00 (-13.32)	-6.05 (-20.15)	20.09 (66.95)	-6.05 (-20.15)	-4.00 (-13.32)

The changes in the deflection curve are now quite excessive. The load is almost completely concentrated on the central rib and the deflections are very large. This is again the result of the length between the ribs being calculated in two, three or four powers in the model calculation.

Decreased inter-rib top slab length

Now the rotation stiffness coefficient is reduced by 25% and 90% respectively to 318.75 and 42.5. Contrary to what was observed when the length was increased, the distribution should now become better and the deflection should decrease. This is for the same reason as before, the length is present in the calculations to the power two, three and four and this causes the changes to become very large. The results of the two decreases in value are shown in figures 5.56 and 5.57 and in tables 5.33 and 5.34 respectively.
As expected the distribution of the load is increased by a fair amount when the length between the ribs is decreased by 25%. The deflection is also significantly decreased.

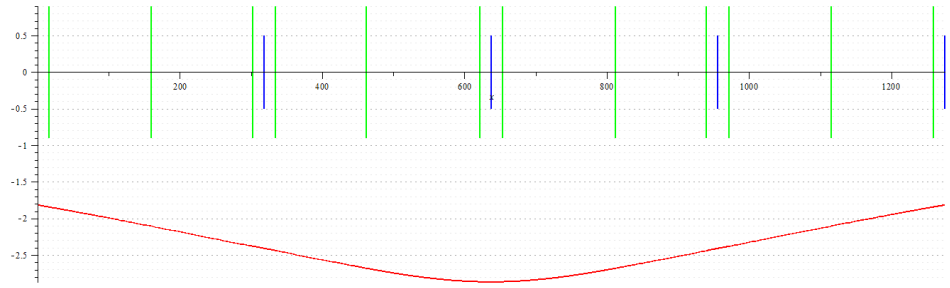

Figure 5.56: The deflection curve given by the model when the inter-rib top slab length is decreased by 25%.

Table 5.33: The output from the model when the decreased values of the inter-rib top slab length are used.

L = 318.75 [75%]		**Load per rib [kN (%)]**				
	Deflection at rib A [mm]	**Rib E**	**Rib C**	**Rib A**	**Rib B**	**Rib D**
Default values	3.38	3.89 (12.98%)	6.63 (22.09%)	8.96 (29.85%)	6.63 (22.09%)	3.89 (12.98%)
Values with changed variable	2.89	4.82 (16.05)	6.38 (21.28)	7.60 (25.33)	6.38 (21.28)	4.82 (16.05)
Change	-0.49 (-14.5)	0.92 (3.07)	-0.24 (-0.81)	-1.36 (-4.52)	-0.24 (-0.81)	0.92 (3.07)

Further reducing the length of the top slab in between the ribs results in the top slab becoming very short and very stiff. The top slab now reacts as though it was a continuous infinitely stiff beam which distributes the load almost completely evenly across the five ribs.

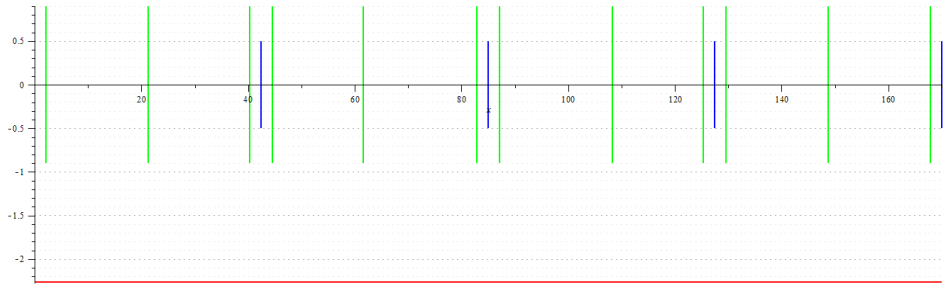

Figure 5.57: The deflection curve given by the model when the inter-rib top slab length is decreased by 90%.

Table 5.34: The output from the model when the strongly decreased values of the inter-rib top slab length are used.

L = 42.5 [10%]		**Load per rib [kN (%)]**				
	Deflection at rib A [mm]	**Rib E**	**Rib C**	**Rib A**	**Rib B**	**Rib D**
Default values	3.38	3.89 (12.98%)	6.63 (22.09%)	8.96 (29.85%)	6.63 (22.09%)	3.89 (12.98%)
Values with changed variable	2.27	5.99 (19.98)	6.00 (20.00)	6.01 (20.02)	6.00 (20.00)	5.99 (19.98)
Change	-1.11 (-32.8)	2.10 (7.00)	-0.63 (-2.09)	-2.95 (-9.83)	-0.63 (-2.09)	2.10 (7.00)

5.4.6. THE RIB SPAN LENGTH

The last parameter to be analysed is the span length of the ribs. This parameter is not directly imputed into the analytical model, but it influences the stiffness of the translation springs. In fact the influence the span length influences the translation spring stiffness to such a degree that increasing it by ten times or decreasing it by that much results in very extreme values. Because of that this parameter will only be analysed for a 25% increase and decrease.

Increased rib span length

First of all the span length is increased from 5.40 meter to 6.75 meter. This results in the increase of the translation spring stiffness 1512.1 N/mm. This decrease in translation spring stiffness will yield similar results as seen in the translation spring section. The results of increase in value is shown in figures 5.58 and in the table 5.35 respectively.

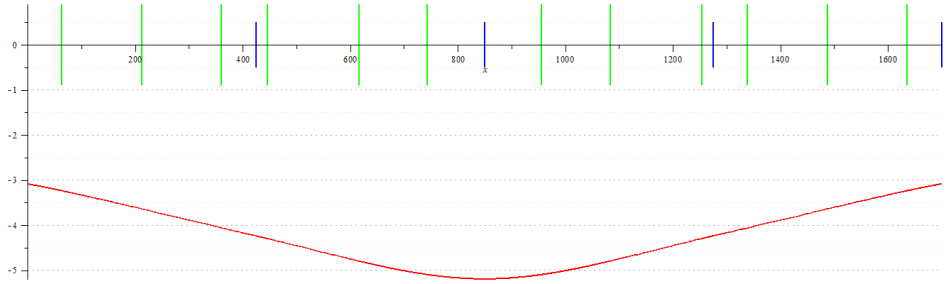

Figure 5.58: The deflection curve given by the model when the rib span length is increased by 25%.

Indeed as expected the load is distributed more evenly over the with of the beam. The effect is even stronger than when the translation spring stiffness is reduced, since the resulting spring stiffness value from increasing the rib span length is actually lower.

Table 5.35: The output from the model when the increased value of the rib span length is used.

L_{span} = 6750 [125%]		Load per rib [kN (%)]				
	Deflection at rib A [mm]	**Rib E**	**Rib C**	**Rib A**	**Rib B**	**Rib D**
Default values	3.38	3.89 (12.98%)	6.63 (22.09%)	8.96 (29.85%)	6.63 (22.09%)	3.89 (12.98%)
Values with changed variable	5.19	4.67 (15.55)	6.41 (21.36)	7.85 (26.17)	6.41 (21.36)	4.67 (15.55)
Change	1.81 (53.6)	0.77 (2.57)	-0.22 (-0.73)	-1.10 (-3.68)	-0.22 (-0.73)	0.77 (2.57)

Decreased rib span length

Now rib span length is reduced by 25% to 4.05 meter. Now the span length is reduced the translation spring stiffness is increased to 7020.8 N/mm which changes the ratio between the stiffnesses of the translation springs and the top slab so that the load will be concentrated more towards the centre rib. The results of increase in value is shown in figures 5.59 and in the table 5.36 respectively.

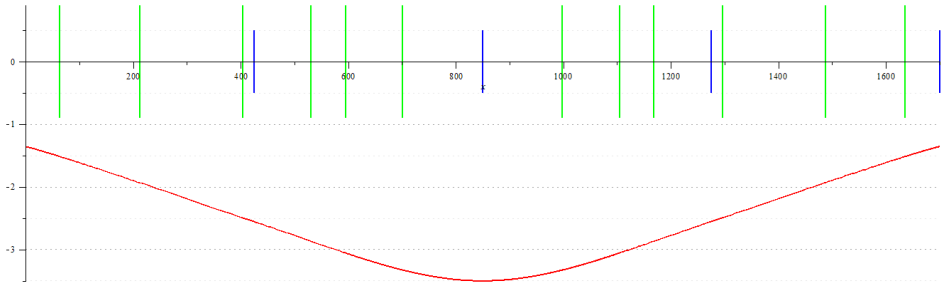

Figure 5.59: The deflection curve given by the model when the rib span length is decreased by 25%.

Table 5.36: The output from the model when the decreased values of the rotation spring coefficient are used.

L_{span} = 4050 [75%]		Load per rib [kN (%)]				
	Deflection at rib A [mm]	**Rib E**	**Rib C**	**Rib A**	**Rib B**	**Rib D**
Default values	3.38	3.89 (12.98%)	6.63 (22.09%)	8.96 (29.85%)	6.63 (22.09%)	3.89 (12.98%)
Values with changed variable	1.68	2.04 (6.80)	7.05 (23.50)	11.82 (39.39)	7.05 (23.50)	2.04 (6.80)
Change	-1.70 (-50.3)	-1.85 (-6.18)	0.42 (1.41)	2.86 (9.54)	0.42 (1.41)	-1.85 (-6.18)

Reducing the rib span length has the effect of concentrating the load more towards the centre of the model. The deflection is also increased significantly.

5.4.7. CONCLUSION ON PARAMETER SENSITIVITY

Now that the parameters above have be analysed for their influence on the distribution and the deflection of the model, it is time for them to be compared to one and another. This comparison is useful because it gives information on what parameter is best changed if a different model output is required. It also gives information on what is likely to change in the output if one of the parameters is changed or is in reality different from what was assumed when making predictions about the results of the experiments for example.

The best way to compare the influence of the analysed parameters is to compare the relative changes to the default output. For that purpose these values are all gathered and shown in table 5.37.

Table 5.37: This table shows all the changes in model output compared to the default output that are caused by changes in the values of the different parameters. All parameters are increased by 25% except for the rib span length which is decreased instead.

Parameter and parameter change		**Relative deflection change [%]**	**Load change per rib [kN (%)]**				
	Parameters	Rib A	Rib E	Rib C	Rib A	Rib B	Rib D
+25%	Translation spring stiffness coefficient k_{rib}	-0.51 (-15.1)	-0.38 (-1.27)	0.10 (0.34)	0.56 (1.85)	0.10 (0.34)	-0.38 (-1.27)
+25%	Positive top slab bending stiffness $EI_{TS,pos}$	-0.17 (-5.0)	0.11 (0.36)	0.01 (0.04)	-0.24 (-0.79)	0.01 (0.04)	0.11 (0.36)
+25%	Negative top slab bending stiffness $EI_{TS,neg}$	0.0 (0.0)	0.01 (0.03)	0.00 (0.00)	-0.01 (-0.04)	0.00 (0.00)	0.01 (0.03)
+25%	Rib rotation stiffness coefficient k_{rt}	-0.08 (-2.4)	0.21 (0.69)	-0.09 (-0.31)	-0.23 (-0.75)	-0.09 (-0.31)	0.21 (0.69)
+25%	Inter-rib length L	0.62 (18.3)	-0.98 (-3.26)	0.16 (0.53)	1.64 (5.47)	0.16 (0.53)	-0.98 (-3.26)
-25%	Rib span length L_{span}	-1.70 (-50.3)	-1.85 (-6.18)	0.42 (1.41)	2.86 (9.54)	0.42 (1.41)	-1.85 (-6.18)

From the table above it can be seen that adjusting the negative bending stiffness of the top slab has a negligible effect on the distribution and the deflection. The positive bending stiffness and the rib rotation stiffness both have an influence with the same order of magnitude. The positive bending stiffness is more effective at decreasing the deflection at the point of load introduction at rib A, while the rib rotation stiffness influences the distribution to the outer ribs to a larger degree. This is due to the fact that the positive bending stiffness is only applied at the centre of the model. This can be found while studying the moment diagram. In figure 5.60 the moment diagram of the default model has been given. Increasing the rib rotation stiffness of the positive bending stiffness by 25% does not alter the shape of this moment diagram. Thus it is seen that only at the centre of the model the bending moment exceeds the cracking moment needed to cause the top slab to crack. An increase in positive bending moment will therefore only affect this area. While, on the other hand, the increase of the rib rotation stiffness affects all the five ribs of the model and increases the distribution towards the outer ribs more. And lastly changing the rib span length has the largest influence on the model output since it has a larger than linear effect on the translation spring coefficient.
Again in figure 5.60 it can also be seen that only a very small part of the model is actually using the negative bending stiffness value. This also explains why the this value has so little influence on the results of the model. The effect the negative bending stiffness has on the output could only be increased if the rotation stiffness of the ribs increases to such a degree that a larger part of the model acts in negative bending moment than in a positive bending moment. This only occurs when the rib rotation stiffness is multiplied by a factor 4 to 5.

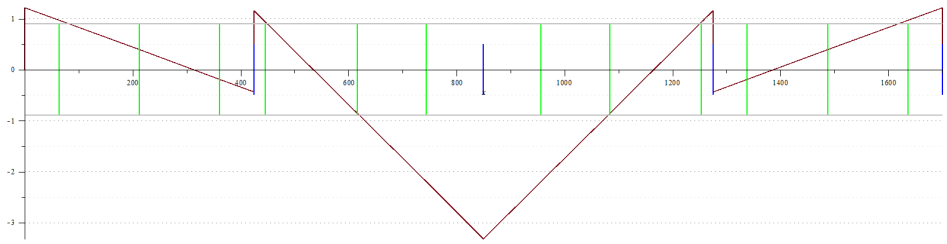

Figure 5.60: The moment diagram of the model while using the default values. The vertical green lines indicate the field separators, the vertical blue lines the locations of the ribs and the horizontal grey lines the height of the cracking moment.

The parameters that influence the output of the model in the largest way are the translation spring stiffness

coefficient and the inter-rib top slab length. The inter-rib length has a larger effect on both the deflection at rib A and the distribution of the load to the outer ribs, but ultimately this parameter is less interesting in this thesis because it can only be adjusted by choosing a different type of steel profiled deck with a different rib spacing. The translation spring stiffness coefficient on the other hand can be influenced by choosing a different concrete strength class or by increasing the height of the concrete cover on top of the steel deck. Because the bending stiffness of the ribs and the translation spring coefficient in the model are directly related an increase of 25% in the translation spring coefficient would correspond to a 25% increase in the rib bending stiffness as well. Getting the bending stiffness of the rib to increase is not easily done, but the effects on the distribution and the deflection are the largest relative to the change of the other parameters.

5.5. OVERVIEW OF ASSUMPTIONS AND CONCLUSIONS ON THE ANALYTICAL MODELLING OF THE COMPOSITE SLAB

The analytical model that has been created in this chapter will be used for the remainder of this thesis. As it is a model it will never give a perfect reflection of reality, but the aim is to give a reasonably close estimation. This will be verified by performing laboratory experiments and by using a FEM model to get similar results. It is important to keep a clear overview of what assumptions have been made while constructing this model because these assumptions can influence the behaviour and output of the model. So in this section a summary of the assumptions that were made are given divided into three subjects: model set-up, material properties and model parameters.

Model set-up

1. The ribs are able to rotate but translation is restricted to the vertical direction
2. The concentrated loads are applied at the centre of each rib.
3. The ribs are modelled as points to which the properties of the ribs are applied.
4. The top slab is modelled as a continuous beam, supported by the ribs.

Material properties

1. The concrete is not able to bear any tensile stresses.
2. The Young's modulus of any cracked concrete in the cross-section of either the ribs or the top slab is assumed to be equal to one third of the Young's modulus of the uncracked concrete.
3. The top flange of the steel of the profiled steel deck is assumed not to contribute to the strength and stiffness of the top slab in the longitudinal and transverse directions.
4. For the calculation of the rib properties, the effective steel cross-section was used.

Model parameters

1. The ribs are considered as simply supported beams which are acted upon by a concentrated load at a distance a. The stiffness coefficient is derived from this model.
2. The bending stiffness of the ribs in that modelling varies in two steps: cracked and uncracked. Where the interface of these two steps is located depends on the cracking moment of the ribs.
3. The three-dimensional effect of the steel-concrete composite slab deflecting under the concentrated load is broken up into an distributive length and distributive width parameter. These parameters are found through iteration.
4. The distributive width and distributive length parameters are conversions of an continuous stress curve into a stress block with an equal stress at every location.

Conclusions
The model that was created is a simplification of what happens in reality. This is inescapable when constructing models to make predictions about real structures. The value of a model should therefore be determined by judging other properties. A good model should have the following traits:

- Accurate predictions of real structure behaviour
- Easy use and application of model results
- Model output is based on actual mechanical behaviour

About the accuracy of the model can, as of yet, no definite statements be made. The accuracy is to be tested by comparing the model results to the results of the FEM model and the experiments that are performed in the laboratory. Though the accuracy of the model is at the end the most important aspect, since an inaccurate model would not be of much use, the evaluation of it will be done at a later point in this thesis.
The way in which the model works, is operated and how the output is used is also a very important aspect of it. Since it becomes increasingly less attractive to use a model if the time and effort to operate it increase as well. The input parameters of the model are, however, quite easily obtained and not many either. In order to use the model only the bending stiffness of the slab and ribs, the span length, the load, the translation stiffness coefficient, the rotation stiffness coefficient and the cracking moments are needed. These values should be already known when doing calculations on these structures and otherwise they are easily obtained through simple calculations.
The operation of the model is not as convenient as it could be though. Since the model consists of a large matrix that has to be solved for the input parameters, a computer and a program capable of doing so are required. Doing these calculations by hand is practically impossible. Apart from the required computer and software, the operation itself is quite convenient though. The matrix should be solved maybe a few times because the interfaces of the bending stiffness areas need to be adjusted and optionally the distributive length and width respectively. But all-in-all this does not take a large amount of time and it is not a difficult task either.
The output of the model can be either a percentage of the load per rib if this is desired or an distributive width over which the load is spread in the transverse direction. These outputs can then be used in further calculations without further need of converting or adjusting the information.
Despite several assumptions the model and model behaviour are based on actual mechanical behaviour. The principles of the model itself are easily understood and adjusted to suit one's personal needs. This is an advantage since the model can then be easily adjusted to suit a range of different situations, without the need to do extensive further testing to prove its validity. Although proving that the model is accurate for multiple situations will require testing and validation at first, these issues could then be avoided for future cases.
To conclude on what was said above, it seems possible that, given the model proves to be sufficiently accurate, it could be a useful tool when examining transverse distribution of concentrated loads steel-concrete composite slabs. The usage is not overly complicated, the model is based on mechanical principles and the output can easily be used in further calculations. It therefore all depends on how accurate the model will prove to be.

6

NUMERICAL MODELLING

This section elaborates on the finite element model that was used to analyse the composite slab. The finite element program that was used to perform the analysis was TNO DIANA. An initial model was set up by Myrsini Michalaki. That model was adapted to suit the exact boundary conditions as were used for the analytical model and the laboratory experiments as well. The model was also adapted in order to perform non-linear calculations instead of linear calculations. All of the items above and the material properties and calculations methods are described in this chapter.

6.1. THE BASIC MODEL

This chapter describes the efforts of modelling the composite slab in a finite element modelling program (FEM). The purpose of doing so is to gain additional insight in the behaviour of the composite slab prior to executing the laboratory tests and to validate the analytical model. This is done in order to make a more accurate prediction of the test results. So it has to be said that the role of the FEM model is fully supportive to the analytical model and the laboratory tests. It is not the main goal of the thesis to construct a FEM model of the composite slab, but it can nonetheless provide valuable information that can be used in the analytical model and in making predictions about the test specimen behaviour. This chapter will make use of work previously done by Myrsini Michalaki. She has already made a FEM model of the same composite slab, that is being modelled in this thesis. This model is used as the basis of the model that is used to do the calculations in this thesis.The overview of the chapter's components is shown in figure 6.1.

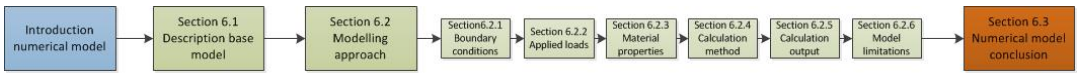

Figure 6.1: The overview above shows the components of which chapter six is made up.

The FEM modelling of the composite slab will be done in the DIANA program which was developed by TNO in the Netherlands. When modelling a structure, several types of analysis can be used. Two calculation types that can be used in DIANA are the 'structural linear static' and the 'structural non-linear' calculations. The linear static analysis method has as advantages that it takes less time to calculate the results of the modelling than it does for a non-linear analysis. The disadvantage however is that the material properties are assumed to be linear elastic and so the non-linear behaviour of cracking in concrete and yielding in steel are not included. The non-linear analysis on the other hand takes longer to calculate, but the advantage is that the non-linear aspects of the materials used can be included in the model. This gives a better representation of the structural behaviour at higher loads when yielding and cracking will start to occur. If the time needed to obtain a stable solution is still within an acceptable limit then it is certainly better to make use of the non-linear model. The material properties that will be used for the calculations can be specified in a number of ways. It is possible to let DIANA follow the conditions specified in material design codes such as the Eurocode for concrete or steel or their American counterparts. On the other hand is it also possible to specify the material properties manually. This means either entering the tabulated stress-strain diagram or choosing a predefined modelling method for the material in question and providing numerical information about for their limit values.

Because this numerical model will be used to provide predictions about the laboratory experiments it will be chosen not to follow the design codes already implemented in DIANA, since they make use of simplifications such as an idealized stress-strain diagram which are well suited to a design approach but not for studying actual material and structural behaviour. The exact modelling that is chosen will be discussed further on in this chapter.

6.2. MODELLING APPROACH

As stated before the model that will be used for analysing the composite slab is the result of work done by Myrsini Michalaki in her report 'Distribution of Concentrated Loads on simply supported Deep Composite Slab ComFlor 210'. The general dimensions of the model are 2750 mm of length and 1500 mm of width as can be seen in figure 6.2. These dimensions are half of the actual composite slab that is being analysed since the FEM model contains only a quarter of the actual composite slab.

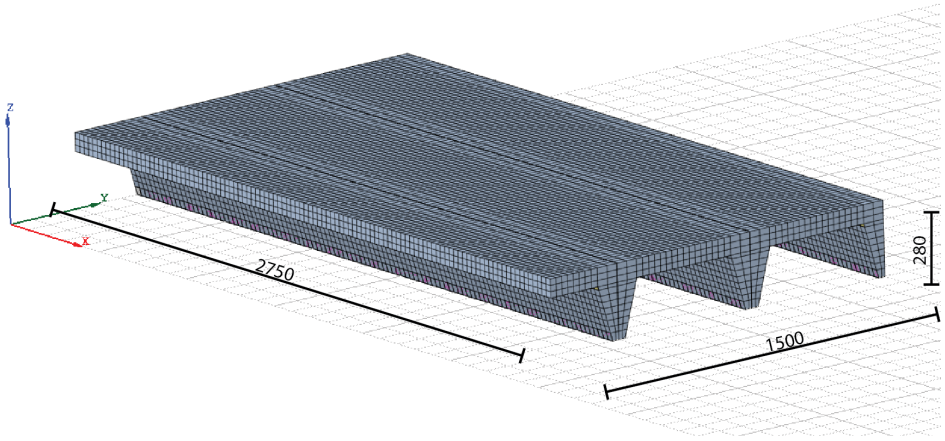

Figure 6.2: The general dimensions of the FEM model are shown in this figure.

The model consists of several components: the effective parts of the steel profiled deck, the concrete and the reinforcement bars in the top slab and in the ribs. The effective steel profile that is used is similar to the effective profile used in the analytical model, it has been reduced to the area that will contribute to the bending moment resistance. The parts that do not contribute towards the bending moment stiffness don't do so because of the embossments that reduce the longitudinal stiffness of the steel plate. The effective steel profile that is used is shown in figure 6.3 and a more detailed view of an actual deck and the reduced profile are shown in figure 6.3. The model also includes a small block of elements at each support which has a large stiffness. This was done to prevent large peak stresses from occurring at that locations. Even though in reality these stiffer parts will not be there, the way in which the boundary conditions are implemented is not completely truthful either. This will be expanded upon in the related paragraph. The model shows only one quarter of the complete composite slab since through the use of symmetry and boundary conditions the other parts will be mirrored copies of the part that is modelled. This approach also reduces the number of elements drastically, thereby reducing the calculation time as well.

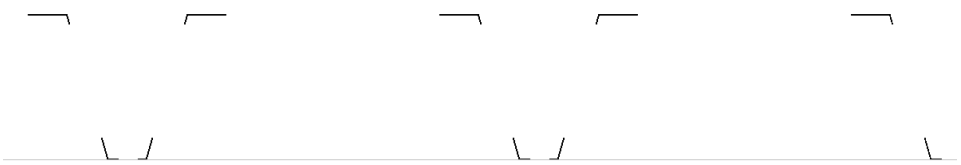

Figure 6.3: The effective area of the profiled steel deck that is used in the FEM calculations. The figure shows the two outer ribs and half of the middle rib. Only the corners of the top flange and the bottom flanges are effective when the slab is loading in bending.

The steel profiled deck is modelled with the element type CQ40F, which is a quadrilateral iso-parametric curved shell element with eight nodes. These elements are two dimensional but can have a certain thickness that is, in this case, equal to the thickness of the steel profiled deck. The element in question is shown in figure 6.5.

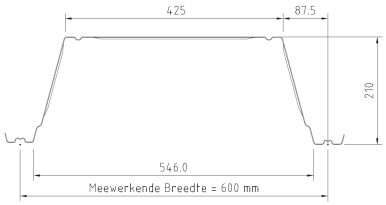

(a) A cross-section of a ComFlor210 steel profiled deck.

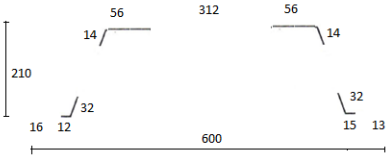

(b) The effective steel profile of a single ComFlor210 steel profiled deck plate.

Figure 6.4: The figures above show a cross-section of a ComFlor210 steel profiled deck and the modelled effective area that is used.

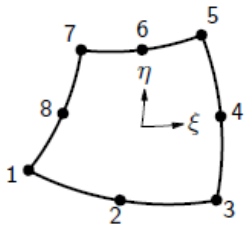

Figure 6.5: A Q20SH type element, which is used to the steel profiled deck. It is a two dimensional curved shell element.

The blocks of several elements with a higher stiffness at the supports (see white elements in figure 6.6) are modelled with the CHX60 element type. This element type, see figure 6.7, is a twenty-node iso-parametric solid block element and uses quadratic interpolation between the nodes. Elements with fewer nodes are not very suitable for non-linear calculations due to the possibility of parasitic shear and volumetric locking. The resulting stresses and strains in the stiff supports are not of interest though, because the only purpose of the stiff blocks at the supports is to prevent peak stresses. Peak stresses could be introduced due to the fact that the boundary conditions are applied to the single nodes in an edge instead of the whole edge model. The concrete in the model is also modelled with CHX60 elements which have 20 nodes. This element type is a three dimensional one and has nodes in the middle of the edges compared to the standard block element HX24L which has only 8 nodes. This element type is better suited for non-linear calculations.

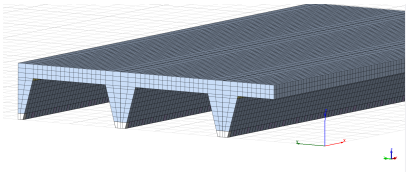

(a) A front view of the concrete elements in the FEM model.

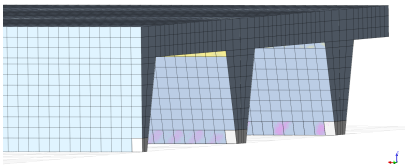

(b) A three-dimensional view of the concrete elements in the FEM model.

Figure 6.6: The stiff supports are shown in white.

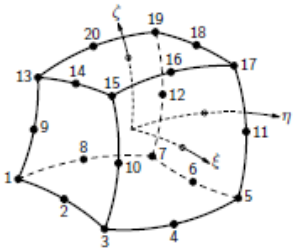

Figure 6.7: A CHX60 element .

(a) Side 1. (b) side 2.

Figure 6.8: The concrete elements are shown in grey.

6.2.1. BOUNDARY CONDITIONS

The boundary conditions are very important because of the fact that only a quarter of the composite slab is modelled. Therefore not only the boundary conditions of the real-life supports but also the symmetry conditions have to be used.
The boundary condition of the composite slab is that the ribs at each end are restricted in the vertical direction but translation is allowed in the longitudinal and transverse direction. Rotation in also direction is also allowed. The application of these conditions are shown in figure 6.9.
The symmetry conditions are as follows:

1. Along the face at x=1500 the nodes are restricted in translation in the transverse (y-axis) direction
2. Along the face at x=1500 the nodes are restricted in rotation around the x-axis.
3. Along the face at L=2750 the nodes are restricted in translation in the longitudinal (x-axis) direction
4. Along the face at L=2750 the nodes are restricted in rotation around the y-axis.

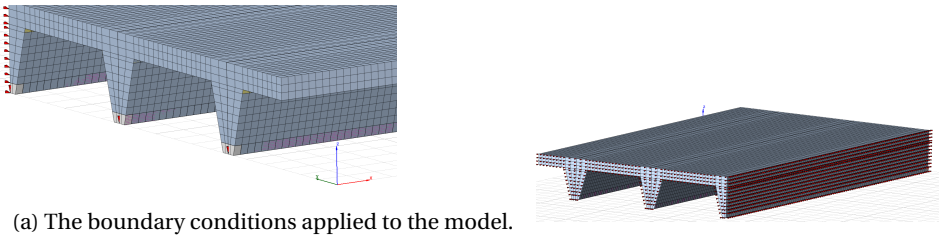

(a) The boundary conditions applied to the model. The three ribs . (b) The symmetry conditions applied to the model.

Figure 6.9: The boundary and symmetry conditions.

6.2.2. APPLIED LOADS

There are two loads applied to the model:

1. The self-weight of the composite slab
2. The concentrated load at the centre of the slab

Both loads can be seen in figure 6.10.

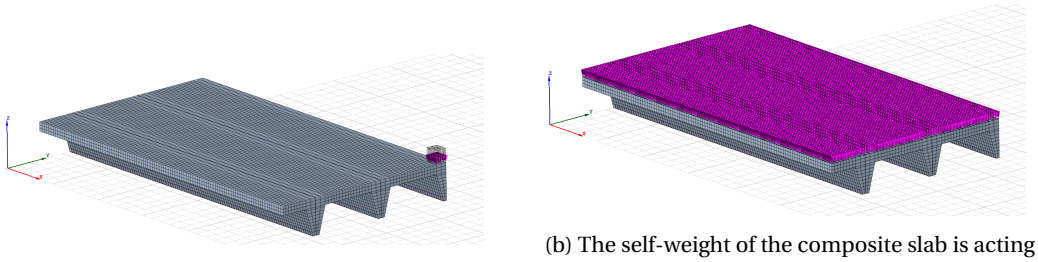

(a) The concentrated load is acting on a 175 mm x 175 mm area at the centre of the composite slab.

(b) The self-weight of the composite slab is acting as a distributed load on the top faces of the elements all across the top side of the model.

Figure 6.10: The loads that are applied to the model. Both loads are applied as distributed loads to the face of elements.

The concentrated load is placed at the centre of the composite slab in the middle of both the length and the width of the slab. This is the main loading position in the analytical model as well. The concentrated load is applied to a 175 mm x 175 mm area. In the FEM model only one quarter of this area can be seen in the model since symmetry has been used to reduce the model to only a quarter of the complete slab.
These loads are applied in the following manner in the mode.

- The self-weight as a distributed load
- The concentrated load as an enforced deformation

It is chosen to apply the concentrated load as an enforced deformation to allow the model to go past the formation of the first large crack during the calculation. If the load would be applied as a force instead then the model would be unable to converge to a solution as soon as the first crack appeared.

6.2.3. MATERIAL PROPERTIES

The implementation of the material properties is of great importance since this will effect both the strength and the stiffness of the components in the model. This section will elaborate on the way in which the material properties of each of the components is applied.

CONCRETE

Concrete is a difficult material to model, because of the non-linear properties in both the compressive and tensile branch of the stress-strain behaviour. There are multiple models which attempt to simulate the concrete for both the compressive and tensile behaviour of concrete. In this paragraph the model type that is used for both sides of the stress-strain curve are explained.
It is also possible to use codes, like the Eurocode, Japanese or American concrete codes, but it is chosen not to do this since it is not clear what properties will be appointed to the concrete when this is done.

Compressive behaviour

For modelling the compressive behaviour of the concrete there are several models available in DIANA, these are the following:

- Bi-linear
- Parabola rectangular
- Parabolic
- Thorenfeldt
- Manual input

The diagrams associated with the models are shown in figure 6.11.
It was chosen to use the parabolic stress-strain diagram to model the compressive behaviour of the concrete as this is preferred by guidelines set up for non-linear analysis by the Dutch Government ([15]).
The parabolic curve is governed by the formulas shown in equation 6.1.

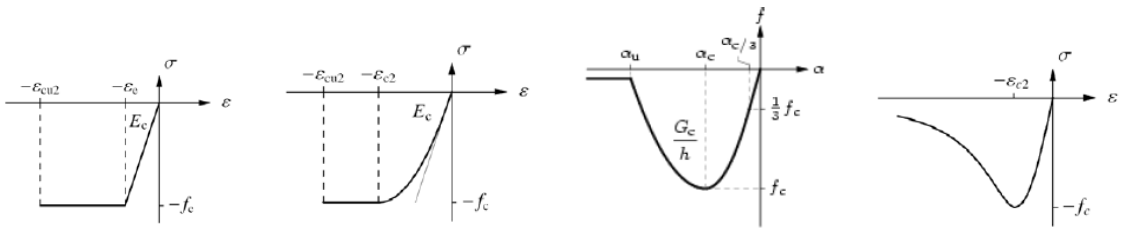

(a) The bi-linear stress-strain diagram.

(b) The parabolic-rectangular stress-strain diagram.

(c) The parabolic stress-strain diagram.

(d) The Thorenfeldt stress-strain diagram.

Figure 6.11: The stress-strain diagrams related to the available models.

$$f = \begin{cases} -f_c \frac{1}{3} \frac{\alpha_j}{\alpha_{c/3}} & \text{if} \alpha_{c/3} < \alpha_j \leq 0 \\ -f_c \frac{1}{3} \left(1 + 4\left(\frac{\alpha_j - \alpha_{c/3}}{\alpha_c - \alpha_{c/3}}\right) - 2\left(\frac{\alpha_j - \alpha_{c/3}}{\alpha_c - \alpha_{c/3}}\right)^2\right) & \text{if} \alpha_c < \alpha_j \leq \alpha_{c/3} \\ -f_c \left(1 - \left(\frac{\alpha_j - \alpha_c}{\alpha_u - \alpha_c}\right)^2\right) & \text{if} \alpha_u < \alpha_j \leq \alpha_c \\ 0 & \text{if} \alpha_j \leq \alpha_u \end{cases} \tag{6.1}$$

In the formulas denoting the parabolic nature of the stress-strain diagram α_j represents the compressive strain in the concrete and the limit values used in the formulas are as follows:

- $\alpha_{c/3} = \frac{1}{3}\frac{f_c}{E}$
- $\alpha_c = 5\alpha)_{c/3}$
- $\alpha_u = \alpha_c - \frac{3}{2}\frac{G_c}{h_e f_c}$

With f_c being the mean concrete compressive strength, E the mean young's modulus of the concrete and G_c the compressive fracture energy which is equal to 250 times G_F, the fracture energy.

Tensile behaviour
The tensile behaviour also has multiple models that can be used in DIANA:

1. Exponential softening
2. Hordijk softening
3. Multi-linear softening
4. Brittle
5. Linear ultimate strain based
6. Idealized
7. Manual input

These models denote the loss of strength in the concrete in tension after a peak stress is reached. The different models are shown in figure 6.12.
It is chosen to use exponential softening since this is again the preferred method by the Dutch governmental guidelines ([15]). The formula governing the exponential softening of the concrete tensile strength is shown in equation 6.2.

$$\sigma = f_t \exp\left(-\frac{\epsilon^{cr}}{\epsilon_u}\right) \tag{6.2}$$

With ϵ^{cr} being the positive tensile strain in the concrete, f_t the mean tensile strength of the concrete and ϵ_u the ultimate strain of the concrete which is determined by equation 6.3. In this equation h_{eq} an equivalent

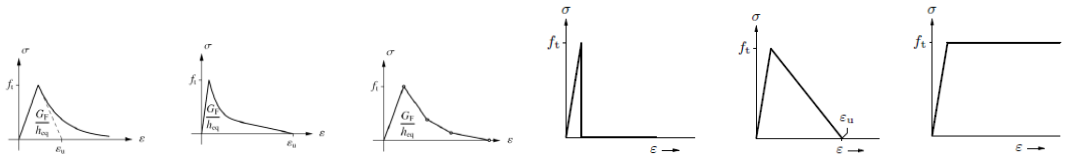

(a) The exponential softening stress-strain diagram.

(b) The Hordijk softening stress-strain diagram.

(c) The multi-linear softening stress-strain diagram.

(d) The brittle stress-strain diagram.

(e) The linear ulitmate-strain based stress-strain diagram.

(f) The idealized stress-strain diagram.

Figure 6.12: The stress-strain diagrams related to the available models for tension stresses in concrete are shown in the figures above.

length. This value is automatically determined by DIANA and depends on the dimensions of the elements used in the model.

$$\epsilon_u = \frac{G_F}{h_{eq} f_t} \tag{6.3}$$

STEEL

For the steel a bi-linear stress-strain diagram was used. This means that it is linear elastic until it reaches the yield stress. The yield stress is determined with the Von Mises plasticity theory. The yield stress has to be given as input. It is possible to model hardening of the steel with several models. It is chosen, however, to not model hardening of the steel since it is expected that the steel components will either not yield before failure occurs, or will not reach the end of the yielding strain before that happens. If it is found in the results that the steel does in fact yields to a strain where normally hardening would occur, than this choice should be revised.

REINFORCEMENT AND SUPPORT

The reinforcement and supports blocks also use a bi-linear stress-strain diagram. It is possible to impose a stress limit for the material and this is done for the reinforcement of the composite slab. This includes both the reinforcement bars in the top slab and the reinforcement bars in the ribs. The support element blocks do not need a limit stress, since their only purpose is to spread the load to a realistic degree and prevent large peak stresses from destabilizing the model.

MATERIAL VALUES

The values of all the material values discussed above are shown in table 6.1.

Table 6.1: The parameters that were used in the FEM model are displayed in this table.

Parameter	**Symbol**	**Value**	**Unit**
Steel Yield stress	f_{ym}	400	mm
Steel poisson ratio	υ_s	0.3	mm
Steel Young's Modulus	E_a	210000	N/mm^2
Concrete ultimate stress	f_{cm}	28	mm^2
Concrete Young's Modulus	E_c	30000	mm^2
Concrete poisson ratio	υ_c	0.15	N/mm^2
Crack orientation model	–	Rotating	N/mm^2
Concrete tensile strength	f_{ctm}	2.8	N/mm^2
Tensile fracture energy	G_F	0.12	N/mm^2
Reinforcement yield stress	f_s	540	N/mm^2
Reinforcement Young's modulus	E_s	200000	N/mm^2
Support Young's modulus	E_{sup}	210000000	N/mm^2

6.2.4. CALCULATION METHOD

The DIANA model is calculated with a 'structural non-linear' analysis. There are a number of non-linearities which can be taken into account:

- Physical
- Geometrical
- Transient

The physical properties are the material properties of the model, the geometrical properties are instabilities in the model due to displacement of the applied loads and transient properties are changes in loads and in the model over time.
There are no time related aspects of the model so transient properties are not included in the DIANA analysis, geometrical non-linearities are also not present in the composite slab. Therefore only the physical non-linearities of the materials are included.
There are two loads applied: the self-weight and the concentrated load. While the loads could be applied at the same time, this is not the case in reality. All the self-weight is acting from the moment the construction of the composite slab is completed. Therefore the self-weight is applied first and thereafter the concentrated load. Both loads are applied in steps since DIANA is unable to apply the loads in one step and converge to a stable solution.
The choice of the size the size of the load steps can be done in a number of ways:

- User specified sizes
- Energy based sizes
- Iteration based sizes
- Automatic step sizes

With the user specified step size option it is possible for the user to specify exactly how many steps and how large each loading step should be. The advantage of this option is that it is known exactly which steps the model will take. The disadvantage is that if DIANA cannot converge on a certain step, because of the step size, there is no way to adjust it's size and the analysis will be stopped due to a lack of convergence.
The second option is to let DIANA automatically decide the step sizes based on the energy. It is possible to set the initial step size, the minimum and the maximum step size. If no convergence is reached at the initially chosen step size DIANA will automatically adjust step size. Then DIANA will try to converge to a stable solution again and if unable after a few iterations keep adjusting the step size until it converges.
Another option is to let DIANA determine the step size automatically based on the number of iterations necessary to achieve convergence. DIANA will increase or decrease the step size to achieve an optimal amount of iterations.
The last option is to let DIANA automatically cutback the step size when no convergence is reached. The cutback factor is user supplied and DIANA will keep reducing the step size until a stable solution is reached after a few iterations.
For all automatic options it is possible to set both a maximum and a minimum step size. Whenever either one of those limitations is broken DIANA will stop the calculation. It is also possible to set the value for which DIANA considers the stable solution to be reached. By default this value is set to be 10^{-2} and the difference between the internal and external forces has to be lower than this value. Apart from the force also the energy and displacement can be used as criteria. Whenever one of the criteria reaches the convergence value, the calculation is considered successful by DIANA. It was chosen the use both the force and displacement criteria while calculating the model. This is also the default setting.
Then it is also possible to provide DIANA with the maximum number of iterations that it does per step. If the convergence limit is not reached within the number of iterations provided then DIANA will again stop the calculation. The calculation is also stopped when the results are found to be divergent.
DIANA determines the results of the next step generally by determining the stiffness matrix of the model subject and then increase the load by the determined increment. There are several methods that DIANA can use to determine the next solution:

- Constant stiffness

- Linear stiffness
- Newton-Raphson
  - Regular (default)
  - Modified
- Secant (Quasi-Netwon)

By default the regular Newton-Raphson method is used. It was chosen to use the modified Newton-Raphson method instead though, because this method is less prone to becoming unstable and more often yields convergence. The difference between the two methods is that the regular Newton-Raphson sets up the tangential stiffness before each iteration while the modified version sets up the tangential stiffness only before the first iteration and keeps it constant during the rest of the step. An additional benefit is that this method is therefore also quicker to reach the answer for each iteration, although it is likely that the modified Newton-Raphson does need more iterations than the regular version.
The methods stated above determine the manner in which the stiffness matrix is set up for the model and at what point in the calculation this is done. The method of solving the system of equations following from this stiffness matrix also has several options. However, this is not further discussed here and the default option in DIANA is found to be sufficient.

6.2.5. CALCULATION OUTPUT

The output that is received from the DIANA calculation can also be chosen from a large list of options. Since the point at which the concrete starts to crack and the deflection of each rib are very important in the analytical model, it is chosen to receive as output the deflection of the nodes, the stresses and strains in all element types and the cracking that occurs in the concrete. All of this output is available per loading step which means that the progression of cracking, stress and strains can be followed closely. The output which is received from the DIANA model is summarized below:

1. Internal stress for all elements
2. Internal strain for all elements
3. The displacement for all nodes
4. The cracking that occurs in the model
5. The support reaction forces

6.2.6. LIMITATIONS

The DIANA model has several important aspects that need to be mentioned. The items are mentioned below:

1. The steel and concrete are assumed to be completely bonded
2. Only the effective area of the steel profiled deck is modelled, the embossments are disregarded
3. The steel is modelled to have no hardening phase
4. Model stability

The assumed complete bond between the steel and the concrete is an important assumption in both the analytical and the FEM model. It ensures complete cooperation between the two materials where in reality this will not be the case. After a certain loading is reached the horizontal shear stress will become too large for the interfaces between the materials and the bond will decay, thereby reducing the overall stiffness of the composite slab. This will cause the FEM model to behave stiffer than the real composite slab and therefore this is a cause of error that needs to be kept in mind.
Furthermore, the areas of the steel profiled deck that are not effective in bending are not modelled. For the bending moment acting in the ribs this might approximate reality fairly well, but any other contributions which these parts of the steel profiled deck might have given are not included in the model. These contributions could be additional vertical shear resistance of the ribs or an increase in top slab stiffness or an additional stress transfer in the transverse direction through the steel deck. The size of these contributions is

not known and they might be negligible. It is, however, still a possible source of errors.
Another aspect to be taken into account is the fact that in the FEM model the steel deck and the reinforcement both have no hardening phase. After reaching their respective yield stresses it becomes impossible for them to bear more stress. This lack of hardening only becomes a problem if at some point a steel component reaches the yielding stress before failure at any other point in the model occurs. If this is the case the material modelling of the steel will have to be adjusted and if it does not the material modelling of the steel will not be an issue.
The stability of the model is a very important aspect to be discussed. Despite efforts to increase the stability of the model, after increasing the load to a certain point DIANA will not be able any more to calculate a stable solution. This could be caused by numerous reasons such as: material failure and calculation instability. If decreasing the step size does not provide the way forward then it means that the FEM model can only be used until that size of loading. This could mean that the FEM model provides only limited information and is more suited to examine the initial distribution in the composite slab rather than the failure behaviour of the composite slab.

6.3. CONCLUSION OF FEM MODEL

Given the limitation which were described above it is concluded that the FEM model should be seen as an additional source of information to help improve the analytical model and support it in while making predictions about the outcome of the experiments' initial stage. It is, however, difficult to use it to predict anything about the failure modes of the composite plates or the behaviour at higher loads due to the instability of the model. The models can only provide information about the early stages of loading where converged solutions are available. It is likely that the results will also be more accurate at this stage because non-linearities in the modelled materials are not yet occurring.
With regards to use in practice of Finite element modelling has the advantages of providing more information of the modelled structure and including a larger range of parameters. However, the disadvantages are that for each new design situation a new model has to be created for which both a FEM program and the knowledge how to use it are required. The creation or adaptation of a model is also relatively time consuming. The accuracy of the finite element model is also not yet known. This will be derived from the comparison to the results from the laboratory experiments. The choice of whether to use a finite element model will in practice depend on the accuracy of the model and the amount of information that is needed from the structure.

7

LABORATORY TESTING

This chapter contains the discussion, explanation and the results of the laboratory testing of the test pieces of the ComFlor210. The results of the tests are used to validate and calibrate the analytical and numerical modelling in the two previous chapters. The analytical and numerical modelling contain several modelling assumptions to predict the transverse stress distribution caused by a concentrated load. These assumptions are validated in this chapter. The analytical modelling is the main point of interest; the Finite Element Modelling is used to verify the analytical prediction of the stress distribution. The experimental results are used to make a comparison with the actual measured behaviour of the composite floor and the analytical prediction. The results are used to validate and calibrate the modelling, as discussed in chapter 5. The flowchart of the modelling approach is shown in Figure 7.1.

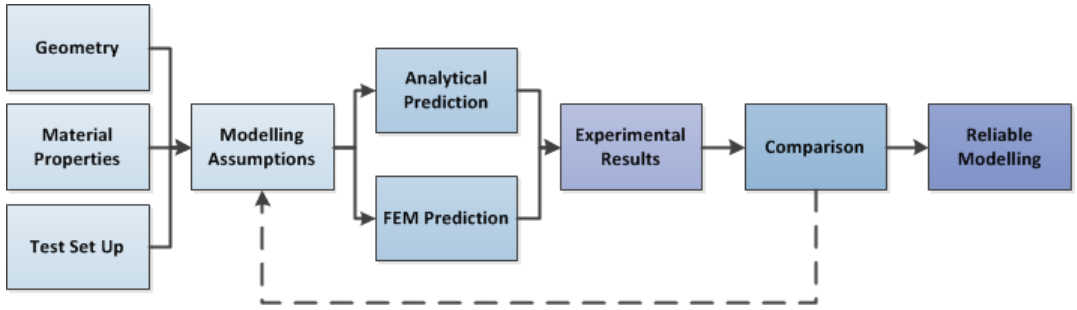

Figure 7.1: The flowchart of the modelling approach in this research

This chapter starts with explaining the test objectives. Three test pieces were constructed in total, with different properties. The properties of the test specimen are discussed in Section 7.2. The geometric and material properties of the test specimens are presented first, followed by the details of the construction process and the precautions taken to prevent the test specimen from being damaged during transport.

The properties and characteristics of the test set-up is presented hereafter. The tests are executed in the Stevin II laboratory of Delft, University of Technology. The final section presents the results of the test series. The discussion of the differences between the analytical modelling and the experimental results is done in chapter 8.

7.1. TEST OBJECTIVES

The thesis goal is defined in the introduction as follows:

"To produce an accurate analytical model for the evaluation of the distribution of stresses over the ribs in the transverse direction, due to loading by concentrated loads in deep composite slabs and validate this model

by doing Finite Element Modelling and experimental tests"

The analytical and Finite Element Modelling procedures are explained and presented in the chapter 5 and chapter 6 respectively. The models are created to predict the stress distribution, caused by a concentrated load, over a deep composite slab. This transverse stress distribution over the ribs is the main objective in this thesis. Conservative and inefficient design rules can be adjusted if the models have proven to be able to predict the stress distribution accurately.

Both models need, however, validation by testing real full scale pieces in the Stevin II laboratory of the TU Delft. The focus lies on the analytical model. The test results are used to calibrate the analytical modelling procedure further. The analytical modelling procedure is based on certain assumptions. These assumptions are verified and evaluated by using the experimental results. The following main and sub objectives can therefore be distinguished in the experiments:

Main objective

- Validate and calibrate the analytical model for the transverse distribution of the concentrated load acting on the deep composite slab.

The numerical models, explained in Chapter 6, are used to firstly validate the analytical modelling procedure. The numerical modelling validation is not the prime objective, but the outcome of one of the analyses is used to construct one of the test specimen, as will be discussed in the next section.

Sub-objective

- Investigate the ability of the concrete to distribute the loads.
- Investigate whether the top flange of the steel deck is active in the transverse direction or not.
- Investigate the influence of the reinforcement meshes on the transverse distribution of the load.
- Investigate the failure mechanism of the composite floors.

The numerical models have shown that the composite floor, without any reinforcement meshes, is able to distribute the stresses in the transverse direction better than expected. This composite floor composition is not used in practice, but this interesting outcome is examined nevertheless to serve as an additional validation point validate both the numerical and the analytical models.

The bending stiffness of the top slab is a very important parameter in the analytical model. This parameter together with the bending stiffness of the ribs determine in a large way how the distribution of the load works out. While calculating the bending stiffness of the top slab it was assumed that the top flange of the steel deck does not contribute to a stiffer top slab in the transverse direction. This is because of the longitudinal embossments in the steel deck. To check this assumption, however, it is necessary to measure the stresses that occur in the top flange.

The bending moment stiffness is also influenced by the presence of the reinforcement meshes in the top slab. Two different reinforcement configurations are used to examine the influence of this parameter on the transverse stress distribution. Both configurations are used in practice.

7.2. TEST SPECIMENS

This section discusses the test specimen used to perform the laboratory tests. The geometric details and material properties are presented in the first two sections, whereby the material properties are obtained by performing tests on the material that is used to construct the composite floors. Subsection 7.2.3 provides the construction method to produce the test pieces. The last section discusses briefly the transportation details that were implemented to prevent initial defects on the composite slab.

7.2.1. GEOMETRY

Three test pieces were constructed at Dutch Engineering in Zoeterwoude. All three test specimen contain the same geometrical dimensions and material properties, but there is a difference in the reinforcement configurations of the slabs. The three test specimen vary in the following manner:

1. A specimen with COMFLOR210 steel deck + no reinforcement meshes
2. A specimen with COMFLOR210 steel deck + top reinforcement mesh
3. A specimen with COMFLOR210 steel deck + top and bottom reinforcement meshes

The total length of all specimens is be 5.6 meters and the span length between the supports is 5.4 meters. The width of the specimens is 3.0 meters. Each test piece is constructed out of 5 separate steel decks and consist of five ribs. The steel deck has a thickness of 1,25 mm. The specimens have a reinforcement bar, with a diameter of Ø20 mm, in the ribs at 56 mm from the bottom and a concrete height on top of the steel deck of 70 mm. The centre-to-centre distance between the ribs is 600 mm. The reinforcement meshes in the top slab are Ø8 – 150 (if present). The top view of the all three test specimen is shown in figure 7.2.

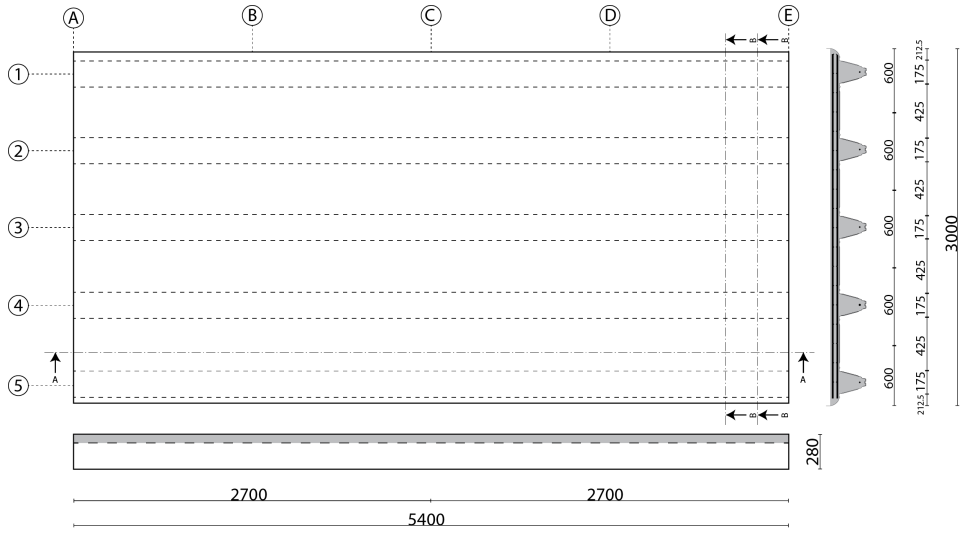

Figure 7.2: A top view of the general shape and dimensions of test pieces 1 to 3.

The outermost ribs on both sides were constructed in a special manner which is explained in the section about the construction method in Section 7.2.3. One steel deck will be cut in half to obtain the geometry as shown in 7.2. A front view of one rib of each specimen with a part of the surrounding slab is presented in figures 7.3a, 7.3b and 7.3c. The difference in reinforcement configuration is clearly visible. The reinforcement bar in each rib is also indicated in the figures.

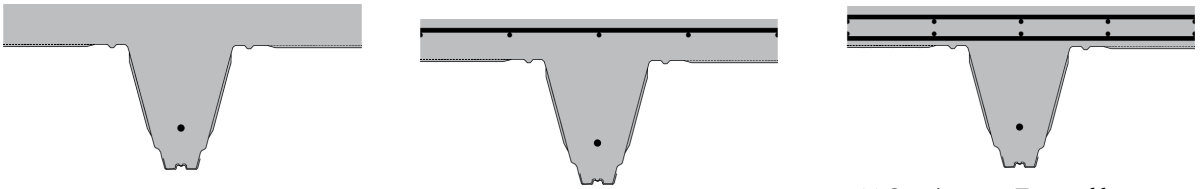

(a) Specimen 1: No reinforcement meshes

(b) Specimen 2: Top Reinforcement

(c) Specimen 3: Top and bottom reinforcement

Figure 7.3: A schematic representation of the three different reinforcement geometry

All specimens have different functions. Specimen 1 without any reinforcement is chosen as a result from the FEM modelling done by Myrsini Michalaki. The FEM model resulting from that research suggested that the

composite slab was able, prior to initiation of concrete cracking, to distribute the concentrated load rather well to the outer ribs. This slab layout is not used in practice, but it is a good reference point for verifying the concrete behaviour by itself and to verify in particular the output of the Finite Element Modelling.

The second specimen is the default option in deep composite slab construction, the ComFlor210 composition is always used with a minimum of one reinforcement mesh. Only top reinforcement in the slab is present. Validating the constructed analytical model for this case is thus a prime motive to use this test specimen layout. Apart from validating the model, it will also provide additional behavioural information about the composite slab with one reinforcement mesh. This is also valuable information since this layout is often used in practice.

The third specimen with both a top and a bottom reinforcement mesh is a layout that will be used in practice in case of a large concentrated load. But the effect of the contribution of this extra reinforcement mesh to the distribution of the concentrated force is not known. This can be predicted again by using analytical and FEM models and validating these models and observing the distribution and failure behaviour is the primary objective.

The exact dimensions of the Comflor210 are indicated in figure 7.4, it shows exactly the half of a steel deck used to create the composite floor. This figure contains both a top and a bottom reinforcement mesh. The position of the top mesh remains unchanged if the bottom mesh is not present.

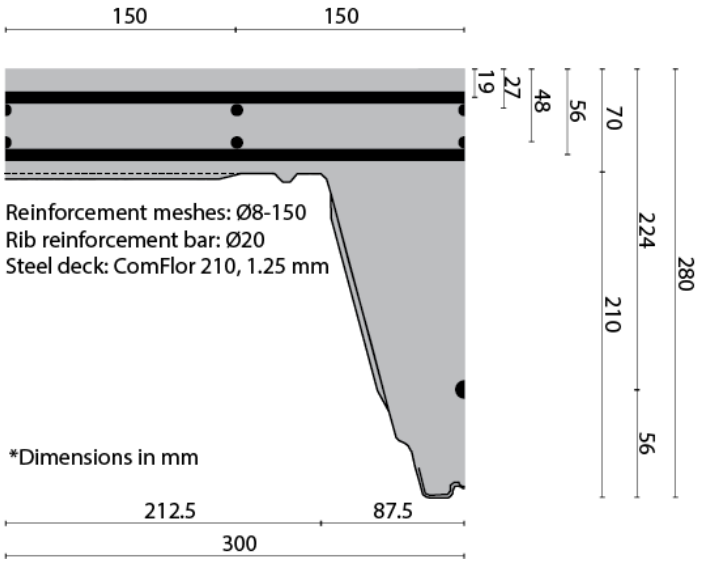

Figure 7.4: The exact dimensions of precisely the half of a steel deck.

Finally, a symbolic representation of the dimensions is shown in figure 7.5. This figure contains an entire rib with corresponding parts of the top slab.

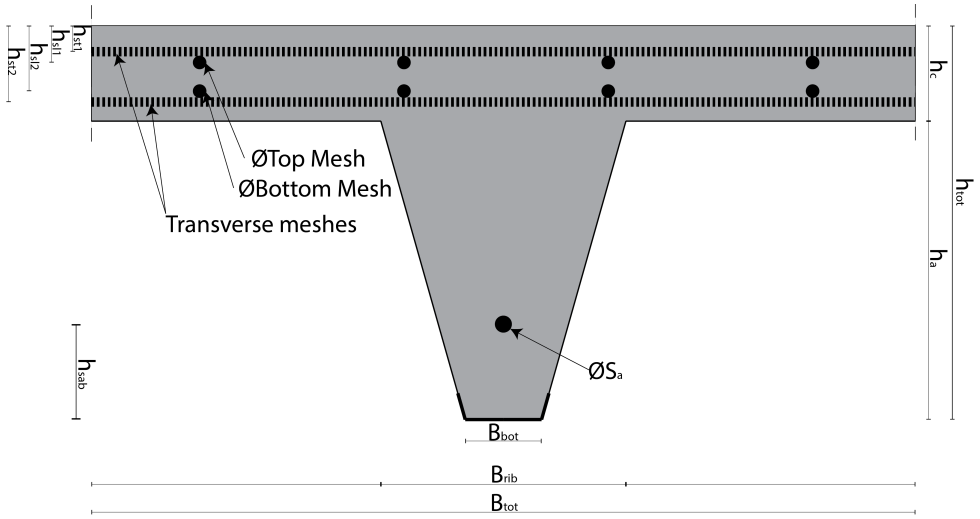

Figure 7.5: A symbolic representation of the dimensions of the ComFlor210.

7.2.2. MATERIAL PROPERTIES

The nominal material properties of the concrete, reinforcement steel and steel deck are stated below. These values are characteristic values that will therefore not be representative of the actual materials that are used. The analytical and numerical models can only be validated and calibrated if the real material behaviour is obtained by performing material tests. The used steel and concrete classes are as follows:

- Steel deck strength class: S355
- Concrete strength class: C20/25
- Reinforcement steel strength class: B500

The real material properties of the steel deck, reinforcement bars and the concrete are obtained by performing material tests in the Stevin laboratory of Delft, University of Technology. This data is required to make an accurate comparison between the analytical modelling and the experimental results. The details regarding the used test set up and results are presented in Appendix F. This section only presents the actual material properties that are required in the analytical modelling procedure.

Tension tests are executed on test specimens of the two used reinforcement bars and the steel deck. The most important characteristics are the yield stress and ultimate stress of the steel. The displacement characteristics are hard to find with the available lab equipment. The modulus of elasticity can therefore not be accurately obtained, but the value that is found is presented nonetheless; this parameter is important for the calculation of the bending stiffness. Table 7.1 presents the relevant material properties. These values are obtained by executing several tests and taking the average value.

Table 7.1: The relevant material properties of the reinforcement bars and the steel deck

	Yield stress (MPa)	Ultimate stress (MPa)	Fraction f_u/f_y	Modulus of Elasticity (MPa)
Reinforcement Ø8	518.040	541.603	1.054	200000
Reinforcement Ø20	560.035	665.302	1.188	200000
Steel Deck	400.3991	462.686	1.157	210000

The actual material properties are all higher than the nominal values, as presented in the beginning of this section. Concrete cubes of size 150 mm were cast at the same moment that the test specimen were cast. The material properties, the compression and tensile strength, of the concrete are obtained at the day each test of

the ComFlor210 specimens is performed to know the exact strength of the concrete at the moment of testing. A test series is also performed when the concrete has hardened 28 days, to check the nominal cubic compression strength the concrete factory should provide. These test results in following averages:

Table 7.2: The average material properties of the concrete

	Compression strength (MPa)	Tensile strength (MPa)	Modulus of Elasticity (MPa)
Specimen 1	29.44	3.17	30000
Specimen 2	32.83	3.55	30000
Specimen 3	33.40	3.31	30000
28 day test	26.27	2.86	30000

The cubic compression strength of the test series after 28 days is higher than the nominal value. The concrete factory provides thus minimal the cubic compression strength the concrete class indicates.

The two tables, Table 7.1 and 7.2, are the result of the material tests that are explained in greater detail in Appendix F.

7.2.3. CONSTRUCTION

The composite floors consist of a steel deck, reinforcement in the ribs (Ø20), additional reinforcement meshes in the slab (Ø8-150), if present, and concrete of strength class C20/25. The various processes to construct the test pieces are shown in figure 7.6, where in addition the responsible manufacturer is indicated. The test pieces were constructed in Zoeterwoude at Dutch Engineering. The most important remarks per part of the construction process are briefly discussed in this section.

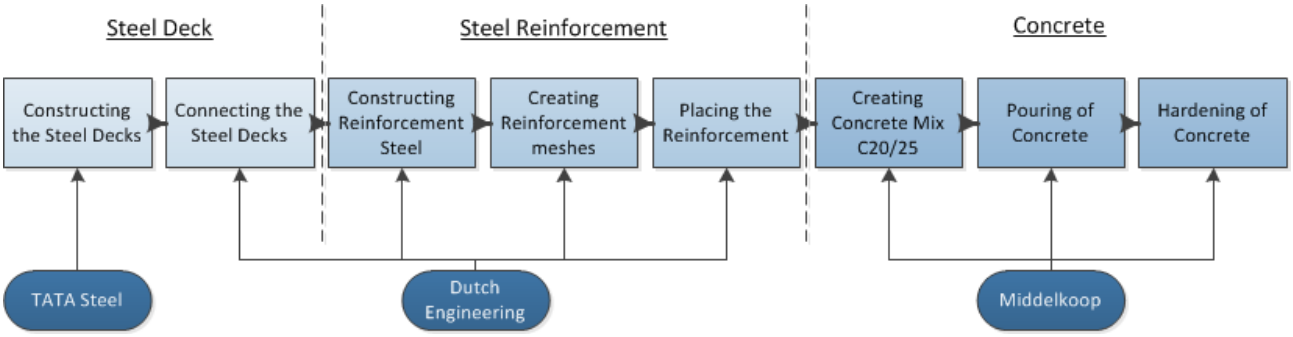

Figure 7.6: A schematic representation of the different construction processes of the composite floors and the responsible construction companies

STEEL DECK

The steel decking plates that are used to construct the composite slab form two halves of a rib and the interrip top flange, see figure 7.7a. They are manufactured by TATA steel, there a steel coil is coldly deformed to form the desired steel deck shape. At the bottom flange of the rib the plates overlap and are nailed together.

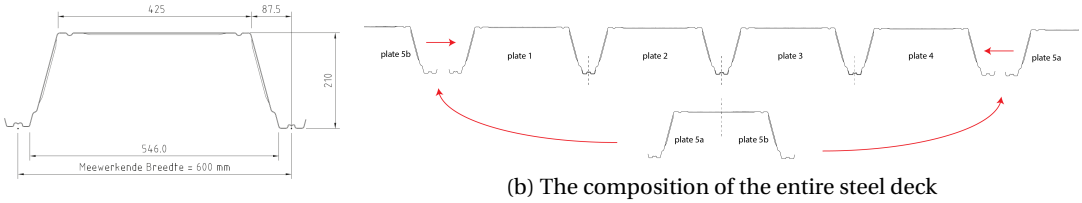

(a) Single steel deck

(b) The composition of the entire steel deck

Figure 7.7: The manufacturing of the steel deck of the test pieces

To create the test specimens a total of five deck plates are used. All the decking plates have the desired length of 5.6 meters and four of the decking plates could be joined together right away. But because the a single decking plate only consists of a top flange and two halve ribs, the outermost ribs were constructed in a different way. The fifth plate is cut in half at the centre across the longitudinal axis and then each half forms a side of the steel deck. An schematic representation of this step is shown in figure 7.7b.

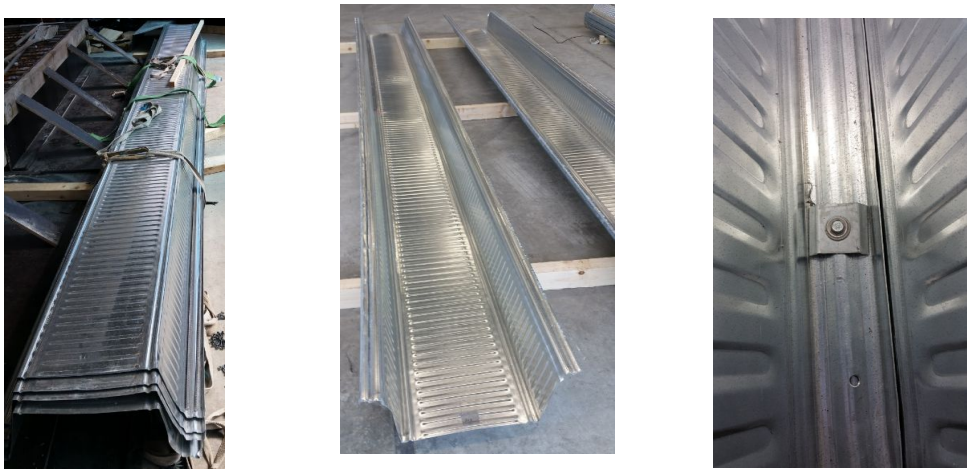

(a) A pile of steel decks

(b) One steel profiled steel deck plate lying upside down

(c) A connection at bottom rib

Figure 7.8: The used steel decks manufactured by TATA Steel

figure 7.8 illustrates different phases of the production process of the steel decks. These pictures were taken at the Dutch Engineering facility where the test specimens were constructed. figure 7.8 depicts the connected steel decks without the reinforcement steel or the concrete.

Figure 7.9: The connected steel decks, constructed out of five single deck elements

STEEL REINFORCEMENT

In each rib of the three test specimens one reinforcement bar with a diameter of 20 mm was applied The reinforcement mesh has a diameter of 8 mm and a centre-to-centre distance of 150 mm. Both types of steel reinforcement are shown in figure 7.10.

(a) The steel reinforcement bars of Ø20 placed in the ribs

(b) The reinforcement meshes of Ø8-150

Figure 7.10: The steel reinforcement used to create the test pieces.

Figure 7.11 shows the placement of the two types of reinforcement in the composite floors. A plastic reinforcement spacer is used to place the Ø20 reinforcement inside the rib at the desired height. Concrete bricks are used to place the single and double reinforcement mesh at the required position. These distances are measured at the construction site and are positioned according to the previously shown dimensions.

(a) Bottom reinforcement bar in a rib

(b) Only top mesh reinforcement

(c) Top and bottom mesh reinforcement

Figure 7.11: The steel reinforcement in the ribs and the reinforcement in the slab, if present.

Figure 7.12 shows the test piece with top and bottom reinforcement mesh and the connected steel plates.

The steel decks are now joined together and the reinforcement is placed. The next phase in the construction process is the mixing, casting and hardening of the concrete.

Figure 7.12: The test piece with connected steel decks and installed reinforcement bars and top and bottom meshes.

CONCRETE

The steel profiled deck is used as permanent form work when the concrete is poured. To prevent possible ponding effects and undesired deformations at the centre of the steel deck, the steel deck is supported at three positions as shown schematically in figure 7.13.

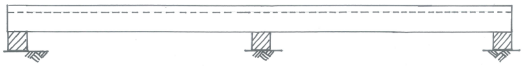

Figure 7.13: A side view of the steel profiled deck, the supports prevents undesirable deformations and ponding.

A special side detail is used at the longitudinal sides to obtain the desired concrete height above the ribs, this is shown in figure 7.14a. At the transverse sides it is slightly more complicated. First, a specialised steel plate is added to close off the space between the ribs. Then a timber beam and plank are clamped to the edges in order to obtain the required concrete height. All these measures are shown in figure 7.11.

(a) A connector preventing the longitudinal sides from bending outwards due to the weight of the wet concrete

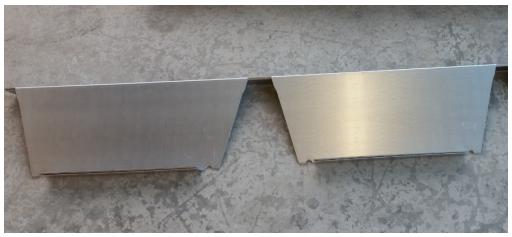

(b) A specially formed steel profile for closing of the space between the ribs

(c) The wooden close-off at the end of the composite slab

Figure 7.14: Measures to prevent spilling of the concrete and to obtain the desired concrete height

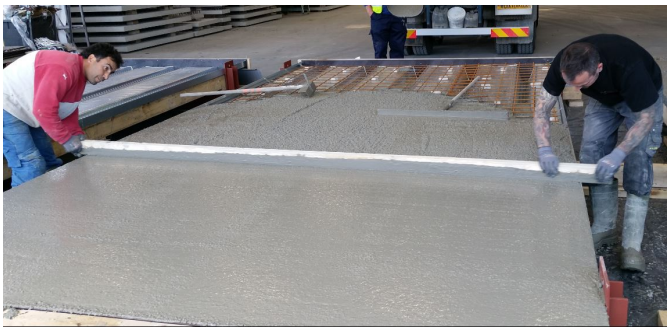

(a) Casting of the concrete

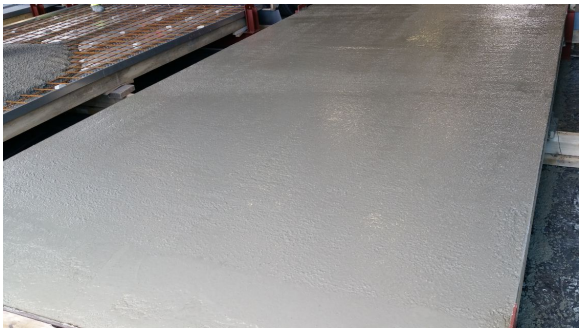

(b) The composite floors with wet concrete

Figure 7.15: The final step in the construction process

The final step of the construction process, the casting of the concrete, is illustrated in figure 7.15. The concrete of the composite slab needs to harden at least two weeks for it to reach a sufficient strength so that it can be transported to the Stevin II laboratory of the TU Delft. The transportation requires careful attention. The concrete can crack during lifting or transportation from Zoeterwoude to Delft. The precautions to avoid undesirable damage to the test pieces are discussed in the next section.

7.2.4. TRANSPORTATION

It is vital that the test specimen remain intact during transportation from Zoeterwoude to the TU Delft. The geometrical and material properties are carefully examined in and after the construction process. Initial cracks in the concrete can negatively influence the tests results. The precautions taken to make sure that the test specimens are not damaged during transportation are briefly discussed in this section. All this is to make sure that the test results are not influenced by rude handling during transport.

Steel profile beams are used to lift the composite floor in order to make sure that lifting of the test specimen can take place carefully and that the specimens will not deflect in the transverse direction. The steel beams are fitted with upstanding plates at the side edges to keep the composite slabs in place and keep them from shifting sidewards. Furthermore, a spacer is inserted between the lifting cables in order to avoid the development of any axial force in the specimens. These features are schematically depicted in figure 7.16.

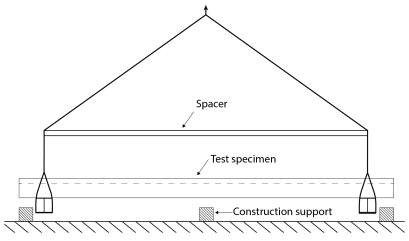

Figure 7.16: The lifting system.

The test specimens are loaded by their own self weight during transportation. The test pieces will be piled up on top of each other during transport. Extra care is required for the test piece without any reinforcement mesh. This test pieces should be on top of the pile. The extra load caused by the other two floors could initiate cracking in the unreinforced floor, while in the two other floors this will not be a problem. The steel profile beams that were used to lift the composite slabs are shown in figure 7.17.

(a) The steel beams used to lift the test specimens. The upstanding stiffened steel plate is to prevent the test specimens from shifting sidewards.

(b) Positioning of the steel beams

Figure 7.17: The precautions taken in order to safely transport the test specimens

Finally, the applied precautions can be seen again in figure 7.18. In these pictures the test specimens are being lifted into the Stevin II laboratorium from the load truck.

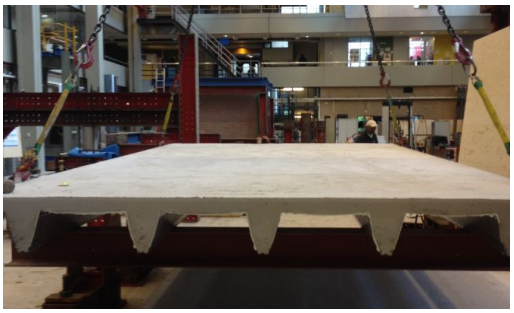

(a) Front view

(b) Side view

Figure 7.18: The lifting of the test specimens from the transport truck into the laboratory

7.3. TEST SET UP

This section describes the test set up that was build in the Stevin II laboratory of Delft, University of Technology. The different parts of the test set up are treated separately:

- Loading frame, Subsection 7.3.1
- Supports, Subsection 7.3.2
- Instrumentation, Subsection 7.3.3

An overview of the test set up is given in figure 7.19

(a) Side view of the test set up

(b) Front view of the test set up

Figure 7.19: An overview of the test set up that was constructed in the Stevin laboratory.

7.3.1. LOADING FRAME

The first part of the test setup that will be discussed in this section is the loading frame. The concentrated force, applied at the centre rib of the test specimen, creates a deflection and a stress distribution throughout the entire floor. The dimensions of the loading frame and reasoning are explained in this subsection.

During the testing the test specimens are subjected to two kinds of loading:

- A concentrated load F
- A distributed load q

The concentrated load F is applied to the test specimen by the hydraulic press of the test set-up. The distributed load is caused by the self-weight of the test specimens, which is approximately 3.05 kN/m^2 (Dutch Engineering). This load is uniformly distributed and will cause an initial deflection even before the testing has begun. This initial deflection is measured and only influences the residual capacity of the composite floor; it will not interfere the desired transverse stress distribution. The capacity of the hydraulic press (or load cell) is 400 kN. The load level is measured during the tests. More information about the load cell is presented in subsection 7.3.3. The hydraulic press is depicted in figure 7.20a.

The force of the hydraulic press will be displacement driven; the load will increase with constant deformation steps. The area to which the concentrated load is applied is 150 x 150 mm2. According to Eurocode 1 ([10]), loads larger than 10 kN need to be checked on a surface area of 200x200 mm, but in order to have a width of the loading area that is smaller than a single rib width (at the top) it is chosen to use a loading area of 150 x 150 mm.

The load level is controlled manually, by making use of a pumping system. Oil is pumped in the cylinder by making use of this pumping system. The load cell is pushed downwards because of this. The load cell introduces a concentrated load on the test specimen. The result is a displacement controlled test. The pumping system is shown in figure 7.20b.

(a) The hydraulic press

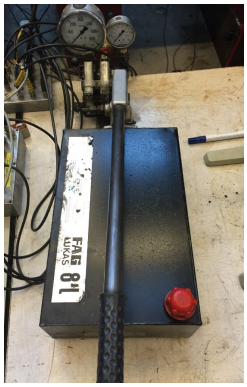

(b) The pumping system

Figure 7.20: Details of the load introduction system on the test specimen

The hydraulic press will load the specimens in two specific places, one at exactly the middle of the composite floor and one at a quarter of the span length, as shown in figure 7.21. The composite slab will be loaded first at location 1. The testing will be stopped when a certain load has been reached. This test will be non-destructive and the aim of this location is to have extra data to compare with the analytical and numerical output. The test specimen should not be damaged during this first test. A destructive test will be done at the second position. At this location the objectives are to measure the distribution of the composite slab and observe what kind of failure behaviour will occur.

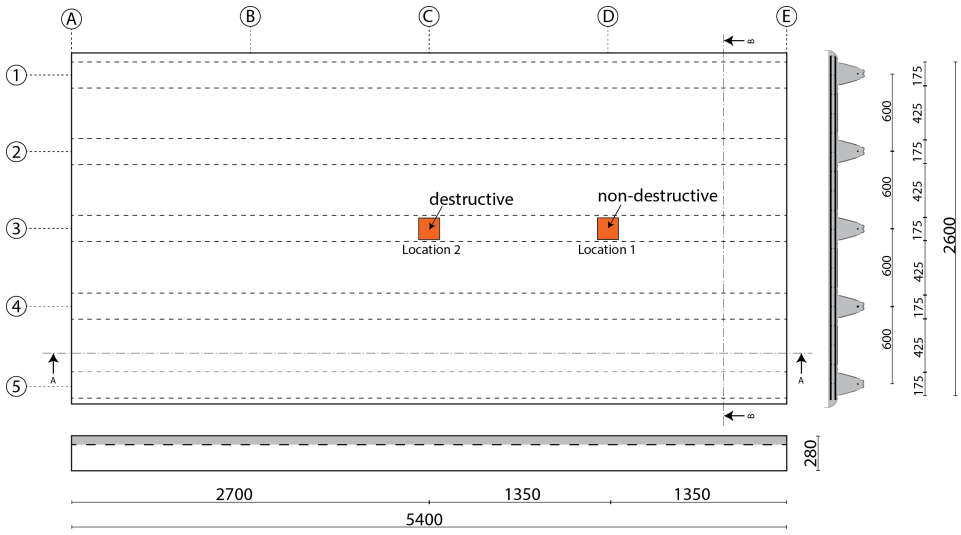

Figure 7.21: A top view of the test specimens with the locations of loading indicated. The first loading location will be a non-destructive test and the second location will be destructive one.

Figure 7.22 shows pictures from the load frame that is used to introduce the concentrated force into the test specimens. The picture on the left side shows the the double horizontal beam and the columns. This entire structure is put over the ComFlor210 pieces. The middle figure shows the cylinder where the load cell is put into. figure 7.22c then finally shows the support of the load frame. The supports are bolted to the floor of the laboratory with anchors that can be seen in the picture, this prevents any deformations and rotations.

(a) Overview load frame

(b) The cylinder for the load cell

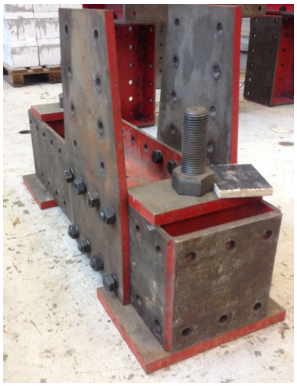

(c) A support of the load frame

Figure 7.22: Pictures of the loading frame that is used to introduce the concentrated force into the test specimens.

7.3.2. SUPPORTS

The supports of the test specimens fulfill an important role: they need to include the load cells for measurements and at the same time they should provide a stable platform for the specimens to rest upon. The required degrees of freedom are also provided by the supports. Each rib is supported at both sides of the test specimen. So ten uniform supports are created. The support reactions at each rib are required to validate the numerical and analytical models. This data provides the knowledge of what part of the load is spread in the transverse direction of the slab into the different ribs.

(a) One row of supports, 5 supports in total

(b) The supports at one side while in use

Figure 7.23: An overview of the supports used in the lab experiments

Because of the deflection of the slab due to the loading, the supported end of the specimen will move horizontally. Therefore horizontal translation capacity is required. To do this it is either possible to give one side of the slab translation capacity and make it so that the hydraulic press is a pendulum or both supports need to be able to move horizontally instead. It was chosen to make the hydraulic press rigidly connected to the frame and instead give both supports translation capacity. Figure 7.23 shows two pictures of one row of the supports. Beside this horizontal freedom, rotation capacity is also required during the loading process. So the supports only restrict vertical movement of the ribs; the test specimen are able to translate horizontally and can rotate freely.

More information is provided regarding the load cells in the next section.
The different parts of the supports are indicated in figure 7.24. Mechano parts are used to place the test specimen at a height that provides easy access beneath the specimen. Instrumentation is placed at the bottom side of the test pieces, as will be discussed in the next subsection. The increased height makes sure that the instrumentation can be adjusted when the test specimens are placed in the test set-up. A roll support is put on top of the Mechano part. The roll supports are made out of round steel bars encased by two metal plates.

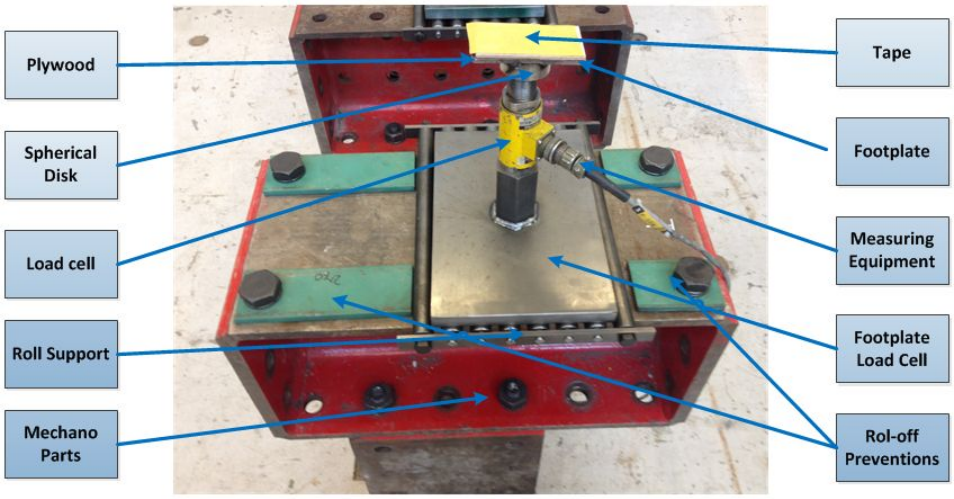

Figure 7.24: The different parts of the supports

These roll supports provide the horizontal degree of freedom. To prevent the test specimens from rolling off the supports they had to be laterally braced though. These precautions are removed during the test.

Load cells are welded onto a foot plate that is put onto the roller plates. The load cells measure the support reactions at each rib. The maximum capacity of these cells is 200 kN. A spherical disc is put on top of the load cells to give the test specimens their rotational freedom. A footplate is welded onto the spherical disk. Small pieces of plywood are placed on top of the footplate. When the test specimens are put in the test set-up the plywood deforms and fixates the test specimen on top of the support. This is done to prevent differences between the supports on which the specimens were constructed and the supports on which the testing is done from causing settlement cracks and damage to the specimens. First the spherical disk is placed at the bottom side of the test specimen with tape, to make sure that the dimensions are accurately checked.

(a) The top side of the support

(b) Placing of the test specimen

(c) Fastened test specimen

Figure 7.25: Some details about the secure placing of the test specimen on the supports

The zero measurement of each individual load cell just before the test starts should be the same. The height of the load cells were therefore adjusted to makes sure that each load cell measures approximately the same load before the test starts. [1]

[1] In practice the composite floors are often supported on the flanges of a steel composite beam. The concrete is then cast in situ, effectively creating a concrete beam along the width of the composite slab. Replicating this in the test specimen would have been an impractical choice, since this would prevent any individual measuring of the ribs in the test specimens. The concrete beam would redistribute the load and would thus skew the results. It was therefore chosen not to replicate the concrete beam, but instead leave the ends of the composite slab free.

7.3.3. INSTRUMENTATION

To perform all the necessary measurements during the tests, several different instruments are used. The instruments are summed up below.

- 10× Thread LVDTs (deflection)
- 2× LVDTs (end slip)
- 4× Strain gauges (transverse strain)
- 5× Rotation gauges (rotation)
- 11× Load cells (support reactions and hydraulic press)

Out of the instrumentation listed above the LVDTs (both types) measure a change in distance. The strain gauges measure the strain of a material at the location of placement and the load cells measure a force that is acting on them. The rotation gauges measure the angle of rotation in degrees of each individual rib. This section will expand upon the locations where the instruments are placed and their function.

THREAD LVDTS, DEFLECTION

The deflection of the composite slab was measured in several places. The stiffness of each individual rib was determined by combining this data with the data obtained from the load cells. The deflection values that were obtained could compared to those that have been predicted before the testing with the analytical and finite-element models.

It is chosen to measure the deflection of each of the five ribs. Each of the five ribs along the width at the locations of loading was measured. So at all five ribs along the width of the load locations of figure 7.26, 10 thread LVDTs are used in total. Because the expected deflection is in the order of centimetres rather than millimetres it was chosen to use thread LVDTs, which can measure such large deflections.

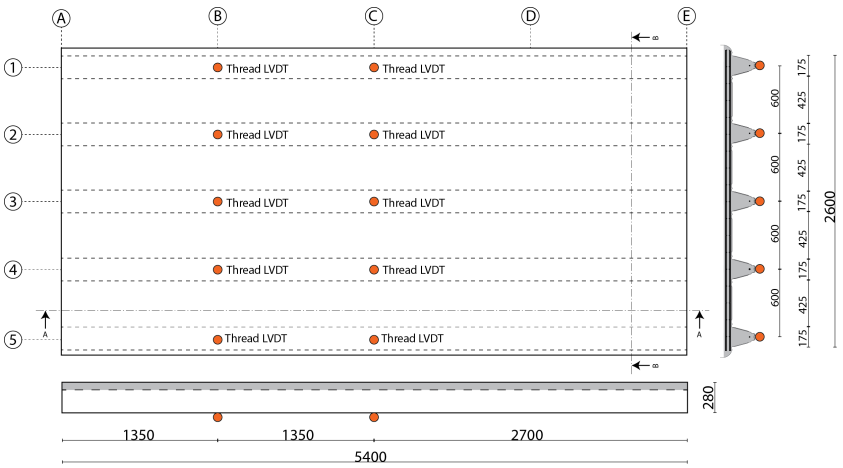

Figure 7.26: A top view of the test specimens with the locations of deflection measurement indicated.

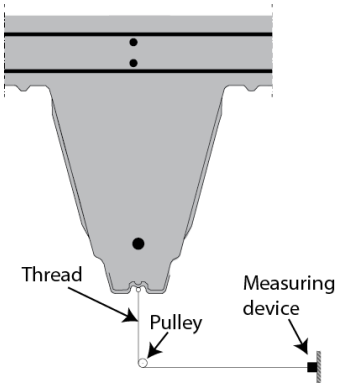

(a) A schematic view of the thread LVDT

(b) The bottom side, at the pulley

(c) A top side, placement at test piece

Figure 7.27: The positioning of the Thread LVDT.

Figure 7.27 illustrates the functioning of the thread LVDT. A small hook is fixed by magnets at the bottom side of the test specimen. A string is attached to the hook and is stretched to a piece of Mechano, that is placed on the ground directly beneath the hook. It is very important that this string is stretched perfectly vertical, in such that the measured deformations of the composite floor are vertical only. The string is attached to a pulley that is attached to the Mechano part. The string exactly follows the deformations of the ComFlor210 test piece. The amount of deformation is measured during the tests.

Figure 7.28 shows an overview of the used thread LVDTs in the lab experiments.

(a) One row of thread LVDTs

(b) A close up of two entire thread LVDTs

Figure 7.28: An overview of the thread LVDTs used in the lab experiments

LVDTs, END SLIP

Normal LVDTs are used to measure the end slip between the steel deck and the concrete. The analytical model assumed full shear connection between the deck and the concrete. This assumption is verified by measuring the end slip at the middle rib only. This rib is loaded most extensively.

Figure 7.30 shows two pictures taken of the LVDTs. The mechanism is fixed to the bottom side of the steel deck. The pin is attached to the concrete and follows the horizontal deformation path of the concrete, caused by the partial shear connection and the applied concentrated load. This accurate deformation path is realized by making use of a spring that holds the measuring device at the surface of the concrete.

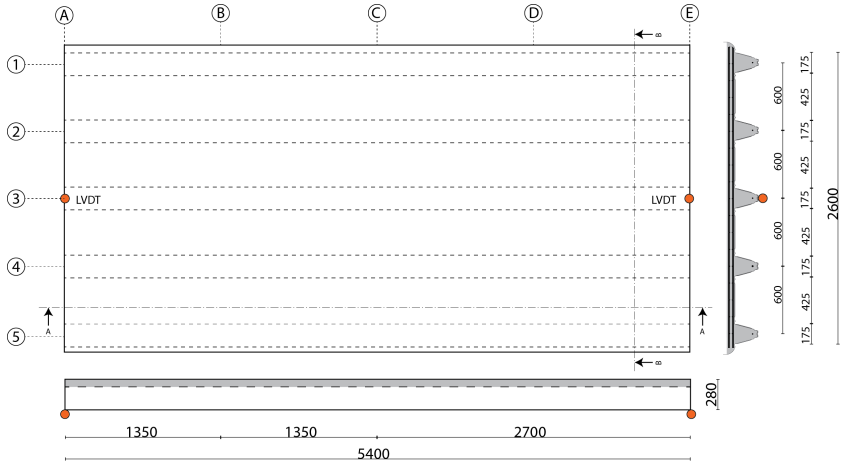

Figure 7.29: A top view of the test specimens with the locations of the LVDTs that measure the end slip of the middle rib.

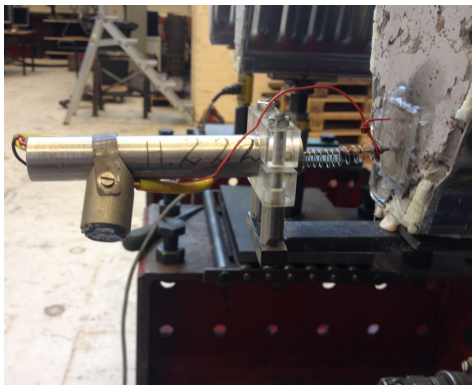

(a) A close up of a end-slip LVDT

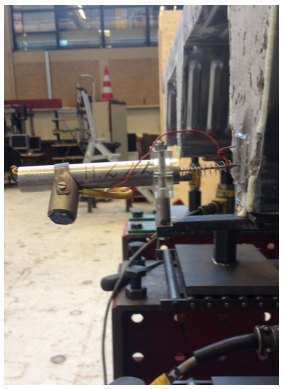

(b) An overview of a end-slip LVDT

Figure 7.30: An overview of the LVDTs used in the lab experiments

STRAIN GAUGES

Strain gauges are used to measure the strain in the top flange in the transverse direction of the steel deck. The contribution of the steel deck is measured in specific points at the bottom side of the top flange. These results can be used to validate the contribution of the steel deck in sustaining the concentrated force and distributing the stress to the outer ribs.

The effective part of the steel deck is around the folded corners. The other parts will not be effective in carrying the applied force and will not contribute to the bending stiffness. The positioning of the strain gauges is therefore very important. The deck area just outside the ribs, thus still inside the effective area, is chosen. The strain gauges are placed in the transverse direction to measure the contribution of the steel deck in transferring the stresses to the outer ribs. The strain gauges are placed at locations where the destructive test is carried out. The contribution of the steel deck is expected to be small in the non destructive test. The positioning of the strain gauges is illustrated in figures 7.31 and 7.32.

The strain gauges are placed before the concrete is cast and the steel decks are connected. This to ensure easier access to the bottom side. The used strain gauges are shown in Figure 7.33.

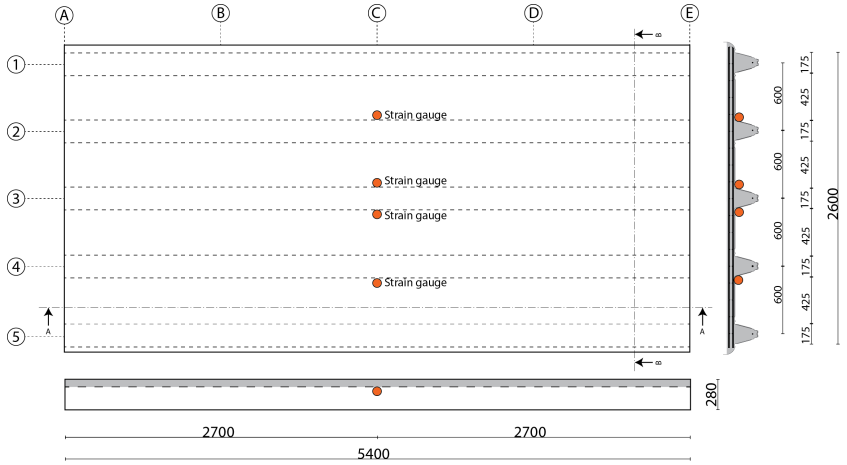

Figure 7.31: A top view of the test specimens with the locations of the strain gauges.

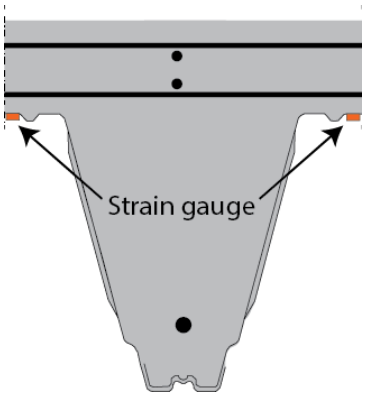

Figure 7.32: A detailed frontal view of the placement of the strain gauges. They are placed on the other side of the longitudinal embossment from the perspective of the rib.

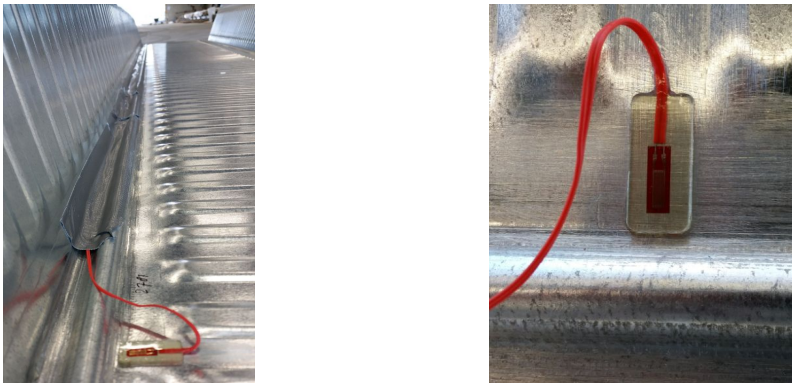

(a) Positioning of the strain gauge (b) Strain gauge detail

Figure 7.33: The strain gauges positioned at the bottom of the steel deck to measure the transverse strain in the deck

ROTATION GAUGES

Rotation gauges are used to measure the rotation of each rib during the test. A rotation gauge is placed at each rib in the middle of the span. It is expected that the ribs will hardly rotate during the non-destructive test, so no rotation gauges are placed at the location of that test. The positioning of the rotation gauges is visualized in figure 7.34.

The rotation gauges were connected to the test specimen by magnets. The measuring equipment is put in a

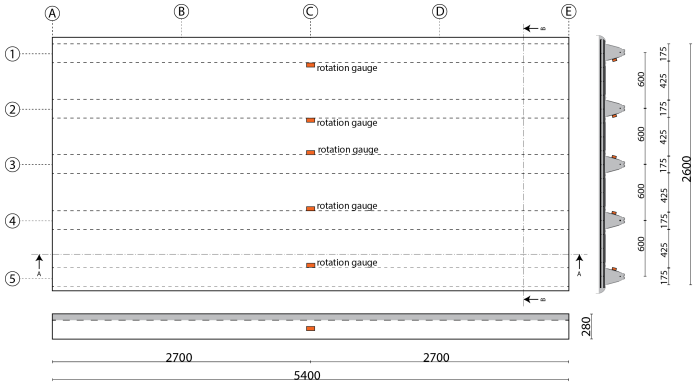

Figure 7.34: A top view of the test specimens with the locations of the rotation gauges

metal holder and then placed at the desired positions at the bottom side of the test specimen. The middle rib will hardly rotate during the tests, but is measured nonetheless as a control measurement.

The positioning of the rotation gauges at each rib is shown in figure 7.35. The instrumentation is shown as well in this figure; this equipment measures the rotation during the test in degrees and these results are shown on a monitor during the test. The entire rotation gauge, including the metal frame, is shown in figure 7.36. An overview of the five rotation gauges is visualized as well.

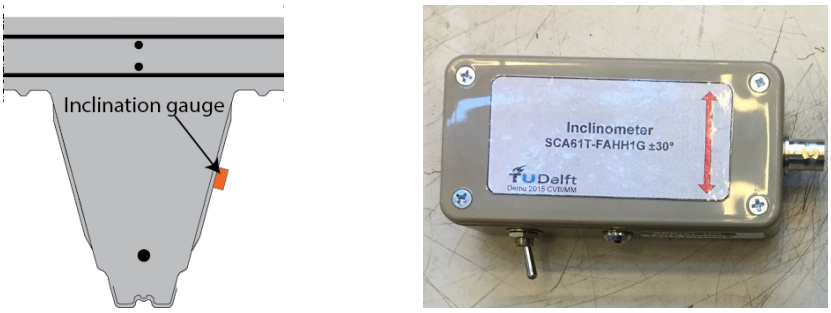

(a) The positioning of the rotation gauge (b) A close up of the used measuring equipment

Figure 7.35: An detailed overview of the inclination or rotation gauges that are used to measure the rotation of the ribs.

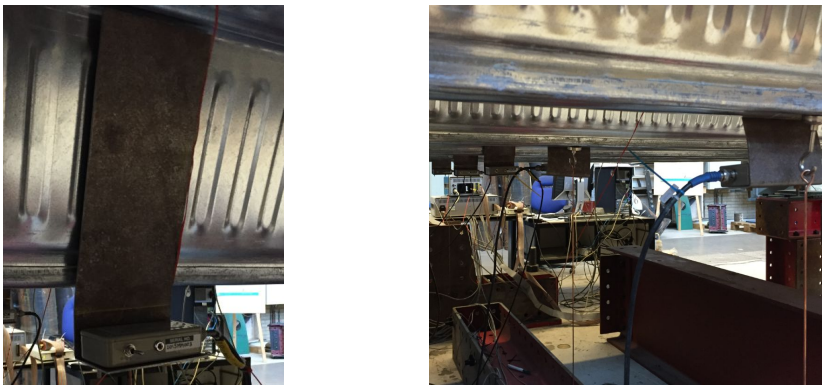

(a) The rotation gauge with metal frame (b) An overview of the rotation gauges

Figure 7.36: An overview of the rotation gauges used in the lab experiments

LOAD CELLS

Load cells are used in two positions:

1. To measure the support reactions
2. To measure the applied concentrated force

The load cells were used to measure the support reactions of the ribs at each end of the slab, so that makes two per rib and ten load cells in total. One more load cell was used to check the force that the hydraulic press was exerting on the test specimen. The locations of the load cells that are used to measure the support reactions are shown in figure 7.37. The support reactions of the ribs are interesting because they indicate how much of the applied load is carried by each rib.

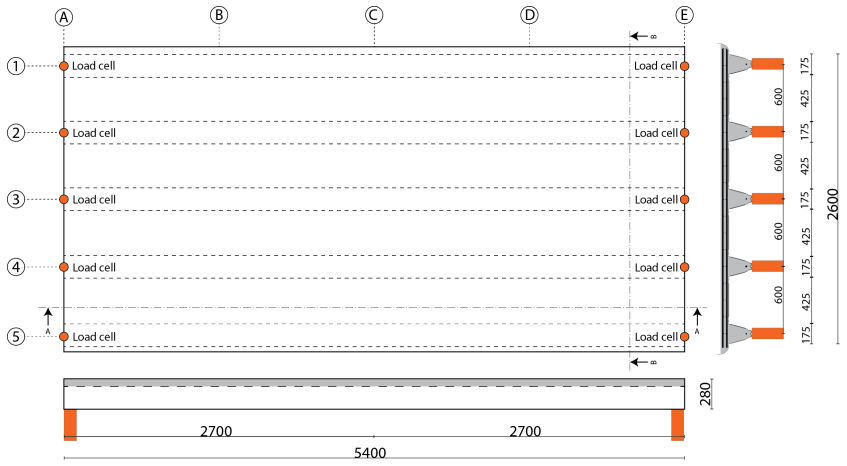

Figure 7.37: A top view of the test specimens with the locations of load cells indicated.

The first test specimen has no top slab reinforcement, so after the concrete cracks the composite slab will sustain permanent damage. This is because it was assumed that the top flange of the steel deck does not contribute towards the moment resistance. So in order to prevent failure or permanent damage to the test specimen. So the maximum allowable moment in the top slab is the cracking moment. With this knowledge the model is run and the results are displayed below.

7.4. TEST RESULTS AND EVALUATION

The tests have been performed in the following chronological order:

1. 2 mesh slab at quarter span length
2. 2 mesh slab at mid span length
3. 1 mesh slab at quarter span length
4. 1 mesh slab at mid span length
5. No mesh slab at quarter span length
6. No mesh slab at mid span length

But for the sake of comparison the test results will be presented per type of test. So the tests at half of the span length for all test specimens will be presented in the first section and the test results of the tests at a quarter the span length on all the test specimens in the second section. For both test types the results will be compared and it will be evaluated why some results might deviate from the expectation. The data that was acquired from the instrumentation during the test is stated below.

- Applied load (hydraulic press)
- Rib load on each side (load cells: RO1-RO10)
- Deflection at half span and quarter span (thread LVDTs: LVDT1-LVDT10)

- Rib rotation at half span (rotation gauges: ROT1-ROT5)
- Strain of deck in transverse direction (strain gauges: REK1-REK4)
- Slip at both ends of the middle rib (LVDTs: Slip1 and Slip2)

The location of all of these instruments can be seen in figure 7.38 and for more detail is referred back to section 7.3.3. Although all of the instrumentation was used at every test, not all of the outputted data is relevant for every test evaluation. The data is given in appendix G.

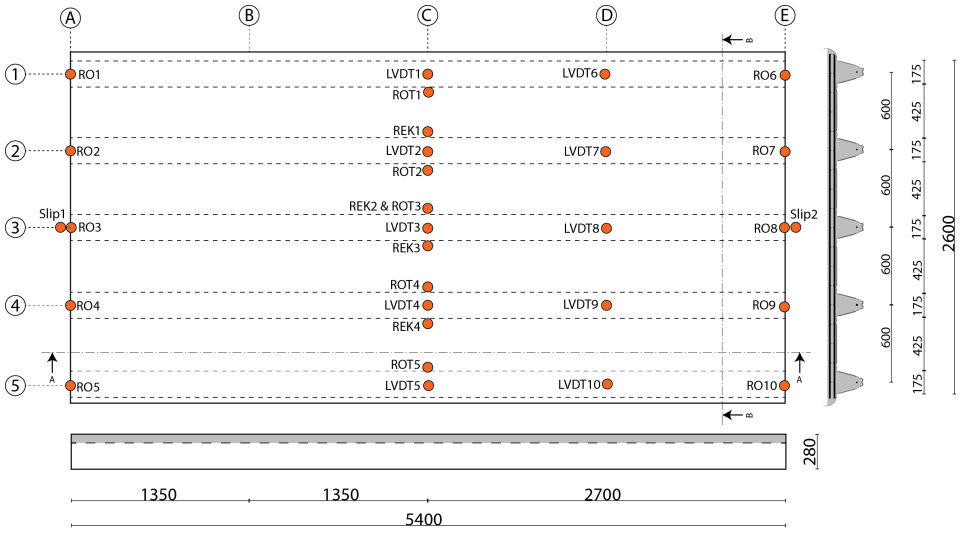

Figure 7.38: A top view of the test specimens with the locations of the instrumentation indicated.

All instrumentation was zeroed before tests were initiated. This means that the measured values were only due to the influence of the applied loading. Only the load cells RO1-RO10 were not zeroed out. The test specimens were hoisted into the test set-up onto the load cells. The values measured by the load cells were very uneven at that point. The load cells were then adjusted in height in order to get an equal measured value in all load cells. This was done in order to provide an equal starting value for all ribs and measure the effects of the experiment in the same manner everywhere. The procedure that was used for the load cells was as follows:

1. Lift test specimen into the test set-up
2. Re-adjust load cells to equalize measured values
3. Execute experiment

The values measured by the load cells looked like the example in figure 7.39. The initial values of the load cells can be seen at the point where the applied load is 0 kN. The uncorrected values of the load cells can be observed in figure 7.39. The initial values of the load cells are roughly the same but not completely. These difference could have an influence on the final results which is significant. The initial values of the load cells are shown in appendix G.

The corrected values of the load cells are shown in figure 7.40.

For both sides of the slab these corrected load cell curves can be made. The first check that is done for each test specimen is to sum up all the load cell measurements on both sides of the test specimens. This sum of RO1-RO5 and RO6-RO10 respectively is then presented as a percentage of the total load, as done in figure 7.41. This graph represents the spreading of the load as seen in figure 7.42. For the tests at a quarter of the span length it is expected that 75% of the load will go towards the side which is closest to the point of application of the load and 25% towards the far side. For the destructive test with the load applied in the centre of the slabs it is expected that each side of the slab carries 50%

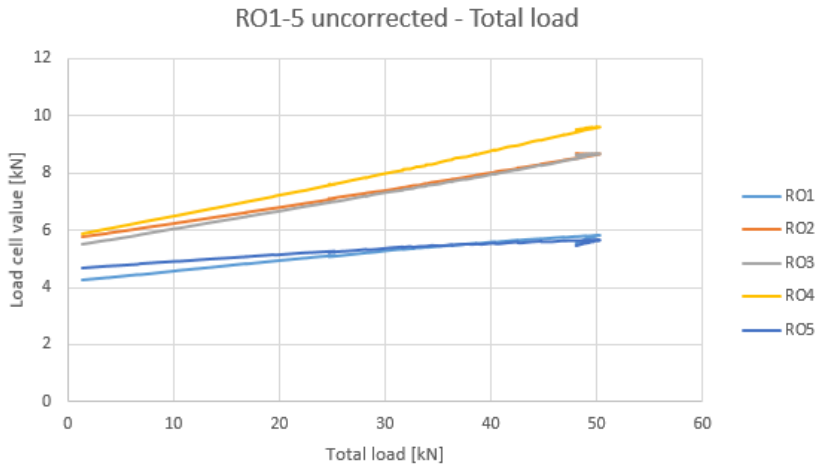

Figure 7.39: Measured values by load cells RO1-5 in the 2 mesh slab loaded at a quarter of the span length.

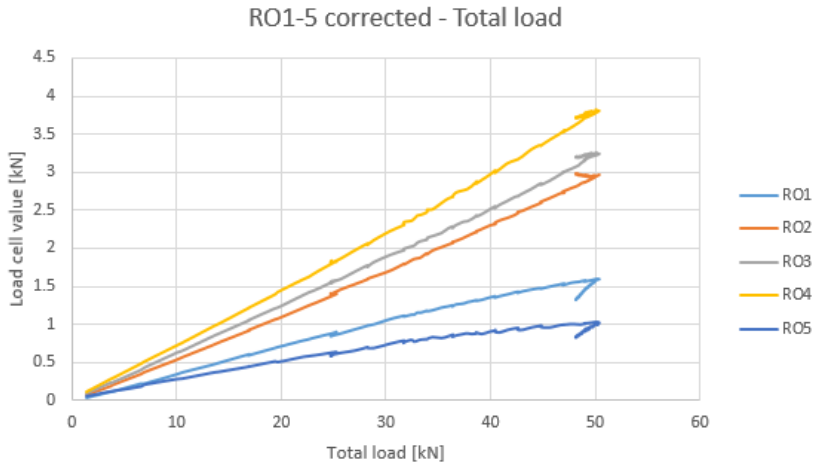

Figure 7.40: Corrected values by load cells RO1-5 in the 2 mesh slab loaded at a quarter of the span length.

In order to analyse the distribution over the width of the test specimens, the contribution of each rib relative to the total load per slab size is then calculated. Examples of such a graphs for both sides of the test specimen can be seen in figure 7.43. These graphs represent both sides of the test specimen shown in figure 7.44. With these graphs the distribution over the width of the specimen on both sides can be analysed thoroughly. In this chapter the results of the load cells will be shown only in the form of percentage based distribution diagrams as shown in figure 7.43. For the corrected absolute values measures by the load cells is referred to appendix G.

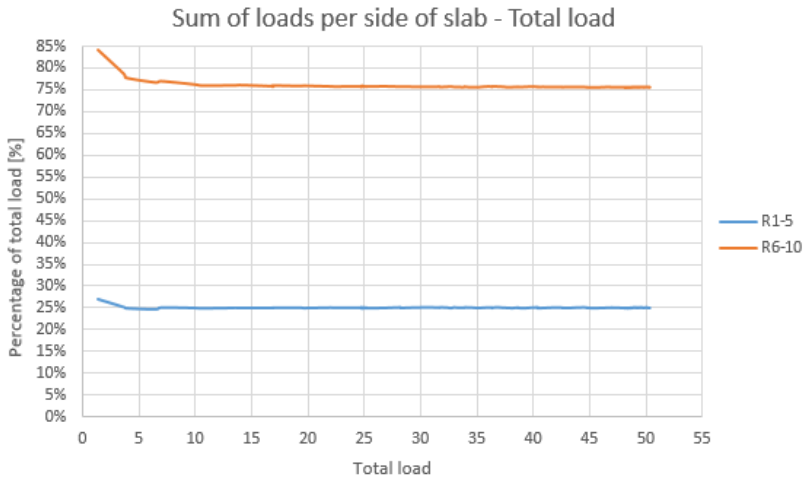

Figure 7.41: Sum of RO1-RO5 and RO6-RO10 in the 2 mesh slab at a quarter of the span length.

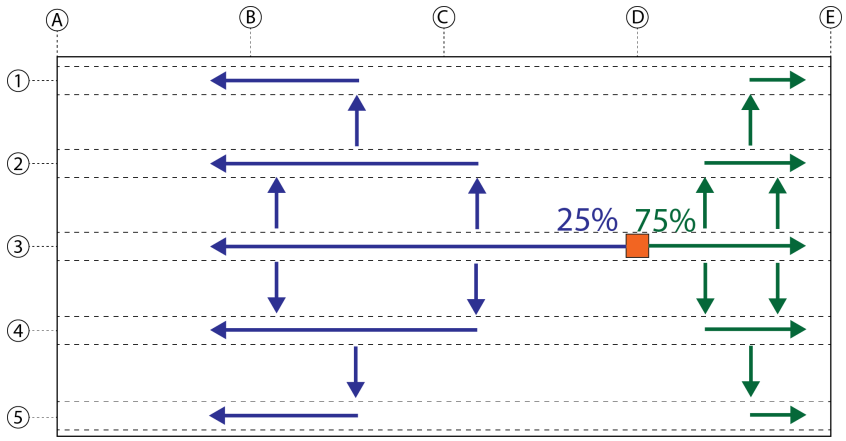

Figure 7.42: A schematic representation of the distribution of the applied load per side of the test specimen.

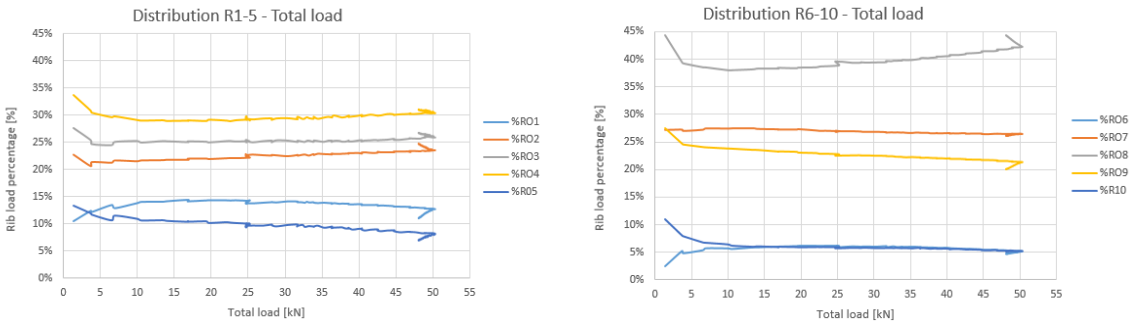

(a) The distribution for RO1 to RO5

(b) The distribution for RO6 to RO10

Figure 7.43: Distribution for R01 to R05 and R06 to R010 of the 2 mesh slab.

The graphs which show the total load applied will often show small decreases in the load at regular intervals. This was often caused by a temporary stop of increasing the applied load. This decrease in loading over time is caused by the hydraulic press. The hydraulic system that was used could not keep the oil pressure at exactly the same value if left alone for a period of time. So increasing the load is stopped for a while, the load slowly decreases somewhat. Since the load was increased in increments and regularly stopped to allow for inspection of the response of the test specimen, this small drop in applied load can be seen throughout the test results. Whenever the drop in applied loading is larger than normal or was not caused by discontinuing

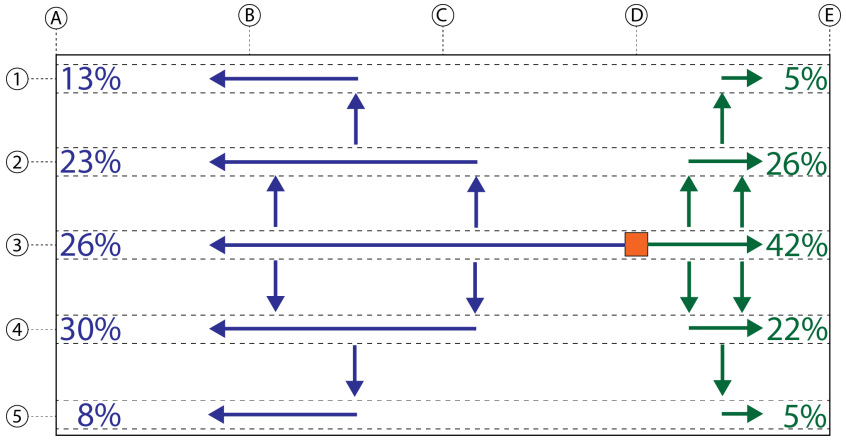

Figure 7.44: A schematic representation of the distribution of the applied per side of the test specimen.

the increasing of the load, it will be mentioned. Another issue that should be mentioned in advance is that the rotation and strain values found in the experiments are all shown as absolute values in order to be better able to compare them with each other. The rotation data of the ribs do not all have the same direction of rotation but only the absolute values are shown. The direction of the rotation that the ribs assume are shown in figure 7.45. The middle rib is not expected to rotate, but it might. If it does then the direction of rotation can be derived from the data acquired from the strain gauges.

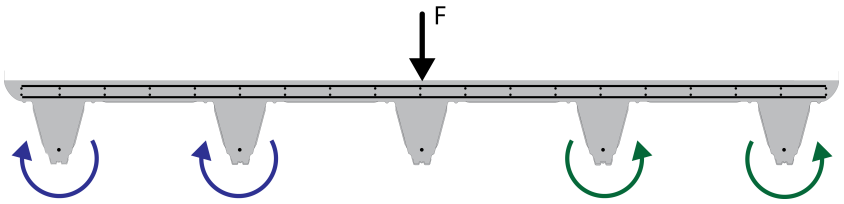

Figure 7.45: A schematic representation of the direction of the rotation in the ribs.

The last point that is mentioned is the 'rib stiffness'. This concept is introduced in the following sections and stems from the analytical modelling approach. In the analytical model the ribs are modelled as translation springs with a certain stiffness and carrying a certain load. The load in the rib, also called the 'rib load', is calculated as the sum of the loads in the load cells on both ends of the ribs. In order to draw up the comparison between the experiments and the analytical model in the following chapter this relationship between the deflection of the ribs at the location at the applied load and the force measured at the location of the supports is called the 'rib stiffness'. The size of the variable will be acquired from graphs relating the aforementioned parameters together.

7.4.1. TEST AT HALF SPAN LENGTH

The testing of the specimens at half of the span length had two major goals: observing the load distribution and observing the failure modes of the slabs. By keeping the slabs in the linear elastic zone in the test at a quarter of the span it was attempted to minimize the effect this would have on the destructive tests. It will have to be checked whether or not this has succeeded.
The test results will be discussed in a similar fashion as was done in the previous section. First the manner of loading and the observed behaviour during the test itself will be reported. Then the resulting graphs of all instrumentation will be presented which will then be discussed.

2 MESH TEST SPECIMEN

First of all, the applied load was quickly increased to 40 kN. At that point the loading was shortly halted and from then on the load was increased in 10 kN increments after each of which it was shortly halted again. This

continued to approximately 105 kN of loading. At that point a loud cracking sound could be heard. It started in the centre of the slab and propagated outwards. The slab was inspected but no cracking could be observed on the outside. What could be observed was that the deck had separated from the concrete at the end of several of the ribs. This can be seen in figure 7.46. Only two ribs are shown, but this phenomenon was to a greater or lesser extend visible in all ribs.

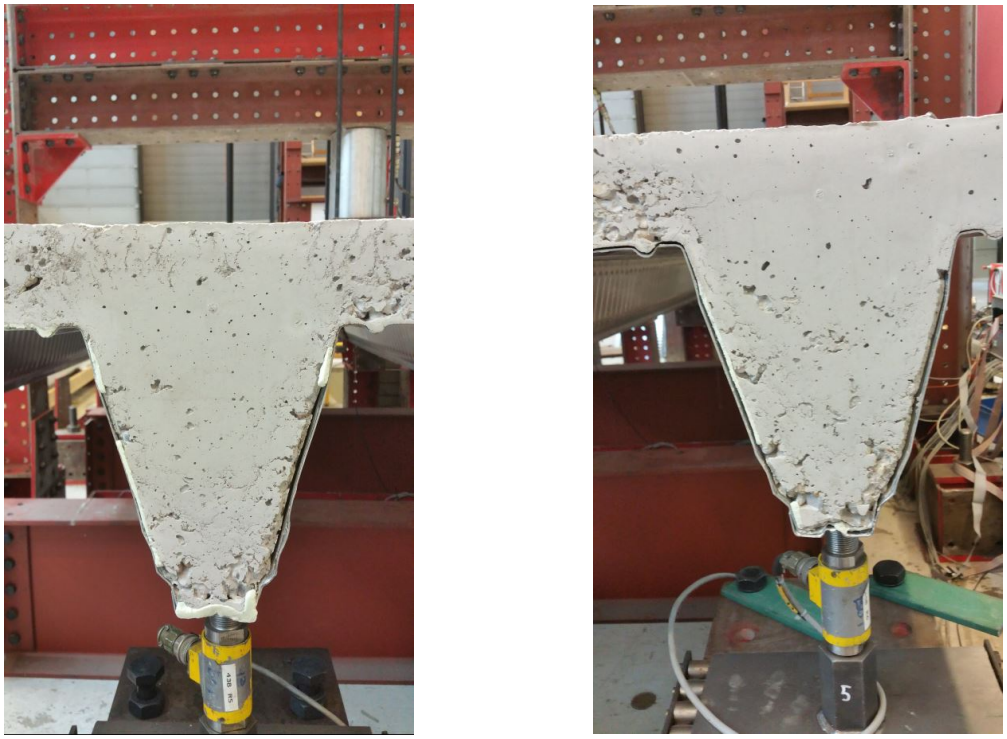

(a) The end of rib 3 at location A3 (see figure 7.38.

(b) The end of rib 5 at location A5 (see figure 7.38.

Figure 7.46: Photographs showing the deck separating from the concrete at the end of ribs 3 and 5.

After inspecting the slab, the load was yet again increased with 10 kN increments until 160 kN was reached. At this point the stiffness of the slab had dropped so far that adding any more load was near impossible because the slab was just deflecting more and more. Therefore the loading was stopped and the load was released.
Again, the sum of the load cells on both sides of the slab have been calculated in order to check the external-internal equilibrium. From this process it was found that the internal forces have a constant error of 0.5% compared with the total applied load. This margin of error is acceptable. Another observation that was done, was that the slab side which was previously loaded in the test at a quarter of the span, carried 49% of the total load. The other side of the slab carried 51% of the total load. In order for a misalignment to cause this effect, the load would have to be placed almost 50 mm away from the centre line. The application point of the load was aligned beforehand, but some misalignment might have occurred. This found 49%-51% distribution remained constant throughout the entire test. This does suggest either some misalignment or a small error in the instrumentation.
The results of the destructive test of the distribution are shown in figure 7.47, the rotation, slip and strain in figure 7.48 and the rib load-deflection diagrams in figure 7.49.

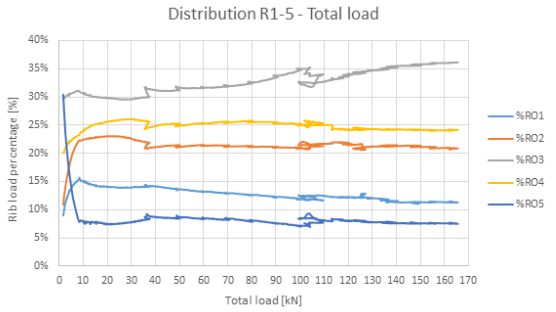

(a) The distribution for RO1 to RO5

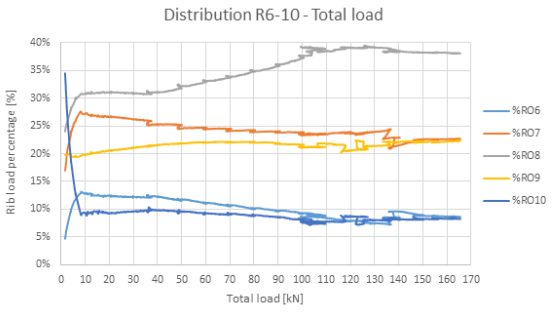

(b) The distribution for RO6 to RO10

Figure 7.47: The distribution for R01 to R05 and R06 to R010 2 mesh slab.

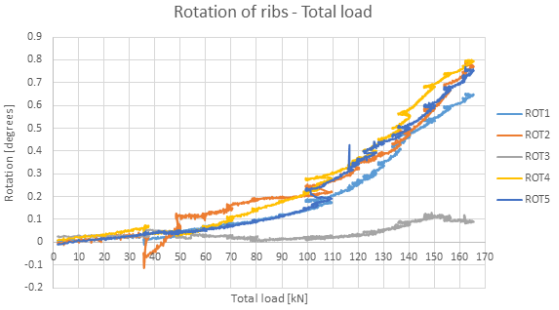

(a) The rotation of the 2 mesh slab

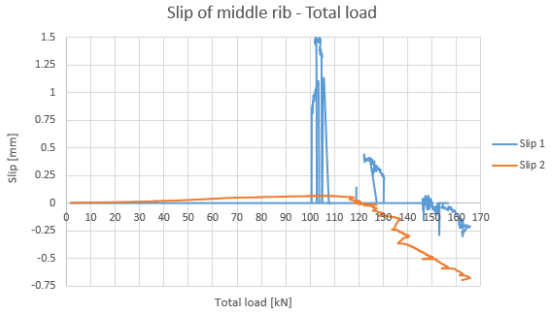

(b) The slip of the centre rib of the 2 mesh slab

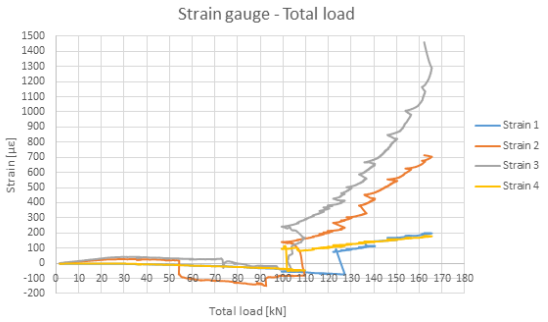

(c) The strain of the 2 mesh slab

Figure 7.48: The rotation, slip and strain of the 2 mesh slab.

First of all the distribution near the point of failure of the slab swill be considered. Since the load is applied in the middle of the slab, it is expected that both distribution diagrams show the same curves. And indeed it seems that the corresponding ribs have on average almost the same contribution. The outer ribs, 1 and 5, carry about 9% on both sides, ribs 2 and 4 about 22.5% and rib 3 36.5% on one side and 37.5% on the other. The largest difference is again in rib 3. This is expected, because any change in rib 3's contribution is then divided over 2 or more ribs, making the relative change in the other ribs smaller. And even the approximate 1% of contribution difference in rib 3 is not very large.
Again it can be seen that for RO1 and RO5 and for RO2 and RO4 the values are not exactly the same. But on average they correspond to the values for RO6 and RO10 and for RO7 and RO9 respectively. For all curves the disturbance at 105 kN can also be seen. The load jumps back a little, but the distribution is in essence not changed.
When comparing these results with the test at a quarter of the span and load cells RO6-RO10 the following can be said:

1. Rib 3 bears approximately 5% less in the test at half span (7.43).

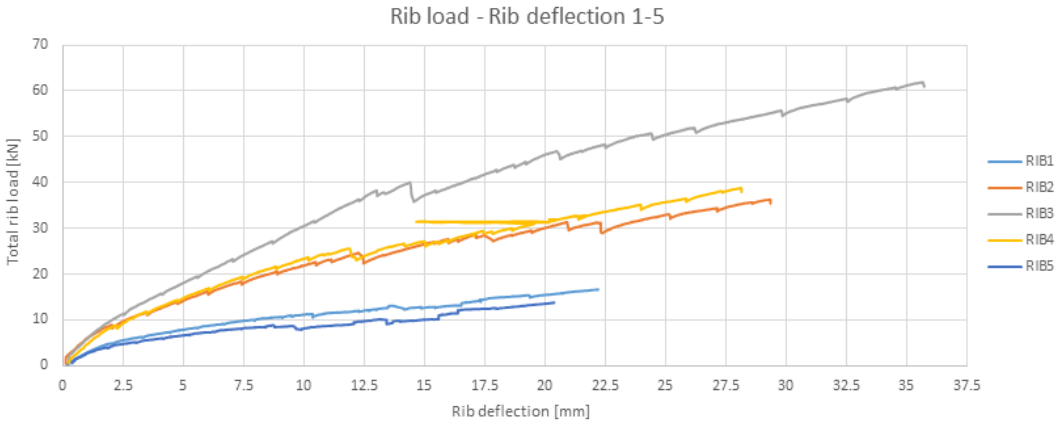

Figure 7.49: A graph showing the deflection at half of the span length for the corresponding force in the ribs.

2. The contribution of RO7 & RO9 decreases from 25% at a quarter span to 22.5% at half span.
3. The contribution of RO6 & RO10 increases from 5% to almost 9% at half span.

The increased distance to the support does promote the equal distribution of the load. Load from the central three ribs is spread more towards the outer ribs, than is the case in the quarter span length test. If this is indeed true, then the results provided by load cells RO1-RO5 would be a logical extension. The length from load to support increases even further and the contribution of rib 3 falls even more, which raises the contribution of ribs 1 and 5. A longer length promotes better distribution. Whether this is due to the increase in stiffness of the top slab and the reinforcement meshes or just due to the decrease in rib stiffness remains to be seen. Comparing these results with the other test specimens will provide more insight.
The distribution of the load does change when the load is increased. It seems that ribs 2 and 4 remain fairly constant, but ribs 1 and 5 drop a few % in contribution, which is added instead to the contribution of rib 3. The contribution of rib 3 rises quite considerably from 30% at the start of the test to about 36.5% at the end. Although it should be noted that until the 40 kN is passed, this increase is not there yet.
This increase in contribution could be explained by the lowering stiffness of the ribs as seen in figure 7.49. It can be seen that the linear elastic zone of the slab really only lasts until rib 3 has deflected 2.5 mm. After that the stiffness starts to go down further continuously. The same is true for the other ribs. Again ribs 1 and 5 react very weak compared to the central three ribs. They carry much less load and yet deflect more than the other ribs at the same load level. This was also observed in the first test. The stiffness results of all ribs are again tabulated in table 7.3. But now the phases over which the stiffness is calculated are chosen independently for each rib, because they vary considerably.

Table 7.3: This table shows the rib stiffness value for each of the ribs in the 2 mesh slab with the load at the centre.

Rib number	**Deflection interval [mm]**	**Stiffness [kN/mm]**	**Deflection interval [mm]**	**Stiffness [kN/mm]**	**Deflection interval [mm]**	**Stiffness [kN/mm]**
1	0.0 - 1.0	4.0	2.5 - 22.0	0.6	-	-
2	0.0 - 1.5	5.3	2.5 - 12.0	1.6	12.5 - 28.0	0.7
3	0.0 - 1.5	5.3	2.5 - 12.5	2.6	14.5 - 35.5	1.2
4	0.0 - 1.5	5.3	2.5 - 12.0	1.6	12.5 - 29.0	0.7
5	0.0 - 1.0	4.0	2.5 - 20.0	0.5	-	-

If one then examines the rotation of the ribs in figure 7.48a, a few observations can be made. First of all the rotation of rib 3 remains small, which is what was expected. Rib 3 is located in the middle after all and should not rotate. Only after 100 kN does it start to rotate a little. Secondly, the rotation of the other ribs is larger but

still remains quite small with a maximum of only 0.8 degrees. And more importantly, the rotation of all the other ribs is more or less equal. If the slab indeed deflected in such a way as a beam would, one would expect the rotation to decrease near the side of the slab, as illustrated in figure 7.50.

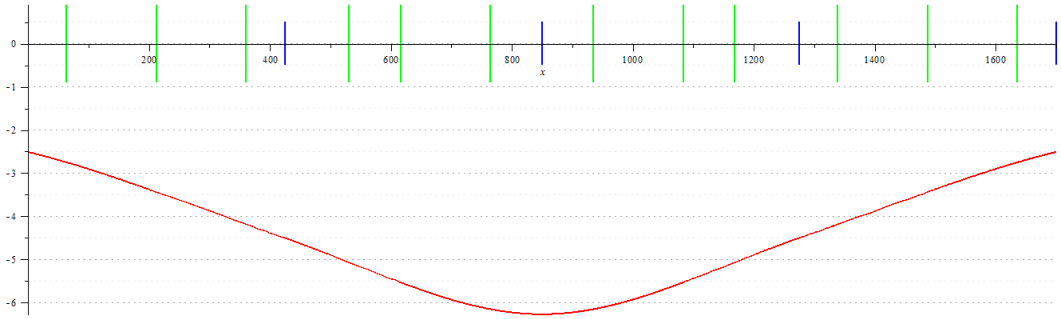

Figure 7.50: A graph showing the deflection at the centre of the slab.

But instead the rotation of all ribs is similar, suggesting that the slab assumes a V-shape during the entire experiment, bending at the location of rib 3 but otherwise remaining straight. If one calculates rotation of rib 5 based on the difference in deflection between rib 3 and rib 5 as done in equation 7.1, then one finds 0.74 degrees which is exactly what is found in the results. This strengthens the idea that the slab is not bending over the width, but instead remains straight.

$$\theta_{rib5} = \arctan\left(\frac{\delta_{rib3} - \delta_{rib5}}{B_{rib3-5}}\right) = \arctan\left(\frac{35.5 - 20}{1200}\right) = 0.74 \quad degrees \tag{7.1}$$

When looking at the slip results of rib 3, one can see the 105 kN cracking again as slip 1 gives a large peak of 1.5 mm and then immediately falls back to 0 mm. Another small peak of 0.4 mm does the same at around 130 kN. The slip 2 LVDT hardly increases at all during the test, until it starts to gradually increase from 120 kN onwards. All of the slip values remain small. A possible explanation for the peaks of slip 1, is that the chemical bond between the steel deck and the concrete broke and they separated at 105 kN. They then shifted about 1.5 mm relative to each other, but the geometric properties of the embossments prevented them from slipping further and even caused them to slide back to the original position.
The strain gauges show very clearly that until the 105 kN cracking event, nothing really happens in the transverse direction of the steel deck. After the cracking has occured though, the strain gauges suddenly start given higher values. Obviously gauges 1 and 4 remain rather small, but gauge 3 and especially gauge 2 start to increase. The steel of the deck does not start yielding until approximately 1900 $\mu\epsilon$, but it does extend. This corresponds nicely with the small rotation to one side that is observed in the rotation curves, since the deck on one side of rib 3 is extending more so than on the other side.

1 MESH TEST SPECIMEN

The load on the slab with one reinforcement mesh was at first increased to 40 kN. Then the load was increased in intervals of 20 kN and after each interval the increase of loading was shortly stopped. At 105 kN the same behaviour was observed as was done with the 2 mesh slab. A large cracking sound was heard. When it started it came from the centre of the slab and from there it propagated to the side of load cells RO6-RO10 first. After increasing the load another 3 kN the same cracking sound propagated from the centre towards the other side. The slab was left to settle for a few minutes during which it was inspected. Several cracks were found on the sides of the ribs, see figures 7.51 and 7.52. The cracks are in locations where, according to the analytical model, one would expect compression instead of tension. This indicates that the modelling of the top slab that was used for the model might conflict with the reality of the slab. If the top slab acts more as a reinforced concrete beam instead of discrete beam elements clamped between the ribs, then the whole bottom side of the top slab is likely to be in tension. This would explain the cracking pattern that is found in this test specimen.

(a) End of the rib at location A1 (see figure 7.38.

(b) End of the rib at location A2 (see figure 7.38.

(c) End of the rib at location A4 (see figure 7.38.

(d) End of the rib at location A5 (see figure 7.38.

Figure 7.51: Cracks in the ribs at the A side of the slab.

(a) End of the rib at location E5 (see figure 7.38.

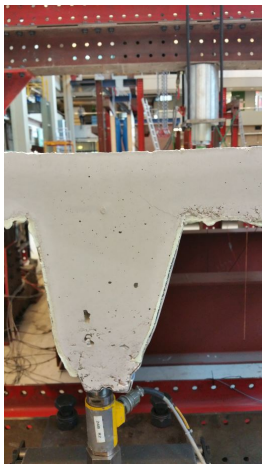

(b) End of the rib at location E4 (see figure 7.38.

(c) End of the rib at location E2 (see figure 7.38.

(d) End of the rib at location E1 (see figure 7.38.

Figure 7.52: Cracks in the ribs at the E side of the slab.

Then the load was again increased until 130 kN and then until 145 kN. During this loading the already observed cracks grew larger, but no new cracks appeared. At that point the metal loading plate, suddenly punched through the top layer of concrete (see figure 7.53). At this point the loading was stopped and the load was released. The load did not punch through the concrete of the 2 mesh slab, even though it reached a higher value. This is most likely because of the extra reinforcement mesh in the top slab of the 2 mesh slab.

The sum of all the load cells varied by 1% or less with the applied load. The sum of load cells RO1-RO5 and the sum of load cells RO6-RO10 were equal to approximately 50.5% and 49.5% of the total load respectively. The load distribution are shown in figure 7.54, the rotation, slip and strain in figure 7.55 and the rib load-deflection diagrams in figure 7.56.

Figure 7.53: The loading plate punched through the top layer of the concrete.

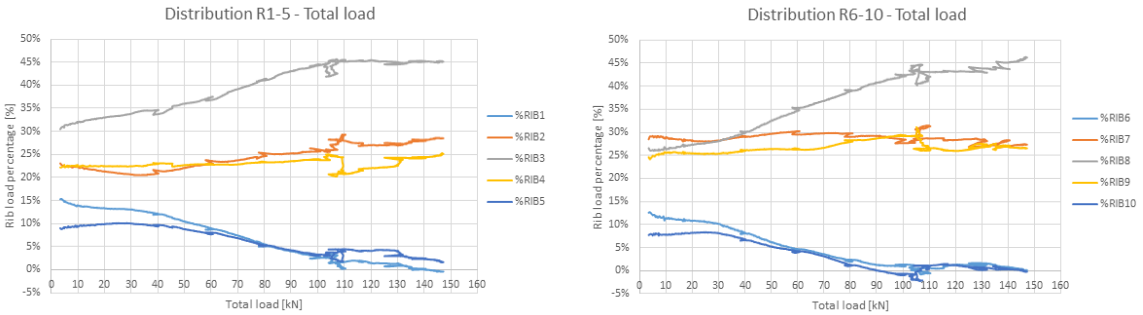

(a) The distribution for RO1 to RO5

(b) The distribution for RO6 to RO10

Figure 7.54: The distribution for R01 to R05 and R06 to R010 of the 1 mesh slab.

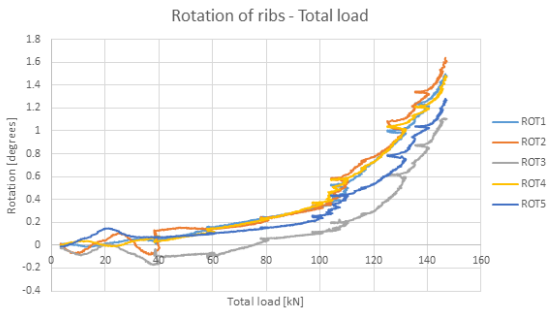

(a) The rotation of the 1 mesh slab

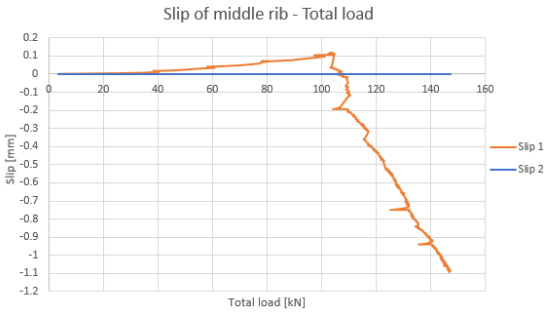

(b) The slip of the 1 mesh slab

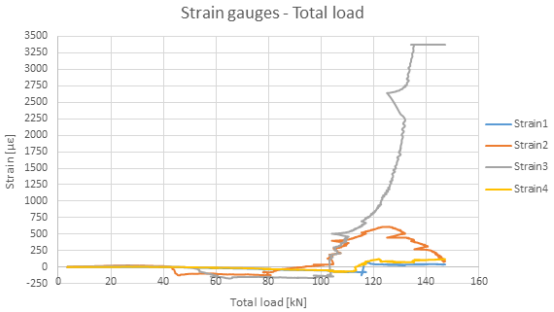

(c) The strain of the 1 mesh slab

Figure 7.55: The rotation, slip and strain of the 1 mesh slab.

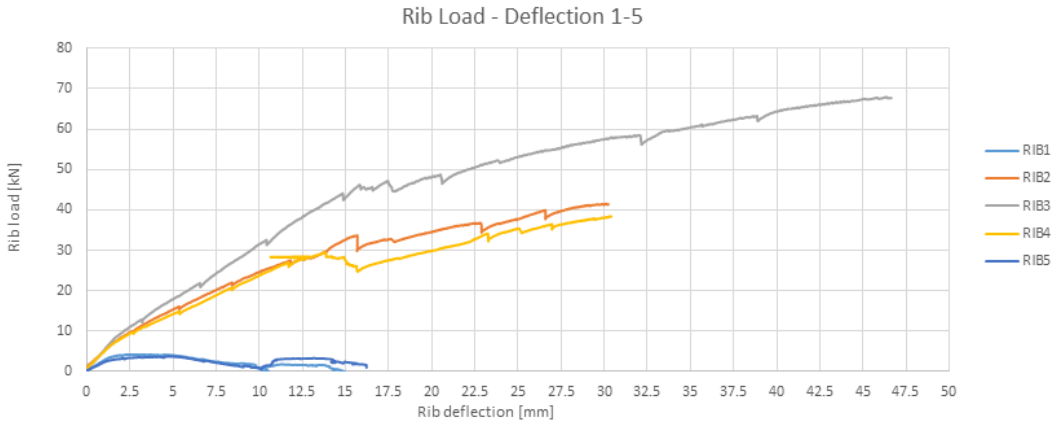

Figure 7.56: The deflection at half of the centre of the ribs.

First of all the distribution of the load will be analysed. At the start the distribution is different at both edges. On the side which was close to the load in the previous test, the middle three ribs have a near equal contribution at an average of 27.5%. While on the other side of the slab the rib 3 bears 30% of the load and rib 2 and 4 only 22.5%. Ribs 1 and 5 are almost equal on both sides, their contribution being slightly higher at 12.5% compared to 10%. This initial difference could have been caused by the test performed at a quarter span length. This initial effect diminishes after increasing the load and at the end, both distribution diagrams look practically the same. After the initial stage, the distribution changes rather drastically up to approximately 105 kN. The contributions of ribs 1 and 5 decrease dramatically from 10% to 0% or nearly 0% on the RO1-RO5 side. Ribs 2 and 4 do not undergo a large change of contribution, but on both sides the average contribution at point of failure is 27%. The contribution of rib 3, at point of failure, ends up with approximately 45%. This distribution differs from the one found for the 2 mesh slab mainly in the contribution of rib 3 and of ribs 1 and 5. Again the disturbance at 105 kN of loading can be seen when the slab exhibited large cracking sounds. But, as in the other tests, the cracking does not disturb the distribution of the load much. Only RO2 and RO4 get upset a bit, but after increasing the load another 20 kN, they are back to the trend line they were following

before the disturbance.
The decrease of load contribution from ribs 1 and 5 can also be seen in the rib load-deflection diagrams in figure 7.56. Ribs 2,3 and 4 show two different phases. All of them have a bend in the curve at a deflection of 15 mm. Ribs 1 and 5 behave very differently though. Their linear phase only lasts until their deflection reaches 1 mm. After that a peak is reached and the load contribution starts to fall. The cracking event occurs when ribs 1 and 5 reach a deflection of 10 mm, then the contribution jumps up slightly as a consequence of the disturbance. After that slight jump the contribution quickly falls back to 0%. The stiffnesses for the ribs are shown in table 7.4.

Table 7.4: The rib stiffness value for each of the ribs in the 1 mesh slab.

Rib number	**Deflection interval [mm]**	**Stiffness [kN/mm]**	**Deflection interval [mm]**	**Stiffness [kN/mm]**	**Deflection interval [mm]**	**Stiffness [kN/mm]**
1	0.0 - 1.0	3.5	1.0 - 15.0	0.0	-	-
2	0.0 - 1.5	5.3	2.0 - 15.0	1.8	15.5 - 30.0	0.7
3	0.0 - 1.5	5.3	2.0 - 15.0	2.7	15.0 - 48.5	0.7
4	0.0 - 1.5	5.3	2.0 - 13.75	1.8	15.5 - 30.0	0.9
5	0.0 - 1.0	3.5	1.0 - 16.25	0.0	-	-

As for the slip measurements, one LVDT fell off the test specimen before the test was started. The other LVDT did provide data. The slip was increasing only slowly until the large cracking could be heard at a load of 105 kN. After that the slip suddenly switched sign and sharply increased in the negative direction. This means that the concrete was moving outwards relative to the steel deck. Although the maximum slip of 1.1 mm is still not very large, this slip, which was observed as well in the 2 mesh slab, could be a significant event.
When analysing the rotation, it is seen that all the ribs have a rotation that is approximately the same. This was also seen in the test of the 2 mesh slab. The rotation that is expected based on the deflection of the ribs, assuming that the top slab remains straight, is calculated in equation 7.2. The calculation is for rib 2 and 4, but the calculation for ribs 1 and 5 yields the same result. The 1.57 degrees of expected rib rotation correspond nicely to what is found by the rotation gauges. A glaring difference with previous results though, is the fact that rib 3 also rotates significantly. Rib 3 rotates in the direction of rib 1 and 2.

$$\theta_{rib4} = \arctan\left(\frac{\delta_{rib3} - \delta_{rib4}}{B_{rib3-4}}\right) = \arctan\left(\frac{46.5 - 30}{600}\right) = 1.57 \quad degrees \tag{7.2}$$

The rotation, that starts to increase more rapidly when the load reaches 105 kN, could be explained by looking at the strain that occurs in the test specimen. It is seen that the strain in strain gauges 2 and 3 starts to increase immediately Shortly thereafter gauges 1 and 4 also show some slight activity, but these gauges never reach any significant value. Gauge 2 also decreases again, while at the same time gauge 3 increases rapidly. The yield strain of the steel deck is 1900 $\mu\epsilon$ and this is exceeded by a large margin. The largest strain reached is approximately 3375 $\mu\epsilon$. The fact that one side of the deck is yielding explains that the other side decreases in strain and that the middle rib starts to rotate towards one side.

NO MESH TEST SPECIMEN

The slab without reinforcement was tested last in the series. The expectation was that the test specimen would collapse rather quickly. Therefore the load was increased very slowly at about 2 kN per minute. The loading was stopped at regular intervals of 15 kN at first and then of 10 kN. The test specimen did not exhibit large cracking until 53 kN of loading was reached. At that point cracks were discovered in several ribs, as can be seen in figure 7.57.

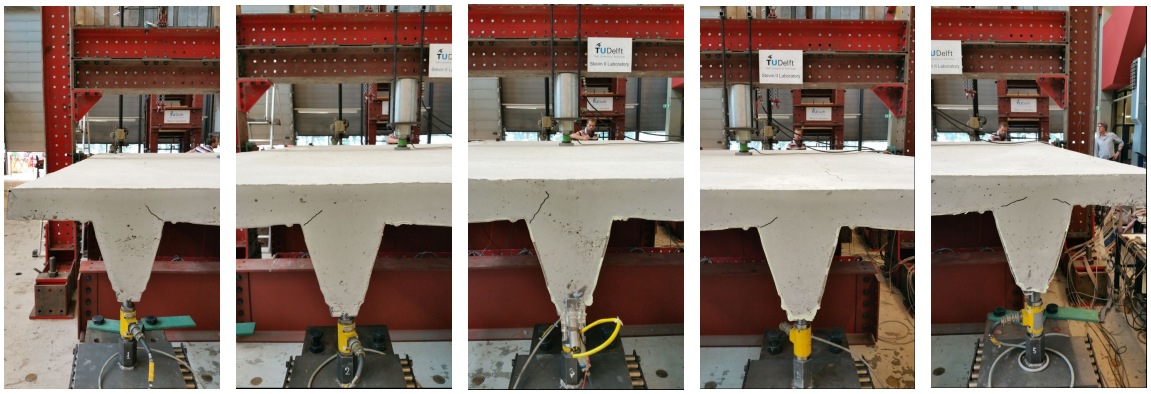

(a) The end of the rib at location A1 (see figure 7.38.

(b) The end of the rib at location A2 (see figure 7.38.

(c) The end of the rib at location A3 (see figure 7.38.

(d) The end of the rib at location A4 (see figure 7.38.

(e) The end of the rib at location A5 (see figure 7.38.

Figure 7.57: Cracks in the ribs at the A side of the slab.

The cracks observed in ribs 1 and 4 are in the same location as in the 1 mesh slab. The cracks in ribs 2, 3 and 5 are curious however. Both ribs 2 and 3 show cracking on the left side of the rib, indicating that they could be rotating in the other direction. Rib 5 even shows cracking on both sides of the rib. The existing cracks propagated throughout the test and all ribs showed signs or had developed cracks on both sides. This phenomenon is discussed further in chapter 8. This was also seen on the other side of the test specimen. Photographs of the propagating cracks on the RO1-5 side and the RO6-10 side respectively can be seen in figure 7.58.

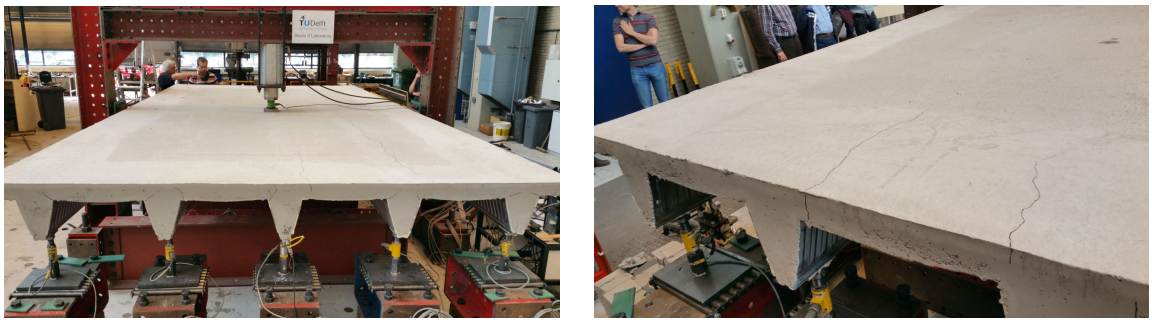

(a) Overview of the A side of the slab (see figure 7.38.

(b) Left side of the E side of the slab (see figure 7.38.

Figure 7.58: Cracks in the ribs at the A side of the slab.

The load was eventually increased until 105 kN and loud cracking noises could be heard as in the other tests. But immediately following the cracking, the test specimen cracked over the length of the slab, this can be seen in figure 7.59.

(a) Longitudinal crack alongside rib 3.

(b) Longitudinal crack alongside rib 3.

Figure 7.59: Longitudinal crack in the slab at a load of 105 kN.

The load suddenly fell back to 90 kN. The load was again further increased after a short inspection of the test specimen. The load did not increase any further though, since the test specimen kept compensating by deflecting more and more. After deflecting further for another 2 mm, the top slab completely cracked on the side of rib 3. The entire top slab cracked through and rib 1 and 2 were no longer connected to the rest of the test specimen, except for the steel deck. The resulting crack can be seen in figure 7.60.After the top slab completely cracked and the load fell back even further, the loading was stopped.

(a) Longitudinal crack alongside rib 3.

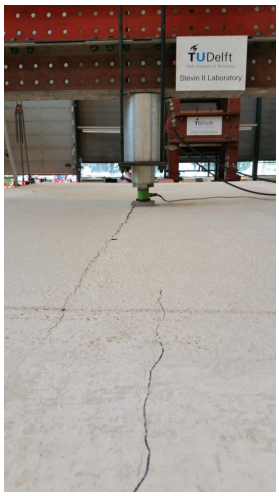

(b) Longitudinal crack alongside rib 3.

(c) Detail of the longitudinal crack alongside rib 3.

Figure 7.60: Longitudinal crack in the slab after the test was stopped.

The sum of all the load cells differs with the applied load by approximately 0.5% throughout the test. Load cells RO6-RO10 bear about 49% of the total load and RO1-5 bear 51% of the load. This is the same distribution of the load that was observed in the 2 mesh and 1 mesh slabs.
The distribution are shown in figure 7.47, the rotation, slip and strain in figure 7.48 and the rib load-deflection

diagrams in figure 7.49.

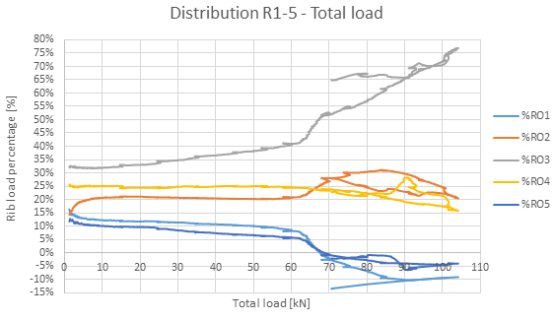

(a) Distribution for RO1 to RO5

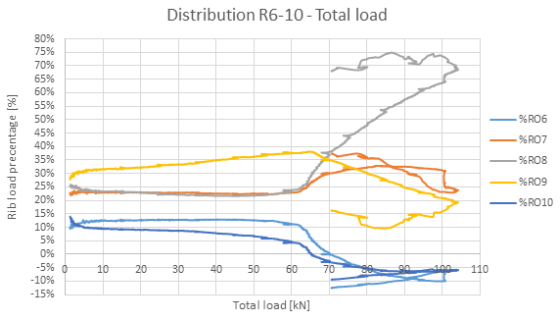

(b) Distribution for RO6 to RO10

Figure 7.61: Distribution for R01 to R05 and R06 to R010 of the 0 mesh slab.

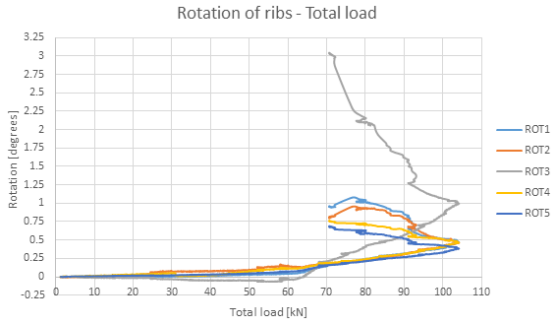

(a) Rotation of the 0 mesh slab

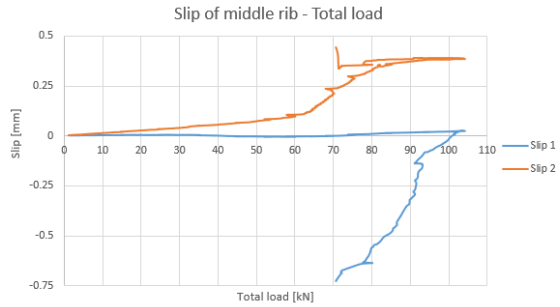

(b) Slip of the 0 mesh slab

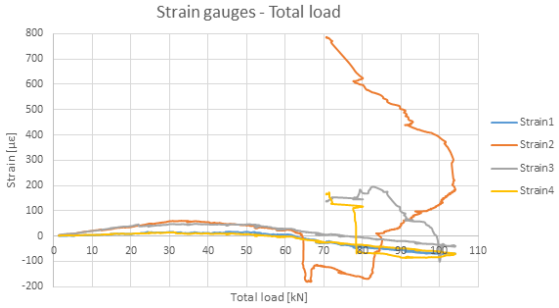

(c) Strain of the 0 mesh slab

Figure 7.62: Rotation, slip and strain of the 0 mesh slab.

At a first glance the distribution graphs for both sides of the slab look fairly similar. The largest difference that can be seen right away is the fact that rib 4 carries more load on the RO9 side of the slab. Another observation is that the distribution graphs have two clear phases. The first phase lasts until approximately 65 kN of loading. After that point the distribution changes completely. rib three increases in contribution rapidly on both sides, while ribs 1 and 5 decrease their contribution at equally rapid rates. Ribs 2 and 4, however, on average remain fairly constant in their contribution. It is striking that RO9 initially contributes much more than RO8. Until the 65 kN mark, the load is quite equally distributed. At 60 kN RO3 bears only 40% of the load, rib 2 and 4 both 22.5% on average and rib 1 and 5 on average 7.5%. This is almost the same distribution that was found in the 1 mesh and 2 mesh slabs. Then the cracks that appeared in the top slab grew larger and larger and this can be seen in the distribution as well. The contribution of the outer ribs, 1 and 5, falls to 0%. The contribution of rib 3 rises much higher to eventually reach 70%. This value of contribution is much higher, than what was found in the other test specimens.
At this point the longitudinal crack along rib 3 appeared and the applied load is reduced. The distribution

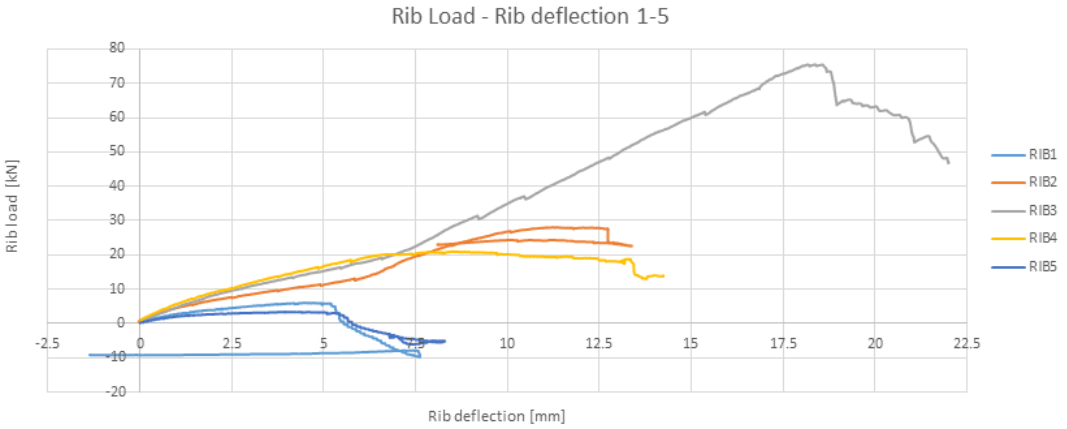

Figure 7.63: A graph showing the deflection at half of the span length for the corresponding force in the ribs.

does not change drastically. Rib 3 keeps about 65% of the load. Strikingly the contribution of ribs 1 and 5 becomes negative. This means that the load measured by the load cells becomes lower than the initial values caused by the weight of the test specimen. This indicates that the sides of the slab are uplifted somewhat. It is possible that the deflection at rib 3 causes the sides of the slab to uplift with ribs 2 and 4 respectively being the rotation points. This would require extra rotation in the centre of the slab and this is exactly what can be seen in the rotation graph. After reaching the 105 kN mark, rib 3 increases rapidly in rotation. It had already rotates far more than the other ribs by that point.

While observing the slip measurements it can be seen that Slip 1 begins to increase after 65 kN. This also the point of loading at which the distribution starts to change. The slip is positive, meaning that the steel deck is moving outwards relative to the concrete. Although the slip values are still low at 0.5 mm, they are in the opposite direction as was expected. This slip starts at the same moment as rib 3 is starting to raise its contribution. So the load is becoming more concentrated in the middle rib. Possibly the steel deck in the middle rib is already yielding at this point and then the increased strain would cause the steel deck to come outwards somewhat. When 105 kN is reached though, slip 2 starts measuring slip in the other direction. The steel deck is now moving inwards relative to the concrete. At his point the deck and the concrete are likely no longer connected by a chemical bond. The concrete therefore starts moving outwards due to the bending of the slab. This is expected behaviour for two components who do not share a shear connection any longer. Interestingly though, the slip on the other side of the slab remains constant. And it has to be noted as well that the total slip on both sides remains low and does not become more than 0.75 mm. More slip is probably prevented by the mechanical connection of the embossments. Regardless the slip measured remains very small throughout the test.
Looking at the strain measurements it can be seen that gauges 1 and 4 remain inactive throughout the test. Even strain gauge 3 hardly exhibits any reaction at all. Strain gauge 2 is again the most active part of the steel deck, but even gauge 2 only reaches 800 $\mu\epsilon$. This is much lower than the 3375 $\mu\epsilon$ found in the 1 mesh slab and even lower than the 1500 $\mu\epsilon$ found in the 2 mesh slab. A question then arises. If rib 3 rotates so much, then where does this rotation come from, if not from yielding of the steel deck. If one again calculates the expected rotation based on the deflection of the ribs, as is done in equation 7.3, one finds the rotation that is more or less equal to the rotation that is found in ribs 1,2,4 and 5. Rib 3, however, rotates up to 3 degrees. This rotation capacity has to come from somewhere and it does not come from the yielding of the steel deck. But the longitudinal crack that appeared, see figure 7.60c, is opened up very wide. This crack will probably provide the slab with enough rotation capacity to allow rib 3 to rotate as far as it did.

$$\theta_{rib5} = \arctan\left(\frac{\delta_{rib3} - \delta_{rib5}}{B_{rib3-5}}\right) = \arctan\left(\frac{22.0 - 7.5}{1200}\right) = 0.70 \quad degrees \tag{7.3}$$

Now the rib stiffness will be analysed again. The rib load-deflection diagram of the slab without reinforcement meshes has two clear stages. In the first phase the behaviour is still quite linear. This was already seen in the distribution graphs. But after a certain load value is reached, the outer ribs 1 and 5 stop contributing

completely. After another small load increase the load in ribs 2 and 4 stops increasing. But the load they both bear does not fall as those of ribs 1 and 5. The curious behaviour of rib 3 is that at a deflection of 7.5 mm the load-deflection behaviour becomes more stiff. Whereas the previous test specimens both had a stiff phase first and a weaker plastic phase afterwards, this rib does not. The other ribs do follow the same stiff-weak pattern and only rib 3 exhibits this behaviour. The explanation of this phenomenon is again sought in the initial values of the load cell. Because of the stiff behaviour of RO9 at the start of the experiment caused RO8 to lag behind what it would otherwise reach. The explanation is visualized by figure 7.64. Because of the higher initial value of load cell RO9, that load cell temporarily draws more load. But while the initial distribution is influenced by the load cell set-up, the ultimate load capacity of the ribs and the top slab are not. The left graph in figure 7.64 shows the expected load-deflection diagrams for all ribs without initial stiffness discrepancies. In the right graph of the same figure the initial stiffnesses of RO9 and RO8 have been increased and decreased respectively without changing their ultimate loading values. Because of the increased load in RO9, it reaches the point (point 2) more quickly, where the load cannot be transferred through to top slab to this rib any more. At the same time point 1, which would normally lie higher than the contributions of RO7 and RO9, at which rib 3 changes from its elastic to its plastic phase, is lowered. After RO9 has reached its ultimate value the new increase in the applied load will now concentrate more on RO8. And because the ultimate loading value of RO8 has not changed, the rib has to gather new load more quickly. Therefore it seems as if the stiffness of rib 3 has increased in the second phase, while actually the initial stiffness was lower than it should have been in the first place. The stiffness values for the ribs are shown in table 7.5.

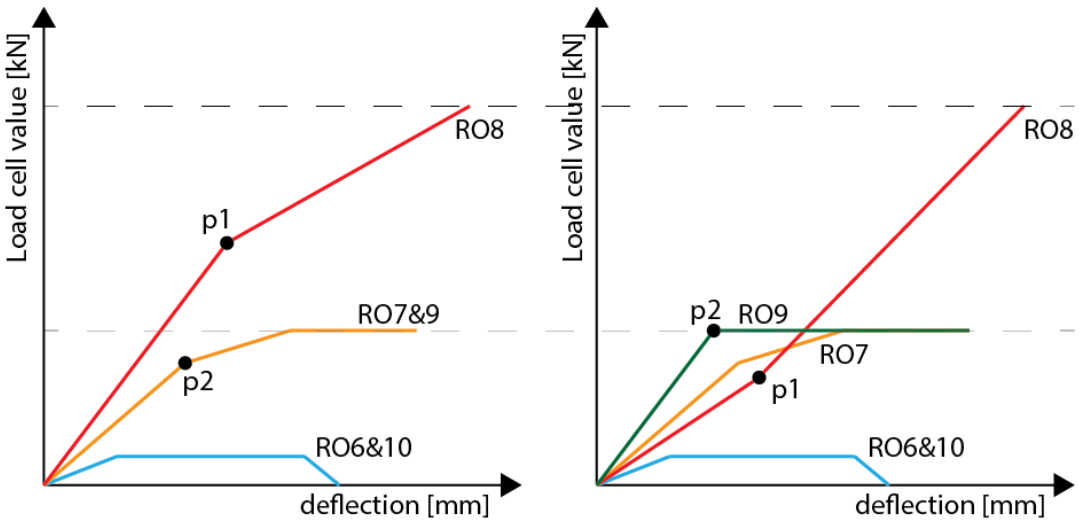

Figure 7.64: A figure showing the load-deflection diagrams for RO6-RO10 with different initial stiffnesses for RO8 and RO9.

Table 7.5: This table shows the rib stiffness value for each of the ribs in the slab without reinforcement mesh with the load at half of the span length.

Rib number	**Deflection interval [mm]**	**Stiffness [kN/mm]**	**Deflection interval [mm]**	**Stiffness [kN/mm]**
1	0.0 - 5.0	1.2	-	-
2	0.0 - 6.0	2.0	6.0 - 9.0	4.3
3	0.0 - 7.0	2.8	2.0 - 15.0	5.0
4	0.0 - 7.0	2.8	7.0 - 13.0	0
5	0.0 - 5.0	0.8	-	-

COMPARISON AND EVALUATION OF TEST RESULTS

The comparison and analysing the differences, will focus mostly on the distribution of the load and the stiffnesses of the ribs. These are, after all, the most important aspects with regards to the analytical model.
First the distribution of the load per side of the slab has to be discussed. The difference between the sum of the load cell values and the applied load remained mostly under 1% and this is an acceptable error margin. However, in all the three tests the side with load cells RO6-RO10 consistently carried about 49% of the total load and the other side of the slab about 51% of the total load. In order to get a 2% difference between both slab sides, the load would have to be misaligned by 54 mm. This misalignment does not have a significant on the test results.
Now the load distribution in the slabs will be evaluated. In order to perform the analysis in a structured manner, the distributions on the RO1-RO5 side of the slab for several load stadia are shown in table 7.6. The corresponding deflection values at the location of the loads are shown in table 7.7. It is chosen to use the values of the RO1-RO5 load cells in order to avoid interference caused by the tests enacted at a quarter of the span length. The loading values 10 kN, 60 kN and the peak load are chosen for the following reasons. 10 kN is the lowest loading value at which the initial imperfections have been evened out and at the same time it is the maximum standard load which can be applied according to the Eurocode. This is thus considered to be the actual initial distribution of the test specimens. At 60 kN the slab without reinforcement has reached the end of its linear phase and also the 1 mesh slab is starting to change its distribution. The peak loading value represents the distribution in the ultimate limit state. All the test specimens' methods of distribution have been utilised, so at this stage the difference between all the mesh configurations should be very clearly observable.

The distribution at at load of 10 kN will be considered first. At this load the initial settlements in each slab has been evened out, so this can be considered the initial distribution for when each test specimen is loaded. The intial distribution is very similar. The largest differences are in the outer ribs and even then the maximum difference is only 3%. Therefore the average initial distribution for each slab is approximately 12%, 22%, 32%, 22% and 12%. This means that reinforcement hardly influences the initial distribution of the load over the ribs. That would mean that the combination of the rib stiffness, the concrete and steel deck of the top slab determine the distribution at this level of loading.
The distribution at a load of 60 kN is different especially rib 1,3 and 5 are affected. The 2 mesh slab still has the same distribution as at 10 kN. But the 1 mesh slab and the 0 mesh slab have an increased contribution of rib 3. This increase in contribution is attracted mainly from ribs 1 and 5. At this point the difference caused by the reinforcement mesh configurations can thus already be clearly seen.
The last load step is the peak loading value. From the size of the ultimate load, the difference can immediately be spotted. The 0 mesh slab, failed right away after the bonding with the steel deck was lost at 103 kN. The load in rib 3 had increased drastically after reaching 65 kN. The cracks, which had already appeared on both ends, grew continuously and caused more load to be concentrated in the centre. The cracks allowed the slab sides to rotate further upwards than was possible in the other slabs. This eventually caused ribs 1 and 5 to uplift somewhat. At the final stage of the test, rib 3 carried 75 % of the load on each side.
For the 1 mesh slab the change in distribution, from the initial values to the ultimate limit state, happens more gradually. From a load of 40 kN onwards, the decrease in load contribution in ribs 1 and 5 can already be observed. At the same time rib 3 starts increasing and ribs 2 and 4 remain almost at the same level. Large longitudinal cracks do not appear in this slab, preventing excessive rotation and complete failure of the concrete top slab. The single reinforcement mesh does not prevent the outer ribs from becoming completely ineffective in carrying the load. In the ultimate limit situation the load is carried only by the central three ribs and of that load 45% is located in rib 3.
The distribution of the 2 mesh slab has hardly changed over the course of the testing. After applying a load of 165 kN, the contribution of rib 3 has risen from 31% to 36% and that of the other ribs has fallen ever so slightly to accommodate this increase. Another striking difference with the other mesh configurations is that outer ribs 1 and 5 still contribute carrying of the load. This was completely absent in the other slabs. The extra distribution of the second reinforcement mesh can be seen in these results. This thought is strengthened by the fact that the strain in the steel deck in the transverse direction is much lower in this slab than it was in the 1 mesh slab. This 1 mesh slab relied much more on the steel deck to transfer the forces sidewards, whereas a second reinforcement mesh alleviates much of the stresses in the steel deck. The slab without reinforcement did not even reach the stage at which the steel deck would start to matter significantly, because the concrete top slab failed immediately after it came loose from the deck.

Table 7.6: Distribution per rib on the A-side of the test specimens

		Test specimen		
Load [kN]	**Rib number**	No mesh [%]	1 mesh [%]	2 meshes [%]
10	1	12	14	15
	2	21	22	22
	3	32	32	31
	4	25	23	24
	5	10	9	8
60	1	8	9	13
	2	21	24	21
	3	41	37	32
	4	25	23	25
	5	6	8	8
103	1	-9	3	12
	2	21	26	21
	3	76	44	35
	4	16	25	25
	5	-4	3	7
145	1	-	0	11
	2	-	29	21
	3	-	45	36
	4	-	25	24
	5	-	2	8
165	1	-	-	11
	2	-	-	21
	3	-	-	36
	4	-	-	24
	5	-	-	8

The behaviour of the steel deck in cooperation with the reinforcement deserves a closer look though. If one examines the distributions of the 1 mesh slab and the slab without mesh, one can see that until 60 kN the distributions are nearly equal. After that point the differences between the two test specimens start to occur. This suggests that the reinforcement mesh starts influencing the behaviour at that point. While the load is increased from 0 to 60 kN, the load is also slowly increasing in rib 3 already although not as strongly. It is therefore thought from the start the concrete in top slab started to crack from the bottom. It is assumed that at 60 kN the cracking has reached the level of the top reinforcement, where it is either stopped by the mesh or it is able to continue in the absence of a reinforcement mesh, see figure 7.65 middle and 7.65 right respectively. In the 2 mesh slab on the other hand the cracking is stopped at a lower level, see figure 7.65 left.

At approximately 105 kN the horizontal shear forces between the steel deck and the concrete have become too large for the chemical bond between the two materials to handle. Thus the steel deck shears away from the concrete. At this point the concrete in the slab without mesh has to bear the vertical shear forces on its own. Since the cracking has propagated so far that the remaining uncracked area is not enough to bear this stress. Thus the top slab cracks completely, as depicted in figure 7.65 right. The slab with 1 reinforcement mesh did not crack as much and also had the mesh to support with transferring the vertical shear load. At this point the steel deck starts to act in conjunction with the compression zone in the concrete of the top slab,

Table 7.7: Centre deflection per rib

		Test specimen		
Load [kN]	**Rib number**	No mesh [%]	1 mesh [%]	2 meshes [%]
10	1	0.33	0.32	0.50
	2	0.34	0.36	0.50
	3	0.51	0.52	0.50
	4	0.34	0.36	0.50
	5	0.33	0.32	0.50
60	1	5.00	4.50	4.30
	2	5.80	5.50	4.80
	3	6.50	6.50	5.60
	4	5.80	5.50	4.80
	5	5.00	4.50	4.30
103	1	7.75	9.00	10.50
	2	13.25	12.25	12.75
	3	18.75	15.50	15.00
	4	13.25	12.25	12.50
	5	7.75	9.50	10.25
145	1	-	15.50	18.50
	2	-	30.00	24.00
	3	-	46.50	28.25
	4	-	30.00	22.75
	5	-	15.50	17.25
165	1	-	-	20.50
	2	-	-	28.67
	3	-	-	36.60
	4	-	-	28.67
	5	-	-	20.50

as depicted in figure 7.65 middle. As for the 2 mesh slab, it can rely on both the steel deck and more so on the bottom reinforcement mesh in order to transfer the loads sidewards, see figure 7.65 left.

As for the slip the following is thought to happen. At first the steel deck is elongating slightly because of the bending stresses in the steel deck. The elongation is more than that of the concrete since the concrete will crack and then stop transferring tensile stresses. When the steel deck and the concrete shear away from each other, the composite action is partially lost and the concrete slips outwards relative to the steel deck, see figure 7.66. The slip is kept small though, because of the mechanical interlocking with the embossments. If the deck would not be embossed, the slip would most likely be much larger.

Finally the rib load-deflection diagrams will be compared and evaluated as well. As found in the non-destructive tests, the outer ribs 1 and 5 react much less stiff than the central three ribs. Their deflection is much greater for a lower amount of load on the rib. It seems as if the stiffness of these ribs even smaller than that of the middle three ribs at very small deflections and loads. Even when one looks at the behaviour of the ribs at deflections smaller than 1 mm, the stiffness of ribs 1 and 5 is still lowered compared to that of ribs 2,3 and 4 (see figure 7.56). This strengthens the idea that the stiffness behaviour of the ribs is not solely based on the rib itself, but also on whether there are ribs on either side or not. These boundary conditions seem to have a

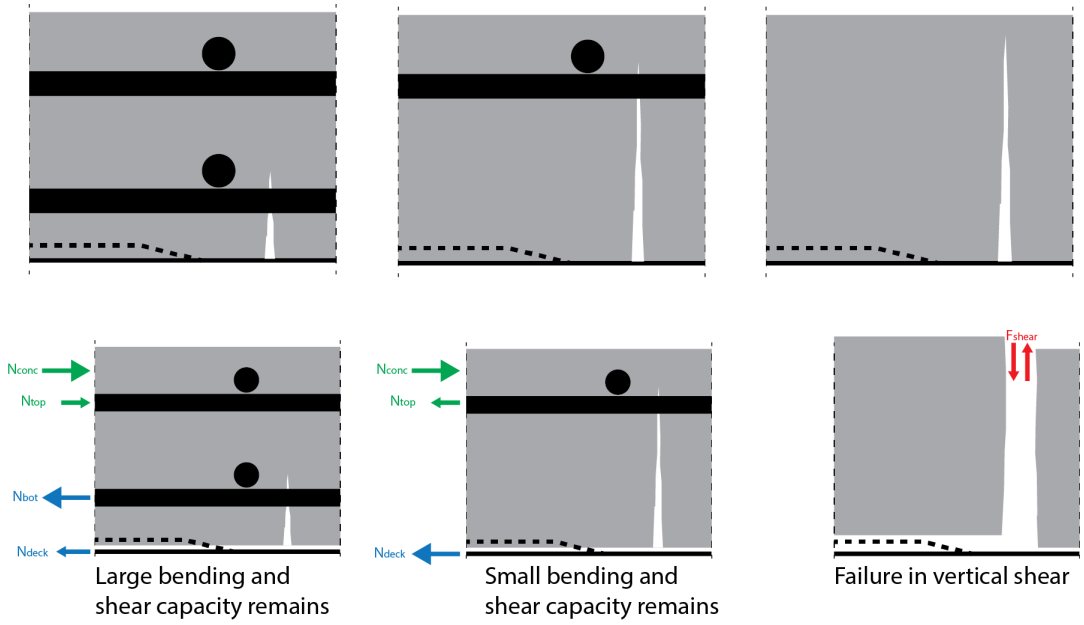

Figure 7.65: A frontal cross-section of the top slab illustrating the expected top slab behaviour for all mesh configurations under increased loading.

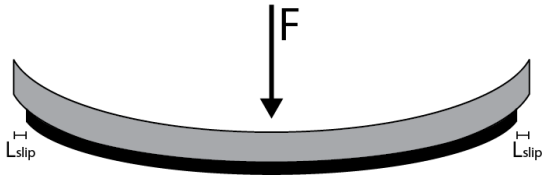

Figure 7.66: A figure illustrating the expected slip that will occur in the test specimens when the deck and concrete are no longer attached to each other.

large effect on the initial stiffness.
Then when the initial phase in which the concrete is uncracked has passed, the reinforcement becomes active. In the 2 mesh slab the stiffness of ribs 1 and 5 still is only about 20% of that of rib 3 and 33% of ribs 2 and 4. To assume that all the ribs have the same stiffness behaviour, is thus most likely not true to reality. With the 2 mesh configuration it is still able to transfer load from the centre towards the slab sides. In the 1 mesh slab this is already very quickly longer the case and the stiffness of ribs 1 and 5 falls to 0. Their load contribution decreases, but their deflection keeps increasing. Therefore it seems as if they are dragged down by the other ribs without resisting this deflection. In the slab without reinforcement mesh an even more extreme thing occurred, the load in the outer rib load cells actually decreased below the values that were initially measured due to the self weight. This indicates that the slab is locally uplifted at that point. Therefore, the following is thought to have happened. When a square plate, which is simply supported on all sides, is loaded by a concentrated force in the centre uplift will occur at the corners. This is visualized in figure 7.67a. Of course the composite plates that were used in the experiments are not simply supported on all sides, but they do have a different ratio of bending stiffness in the transverse direction and the longitudinal direction.

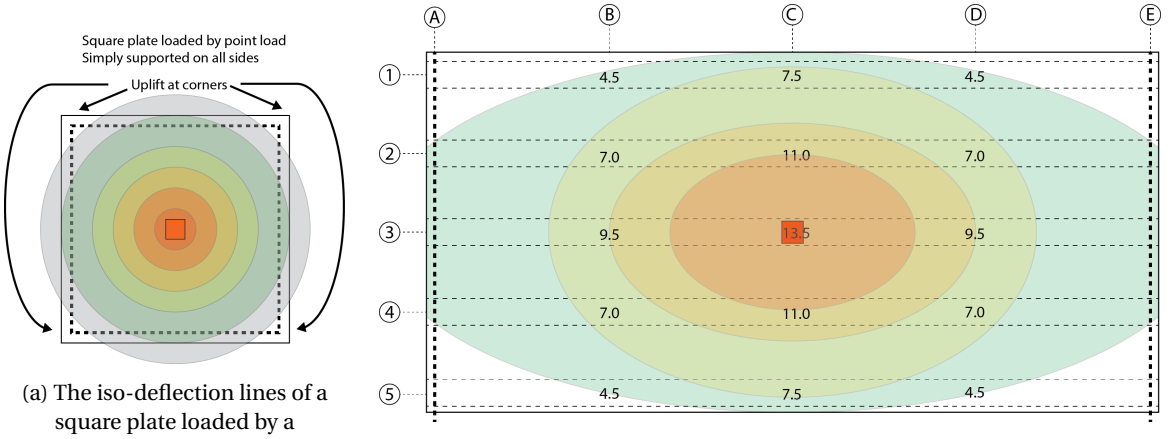

(a) The iso-deflection lines of a square plate loaded by a concentrated force in the centre.

(b) The approximate iso-deflection lines of the slab without reinforcement mesh loaded by a concentrated force of 90 kN.

Figure 7.67: The graphs depicting the rotation, slip and strain of the slab without reinforcement meshes set against the total load in the centre.

Because of the different bending stiffnesses in the both cardinal directions the deflection iso-lines are oval. In the case of the square plate with equal bending stiffness in both directions they are circular and in the case of a plate simply supported on both edges and with equal bending stiffnesses they would be straight, with an equal deflection at every length of the slab across the with. A approximate iso-deflection diagram of the slab without reinforcement mesh is shown in figure 7.67b. It can be seen that the deflection is indeed oval shaped with the centre being around the middle rib. The supports of the outer rib are in the lowest deflection zones and if the load is increased far enough should begin to uplift as they would do for the square plate. This would explain why the load decreased to below the initial load cell values for the test specimen without a reinforcement mesh. The ends of the slab were pushed upwards by the deformation of the slab and thus the load decreases. The 1 mesh slab would have been influenced by the same effect but to a lesser extend because the slab is more stiff in the transverse direction because of the added reinforcement mesh. Thus eventually the load in the outer ribs does decreases to zero, but does not get uplifted. This effect would also explain why the outer ribs continue deflecting while no increase in load is measured at the supports. At the centre of the slab, some load is indeed distributed towards the sides by the remaining parts of the top slab, but at the ends of the slab, this load increase is negated by the uplift caused by the deformation of the slab. This theory is strengthened when one compares the same iso-deflection diagram made for the 2 mesh slab which is shown in figure 7.68. There it can be seen that the iso-lines are much more circle-shaped and have even begun to become slightly elliptical in the other direction. This means that at the length of the supports, the deflections will have evened out a lot and the differences per rib will be quite small. Therefore no uplift occurs in this test specimen and the load increase in the outer ribs can be measured at the supports.

The phenomenon above also partially explains why in the rib load-deflection diagrams seem to show that the outer ribs are less stiff than the central three ribs. Because the load deflection diagrams show the deflection at the point of loading, but the load is measured at the end of the rib. Between these two points redistribution of the load has already taken place. At the location of load application the load has a certain distribution over the ribs, but at the end of the slab where the load cells are located, the distribution has changed again. This redistribution strongly depends on the stiffness of the top slab and the damage that it has or has not sustained. The idea of considering each rib as a separate beam with a separate stiffness has thus been thoroughly undermined. Because comparing the load found at the end of the slab with the deflection found in the middle at the location of the load, thus incorporates not only the stiffness of the rib itself, but also that of the top slab and the damage it has taken up until that point. The value that is found by measuring the slope of the rib load-deflection diagram is thus more of an effective stiffness property of the slab as a whole instead of only the single rib. This knowledge can also be used again in chapter 8, where the analytical model will be used to reproduce the test results.

The total size of the deflection differs for each specimen as well. The addition or removal af the extra reinforcement mesh seems to matter greatly in this regard. The 2 mesh slab reaches a maximum deflection of

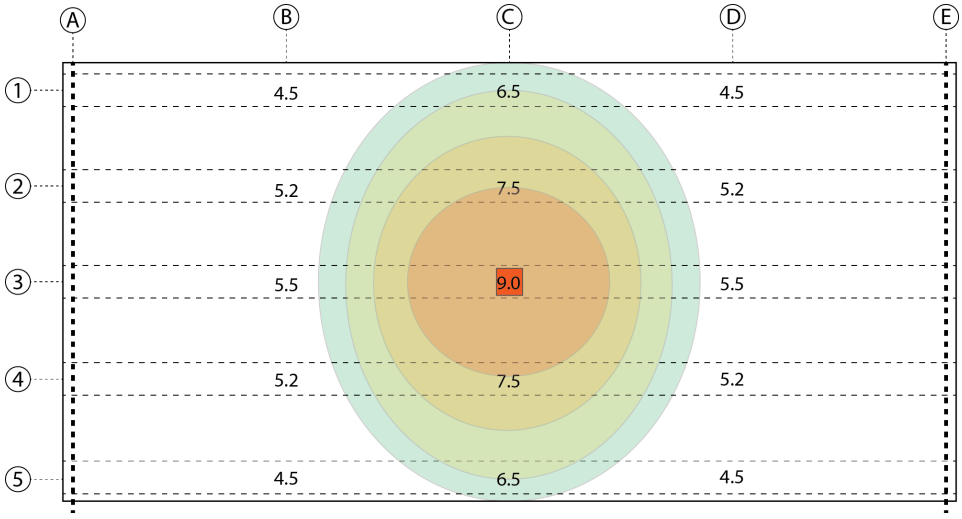

Figure 7.68: The approximate iso-deflection lines of the 2 mesh slab loaded by a concentrated force of 80 kN.

approximately 35 mm at a load of 165 kN, while the 1 mesh slab is already deflected to 46 mm at a load of 145 kN. The weaker top slab causes the load to concentrate more in the middle rib. This in turn causes the middle rib to deflect more and indeed the difference in deflection between the middle rib and ribs 2 and 4 is greater in the 1 mesh slab than it is in the 2 mesh slab. Comparing the slab without reinforcement with the 1 mesh slab, the effect is less profound. Indeed the slab without a reinforcement mesh only reaches a maximum load of 105 kN, but at this load level the deflection is 11 mm and this is only 1 mm more than the 10 mm in the 1 mesh slab. The greatest effect for the slab without mesh is that the ultimate load has decreases so significantly. But even at the small load of 10 kN the difference in deflection can already be seen, see table 7.7. The 2 mesh slab has equal deflection across all ribs, while the other two slabs have an increasingly smaller deflection towards the sides of the slab. So even while the distribution of the forces at this point is very similar, the deflection is already starting to diverge between the three types of mesh configurations.

And finally the cracking patterns that were found during the experiments will be examined more closely. Initially it was expected that the moment diagram would have the shape that is shown in figure 7.69a because of the rotation resistance of the ribs. Because of this it was thought that the top slab would crack at the bottom and the top in an alternating way, because of the alternating bending moments.

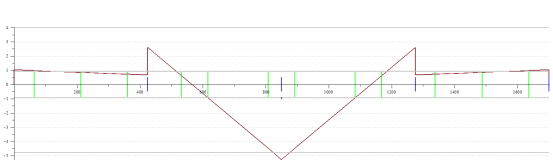

(a) High rib rotation stiffness

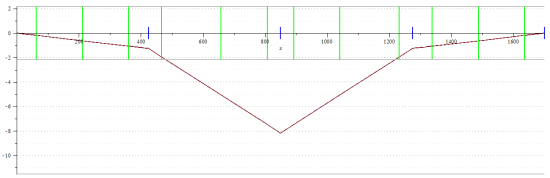

(b) No rib rotation resistance

Figure 7.69: The shape of the moment diagram over the width of the top slab with and without rib rotation stiffness respectively.

But since the ribs are not joined to another structure by concrete or restrained in any other way, the rotation resistance of the ribs is likely to be very low. It is therefore probably that the moment diagram has a shape similar to what is shown in figure 7.69b. This means that the entire top slab is subjected to a positive bending moment across the width of the slab. In the 2 mesh slab, no cracks where found because this slab did not only have the steel deck but also two reinforcement meshes to support it. The 1 mesh slab showed cracks because it did not have the bottom mesh and the slab without reinforcement meshes showed the largest cracks entirely according to expectations.

7.4.2. TEST AT QUARTER OF SPAN LENGTH

The test at a quarter of the span length was performed first for all test specimens. This means that the test specimen was yet uninfluenced by previous testing, but of course it is possible that transportation did influence it in some way. The influence of transporting the test specimens is hard to determine though, since any cracks that did occur are on the bottom side of the concrete where the steel deck is covering the slab.
Because the test at a quarter of the span length was non-destructive for all test specimens, the applied load was not very large. This was done so in order to keep the test specimens in the linear elastic zone. Consequently the deflections, rotation, strain and slip were also quite small. Therefore the slip, strain gauge and rotation measurements will not be shown in this section and are instead given in appendix G. For each test the maximum values of the slip, rotation and the strain that occurred will be given first. The sum of all the measurements of the load cells on one side and on the other side of the test specimen was also taken. This was compared to the total applied load, to find which percentage of the total load both sides of the slab were carrying. Since the load was applied at a quarter of the span it is expected that the far side of the slab will carry about 25 % of the load and the side close to the press about 75%. The sum of all load cells was also taken in order to find the difference between the external and internal forces. This deviation value will also be mentioned per test.
Then the distribution of the load over the ribs will be discussed. That is the most important issue of course. Secondly, the load in each rib and the deflection of said ribs will be evaluated. Doing this gives a means of evaluating the stiffness of each of the ribs and doing so is also important for the rib stiffness features strongly in the analytical model. For the load-deflection diagram of the ribs the values of both load cells on each side of a rib are summed up and the deflection at the location of the load is also used.

2 MESH TEST SPECIMEN

The test specimen with two reinforcement meshes in the top slab was the first to be tested of the series. The load acting on the test specimen was first increased relatively quickly within a few minutes until 25 kN. After that increasing the load was shortly stopped to inspect the reactions occurring in the test specimen. Then the load was again increased until it peaked at 50 kN, after which the set-up was left standing for a while and so the load drifted back to about 48 kN.
The rotation of the ribs remained nearly constant throughout the test and never rose over 0.05 degrees. The slip 1 measurement steadily rose throughout the test to a maximum of approximately 0.03 mm and the slip 2 measurement also rose steadily to about 0.0125 mm. Strain gauges 1 and 4 gave almost constant values of no more than 5 $\mu\epsilon$ and strain gauges 2 and 3 rose to their respective maximums of 20 and 30 $\mu\epsilon$. The sum of the load cells indicates that the far side of the slab indeed carries 25 % of the load and the close side 75%. The difference between the applied load and the sum of the load cell values remained fairly constant at about 0.5% and thus was quite small.

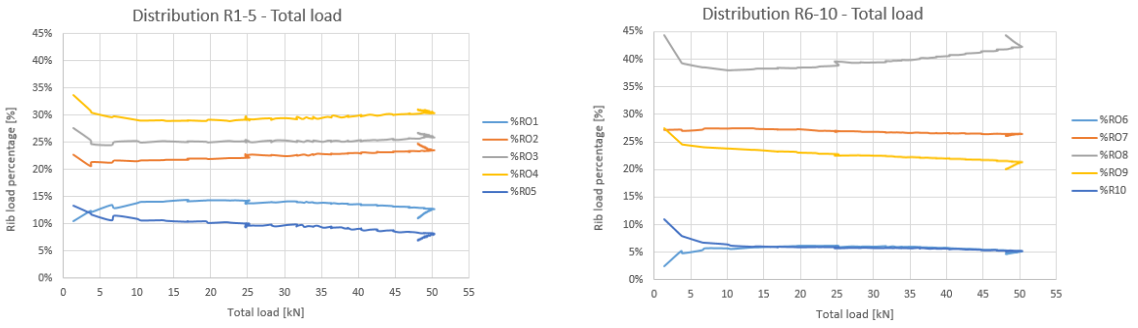

(a) The distribution for RO1 to RO5

(b) The distribution for RO6 to RO10

Figure 7.70: Distribution for R01 to R05 and R06 to R010 in the 2 mesh slab.

Figure 7.70 shows the distribution for both sides of the slab. The distribution of RO6 to R010 shows clearly that central rib carries the larger part of the load. Although the contribution of RO8 does increase proportionally to the applied load, it does not increase far above 35%. The ribs directly adjacent to the central rib, RO7 and RO9, do not have exactly the same contribution but on average they both contribute about 25%. The difference could be caused by the differing initial values of their respective load cells. These values where

about 1 kN apart and remain so throughout the test. Both of the outermost ribs carry 5% each. RO1 and RO5 again do not give the exact same contribution, but this is probably also caused by the difference in the load cells.
For load cells RO1 to RO5 a different pattern emerges. The middle three ribs, RO2, RO3 and RO4, are now very close together in terms of contribution. They vary from 23% to 30% and interestingly the central rib does not carry the largest load but only 26%. The outermost ribs do not carry the same amount this time but carry about 8% and 12.5% respectively. It is obvious that the load is far more equally spread out over the central three ribs and also the outermost ribs have increased contributions. This is likely due to the longer distance between the applied load and the load cells RO1-RO5, giving the slab more length to redistribute the loads.

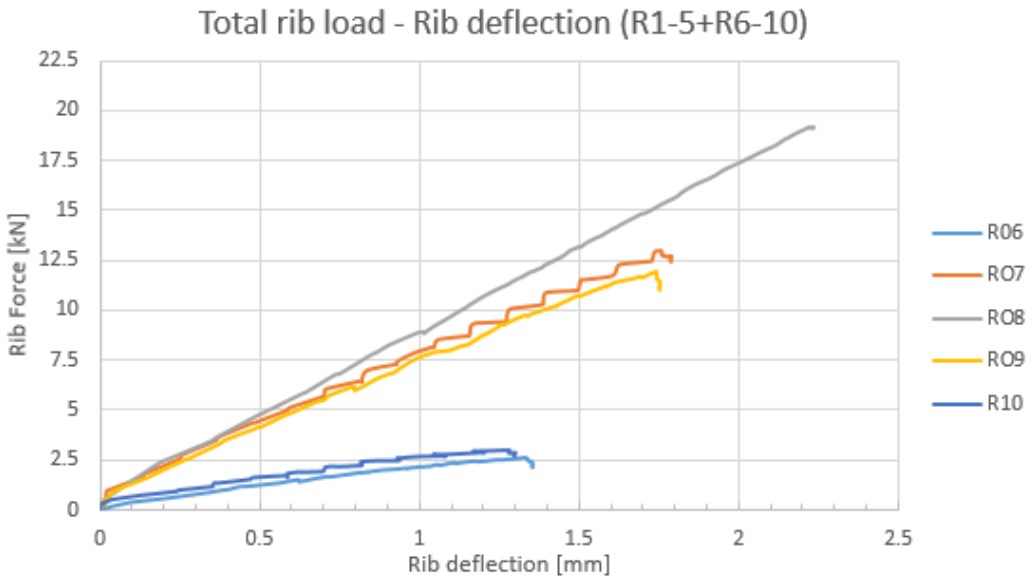

Figure 7.71: Deflection at a quarter of the span length for the corresponding force in the ribs.

The graph in figure 7.71 shows the deflection directly underneath the load in each of the ribs set against the force in the ribs. From the slope of this graph the stiffness of each rib can be calculated. The interesting thing to note is that the ribs have different stiffnesses. The central rib acts much stiffer than the other ribs and deflects less when bearing the same amount of load. The outermost ribs react much weaker than the middle three ribs. They deflect only about 40% less than RO8 while bearing about 85% less load. It seems as if the outer ribs get dragged down by the deflection of the central rib without the outer ribs resisting this motion.
Because the rib stiffness is a major point of interest for both the comparison of the test results and for the analytical model, these values are given in table 7.8.

Table 7.8: Rrib stiffness value for each of the ribs in the two mesh slab with the load at a quarter of the span length.

Rib number	Stiffness [kN/mm]	Relative size to rib 3 [%]
1	2.5	28.6%
2	7.5	85.7%
3	8.75	100.0%
4	7.5	85.7%
5	2.5	28.6%

1 MESH TEST SPECIMEN

The second test specimen to be tested was the slab with only 1 mesh of reinforcement in the top slab. The load was first increased to about 20 kN and at that point it was shortly kept there. Then the load was further increased until 40 kN. Then a slightly longer break was held and finally the load was increased to 50 kN which was the peak load for the test at a quarter of the span length.

The rotation of all ribs remained very small during the test and none came higher than 0.005 degrees, except rib 1 which steadily increased and rotated by maximum of 0.035 degrees. The slip of slip 1 increased to 0.08 mm and slip 2 hardly showed any displacement at all. Strain gauges 1 and 4 got to a strain of 10 and 15 $\mu\epsilon$ respectively and gauges 2 and 3 both reached about 35 $\mu\epsilon$. The 25%-75% distribution of the load per slab side was again found. Although the sum of all the load cells did have about 1.5% less load than the totally applied load throughout the test. This is a slightly larger error than in the other tests, but it is still acceptable.

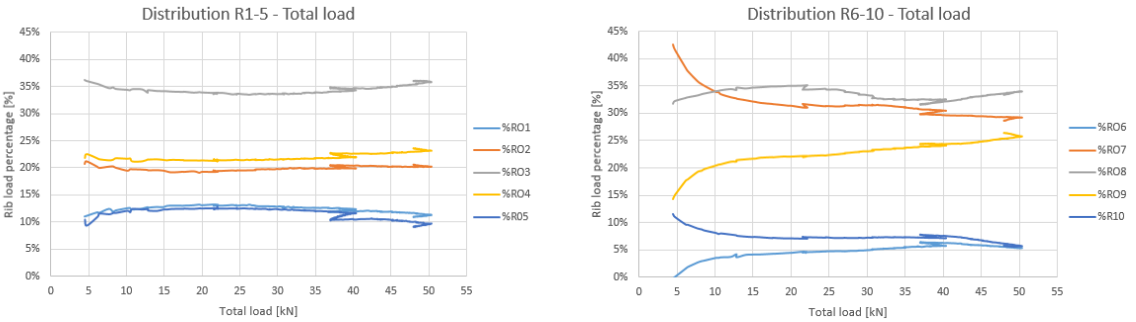

(a) The distribution for RO1 to RO5

(b) The distribution for RO6 to RO10

Figure 7.72: Distribution for R01 to R05 and R06 to R010 respectively of 1 mesh slab.

In figure 7.72a the distribution on the side close to the load can be seen. Contrary to the slab with two meshes, this slab shows that the middle three ribs have a very similar contribution. RO8 still carries the most load with 35%, but RO7 and RO9 also carry 25% and 30% respectively. The outermost ribs are again close together, both at 5% of the load. There are some slight changes in the distribution throughout the test. But the changes that did occur are quite small. Only at the start of the test large changes can be spotted, indicating that there were some initial imperfections in the slab that had to be overcome first before the actual distribution was reached. The difference probably cannot be attributed to the difference of the load cells, since their initial values are quite close together.
On the other side of the slab at RO1 to RO5 a different distribution can be seen. The distribution on this side remains quite constant throughout the testing. The central rib, RO3, clearly carries the largest part of the load with 35%. The adjacent ribs, RO2 and RO4, are close together at approximately 21.5% and the outer ribs are also close together at about 11.5% of the load. For both sides of the slab the loads of RO1-RO6, RO2-RO7, RO4-RO9 and RO5-RO10 are reasonably close in terms of load contribution. More so than was seen in the results of the two mesh test. In all of the graphs the dip in load around 40 kN can be observed, when the load was not increased for a few minutes, before resuming the test.

Figure 7.73 again shows the rib load-rib deflection diagram of the 1 mesh slab. It can be observed that the middle three ribs have a very similar load-deflection behaviour and the load borne by ribs 2 and 4 is almost of the amount as that of rib 3. But again ribs 1 and 5 react much less stiffly than the others. Both of them carrying only about 4 kN while ribs 2 through 4 carry almost three times that amount at the same deflection. This result is very similar to the results found in the two mesh test. It is interesting to note though, that there is a bend in the curve at approximately 1 mm of deflection for all ribs. The outer ribs start to go flat, deflecting without increasing in load. This indicates that some sort of plastic behaviour phase has been reached in the process that distributes load to these ribs. Probably the concrete in the top slab that has begun to crack. For the rib 3 and the ribs 2 and 4 this is not a satisfactory explanation though. The load is placed directly above rib 3 and does therefore not rely on the top slab. It is possible that the concrete in the ribs has begun to crack at this load, thereby reducing the stiffness of the rib. All of the three central ribs exhibit the same curve and continue on a linear path thereafter. Thus a transition from an uncracked to a cracked phase could be the logical answer in this case.
The values of the rib stiffnesses are again given in table 7.9. Because two distinct stiffness phases can be distinguished in the graphs, these phases are also indicated separately in table 7.9. Phase 1 is defined from 0 to 0.9 mm of deflection and phase 2 is defined from 0.9 mm deflection onwards.

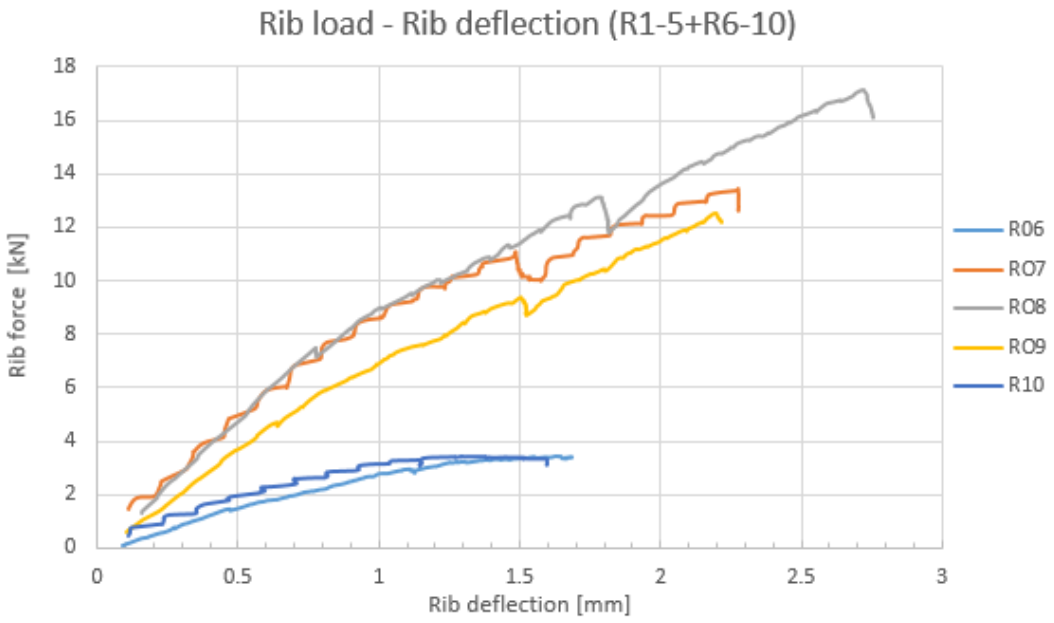

Figure 7.73: Deflection at a quarter of the span length for the corresponding force in the ribs.

Table 7.9: Rib stiffness value for each of the ribs in the one mesh slab with the load at a quarter of the span length.

	Phase 1		Phase 2	
Rib number	**Stiffness [kN/mm]**	**Relative size to rib 3 [%]**	**Stiffness [kN/mm]**	**Relative size to rib 3 [%]**
1	2.7	30.9%	0	0%
2	8.75	100.0%	4.5	84.9%
3	8.75	100.0%	5.3	100.0%
4	7.5	85.7%	4.6	86.8%
5	3.5	40.0%	0	0%

NO MESH TEST SPECIMEN

Before the discussion of the results is discussed it should be noted that the slab was not completely undamaged before the testing started. In figure 7.74 a photo of the slab can be seen where a crack running along the length of the slab is indicated on top of the slab. This crack was discovered after the transportation to the laboratory. But the crack does not propagate further across the slab than to the half way point. It also does not reach the end of the slab on the closer side in the photo. So it is suspected that this crack was caused by the shrinking of the concrete. Although it remains possible that it was caused by rough handling during transportation. But since during the hardening af the concrete the larger volumes in the ribs dry out at a slower rate than smaller volumes in the top slab. These differing rates in drying and hardening are likely to cause shrink cracks in the concrete since there is no reinforcement mesh to keep it together. The crack is visible on the top side of the slab. If the depth of the crack remains within the compression zone of the top slab, the influence on the test results should be small. But the depth of the crack is unknown, thus this cannot be said with certainty. It is also possible that there are more cracks which are not visible since the steel profiled deck covers the bottom side of the concrete slab.

The slab without top slab reinforcement meshes was performed last in the series. The load was very slowly increased to 10 kN and then the load was not increased any further. This was done because of the fear of damaging the test specimen in such a way that the destructive test would become meaningless. Therefore the load was very slowly increased until 10 kN and then no further. The speed of increase of the load matters, because the equipment was set to take a data point every second. So in order to get a sufficient amount of

Figure 7.74: 0 mesh slab in the test set-up with the crack indicated with a marker on the top.

data points, the load was increased with only about a kN per minute.
The rotation of all ribs during this test was very small and constant over the ribs and only increased to about 0.03 degrees. The slip 1 measurement did not give any deflection at all. But this was due to the fact that the LVDT measuring the slip was accidentally knocked off, when hoisting in the new test specimen. This was not found out before the first test and thus only slip 2 provided data. Slip 2 rose to exactly 0.03 mm. Strain gauges 1 and 4 reached about 6 $\mu\epsilon$ and strain gauges 2 and 3 got to around 10 $\mu\epsilon$. The 25%-75% load distribution over the slab sides was again spot on. The sum of all the load cell forces differed from the applied load by never more than 1% which is acceptable.

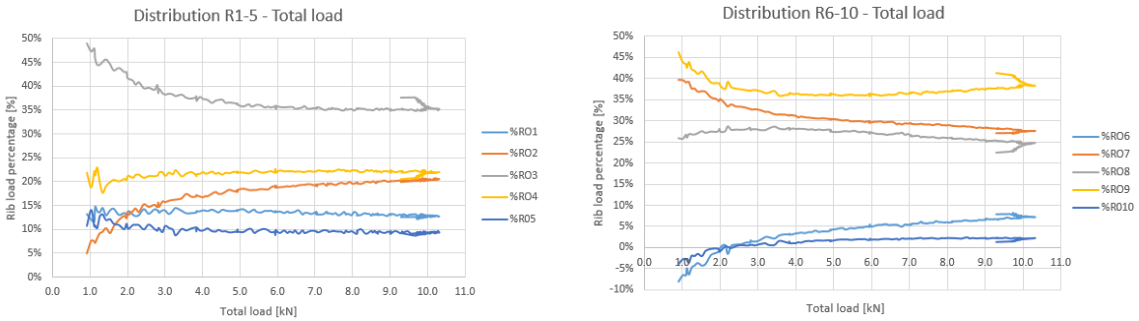

(a) The distribution for RO1 to RO5

(b) The distribution for RO6 to RO10

Figure 7.75: Distribution for R01 to R05 and R06 to R010 in the 0 mesh slab.

In figure 7.75 the distribution of the slab without reinforcement in the test at a quarter of the span length can be observed. The distribution of RO6 through RO10 is very interesting. The middle rib, RO8, does not bear the largest load and only carries 25%. The adjacent ribs, RO7 and RO9, both bear more at 27.5% and 44% respectively. This is unlikely to be caused by the initial load cell values since the values of RO7 and RO8 are very close and RO9 is only 1 kN higher. Both RO7 and RO9 are also quite far apart in terms of contribution. And also RO6 and RO10 do not have exactly the same contribution with 2.5% and 7% respectively. Perhaps these results can be explained by the fact that the load is still very low and that the slab did not deform enough yet to settle in the expected distribution and even a small difference in load will be relatively large in terms of changes in percentage. Or perhaps it is because the load is placed so close to the supports on this side. Or it is possible that other shrink cracks have formed in this part of the slab can not be observed because of the

steel deck. The slab hardly deflects at all as can be seen in figure 7.76, less than 0.5 mm. So if the slab has some initial imperfections which favour the distribution to the adjacent ribs, the slab does not have sufficient length to assume a distribution in which the central rib carries most of the load.
This second thought seems to be confirmed by the values found in load cells RO1 through RO5. AFter the initial settlement period, RO3 clearly bears most of the load (35%) on that side of the slab. Load cells RO2 and RO4 have very similar contributions, both around 21%. The outermost ribs, RO1 and RO5 are slightly farther apart at 10% and 13% respectively. This distribution is actually very similar to what was found on the far side in the 1 mesh slab test. The central rib still only bears 35% which is not a very large amount, considering there is no reinforcement in the top slab to assist in the distribution process. This means that the concrete without reinforcement still distributes the load quite nicely, at least for small loads such as these.

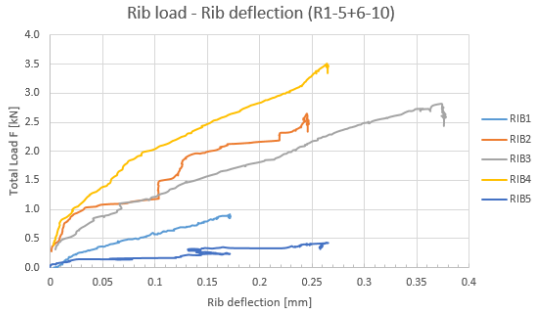

(a) Deflection at a quarter of the span length for the corresponding force in the ribs.

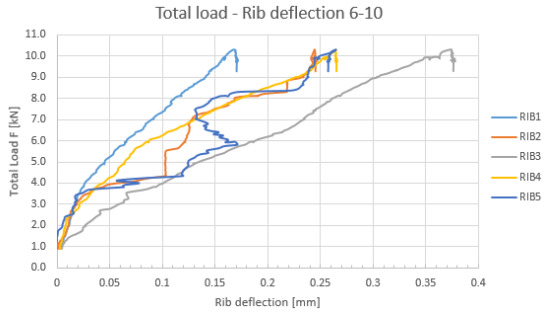

(b) Deflection at a quarter of the span length for the corresponding total applied force on the slab.

Figure 7.76: The left graph depicts the total applied load and the rib deflection and the right graph depicts the rib load and the rib deflection.

The rib load-deflection diagram can be seen in figure 7.76a. It again shows that rib 2 and 4 bear a large part of the load than the middle rib and also react more stiffly. It is interesting to note that the middle rib does deflects about 40% more than both rib 2 and 4, despite bearing a smaller percentage of the load. This could mean that the middle rib is somehow less stiff than the ribs around it, perhaps due to issues with the concrete during casting. This cannot be checked without removing the steel deck though and that thought is therefore mere speculation.
Another interesting thing to note is that rib 5 is reacting much weaker than rib 1, even though they are at equal distances from the middle rib. And, as can be seen in figure 7.76b, the deflection in rib 5 starts increasing sharply around 4 kN of total load but jumps back again at 6 kN. The load in the rib does not increase or decrease during the jumps in deflection. This suggests that this behaviour is possible caused by the adjacent rib 4 dragging rib 5 down and then at some point it is released again. Again, the exact cause of this behaviour is unlikely to be found without removing the steel deck. And it should be placed into perspective as well. Although the other ribs do not exhibit this behaviour, the actual deflection is still very small.
Table 7.10 shows the stiffnesses of the ribs in this particular test.

Table 7.10: Rib stiffness value for each of the ribs in the 0 mesh slab with the load at a quarter of the span length.

Rib number	Stiffness [kN/mm]	Relative size to rib 3 [%]
1	5.7	68.4%
2	11.25	135.5%
3	8.33	100.0%
4	13.33	160.0%
5	1.6	19.2%

COMPARISON AND EVALUATION OF TEST RESULTS

The results from the tests at a quarter of the span length are shown above. The next step is to compare the results with each other. And find out what the effects are of adding or removing reinforcement meshes to the top slab of the composite plates. The main focus of this comparison will be on the distribution on both sides of the test specimens and on the stiffness behaviour that the ribs of the test specimen exhibit.
First of all, it has to be mentioned that the goal of keeping the test specimens in the linear elastic zone seems to have been reached. The distributions of all slabs remains nearly constant, except for the initial settling behaviour that is exhibited. During the tests no large cracking was observed or heard either. These are positive observations, because the effect of that this test will have had on the following test for each slab will have been minimal.
Next, the far side of the test specimens looks different. Because this side of the slab is farther away from the point of loading, the slab has a larger length over which to redistribute the load. It is expected that this length gives the top slabs of the test specimens the opportunity to divide the load according more equally. This distribution would depend on the stiffness of the top slabs. This would explain why the slab with two meshes distributes the load so equally over the central three ribs. On the other hand It seems that the top reinforcement mesh does not influence the distribution much, since the distribution of the slab with one mesh and the slab without mesh are practically identical at a load of 10 kN. It should also be noted that the changes in reinforcement mesh configuration seems to mainly affect load contribution of the central rib and to a lesser extend that of the ribs adjacent to the middle rib. The outer rib contributions are roughly the same for all of the mesh configurations at approximately 10%.
Now the distribution of load on the side close to the applied load will be evaluated. It should immediately noted that the slab with two reinforcement meshes has the highest load contribution in the middle rib. Both the slab without reinforcement mesh and the slab with one mesh have more equally distributed loads in the central three ribs. The outer ribs seem to be hardly affected again. All of the test specimens show that they bear an average of 5% of the load throughout the tests. Ribs 2 and 4 adjacent to the central rib are relatively equal in contribution as well, if the differences between the middle rib contribution are taken into account. All of the test specimens slow an average contribution of approximately 25% for both rib 2 and 4. Therefore, it seems that the contribution of the middle rib is effected the most by the reinforcement mesh configuration. The adjacent ribs to a lesser extend since the load transferred from the middle rib can then be divided over two ribs instead, making the relative change smaller.
Since the length from the load to the support on this side is so short, it was expected that the distribution would have been similar to what was found for the two mesh slab for all mesh configurations. The deviation of the slab without reinforcement could be explained by the stiffness behaviour of the central rib. When examining the deflection of the central rib compared to that of the ribs adjacent to it a striking observation can be made. The deflection of the central rib in the slab without reinforcement is 40% higher than that in the adjacent ribs, while in the other two slabs the deflection is only about 22%. It seems therefore that the central rib acts less stiffly in the slab without mesh, which would increase the contributions of the adjacent ribs.
The difference between the slab with two meshes and the one with only a single mesh, could perhaps also be explained by the stiffness of the ribs. The slope of the load-deflection diagram of rib 3 in the slab with two meshes is steeper. This means that the stiffness is also larger than that of the slab with one mesh. Rib three in the two mesh slab is 25% stiffer than that of the one mesh slab. Another observation that can be made is that the two mesh slab diagram is completely straight. While on the other hand the one mesh slab shows a bend in the curve at approximately 9 kN of rib loading. It is expected that at this short distance to the supports, the rib stiffness governs the distribution at first. The ribs can be thought of as translation springs. If the translation spring, on which the load is applied, is very stiff, then it will also absorb a large part of the load. The top slab which is draped over the springs as a membrane or beam does not get much chance to redistribute the load in that situation. But if slab rib starts to crack and weaken, as is suggested by the bend in the one mesh slab curve, then more load could be distributed to the neighbouring ribs.
The thought that the two mesh slab is still firmly in the linear elastic zone is confirmed by the fact all rib-deflection curves are still very much straight. Even the outer rib loads are still increasing. Although the outer ribs react with a stiffness that is much lower than that of the the middle three ribs. Their stiffness is only about 30% of that of the middle rib, despite rib 2 and 4 having a much smaller difference.
Finally the stiffness behaviour of the outer ribs in all test specimens should be discussed. Although the contribution to the load they provide is fairly consistent with what was expected, their stiffness behaviour is not. The outer ribs deflect far more than the middle ribs at the same load level. This is ubiquitous for all tests and indicates that the assumption that all ribs have an equal stiffness is probably wrong. With the exception of

the slab without mesh, both other test show that the central rib acts most stiff. Then ribs 2 and 4 act slightly weaker and ribs 1 and 5 act much weaker. Rib 3 is enclosed by 2 layers of ribs on both sides. Ribs 2 and 4 have 1 rib on each side of them. But ribs 1 and 5 have a free edge and this fact probably influences their load-deflection behaviour. This means that the ribs cannot be seen as separate translation springs, that are not influenced by their neighbours. This behaviour will be analysed again in the evaluation of the test results at half span length.
A final word about the predictions that were made in the previous section in the analytical model. Except for the slab without reinforcement, the predictions were not very accurate. The analytical model needs to be fine-tuned in order to model the composite slabs more accurately. This will be done in chapter 8.

7.4.3. EVALUATION LENGTH BETWEEN SUPPORT AND LOAD APPLICATION

Until now the tests at a quarter and at half of the span length have been examined separately. The distribution as a function of the load and reinforcement mesh configuration has been illustrated and explained. But the main goal of the test at a quarter of the span length was to confirm the effect of distance between the support and the point of load application. To that effect, this section will display the distribution in each slab at the lengths 1/4, 1/2 and 3/4 span length. For this the results of the load cells on both side of the test specimens in the test at a quarter of the length have been considered separately. After all, the length between the load and the supports RO1-RO5 was 75% of the span length and to the other side the length was 25% of the span length. The total amount of load per side of the slab was different, but only the distribution is compared so that does not matter in this case.
In this section two load levels will be used: 10 kN and 50 kN. 10 kN is chosen because this is the maximum load that all test specimens reached at all distances. It is also chosen to compare the 1 mesh and 2 mesh slabs at 50 kN, because at that stage they are still linear but the initial discrepancies have been evened out somewhat. The slab without mesh did not reach 50 kN in the non-destructive test and is thus not comparable at that load level. The results for 10 kN and 50 kN are shown in figures 7.77 and 7.77 respectively.

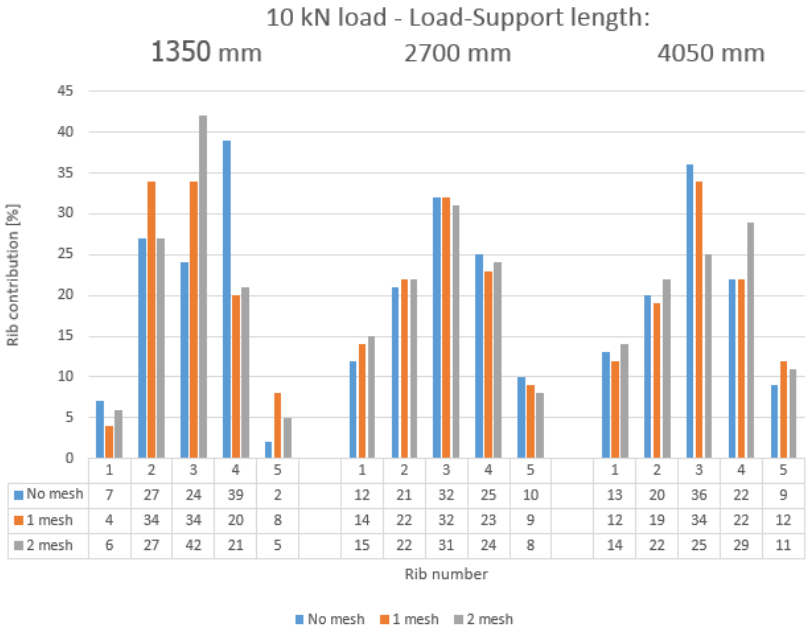

	1	2	3	4	5	1	2	3	4	5	1	2	3	4	5
No mesh	7	27	24	39	2	12	21	32	25	10	13	20	36	22	9
1 mesh	4	34	34	20	8	14	22	32	23	9	12	19	34	22	12
2 mesh	6	27	42	21	5	15	22	31	24	8	14	22	25	29	11

Figure 7.77: The centre deflection.

At a load of 10 kN the test specimens are still very much undamaged. Initial imperfections and discrepancies have been mostly evened out, but at 1/4 span length rib 2 and rib 4 of the 1 mesh slab and no mesh slab respectively are still behaving unexpectedly. Since the load is so small, it is really only possible to make observations about the initial distribution at different lengths to the support. At 2700 mm the distribution is equal for every mesh configuration. At 4050 mm one can see that the 1 mesh slab and no mesh slab already con-

centrate more of the force in rib 3. While at 1350 mm the 2 mesh slab has a more concentrated distribution. This trend suggests that top slab stiffness becomes more important for the distribution with increased length to the support. When the length becomes shorter, it would be expected that the 2 mesh slab distributes more because of its stiffer top slab. But instead it has a more concentrated loading pattern, suggesting that the rib stiffness becomes more dominant at shorter lengths to the support. The 1 mesh and no mesh slab show irregular distributions at this distance, therefore it is hard to state whether their distribution differs from the 2 mesh slab or not.

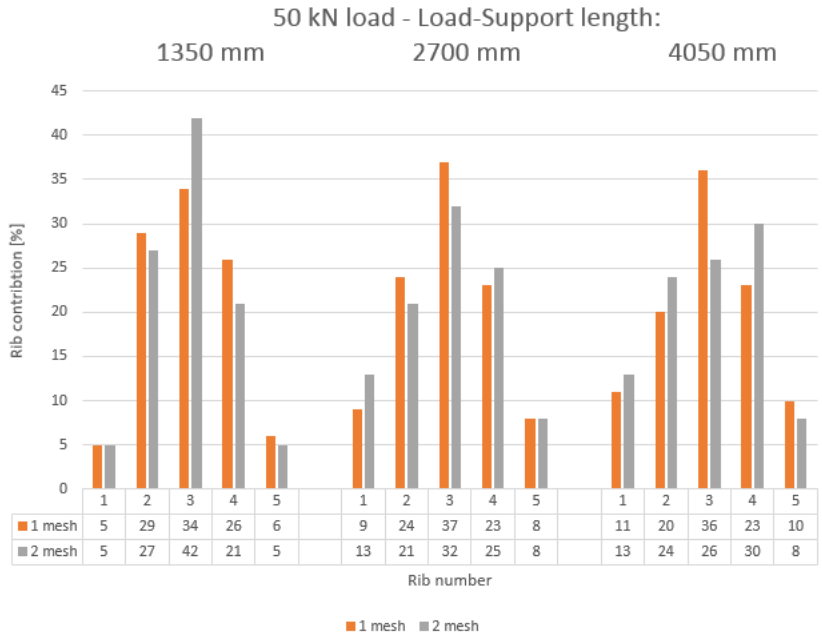

	1	2	3	4	5	1	2	3	4	5	1	2	3	4	5
1 mesh	5	29	34	26	6	9	24	37	23	8	11	20	36	23	10
2 mesh	5	27	42	21	5	13	21	32	25	8	13	24	26	30	8

Figure 7.78: The centre deflection.

At a load of 50 kN the slab without mesh can no longer be compared to the other specimens and is therefore left out. The distributions are more symmetrical in these graphs as opposed to the 10 kN load graphs. At 2700 mm the distributions of the 1 mesh and 2 mesh slabs are still quite similar. The load is slightly more concentrated in the 1 mesh slab. At 4050 mm the load is clearly more equally spread by the 2 mesh slab. The extra stiffness of the top slab is influencing the distribution there. At 1350 mm the results are more symmetrical now. It can be seen that the load is more concentrated in the 2 mesh slab.
This may be caused by two different reasons. Either the 1 mesh slab is able to mobilize a large part of the top slab to distribute the load towards the sides or it is possible that the addition of the extra reinforcement mesh made the ribs of the 2 mesh slab more stiff in bending. Stiffer ribs would cause more load to be borne by the middle rib because it is located directly under the load. It seems unlikely that the 1 mesh slab is able to mobilize a larger part of the top slab, after all it lacks the second reinforcement mesh, but it is also not clear whether the difference is caused by the ribs having a larger bending stiffness. When the longer distance of 4050 mm is considered the explanation seems more obvious. Over the longer length that is available to distribute the load, the 2 mesh slab is able to do so more strongly due to the second reinforcement mesh than the 1 mesh slab. That's why the load in 1 mesh slab is more concentrated in the 1 mesh slab.

7.4.4. EFFECTIVE WIDTH OF THE COMPOSITE SLABS

Another aspect that can be analysed which is more practical for using in practice is the distributive width as it was already discussed in chapter 5. The design of deep composite slabs is done per unit of width instead of per rib. It is therefore useful to be able to say something about how much of the slab is contributing towards bearing the load. In order to do this the distributions found in the laboratory experiments will be used. It has to be noted though that the conclusions drawn from these results will of course only apply to situations in practice with the same kind of steel profiled deck and similar span lengths. The data that will be used to

determine the is the distributions of the load in load cells RO6-RO10 for each test specimen, these are shown in figure 7.79.

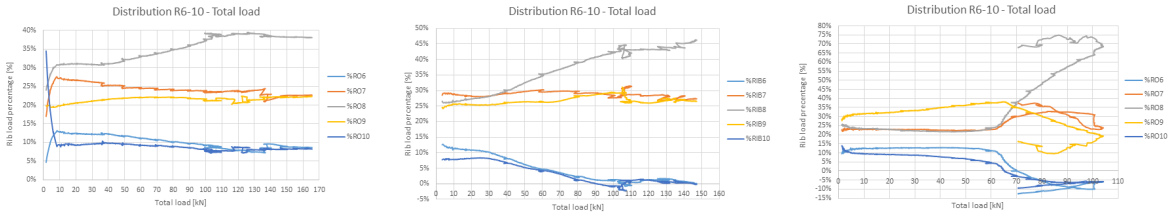

(a) Distribution of the load in load cells RO6-RO10 in the 2 mesh slab.

(b) Distribution of the load in load cells RO6-RO10 in the 1 mesh slab.

(c) Distribution of the load in load cells RO6-RO10 in the 0 mesh slab.

Figure 7.79: Distributions of the load in load cells RO6-RO10 in the test specimens.

From the distributions shown in the graphs it can be seen that in the 2 mesh slab all three ribs keep contributing towards bearing the load, while in the other slabs the outer ribs' contribution falls away after a certain point. Ribs 2, 3 and 4 are bearing some load in any situation. In table 7.11 the minimal effective widths for this type of deep composite slab that is taking part in the load bearing process are shown.

Table 7.11: The minimal effective width of the test specimens as derived from the distribution graphs.

Slab type	**Load interval [kN]**	**Distributive width [mm]**	**Load interval [kN]**	**Distributive width [mm]**
2 mesh slab	0 - 165	3000	-	-
1 mesh slab	0 - 100	3000	100 - 145	1800
0 mesh slab	0 - 65	3000	65 - 100	1800

It has to be noted that the effective width is increased or decreased with increments of 600 mm, which is the distance between the individual ribs. The outer ribs of the 1 mesh slab are still contributing a little towards carrying the load at the load of 100 kN, but the contribution at that stage is so low that it is safer to assume that they do not carry any load any more.

7.5. TEST CONCLUSION

In conclusion, the influence of the extra reinforcement compared to the 1 mesh slab is mostly felt in ribs 1,3, and 5. At higher loads the outer ribs keep bearing more forces because of the second reinforcement mesh. This means that the load is barely more concentrated at the start of the loading than in the ultimate limit state. The 1 mesh slab eventually losses the contribution of ribs 1 and 5 and this load is added to that of rib 3. For the test specimen without mesh this effect is felt even more strongly and more quickly. The load is even more concentrated than in the other two test specimens. The effect of the reinforcement meshes is also felt in the deflection behaviour. The 2 mesh slab is the most stiff and deflects much less than the 1 mesh slab. The slab without reinforcement mesh on the other hand deflects even less because it is too weak to pass beyond the shearing away of the steel deck from the concrete. The deflection is therefore not as large as the other slabs and the failure behaviour is brittle instead of plastic such as it was for the 1 mesh and 2 mesh slabs. The slab without mesh is only saved from complete collapse by the steel deck.
The complete composite behaviour of the composite slabs is only lost at a load of 105 kN independent of the mesh configuration. Even after the deck is sheared away, the embossments prevent excessive slip, retaining at least partial composite behaviour. The steel deck can be used to transfer load towards the side of the slabs. However, for the 2 mesh slabs the additional reinforcement mesh largely fulfils this task already and the slab without reinforcement mesh fails before the deck can start transferring load in a significant manner. Only in the 1 mesh slab the steel deck is fulfilling a large role in transferring of the load.
Now that these conclusions have been drawn, it is vital to analyse how well these results can be applied to real

life situations and whether the test results are deemed representative of this type of composite flooring or not. It will be reiterated that the composite slab without mesh is never used in practice. But both the other mesh configurations are applied. The 1 mesh slab is the default option when constructing this type of composite flooring and the second reinforcement mesh is added when high point loads are expected in the design. The reinforcement bars in the ribs can also be reasonably be applied in practice. The material qualities that were used in the experiments are also representative of the materials used in practice. The common concrete class C20/25 was used. The average strength of this class was indeed reached and the last test specimen was only slightly stronger than this average value. The steel deck was of a strength class S350 and the strength values found were exactly average for this strength class. The reinforcement was also close to its nominal strength values and therefore representative.
The boundary conditions on the other hand differed from the way in which this composite slab is implemented in practice. In practice the steel decks will either be placed on the bottom flange of a steel beam or on top of a steel beam in order to include them in a composite floor system or composite beam respectively. When the concrete is then cast, the composite deck slab and composite beam are joined together. This means that the composite slab is either fixed rigidly at the end or part of a continuous floor. The fact that the end of the composite slab is rigidly connected to the rest of the structure has two consequences. The steel deck will be cast in place, thus will experience a form of end anchorage. This will raise the load at which the steel deck shears away from the concrete due to horizontal shear forces. This will probably raise the ultimate limit load of the slab without mesh, because it relies on the steel deck for load transferring. But since this configuration is not used in practice it does not matter as much. The 1 mesh and 2 mesh both do not suffer as much from the shearing away of the steel deck as the slab without reinforcement mesh. They might behave more stiffly though. A second effect of the cast slab ends is that the ribs do not have as much rotation and translation freedom as they did in the experiment set-up. The ribs ends are essentially part of a concrete beam. This effective concrete beam ensures a more equal distribution by increasing the rotation stiffnesses of the ribs. Thus it is likely that the distribution of the load in practice will be more equally spread over the ribs than it was in the experiments. The different boundary conditions that are met in practice likely mean that the load becomes more equally spread. This is a positive conclusion, since it means that the experiments are a conservative situation and estimations of the maximum load contribution of the central rib is also conservative. This is only an assumption though and should be checked by using the tweaked and updated analytical model or by further research into the topic.
As for the analytical model, the test results are very useful regardless of which boundary conditions or material properties are used. Because all these factors can be changed or adjusted in the model. So in chapter 8 the analytical model will be adjusted in order to replicate the test results that were found in the experiments and in that way provide more accurate estimations of other design situations. This will increase the accuracy of the predictions that can be made. Because the initial predictions did not take into account several of the issues stated above that were found in the experiments.
In short, at a load of 10 kN the distribution with all reinforcement meshes is nearly equal, but the deflection already differs between them. At approximately 60 kN the removal of a reinforcement mesh causes about 5% of the load to go to the middle rib and the deflections are diverging even more at this point. At about 100 kN the slab without reinforcement mesh fails after shearing away from the steel deck and having about 75% of the load in the middle rib. The 1 and 2 mesh slabs fail at roughly 145 kN and 165 kN respectively. The addition of the extra mesh reduces the load percentage in the middle rib from 45% to 36% and the outer ribs are still active in the 2 mesh slab. But the effect of the extra mesh is felt very strongly in the deflection. The 1 mesh slab has almost 30% more deflection in the middle rib than the 2 mesh slab. The length from the load to the support does matter in the distribution. However at a load of 10 kN this difference is still very small. When the load reaches 50 kN the load is more concentrated in the 2 mesh slab than in the 1 mesh slab at a shorter distance, while at a longer distance the load is more concentrated in the 1 mesh slab instead.
Lastly the distribution results from the experiments can be used to determine how many ribs carry the concentrated load and this in turn can be used to determine an effective width of the composite slab. This information is useful in practice. The 2 mesh slab is effective over the full width of the slab until the ultimate load was reached. The 1 mesh slab's effective width was reduced from 3000 mm to 1800 mm at an approximate load of 100 kN and for the 0 mesh slab this already happened at a load of about 65 kN.

8

COMPARISON OF MODEL AND TEST RESULTS

This chapter will use the results from the laboratory experiments to compare the analytical model and the FEM model to the actual behaviour of the composite slabs. The analytical model was not very accurate yet in predicting the right behaviour. Therefore it will be fine-tuned with the help of the test results. Then the FEM model will be evaluated and compared against the test results in order to review the design assumptions that were made in the modelling process.

8.1. ANALYTICAL MODEL COMPARISON

The test results have been reported on in chapter 7. With these results it is now possible to adjust the analytical model in order to improve its accuracy and make it applicable to other design situations as well. To achieve this improvement, the analytical model will be used in order to recreate the results for all the slabs at both the non-destructive and the destructive test. It was found that the stiffness of the ribs is not equal for all ribs. The stiffness ratio of the top slab and the rib translation springs is also likely to differ. These and the other parameters used in the analytical model, that will be varied in order to reproduce the test results are shown in table 8.1.

Table 8.1: The parameters used to compute the section modulus of the uncracked top slab of the composite slab.

Parameters	Symbol	Unit
Translation spring stiffness	k_{rib}	$[N/mm]$
Distributive length	L_{dis}	$[mm]$
Rotation spring stiffness	$k_{rib,t}$	$[Nmm/rad]$
Positive top slab bending stiffness	$EI_{TS,+}$	$[N/mm^2]$
Negative top slab bending stiffness	$EI_{TS,-}$	$[N/mm^2]$
Uncracked top slab bending stiffness	$EI_{TS,uc}$	$[N/mm^2]$

In the previous chapter it was already stated that the stiffness of the ribs, as it was used in the analytical mode, is not equal for every rib. Because the location where the support reactions are measured and where the deflections are measured are not the same, there is a disconnect between the two data sets. The measured distribution by the load cells is a combination of the distribution occurring at the centre of the test specimen and the redistribution that happens while the load travels towards the supports. This redistribution is the results of a combination of the stiffnesses of the top slab and the ribs and the amount of damage they have both sustained. In the analytical model, on the other hand, the ribs are modelled as translation springs with a certain spring stiffness coefficient, see figure 8.1.
The spring stiffness is an important parameter in the model, which determines the distribution of the load together with the stiffness of the top slab. But in the analytical model the force in a rib is directly related to

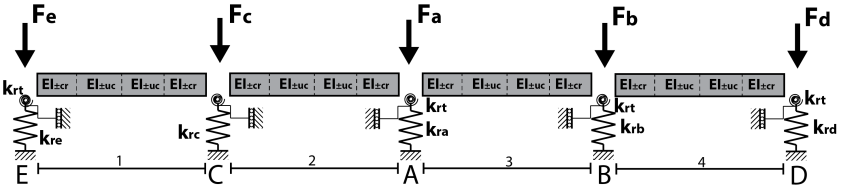

Figure 8.1: A schematic depiction of the analytical model used to model the composite slabs.

the deflection occurring in that rib. The relationship that governs this process is shown in equation 8.1.

$$F_{rib} = k_{rib} \times \delta_{rib} \tag{8.1}$$

In the elastic phase of the experiments the value of the translation springs can be easily determined. The load-deflection diagrams of the ribs show exactly the coefficient in the relation between the amount of load in the rib and the deflection of the rib. This coefficient is of course the slope of the diagram. However, then the ribs in the experiment reach a phase in which their load does not increase as quickly any more, but their deflection does. For each point that is considered in the analytical model the exact stiffness of that point has to be calculated. Both situations mentioned can be seen in 8.2.

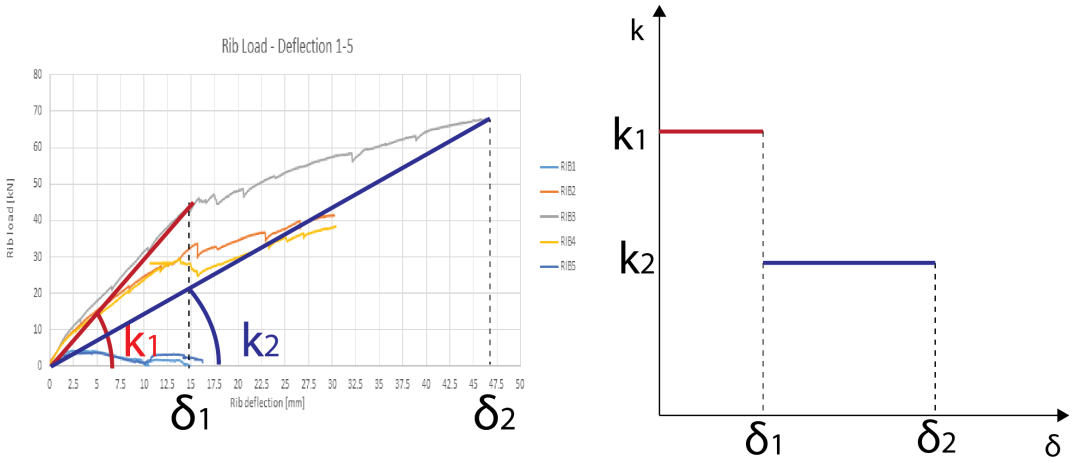

Figure 8.2: A figure showing the different values and relations with the rib stiffness.

Another situation arises whenever the load in a certain rib no longer increases but the deflection does. The slope of the diagram is now equal to zero, but the translation spring stiffness in the model is not. Because a translation spring stiffness of 0 kN/mm would mean that there is no load in the rib no matter the deflection. This is not the case. The load remains constant but the deflection increases, therefore the stiffness of the translation spring must decrease. Because the load in the ribs remains constant and the deflection increases, the rib stiffness has to decrease. This phenomenon is shown in the right hand side of figure 8.3. With the graphs described above, it is possible to introduce the plastic behaviour into the translation stiffness coefficient. It is not possible though to have a negative values for the translation stiffness coefficient. Because this means that the supports would pull the slab down in the analytical model. The test specimens were not attached to the supports and therefore this is not possible.

The rib torsion stiffness coefficient $k_{rib,t}$ was included in the model in order to simulate the ribs' resistance against rotations. Although this may be a factor with influence in practice, it is not likely to be so in the experiments. Because the ribs are not joined to a composite beam or floor system by casting the ends of the ribs in concrete, there is no structure at the end of the ribs which is resisting rotations. Therefore it is chosen to set the rib torsion resistance to 0 in the analytical model. Even if the ribs resist the rotation somewhat, this effect is likely to be insignificant compared with the bending resistances of the ribs and the top slab respectively. The distributive length L_{dis} was already calculated before in chapter 5, but the values obtained

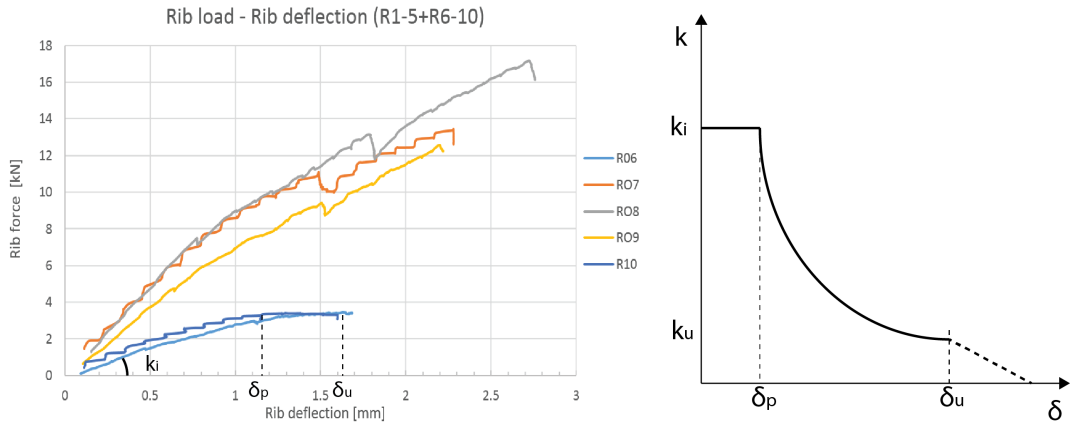

Figure 8.3: A figure showing the different values and relations with the rib stiffness when the rib does not increase in load any more.

there were mostly educated guesses. So the distributive length will be freely varied in this chapter in order to reproduce the distribution results and find out in what manner the distributive length is influenced. The resulting distributive length is a value that determines how much of the top slab is taking part in distribution of the load in the analytical model. Seeing in what way this parameter is influenced by the varying situations in the experiments might give more insight into the behaviour of the composite slabs.

The calculated bending stiffnesses for the to slab in all states will not be altered, unless the top slab reaches the calculated elastic bending moment capacity. It was already explained in chapter 5 that the bending moment stiffness of the top slab is lowered whenever it is past the elastic moment capacity to simulate the yielding of the reinforcement steel. Because in that situation it is impossible to increase the moment further until the reinforcement steel would reach the hardening phase. But for the reinforcement steel a bi-linear stress-strain diagram was assumed. Thus the bending stiffness of the top slab will be lowered in the situation where the top slab reaches the plastic phase. Although the results of the experiments have shown that the top flange of the steel deck is actively assisting in the distribution of the load towards the sides of the slab, the calculated bending stiffness values are not adjusted to compensate for this. The steel deck is became only really active in the later stage of the test on the 1 mesh slab. Before that point and in the other slabs the strain in the deck was still low and therefore it is assumed that its contribution to the bending stiffness is low. Even when the deck becomes active in the one mesh slab, the top slab is already severely damaged and thus the bending stiffness is unlikely to overtake the bending stiffness of the undamaged top slab.

The behaviour of the composite slabs is dependent on the load level. The initial distribution at approximately 10 kN is important from a design point of view. Because the maximum standard concentrated load according to the Eurocode 1 [10] is 10 kN. Thus the default configuration will have to be designed for such a load case regularly. The end of the elastic phase at 60 kN and the ultimate loads are loading values at which it is important to know more about the slab behaviour as well. It is thus chosen to reproduce the test results in these key points. For the non-destructive test only the initial load of 10 kN and the highest load of 50 kN will be examined. The complete list of loading points at which the composite slabs will be examined are stated below.

- Slab with 2 mesh
    1. 1/4L span: 10 kN
    2. 1/4L span: 50 kN
    3. 1/4L span: 10 kN
    4. 1/2L span: 60 kN
    5. 1/2L span: 165 kN
- Slab with 1 mesh

1. 1/4L span: 10 kN
2. 1/4L span: 50 kN
3. 1/2L span: 10 kN
4. 1/2L span: 60 kN
5. 1/2L span: 145 kN

- Slab without mesh

1. 1/4L span: 10 kN
2. 1/2L span: 10 kN
3. 1/2L span: 60 kN

The reproduction of the test results has been performed. The distributions found in the test specimens in the experiment have been approached as closely as possbile by making use of the analytical model. First the results of the non-destructive test were be replicated and then the same was be done for the destructive test. The exact data from this process is shown in appendix H and in this chapter only the conclusions that are drawn from that data will be shown. For each test and specimen the initial distribution will be given and then the reproduced distribution. The translation spring stiffness values that were used and the deflections of the all ribs respectively are also shown. For each of the slabs all phases and the corresponding distributions will be given. Then the changes in parameters that were done to achieve the adjustment will be explained. For each of the situations the resulting moment and deflection diagrams will also be given as a reference. The test results are not symmetrical most of the time. In order to eliminate some variations that occurred in the experiments, the symmetrical ribs will be averaged if they do not have the same value. An example of this process is shown in table 8.2.

Table 8.2: An example of averaging the distribution found in the experimental results to gain a symmetrical distribution.

Rib number	Actual distribution [%]	Average distribution [%]
1	15	11.5
2	22	23.0
3	31	31.0
4	24	23.0
5	8	11.5

8.1.1. EVALUATION OF DISTRIBUTIVE LENGTH AND RIB STIFFNESS

The distributions that are examined in this chapter have already been extensively discussed in the previous chapter and so they will not be commented upon again. The translation spring stiffness is obtained from the rib load-deflection diagrams as described in the previous section and the top slab bending stiffness was already calculated. The parameter that will be discussed in this section is the distributive length. This parameter determines the surface area of the top slab that is involved in distributing the concentrated force towards the sides. In order to reproduce the distributions found in the test results, different values for the distributive length were used. These used values will be discussed in this section. The analytical model was used to approach the distributions found in the test results but it was impossible to reproduce them perfectly. Therefore, along with the distributive length, the error between the two distributions will be given as well.
The error is determined in the following two ways. The distribution of the force on a side of the slab is given in percentages for both the test results and the analytical model reproduction. Then the average difference in contribution per rib will be given for a loading situation, according to equation 8.2. The average error is given in percentages.

$$\Delta Contribution_{avg} = \frac{\sum_{1}^{5}\left(\left|Contr_{test,i} - Contr_{analytical,i}\right|\right)}{5} \quad [\%] \tag{8.2}$$

The other measurement of error that is given, is the error between the deflection diagrams, $\Delta\delta_{avg}$, of the test result and the analytical model. The error is calculated according to equation 8.3 and is again presented as a percentage of the deflection found in the test results.

$$\Delta\delta_{avg} = \frac{\sum_{1}^{5}\left(\left|\delta_{test,i} - \delta_{analytical,i}\right|\right)}{\sum_{1}^{5}\left(\delta_{test,i}\right)} \times 100 \quad [\%] \tag{8.3}$$

The resulting distributive lengths and error values for the distribution and the deflection for all loading situations previously mentioned are shown in table 8.3.

Table 8.3: Distributive length and error values for all reproduces distributions with the analytical model.

Test type	Number of meshes	Applied load [kN]	Distributive length [mm]	Contribution error [%]	Deflection error [%]
Non-destructive	2	10	1800	0.68	30.0
		50	1300	1.52	2.6
	1	10	1900	1.52	2.6
		50	3000	0.98	5.3
	0	10	1700	0.68	10.7
Destructive	2	10	5400	0.08	13.6
		60	3100	0.50	3.5
		165	1100	0.26	4.1
	1	10	3000	1.90	7.4
		60	3000	0.82	4.1
		145	1100	0.52	6.2
	0	10	4000	0.94	11.9
		60	3000	1.88	5.3

From the table above some global observations can be made. First of all the distributive length is larger in the destructive test than in the non-destructive test. This was to be expected since the load is placed closer to one support than the other, it is likely that less of the composite slab will participate in load distribution. Secondly, the distributive length decreases if the load increases. This is also expected, since the slabs will get damaged more at higher loads and thus fewer parts of the slab can be mobilized in order to distribute the load. It is also clear that the variation between the slabs with regards to the distributive length is fairly large at the small load of 10 kN. This is the case especially at the destructive test. But at higher loads the lengths seem to be quite similar with the differences being only about 100 mm between the slabs. It thus seems that the distributive length is not influenced by the mesh configuration but definitely by the length from the point of load application to the support and also by the size of the applied load. These trends can be observed but in order to be more certain of the exact influence of those factors and of the exact size of the distributive length, more research into this topic is required. The exception can be seen at the non-destructive test of the 1 mesh slab. There the distributive length increases instead. The reason for this behaviour is unclear.

About the error in the contribution values fewer can be said. The error values vary wildly. Increasing the load does not seem to reduce the error reliably. Perhaps it can be concluded that the 2 mesh slab has a slightly lower error than the 1 mesh slab and the 0 mesh slab. This could be due to the fact that the 2 mesh slab has

a higher positive bending stiffness and retains this over the entire width of the top slab for a longer time. The model is longer in the elastic phase and that makes it easier to obtain the right distribution. About the deflection error it can be said with certainty that increasing the load decreases the deflection error. This makes sense since the absolute error in the deflection remains approximately the same, but the total deflection of the ribs increases dramatically. The only exception is the non-destructive test of slab 1, which does not follow the same pattern and is slightly higher.

And lastly some observations about the translation spring stiffness coefficient should be made. From the stiffnesses found in the test results and shown in appendix H one can see that the stiffnesses greatly vary over the test types, mesh configurations and load levels. Because the translation spring stiffness is defined as the coefficient between the reaction force at the end of a rib and the deflection at the length of the applied load it is influenced by various factors. The place where the load is applied is a major factor of influence, but the redistribution that occurs between the application of the load and the supports also influences it. This redistribution is in turn dependent on the stiffness of the ribs, the top slab and the ratio between the two. Also the size of the area of the composite slab that assists in redistribution matters and this size is reduced when the applied load is increased and the composite slab sustains more and more damage. It is also likely that whether a certain rib has other ribs on either side and how many of them will also influence its stiffness. All the factors mentioned above work together in determining the load-deflection behaviour of the ribs. If one wants to view each rib as a separate beam with a separate stiffness, then all these effects have to be included in that single stiffness factor. This results in the situation where the translation spring stiffness varies wildly over all specimens, load sizes and load locations. This would require more experimentation and research in order to determine exactly how the rib stiffness k_{rib} changes in all those situations so an accurate estimate can be done. And this would negate the initial advantages of the analytical model.
Lastly the effect of setting the rib torsion stiffness to zero should also be mentioned. When the torsion rib stiffness was not equal to zero, the moment diagram looked approximately as the example shown in figure 8.4. The moment would become negative farther away from the applied load in the centre. The top slab would behave similarly to separate clamped beams in between the ribs.

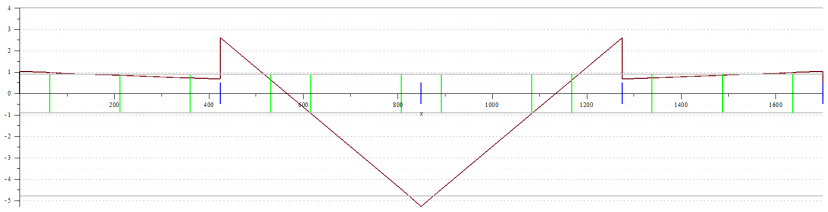

Figure 8.4: A figure showing a moment diagram of the analytical model with the rib torsion stiffness coefficient not equal to zero.

But when the rib torsion stiffness was set to zero, the moment diagram would look more like the example shown in figure 8.5. The entire top slab is now subjected to a positive bending moment. This can explain why the cracks that appeared in test specimens during the experiment, appeared on both sides of the ribs at the bottom of the top slab and not at the top. This type of moment diagram also results in the V-shaped deflection diagram that was observed in the experiments, where the rotation found in all ribs was approximately the same. Because the moment decreases towards the edges of the slab, the added deflection decreases as well and the shape of the deflection diagram begins to resemble a V-shape.

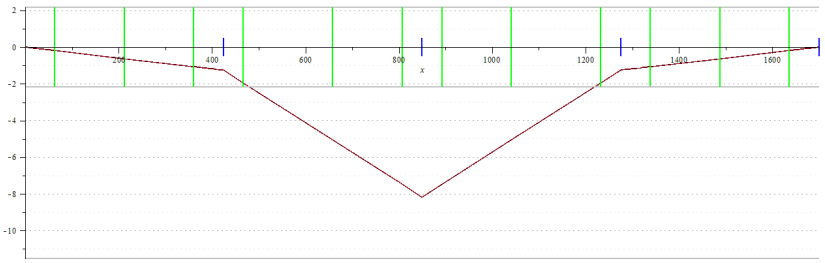

Figure 8.5: A figure showing a moment diagram of the analytical model with the rib torsion stiffness coefficient equal to zero.

8.2. FEM COMPARISON

In this section the finite element model will be compared to the results from the laboratory testing. From the model the support reactions and rib deflections were obtained. Therefore the distribution diagrams that were composed for the experiments can also be made from the FEM data. Also the rib force-deflection diagrams will be made in order to compare them. Furthermore the stresses and strains in all components of the model can be observed and thus critical cross-sections and interesting aspects will be shown as well. First of all the distribution and load-deflection diagrams will be compared. The strain progression in the concrete will be shown in appendix H and finally the stress and strain data of the steel deck components and the steel reinforcement bars will be shown in tables which are also given in the appendix.
For each specimen the load was applied as an enforced deformation. The applied load is then calculated from the sum of the support forces instead. This manner of load application allows the model to calculate more steps and even allowed the 2 mesh model to go beyond the peak load. But after that and for the 1 mesh and 0 mesh slab even before the peak convergence eventually cannot be reached any more.

8.2.1. 2 MESH SLAB

This model reaches an ultimate load of 104 kN and after that the load decreases somewhat until finally convergence cannot be reached any more. The largest deflection reached in the middle rib is 50 mm at the largest load. In figure 8.6 the distribution diagrams of the model and the experiment are shown. In figure 8.7 the rib load-deflection diagrams are shown of the model and the experiment.

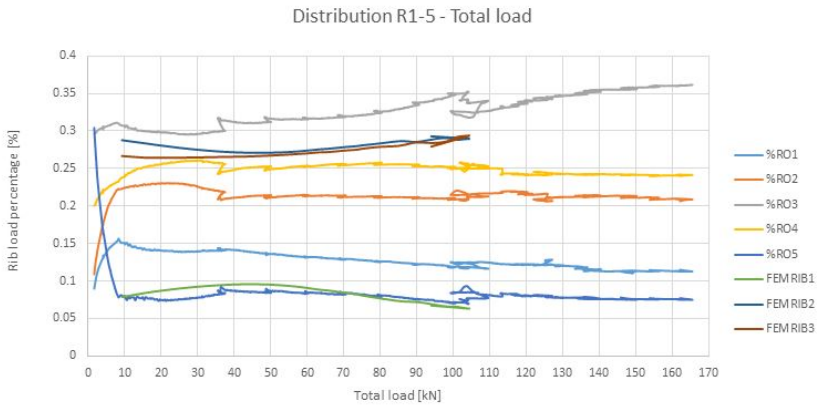

Figure 8.6: The distribution found in the experiment and in the FEM model.

When comparing the distributions of the model and the experiments it can immediately be seen that rib 2 and 3 have the same amount of contribution in the model. The outer rib has a contribution that is similar to what was found in the experiments but it is not as constant. The outer rib is already starting to decrease while in the experiments they were constant throughout the test.

In the rib load-deflection diagrams it can again be seen that rib 2 is reaction much in the same way as the middle rib. It can also be seen that the outer rib is already becoming very flat, while in the experiments this effect was not as strong.

8.2.2. 1 MESH SLAB

The 1 mesh slab reached a 84 kN load at which point the deflection in the middle rib was 37 mm. In figure 8.8 the distribution diagrams of the model and the experiment are shown. In figure 8.9 the rib load-deflection diagrams are shown of the model and the experiment.

Comparing the two distribution graphs it can be seen that the shapes are roughly similar. The outer ribs also drops off although it happens at a lower load and the outer ribs are already uplifted while this did not happen in the experiments. Rib 2 also follows rib 3 until it drops off at a load of 70 kN, while ribs 2 and 4 are more or

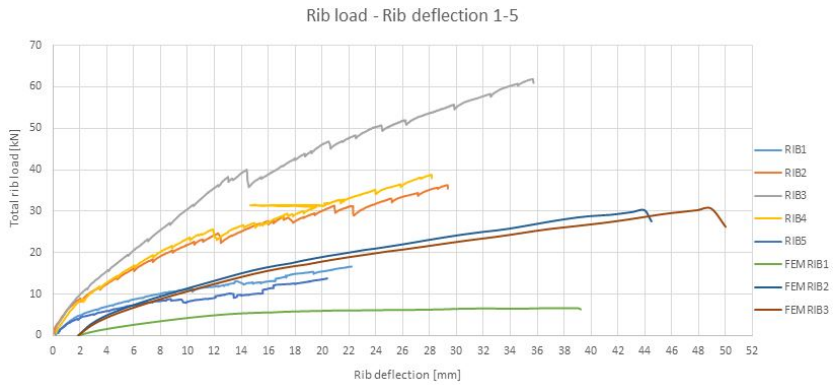

Figure 8.7: The rib load-deflection diagram found in the experiment and in the FEM model.

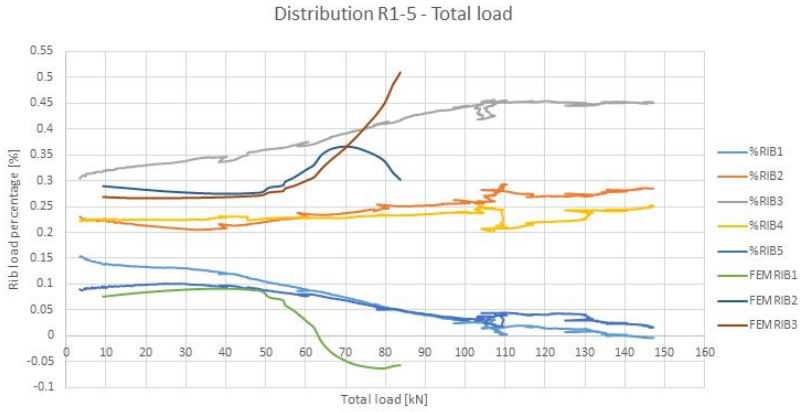

Figure 8.8: The distribution found in the experiment and in the FEM model.

less constant in the experiment. Rib 3 is also raising rapidly in the model than the experimental data.

When looking at the rib load-deflection diagrams of the 1 mesh slab one can see that in the model the middle rib again seems to react less stiff until a certain load and after that the curve becomes more steep. This is in direct contrast to what was observed in the experiment. The deflections observed in the model are also much larger then seen in the experiments. The deflection of all ribs in the model is also much more equal than was found in the experiments where the outer ribs reached a much lower deflection.

8.2.3. 0 MESH SLAB

The 1 mesh slab reached a 71 kN load at which point the deflection in the middle rib was 25 mm. In figure 8.10 the distribution diagrams of the model and the experiment are shown. In figure 8.11 the rib load-deflection diagrams are shown of the model and the experiment.

The model again shows a distribution diagram that is roughly similar to the experiment. The contribution of the outer ribs drops off rather abruptly and is uplifted as well. This happens at a slightly lower load in the model though. Rib 3 is also going up but much faster than the experimental data. Rib 3 already reaches 60% at a load of 70 kN while in the experiment the contribution was only 50% at that point. Until a load of 60 kN rib 2 and 3 are equal in contribution in the model, while this is not the case again in the experimental data.

Looking at the rib load-deflection diagrams one can see that the outer rib in the model is uplifted severely. Rib 2 and 3 are behaving exactly the same until a load of 60 kN. The occurring deflection in the model is very different from what was found in the experiments. All ribs in the model have a roughly equal deflection and rib 3 even reaches a deflection of 30 mm at a load of 70 mm while the experimental results show that rib 3

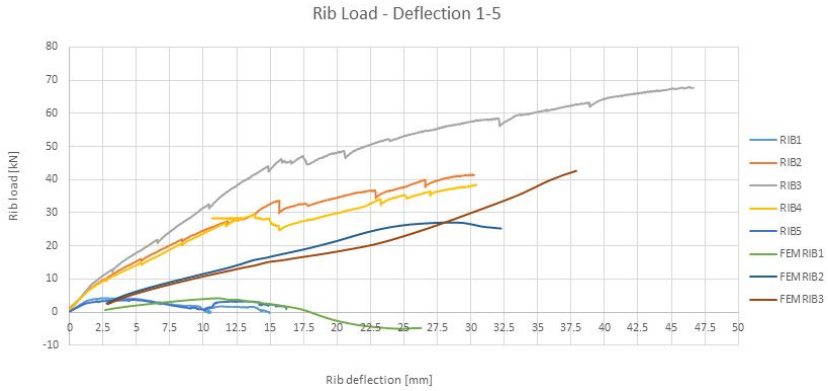

Figure 8.9: The rib load-deflection diagram found in the experiment and in the FEM model.

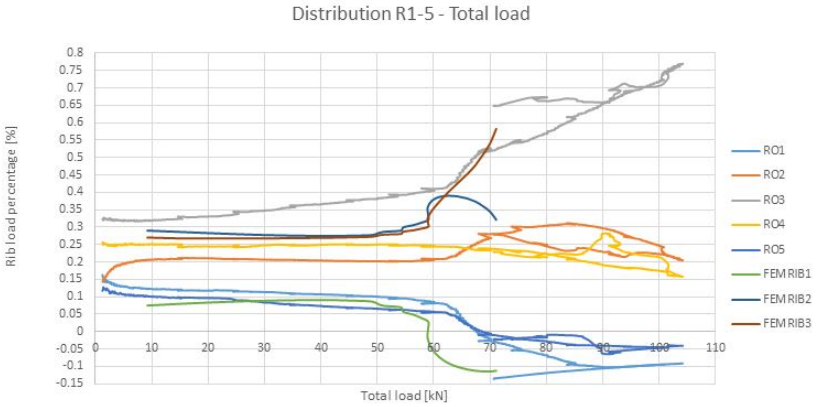

Figure 8.10: The distribution found in the experiment and in the FEM model.

only reached a total deflection of 18 mm at a load of 100 kN.

8.2.4. FEM COMPARISON EVALUATION

From the comparison in the previous section it appears that the deflection of the ribs in the finite element model very large when compared to the experimental data. At a load of 100 kN the 2 mesh slab already deflects 50 mm in rib 3, while this deflection was never reached in the experiments. The 1 mesh and 0 mesh slabs both reach a deflection of about 30 mm. While in the experiments the deflection of the 1 mesh slab at the same load only reached about 10 mm and the same occurs in the 0 mesh slab.

Apart from the size of the deflection, another aspect that is striking is that in the finite element model all ribs have a similar deflection. While in the experiments it was observed that the all non-symmetrical ribs had distinctly different deflection. This happened because the transferring of the load towards the outer ribs was at a certain point no longer possible and thus the load did not increase much any more. The ribs were still dragged down by the deformation of the composite slab. This also seems to happen in the finite element model, because the deflection still increases in all ribs even when the load measured at the supports starts to fall. This effect is especially strong in the outer ribs where the contribution eventually becomes negative, but still the deflection increases. This suggests that the dragging down of the ribs is much stronger in the finite element model. Even when the concrete is heavily cracked in the final stages of calculation this dragging down still does not stop.

The distribution of all modelled slabs also differs from what was found in the experiments. The shapes of the distribution diagrams of the models roughly coincide with those found in the experiments. But The values differ by large margins. In each of the slabs of the finite element model ribs 2 and 3 had an identical contribution up until a certain point was reached were they started to diverge. In the the 2 mesh slab this never occurred though. But in the 2 mesh slab rib 2 had a contribution of almost 5% too high and rib 3 had a contribution of 5% to low, when compared with the experiments. The outer rib was also not as constant

Figure 8.11: The rib load-deflection diagram found in the experiment and in the FEM model.

in contribution and too low in value as found in the experiments. For the 1 mesh and 0 mesh slabs a similar distribution is found. But at a load of around 70 kN the outer rib drops off to negative values, more so for the 0 mesh slab. And rib 3 starts to rise rapidly, much more rapidly than in the experiments.
And lastly it is observed that in the load deflection diagram of the 1 mesh slab rib 3 initially acts less stiffly that rib 2 and then at a load of roughly 70 kN starts to overtake rib 2 again. This is not at all what was observed in the experiment. And in the 0 mesh slab the deflection of rib 2 exceeds that of rib 3. The deflection pattern is the same as those found in the other models but the order is reversed.
A possible cause for this differing behaviour of the finite element model is the fact that the effective area of the steel profiled deck was used in the model, as opposed to the entire steel deck area. While in the experiments it was observed that the top flange of the steel deck was active in the transverse direction at certain loads. But these parts were not modelled. Also not the entire trough area of the steel ribs was modelled. The parts of the steel deck that are not modelled are likely to have an influence on the final results.
Another aspect that was not modelled is the bonding capacity between the steel deck and the concrete. In the experiments the bonding capacity was reached at around 105 kN in all specimens. Although is load was not reached in any of the modelling calculations, but if one was to model the composite slabs at higher loads this factor would certainly become important.
The material strength properties could also have made a difference. The concrete tensile strength for instance was taken as 2.8 N/mm^2 but in reality this could have been higher.
With the results above it is clear that the finite element model used does not the composite slabs accurately enough to be practical. Ribs 2 and 3 react too similar in the model and the outer rib reacts too weakly. The deflection that is found in the model is also a lot larger than the deflection values found in the experiments. And until the model is improved by adding the aspects mentioned above it does not provide an accurate validation method. The shape of the diagrams is similar. Therefore it might be possible to improve the model by performing parameter studies and by checking the assumptions and composition of the model.

8.3. CONCLUSION

Now that both the analytical and the FEM model have been compared to the test results, some conclusions can be drawn on the results. First of all it can be said that the analytical model, as it was proposed in chapter 5, was not very accurate yet. In order to improve the accuracy, it was compared with the results from the laboratory experiments. In this way it was attempted to find more accurate values for the rib stiffness and the distributive length. It was chosen to eliminate the rib rotation stiffness, because its effect in the experimental values is likely extremely low. This immediately resulted in a drastic change in the shape of the moment diagram. The entire top slab was subjected to a positive bending moment instead of a bending moment that switched signs at every rib. At the same time this also results in the V-shaped deflection as it was observed in the laboratory experiments.
It was found that the analytical model was able to duplicate the results found in the experiments quite well. But in order to do this it was necessary to extract the rib stiffness values from the test results. While doing this it was found that the rib stiffness value depends on many factors and varies greatly in different situations. The initial idea that the ribs each have their own independent stiffness value is thus not right. The same can

be said about the distributive length of the analytical model. This value depends on the loading level and the load location. For both parameters extra research and experience is necessary in order to predict their size and do accurate estimations with the analytical model. This undermines the initial goal of the analytical model, which was to give the designer a tool where the material properties of the composite slab could be easily used to do accurate estimations of the slab's behaviour.
The last major parameter of the analytical model is the stiffness of the top slab. This parameter can be calculated and the effect of the reinforcement meshes can be easily incorporated. But the contribution of the top slab depends on the distributive length. However, the effect of the steel deck of the composite slab on the stiffness of the top slab is not clear yet. In the 1 mesh slab, the deck was yielding indicating that it was actively spreading the load. But in the other slabs this never happened. Thus it is clear that the deck does contribute to the stiffness and strength of the top slab, but not how much.
All the items mentioned above mean that the analytical model does not quite fulfil its goal. The model is easy to use, but the physical behaviour of the composite slabs is different from the beam-spring model behaviour. This results in the parameters translation spring stiffness and distributive length encompassing more than one physical effect. In order to estimate these parameters, more detailed knowledge is necessary about the behaviour of precise configurations. And this means that other design situations cannot be easily put into the model. So accuracy and ease of applicability cannot be obtained without further experimentation or adaptations to the model. Additional analysis or experimentation could help further determine the size of the translation spring stiffness and the distributive length in an accurate manner. Or it could be chosen instead to chose a different modelling for the ribs. Perhaps in such a way that the deflection over the entire width is determined and the interaction with the neighbouring ribs is also included.
The finite element model also does not fulfil its purpose as a validation method very well. When compared to the data found in the experiments the results of the finite elements models were not very accurate. The deflection that was found was too large, the difference between the deflections of the ribs were not large enough, the contribution sizes of all the ribs were not the same as found in the experiments and the rib load-deflection diagrams have shapes roughly similar in shape to what was found in the experiments but the values still differ.

9

CONCLUSIONS

9.1. CONCLUSION ON THESIS RESULTS

The goal of this thesis was to investigate the horizontal distribution of the stresses caused to the application of a concentrated load in ComFlor210 deep composite steel-concrete slabs. A part of this investigation into the composite slab's behaviour was to find out what influence the number of reinforcement meshes in the top part is. In practice the ComFlor210 is constructed with one reinforcement mesh by default and if large concentrated loads are expected a second mesh is added. In order to investigate the horizontal distribution behaviour an analytical model was constructed and this model was supplemented by finite element calculations and experiments on life-sized test specimens in the Stevin II laboratory of the Technical University in Delft.
Before the conclusions on the analytical model are drawn, some observations have to be made first about the laboratory experiments that were used to fine-tune the analytical model.

- In the test set-up that was used during the experiments the ribs were each simply supported and had complete rotational freedom. This situation differs from the situation in practice where the ribs are often rigidly supported. This also means that the steel deck receives no benefit from being anchored in concrete at both ends. This difference makes the test results conservative, since the lack of rib rotation resistance and end anchorage cause the load to be more concentrated in the middle rib and quicker loss of composite behaviour between the concrete and steel deck respectively. These different boundary conditions make no difference for the fine-tuning process of the analytical model because the boundary conditions can be changed at will there. But when comparing the test results to a situation in practice, these differences need to be kept in mind.

- The influence of adding or removing a reinforcement mesh can be observed in a number of ways. Both for the distribution of the load on per rib and the deflection measured the divergence caused by the varying mesh configuration depended strongly on the size of the applied load.
  At a load of 10 kN the distribution of the load over the ribs is still almost identical for every mesh configuration. But from that point on the distributions start to diverge. At a load of 60 kN the load contribution of the middle rib increases with approximately 5% of the total load for each reinforcement mesh that is removed. It this load it can also be seen already that the outermost ribs decrease the amount of load they are bearing. The ultimate load that could be applied to each composite slab also varied. At approximately 105 kN all slabs lost the chemical bond between the steel deck and the concrete. The slab without reinforcement mesh failed when this bond was lost. At that point the middle rib was carrying roughly 75% of the total load. The slab with one reinforcement mesh was able to continue to a load of 145 kN. At that time the middle rib was carrying 45% of the total load. The distribution of the slab with two reinforcement meshes hardly changed during the experiment and at the ultimate load of 165 kN the middle rib was still only carrying 36% of the total load. The outermost ribs in the two mesh slab were still carrying a significant part of the load, while in the one mesh slab they were not carrying at all and in the slab without mesh the outer ribs had even begun to be uplifted from the supports due to deformation of the slab. The contributions of the ribs right next to the middle rib remained almost constant during the entire test for all mesh configurations. For the two mesh slab it did not change at

all and for the one mesh slab and the slab without mesh they slightly rose and fell respectively.
With regards to the deflection a clear difference could be seen as well. Already at a load of 10 kN a small divergence in deflection between the mesh configurations could be seen. At a load of 60 kN the maximum difference was roughly 15%. At the ultimate load the one mesh slab had a deflection approximately 30% higher, at 46 mm, in the middle rib than the two mesh slab. The slab without reinforcement meshes only reached about 20 mm of deflection since it did not reach as high an ultimate load as the other two slabs.

- The distance from the point of load application to the support also matters for the horizontal distribution of the load. At the shorter distance of 25% of the span length the 2 mesh slab has a more concentrated load at more than 40% of the total load when compared to the near 35% of the total load in the 1 mesh slab. But when the distance is increased the ability to distribute the forces more of the 2 mesh slab becomes clear because at 75% of the span length the 2 mesh slab bears only slightly more than 25% of the total load in the middle rib while the this has increased to more than 35% in the 1 mesh slab.

The following remarks can be made about the two dimensional analytical model that was created in order to model the behaviour of the composite slab. With help of results from the laboratory experiments the analytical model was fine-tuned in order to reproduce the results that were found in the experiments. By doing this it was hoped to obtain more information about the size of the model parameters and in what manner these parameters are influenced by the boundary conditions, the mesh configuration and the location of the load.

- The goal of the analytical model was to create an easily usable tool that is based on mechanical behaviour of the composite slab so it could be changed to suit different design situations. In order to achieve this the model was made to be two dimensional, modelling only a strip of the slab over the entire width. The three dimensional effects of the slab configuration were included into the model parameters such as the translation spring stiffness, the rib rotation resistance and the bending stiffness of the top slab and the distributive length. This goal was indeed reached. The model simulated the behaviour of the composite slab by assuming the ribs as translation springs and the top part of the cross-section as a continuous beam spanning the width of the model. The model had only a few parameters which are based on the assumed mechanical behaviour of the composite slab. The model was also made to be two dimensional instead of three dimensional in order to keep the complexity as low as possible.

- The parameters that are used in the model to determine the distribution of the concentrated load over the width of the slab are the bending stiffness of the ribs, the rib span length, the bending stiffness of the top slab, the rib rotation stiffness, the centre-to-centre length between ribs and the distributive length. All of these factors were calculated based on the dimensions of the composite slab. Of these parameters ribs span length and bending stiffness which were combined into a single translation stiffness coefficient, which relates the force acting on that rib and the deflection at the point of loading. The rib translation spring stiffness had the largest impact on the distribution of all parameters. However, when the model results were compared to the laboratory experiments it appeared that the assumptions that were made about the translation stiffness of the ribs and the distributive length were not correct. In the model it was assumed that the ribs were each acting as separate composite beams that are spanning the length of the slab with the top slab spanning the simulated beams over the width. But during the experiments it was found that the rib translation coefficient was acting differently from what was expected. The distributive length was also different in size from what was calculated beforehand and this value differed far more when the boundary conditions were changed than was expected during the initial calculations.

- A problem with the concept of the ribs acting as separate beams was discovered while analysing the experiment results. Because it was chosen to evaluate the distribution of the concentrated load with the support reactions at the end of the ribs and the deflection of the ribs at the location of the load. These two variable were linked by the translation spring stiffness in the model. Because the ribs were considered as separate in the model, this parameter only included one physical effect: the bending stiffness of the ribs which was variable over the size of the applied load. This assumed that the distribution happened completely at the location of load application. However, by examining the deflection and load results the conclusion was reached that the load is also being continuously distributed along

the width when travelling from the load application point towards the supports. This distribution happens through the combination of the stiffness of the ribs, the top slab and the damage state they both are in at that specific load level. Thus the translation stiffness coefficient in the analytical model embodies more than one physical effect: the bending stiffness of the ribs which is affected by damage and the distribution over the length between the supports and the load by the top slab and the manner in which this is affected by damage in the top slab. This means that the parameter in the analytical model that represents these processes becomes increasingly difficult to estimate and it is influenced by more factors than was thought before. Not only is it influenced by the components of the ribs but also the components of the top slab and the level of the load. Because of the increased complexity of the translation rib stiffness further analysis of this parameter and possibly extra research and experiments are required in order to estimate the translation stiffness correctly. Unfortunately this means that the analytical model is in the current state is not able to give accurate predictions of the horizontal distribution of the load in the composite slab except for the situations that were simulated in the laboratory experiments.

- It is possible to increase the accuracy of the analytical model by analysing the translation spring coefficient and the distributive length further and possibly perform more experimentation to determine its size under various boundary and loading conditions. However, this would defeat the purpose of an easily applicable and general analytical model. Thus a more appropriate solution would be to find a way to model the deflection of the ribs in a different manner so that the interaction with the neighbouring ribs can also be included. This would make it easier to estimate the value of the model parameters without the need for additional laboratory experimentation.

The finite element model was meant to serve as a validation method for the analytical model. But after comparing the behaviour of the models to the results found in the laboratory experiments the following remarks can be made.

- Instead of the full steel profiled deck with all the horizontal and longitudinal embossments, a reduced steel profile was used in the model. This reduced area is the area of the steel deck that is effective when a bending moment is acting on the steel deck. This did reduce the number of elements that had to be modelled but it did mean that the influence of the steel that is not modelled is neglected.

- In order to reduce the calculation time of the model, the model was reduced to a quarter of the entire composite slab. This could be done because the composite slab is symmetrical along the longitudinal and transverse central lines. The result of this decision is that the number of elements was reduced to a quarter of the original, but it also means that only the load case where the load is applied at the centre of the span length is the only load case that can be modelled. The load case where the load is applied at a quarter of the span length could not be modelled any more.

- The results of the finite element model calculations and the data found in the laboratory experiments differed quite a lot, but the overall shape is similar. In the model the contributions of rib 2 and 3 are almost identical until a certain loading. The middle rib and the outer rib act too weakly and the rib in between acts to stiffly. Another point in which the results differ is the deflection. The deflection found in the model is three times as high as that found in the experiments. The deflections in all ribs were also nearly equal while in the experiments they differed much more. Because of the lack of accuracy in the points mentioned here the finite element model cannot be used as a validation method for the analytical model or as a tool to analyse the behaviour of the test specimens in the experiments. But it might be possible to improve the model to become more accurate and usable in practice.

- A possible cause of these difference mentioned above is the use of the effective area of the steel deck instead of the full area. And perhaps the behaviour of the concrete was not entirely as planned either, because even when it was heavily cracked the outer ribs were still dragged down, increasing in deflection but not in loading found at the supports.

Finally a conclusion that could be drawn that is of use for designers in practice concerns the effective width of the composite slab type that was researched in this thesis. The effective width length over which a concentrated load can be spread in order to calculated the resistance needed to bear the load is indeed influenced by the number of meshes that are added to the composite slab. With two reinforcement meshes the concentrated load can be spread out over all five ribs. If there is only one mesh or no mesh at all the load eventually

concentrates to only the middle three ribs and the outer two ribs stop contributing.

9.2. SUGGESTIONS FOR FURTHER RESEARCH

From the data and results that were acquired during the course of this thesis several areas and subjects were encountered in which more investigation or research is still required. They are split up in the following categories: analytical model, finite element model, laboratory experiments and subjects that lie outside the scope of this thesis but nevertheless deserve to be researched.

Topics related to the analytical model are the following.

- With regards to the analytical model there are several improvements that could be made. First of all the model assumed that all supports where at an equal height. Because the ribs were individually supported during the experiments this might not have been the case. Looking further into the influence that a varying height in the supports has may provide additional insights into the behaviour of the composite slab. Although due to the way in which this floor type is installed in practice, the influence it has should be relatively low.
- Another aspect that was not taken into account is the stiffness of the supports. All supports where assumed to have an equal and infinite stiffness. This might not be true especially in practice, since the decks are often placed on the bottom flange of steel profile beams. Some ribs might therefore experience a different support stiffness than others. The influence this has on the distribution was not taken into account in the analytical model and should be looked into.

With regards to the finite element model the following topics should be addressed.

- The finite element model uses only the area of the steel profiled deck that is considered effective in bending. While this assumed area makes the analytical analysis easier to perform, it is not conforming to reality and may decrease the accuracy of the model. It would therefore be informative to run FEM simulations with a model that contains the complete steel profiled deck. It would be even better if all of the embossments are also included into the model.
- Another aspect which could be improved was the fact that the model contained only a quarter of the entire slab and was cut down along the axis of symmetry. This does reduce the calculation time and the number of elements but it meant that only the load in the centre of the span could be modelled. Modelling the entire slab would make it possible to place the load anywhere on the slab to study its effects.
- The material properties of the model could also be improved. The assumed strength of the concrete compressive and tensile strength might have been underestimated. And the effective cross-section of the steel deck that was assumed to be active in the composite slab might be larger than was modelled.
- In order to better understand the influence of the model parameters, it is also advised to perform a parameter study.
- Lastly it is also suggested to also model only a single rib. This model could provide more information about the effective cross-section of the steel deck and if this model is validated through testing then it can be expanded to include multiple ribs.

In relation to the laboratory there are the following subjects that are deserving of extra research.

- First of all the influence of the steel profiled deck on the distribution of the load is still not clear yet. It was checked during the laboratory experiments whether or not the steel deck was active in the transverse direction while the load was being distributed towards the sides. This appeared to be the case, although the stress in the deck was different in the various test specimens. But the exact size of the contribution of the steel deck is not yet known. In the 1 mesh slab the steel stress in the transverse direction even passed far beyond the yield stress of the steel. This indicates that the steel's contribution is

quite significant and since the 1 mesh deck is the default configuration when the composite deck type considered in this thesis is constructed, learning more on this subject is advisable.

- After the bond between the concrete and the steel deck was lost part of the composite action in the slab was lost. Yet the slip at both ends of the middle rib increased only very little. This was likely due to the mechanical interlocking of the concrete and the embossments in the steel deck. Excessive slip was likely prevented because of the embossments but the slip still increased slowly. The maximum load at which the mechanical interlock would fail is not known however and also whether the embossments would fail in a brittle or a ductile manner was not observed during the experiments since they were not the critical component.
- Another aspect of the behaviour of the composite slab that could not be observed was the crack propagation in on the bottom side of the concrete. This was because there the steel deck was obstructing the view and it was impossible to remove the steel deck after the experiments were done. Thus in what manner the concrete was cracked between the deck and the concrete is not known and should be looked into.
- The non-destructive tests at a quarter of the span length already provided much information about the distribution and the influence of the length from the support to the point of load application. However the test specimens were only loaded until a relatively low load size, especially the slab without reinforcement mesh because it was faired that the influence of this test on the destructive test would otherwise become too large. Thus the distribution behaviour of the slabs at higher load levels is not known. It might provide new information if destructive tests were performed with the load applied at various different lengths from the support in order to gain more insight into the precise influence this factor has on the horizontal distribution.

Then there are subjects which were not part of this thesis but are not yet known completely.

- The horizontal and vertical shear capacities of the composite deck are another area in which more knowledge is required. Both of these subjects fell outside the scope of this thesis, but both the horizontal and vertical shear play an important role in the behaviour of the composite slab. During the experiments the load was placed in the centre and thus the vertical shear capacity was not critical, but whenever load is placed closer to the support it does become critical. The contribution of the steel deck towards bearing this vertical shear load is at the moment not known. It other research that was done on this subject indicating that just using the capacity of the concrete is an underestimation was already mentioned in chapter 3. But the exact contribution of the steel deck is not yet done. The horizontal shear capacity of the steel deck did play a role during the laboratory experiments. The shearing away of the steel deck from the concrete was observed in all test specimens at approximately the same load level. But the exact stress at which the chemical bond between the concrete and the steel fails is not known and thus the vertical shear capacity of this type of composite floor.

A

FIGURE SOURCES

Figures not mentioned in this list were made for the purpose of this thesis.

Figure 1.2: from website: http://tanya1.myblog.arts.ac.uk/2013/04/29/task-8-ludwig-mies-van-der-rohe-alumni-hall/
Figure 1.3: from Abspoel [16]
Figure 1.4: from website: http://www.steelconstruction.info/Composite_construction
Figure 1.5: from website: http://www.steelconstruction.info/Composite_construction
Figure 1.6: from Shobaki [3]
Figure 1.7: from Shobaki [3]
Figure 1.9: from website: http://www.dutchengineering.nl/
Figure 3.2: from NEN6725 [11]

B

THESIS COMMITTEE COMPOSITION

B.1. THESIS COMMITTEE

Prof. ir. F.S.K. Bijlaard
Supervisor

Position:	Professor of Steel Structures
University:	Delft University of Technology
Faculty:	Civil Engineering and Geosciences
Department:	Structural Engineering
Address:	Room 2.53 Stevin II
	Stevinweg 1
	2628 CN Delft
	the Netherlands
Phone number:	T +31 (0)15 2784581
E-mail:	F.S.K.Bijlaard@tudelft.nl

ir. R. Abspoel
Specialist composite structures

Position:	Staff of the Structural Engineering department
University:	Delft University of Technology
Faculty:	Civil Engineering and Geosciences
Department:	Structural Engineering
Address:	Room 2.54 Stevin II
	Stevinweg 1
	2628 CN Delft
	the Netherlands
Phone number:	T +31 (0)15 27853581
E-mail:	R.Abspoel@tudelft.nl

Dr. ir. M.A.N. Hendriks
Specialist finite element modelling

Position:	Assistant professor computational modelling of structures
University:	Delft University of Technology
Faculty:	Civil Engineering and Geosciences
Department:	Structural Mechanics
Address:	Room 6.70 Stevinweg 1 2628 CN Delft the Netherlands
Phone number:	T +31 (0)15 2786988
E-mail:	M.A.N.Hendriks@tudelft.nl

Em. Prof. ir. J.W.B. Stark
Company director, specialist composite structures

Position:	Emeritus Professor Steel Structures
University:	Delft University of Technology
Faculty:	Civil Engineering and Geosciences
Department:	Structural Engineering
Address:	Room 6.70 Stevinweg 1 2628 CN Delft the Netherlands
Phone number:	T - M -
E-mail:	janstark@planet.nl

ir. H. Prins
Company director, Designer and distributor of composite floor systems

Position:	Company director
Company:	Dutch Engineering raadgevend ingenieurs B.V.
Address:	Energieweg 46 2382 NL Zoeterwoude the Netherlands
Phone number:	T +31 (0)71 5418923
E-mail:	Henk.Prins@dutchengineering.nl

B.2. CANDIDATE

M.S. Dracht
Structural Engineering Student

Specialization:	Company director
University:	Delft University of Technology
Faculty:	Civil Engineering and Geosciences
Address:	Korvezeestraat 379 2628 DS Delft the Netherlands
Phone number:	M +31 (0)6 34784433
E-mail:	M.S.Dracht@student.tudelft.nl

C

EXPANDING THE TWO-DIMENSIONAL MODELS

This appendix will provide further explanations and more detailed computation on the manner in which the two-dimensional models were expanded with more ribs

C.1. MODEL TYPE 1

Model type 1 was established for a slab supported by three ribs. But by using the same methods as done when first setting up this model, it can be expanded into one that encompasses more ribs. The equations that are used to produce a model of five ribs connected by intermediate slabs are shown in the equations below. All of the ribs can be loaded by a concentrated force. The schematic representation of what is modelled is shown in figure C.1.5.8. According to what is written in section 5.2.2, it is assumed that the bending moments on either side of an intermediate slab are not equal but can be determined and expressed as a product of the rotation of the intermediate slab and a coefficient that is computed using the methods from section 5.2.2.

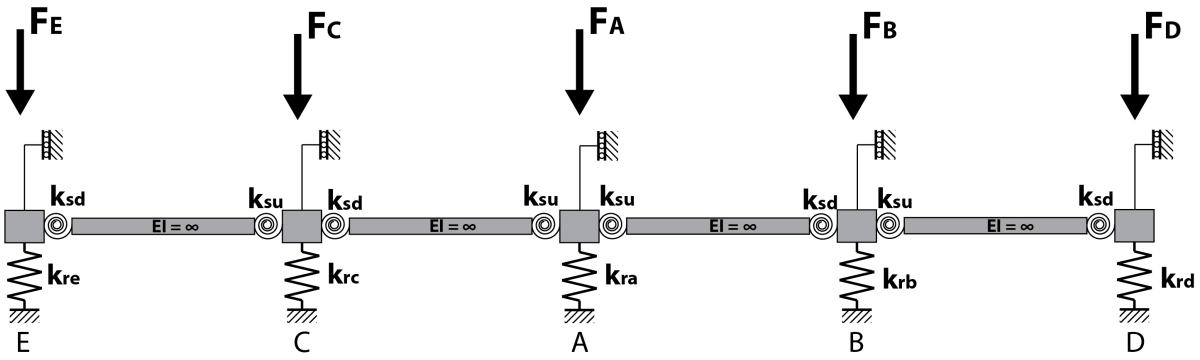

Figure C.1: Model type 1 with five separate ribs.

The internal forces in this model will be determined by setting the equilibrium equations for one rotation spring per intermediate span and relating the internal forces and deflections of the ribs to the rotations occurring in these rotation springs. First of all the following equations C.1,C.2,C.3,C.4 and C.5 are used to relate the shear forces in the ribs with the deflections of those ribs.

$$\delta_e = \frac{F_E + V_{ce}}{k_{re}} \tag{C.1}$$

$$\delta_c = \frac{F_C + V_{ac}}{k_{rc}} \tag{C.2}$$

$$\delta_a = \frac{F_A - V_{ab} - V_{ac}}{k_{ra}} \tag{C.3}$$

$$\delta_b = \frac{F_B + V_{ab}}{k_{rb}} \tag{C.4}$$

$$\delta_d = \frac{F_D + V_{bd}}{k_{rd}} \tag{C.5}$$

Where δ is the deflection of a rib, F is a concentrated load and V is a shear force. The relations of the shear forces in the ribs and the bending moments acting in the intermediate beams are as shown in equations C.6, C.7, C.8 and C.9. In these formulas the indices indicate the at which rib the bending moment in an intermediate slab occurs and on which side of the rib it occurs (left L or right R).

$$V_{ce} = \frac{M_e + M_{cL}}{L_{ce}} \tag{C.6}$$

$$V_{ac} = \frac{M_{aL} + M_{cR}}{L_{ac}} \tag{C.7}$$

$$V_{ab} = \frac{M_{aR} + M_{bL}}{L_{ab}} \tag{C.8}$$

$$V_{bd} = \frac{M_{bR} + M_d}{L_{ad}} \tag{C.9}$$

Where V is a shear force and M is a bending moment. The deflections of the ribs, and thus also implicitly the shear forces and the bending moments, are related to the rotation of the intermediate beams and the rotation springs with the equations C.10, C.11, C.12 and C.13.

$$\theta_{ce} = \frac{(\delta_c - \delta_e)}{L_{ce}} \tag{C.10}$$

$$\theta_{ac} = \frac{(\delta_a - \delta_c)}{L_{ac}} \tag{C.11}$$

$$\theta_{ab} = \frac{(\delta_a - \delta_b)}{L_{ab}} \tag{C.12}$$

$$\theta_{bd} = \frac{(\delta_b - \delta_d)}{L_{bd}} \tag{C.13}$$

Where θ is the rotation of the rotation springs and δ is the deflection of a rib. The bending moments acting in the intermediate beams cause rotation in the rotation springs according to equations C.14, C.15, C.16 and C.17. The bending moments on either side of an intermediate slab are related to each other by equations C.18, C.19, C.20 and C.21, where the coefficients k_{su} and k_{sd} are determined through the methods used in section 5.2.2.

$$\theta_{ce,s} = \frac{M_{cL}}{k_{su}} \tag{C.14}$$

$$\theta_{ac,s} = \frac{M_{aL}}{k_{su}} \tag{C.15}$$

$$\theta_{ab,s} = \frac{M_{aR}}{k_{su}} \tag{C.16}$$

$$\theta_{bd,s} = \frac{M_{bR}}{k_{su}} \tag{C.17}$$

$$\frac{M_e}{k_{sd}} = \frac{M_{cL}}{k_{su}} \tag{C.18}$$

$$\frac{M_{cR}}{k_{sd}} = \frac{M_{aL}}{k_{su}} \tag{C.19}$$

$$\frac{M_{aR}}{k_{su}} = \frac{M_{bL}}{k_{sd}} \tag{C.20}$$

$$\frac{M_{bR}}{k_{su}} = \frac{M_d}{k_{sd}} \tag{C.21}$$

All of the equations given above are combined into the equilibrium equations C.22, C.23, C.24 and C.25 for one rotation spring of each of the intermediate beams.

$$\theta_{ce} - \theta_{ce,s} = 0 \tag{C.22}$$

$$\theta_{ac} - \theta_{ac,s} = 0 \tag{C.23}$$

$$\theta_{ab} - \theta_{ab,s} = 0 \tag{C.24}$$

$$\theta_{bd} - \theta_{bd,s} = 0 \tag{C.25}$$

From these equilibrium equations all moments in the rotations springs and all shear forces in all the translation springs can be determined. This makes it also possible to calculate the deflection of the translation springs and thus create a deflection diagram for the entire width of the model.

C.2. MODEL TYPE 2

The type 2 model for modelling a composite slab in a two-dimensional way was already established in chapter **??**. This section will give detaile explanations on the steps done to include more features into this model type that were not highlighted in the main report. The features that will be discussed in this section are inclusion of additional ribs, varying bending stiffness of the top slab and addition of the self-weight of the composite slab as a distributed load.

C.2.1. A MODEL WITH FIVE RIBS

Model type 2 initially included only 3 ribs, but by using the same methods of modelling it can be expanded by however many ribs to either side as is necessary. When including two ribs on both side of the central rib, so five in total, the set of linear equations that defines the system becomes as shown in equation C.26. Since there are four intermediate spans now, the model consists of four fields. The model that is computed is schematically shown in figure C.2.

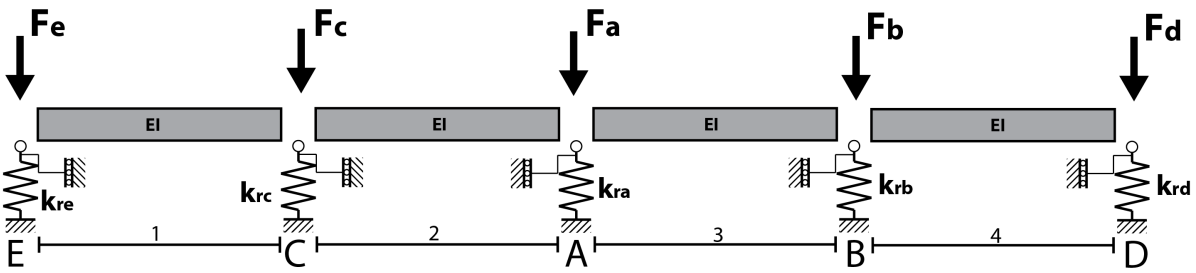

Figure C.2: Model type 2 with five separate ribs and a concentrated load acting on each of the ribs. The top slabs have a constant bending moment EI. The translation springs are supported in the horizontal direction and can only move vertically.

$$\begin{bmatrix}
0 & -1 & 0 & 0 & 0 & 0 & 0 & 0 & 0 & 0 & 0 & 0 & 0 & 0 & 0 & 0 \\
1 & 0 & 0 & \frac{k_r e}{EI} & 0 & 0 & 0 & 0 & 0 & 0 & 0 & 0 & 0 & 0 & 0 & 0 \\
-L & -1 & 0 & 0 & L & 1 & 0 & 0 & 0 & 0 & 0 & 0 & 0 & 0 & 0 & 0 \\
-\frac{L^2}{2EI} & -\frac{L}{EI} & -\frac{1}{EI} & 0 & \frac{L^2}{2EI} & \frac{L}{EI} & \frac{1}{EI} & 0 & 0 & 0 & 0 & 0 & 0 & 0 & 0 & 0 \\
\frac{L^3}{6EI} & \frac{L^2}{2EI} & \frac{L}{EI} & \frac{1}{EI} & -\frac{L^3}{6EI} & -\frac{L^2}{2EI} & -\frac{L}{EI} & -\frac{1}{EI} & 0 & 0 & 0 & 0 & 0 & 0 & 0 & 0 \\
\frac{k_r cL^3}{6EI} & -1 & \frac{k_r cL^2}{2EI} & \frac{k_r cL}{EI} & \frac{k_r c}{EI} & 1 & 0 & 0 & 0 & 0 & 0 & 0 & 0 & 0 & 0 & 0 \\
0 & 0 & 0 & 0 & -2L & -1 & 0 & 2L & 1 & 0 & 0 & 0 & 0 & 0 & 0 & 0 \\
0 & 0 & 0 & 0 & -\frac{(2L)^2}{2EI} & -\frac{2L}{EI} & -\frac{1}{EI} & 0 & \frac{(2L)^2}{2EI} & \frac{2L}{EI} & \frac{1}{EI} & 0 & 0 & 0 & 0 & 0 \\
0 & 0 & 0 & 0 & \frac{(2L)^3}{6EI} & \frac{(2L)^2}{2EI} & \frac{(2L)}{EI} & \frac{1}{EI} & -\frac{(2L)^3}{6EI} & -\frac{(2L)^2}{2EI} & -\frac{(2L)}{EI} & -\frac{1}{EI} & 0 & 0 & 0 & 0 \\
0 & 0 & 0 & 0 & \frac{k_r a(2L)^3}{6EI} & -1 & \frac{k_r a(2L)^2}{2EI} & \frac{k_r a(2L)}{EI} & \frac{k_r a}{EI} & 1 & 0 & 0 & 0 & 0 & 0 & 0 \\
0 & 0 & 0 & 0 & 0 & 0 & 0 & -3L & -1 & 0 & 0 & 3L & 1 & 0 & 0 & 0 \\
0 & 0 & 0 & 0 & 0 & 0 & 0 & 0 & -\frac{(3L)^2}{2EI} & -\frac{3L}{EI} & -\frac{1}{EI} & 0 & -\frac{(3L)^2}{2EI} & \frac{3L}{EI} & \frac{1}{EI} & 0 \\
0 & 0 & 0 & 0 & 0 & 0 & 0 & 0 & \frac{(3L)^3}{6EI} & \frac{(3L)^2}{2EI} & \frac{(3L)}{EI} & \frac{1}{EI} & -\frac{(3L)^3}{6EI} & -\frac{(3L)^2}{2EI} & -\frac{(3L)}{EI} & -\frac{1}{EI} \\
0 & 0 & 0 & 0 & 0 & 0 & 0 & 0 & \frac{k_r b(3L)^3}{6EI} & -1 & \frac{k_r b(3L)^2}{2EI} & \frac{k_r b(3L)}{EI} & \frac{k_r b}{EI} & 1 & 0 & 0 & 0 \\
0 & 0 & 0 & 0 & 0 & 0 & 0 & 0 & 0 & 0 & 0 & 0 & -4L & 1 & 0 & 0 \\
0 & 0 & 0 & 0 & 0 & 0 & 0 & 0 & 0 & 0 & 0 & 0 & \frac{k_r d(4L)^3}{6EI} & -1 & \frac{k_r d(4L)^2}{2EI} & \frac{k_r d(4L)}{EI} & \frac{k_r d}{EI}
\end{bmatrix} \times \begin{bmatrix} A_1 \\ A_2 \\ A_3 \\ A_4 \\ B_1 \\ B_2 \\ B_3 \\ B_4 \\ C_1 \\ C_2 \\ C_3 \\ C_4 \\ D_1 \\ D_2 \\ D_3 \\ D_4 \end{bmatrix} = \begin{bmatrix} 0 \\ F_e \\ 0 \\ 0 \\ 0 \\ F_c \\ 0 \\ 0 \\ 0 \\ F_a \\ 0 \\ 0 \\ 0 \\ F_b \\ 0 \\ F_d \end{bmatrix} \tag{C.26}$$

Where A_i, B_i, C_i and D_i are the integration constants from all the differential equations that were used. From this set of equations the expressions for the deflection and thus implicitly the rotation of the cross-section, the moment and shear can be obtained in the form of equation C.27. Where expression 1 with constants A runs from $x = 0$ to $x = L$, expression 2 from $x = L$ to $x = 2L$, etc.

$$w_i = \frac{A_1 x^3}{6EI} + \frac{A_2 x^2}{2EI} + \frac{A_3 x}{EI} + \frac{A_4}{EI} \tag{C.27}$$

In the matrix above a pattern can be seen across the diagonal. Repeating this pattern to expand the matrix allows for including as many ribs on either side as necessary.

C.2.2. CRACKED AND UNCRACKED INTERMEDIATE SLABS

In chapter 5 it was already discussed how model type 2 could include varying bending stiffnesses along the intermediate slabs. This is done by dividing the intermediate slabs into multiple fields, each with its own differential equation and bending stiffness. It was already shown for a subdivision into two separate fields, but in order to take into account not only the direction of the bending moments, but also the cracking of the concrete in the top slabs. Since the cracked sections of the top slab will have a lower bending stiffness, this requires the top slab to be divided into four fields namely:

- Negative bending moment and cracked concrete
- Negative bending moment and uncracked concrete
- Positive bending moment and uncracked concrete
- Positive bending moment and cracked concrete

So four fields per span and four spans results in a set of 64 equations and 64 unknowns. Because the bending stiffness depends on the direction of the bending moment, which is variable, they will be numbered. The indices indicates the span and its number in a field of a certain bending stiffness. The resulting matrix equation is shown in equation C.28. The accompanying schematic model that this equation is describing is shown in figure C.3.

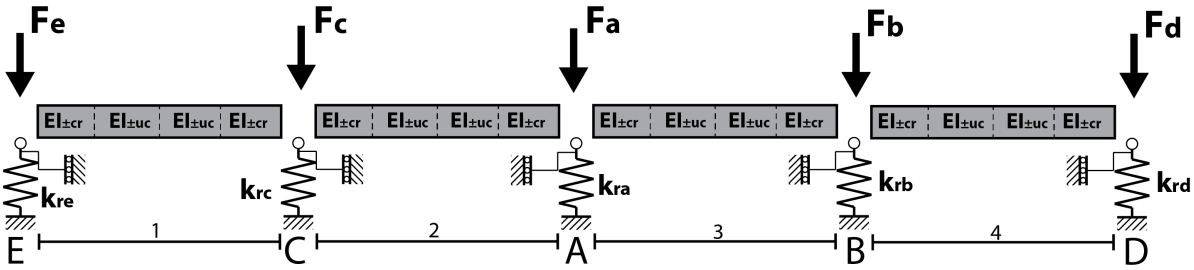

Figure C.3: Model type 2 with five separate ribs and a concentrated load acting on each of the ribs. The top slabs have a varying bending moment EI. The translation springs are supported in the horizontal direction and can only move vertically.

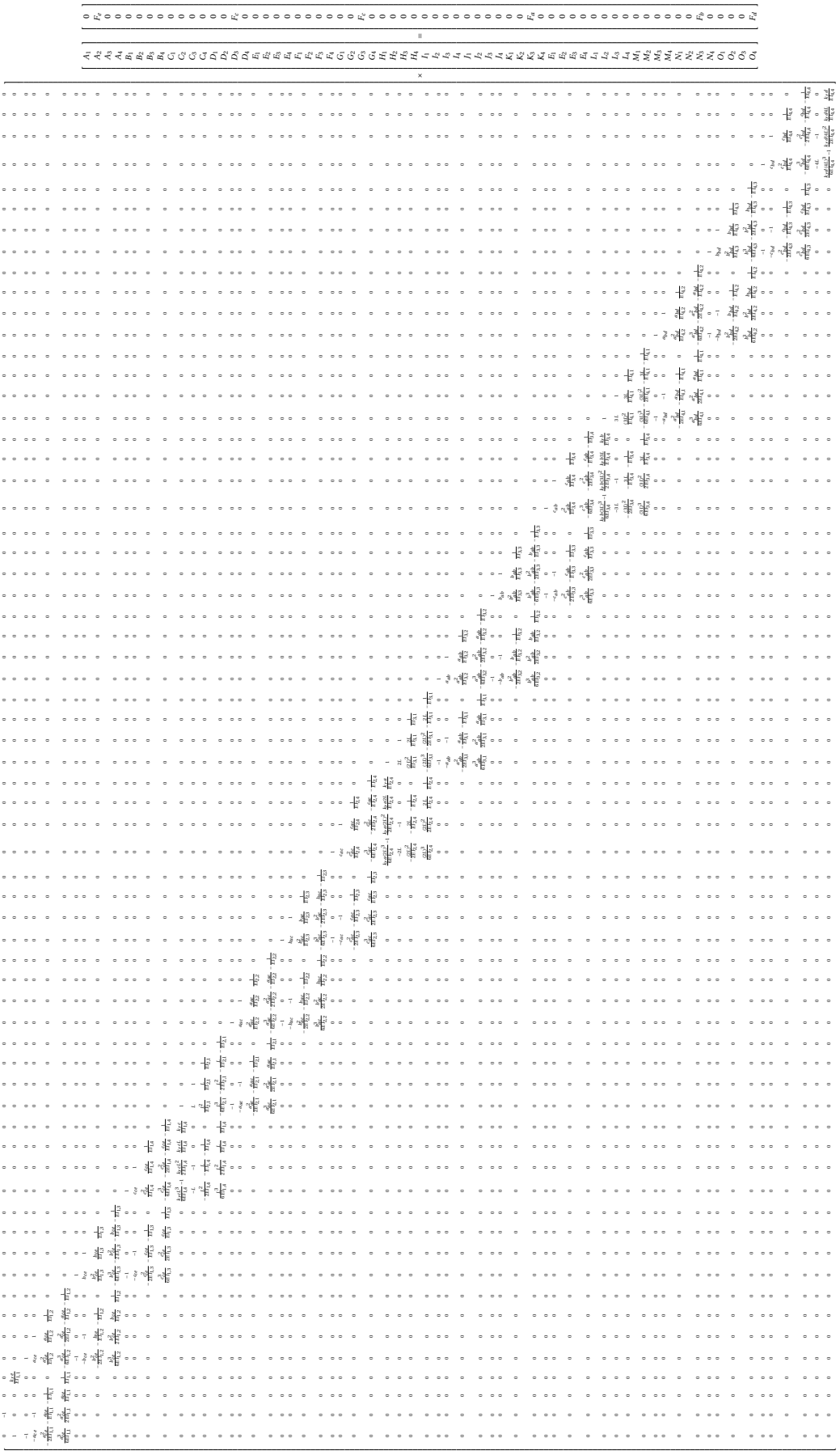

(C.28)

C.2.3. ADDING ROTATION RESISTANCE OF THE RIBS

When the rotation resistance of ribs is added to the five rib model from above the result becomes as can be seen in equation C.29. The model now looks as is shown in figure C.4.

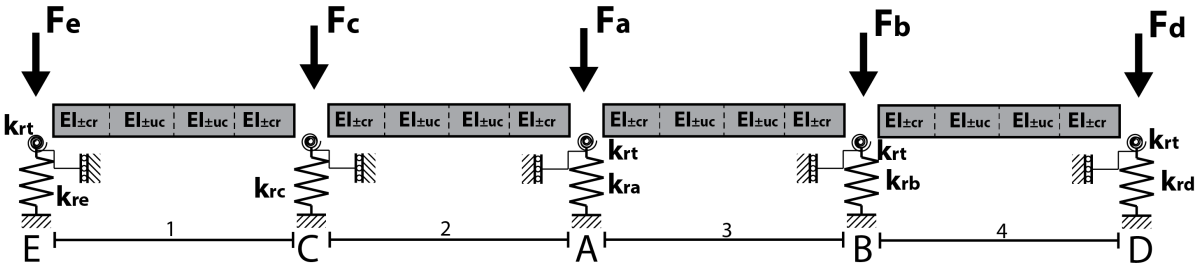

Figure C.4: Model type 2 with five separate ribs and a concentrated load acting on each of the ribs. The top slabs have a varying bending moment EI. The translation springs are supported in the horizontal direction and can only move vertically. The translation springs and the intermediate slab are connected with rotation springs

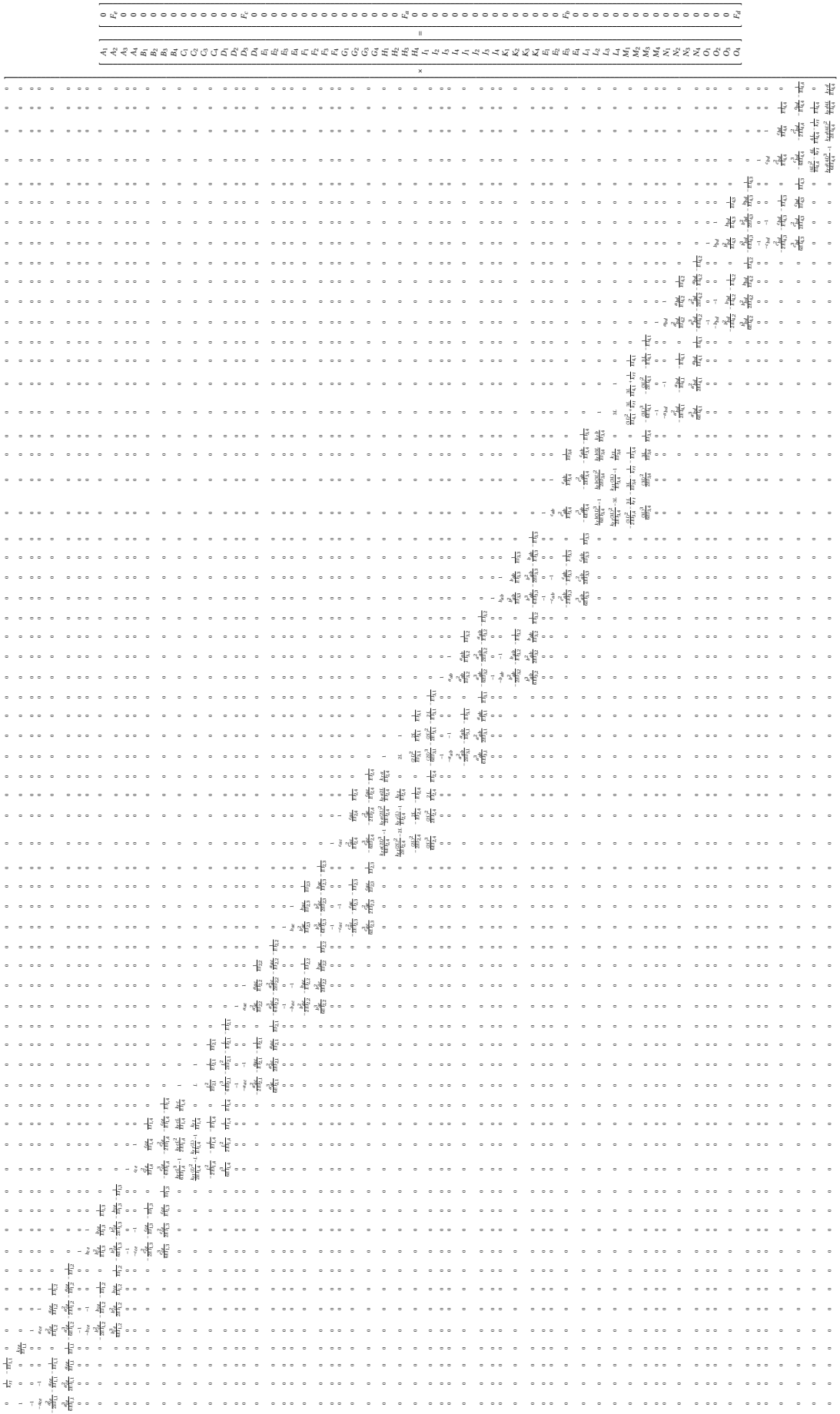

(C.29)

C.2.4. LINE LOAD

With the addition of a line load to the composite slab, the differential equation used to determine the slab behaviour changes slightly. Differential equation C.30 is now integrated into the shear force C.31, moment C.32, rotation C.33 and deflection C.34 respectively.

$$EI\frac{d^4w}{dx^4} = q \tag{C.30}$$

$$V(x) = -EI\frac{d^3w(x)}{dx^3} = -\left(qx + C_1\right) \tag{C.31}$$

$$M(x) = -EI\frac{d^2w(x)}{dx^2} = -\left(\frac{1}{2}qx^2 + C_1x + C_2\right) \tag{C.32}$$

$$\varphi(x) = -w(x) = -\frac{1}{EI}\left(\frac{1}{6}qx^3 + \frac{1}{2}C_1x^2 + C_2x + C_3\right) \tag{C.33}$$

$$w(x) = \frac{1}{EI}\left(\frac{1}{24}qx^4 + \frac{1}{6}C_1x^3 + \frac{1}{2}C_2x^2 + C_3x + C_4\right) \tag{C.34}$$

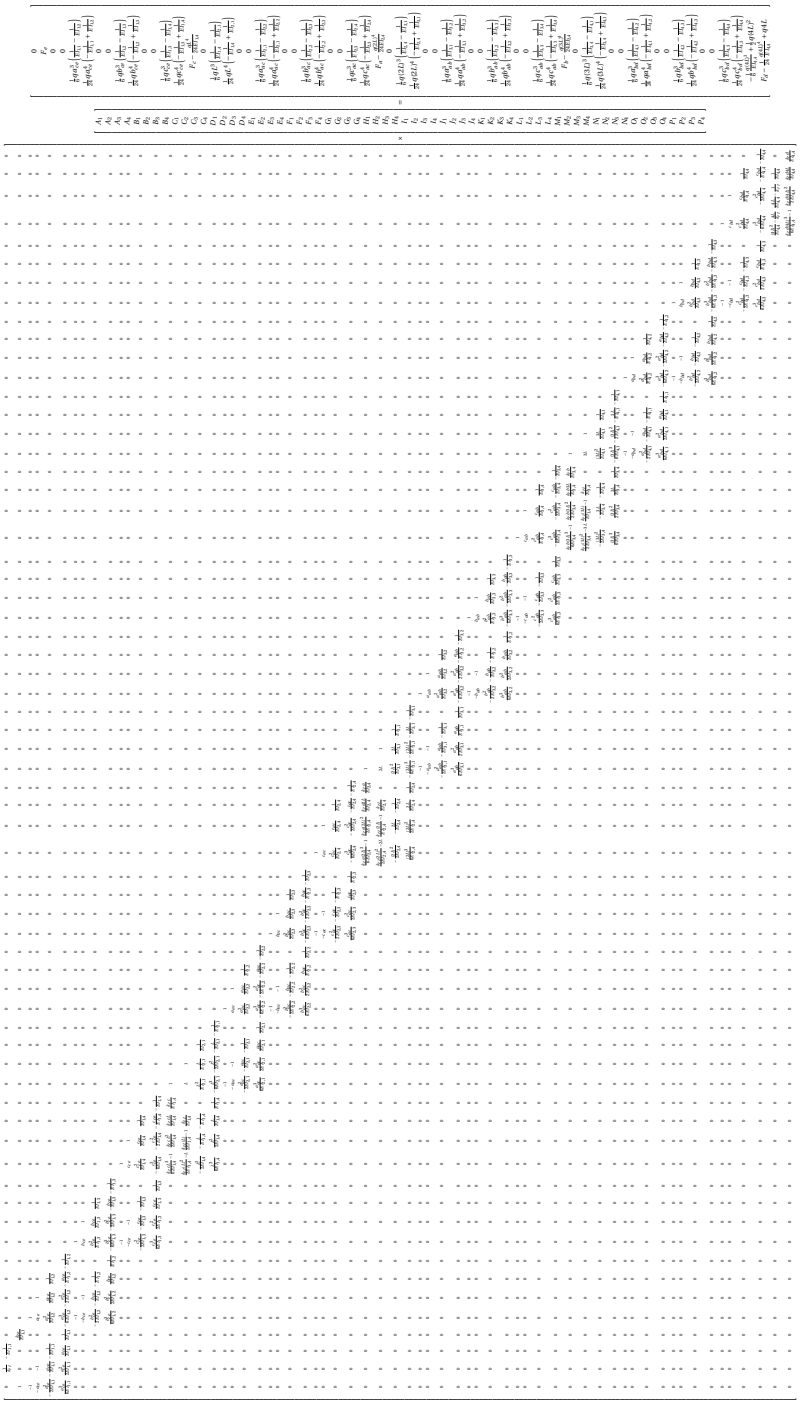

(C.35)

C.2.5. MODELLING SEVEN RIBS

Now the model has been improved with a number of features. The model will be expanded with two extra ribs one more time. This will give still improved accuracy, because some load may be distributed towards the outermost rib in a seven rib model. Or it is possible that the contribution of these ribs is so small that they can be neglected all together. To find the answer to this question the model will be expanded once again.

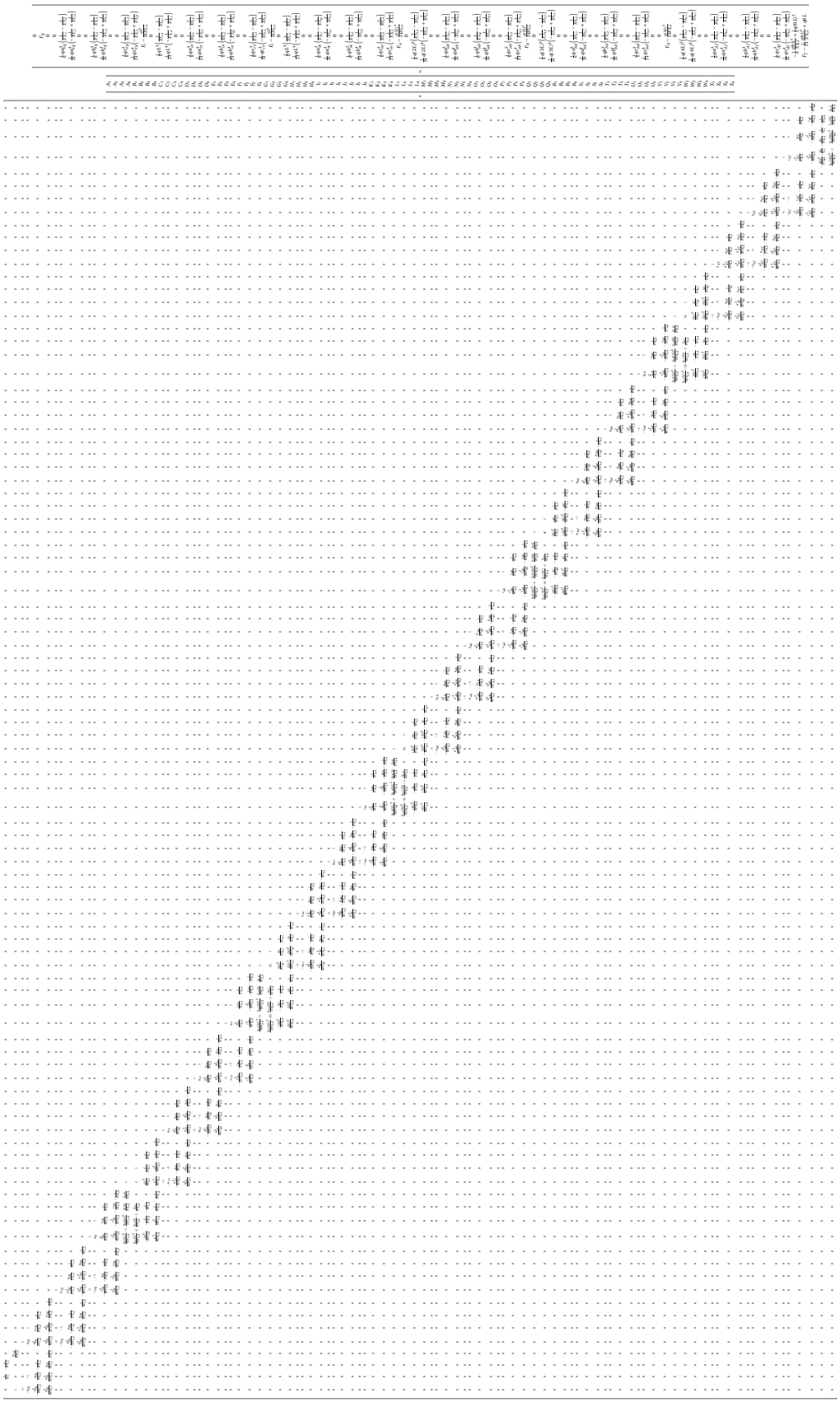

(C.36)

D

DETAILED COMPUTATION OF MODEL PARAMETERS

This chapter details how the model parameters that are used for the analytical models were computed, if this was not already done so in the main report. The parameters influence the outcome of the analytical model and thus their computation should be done in a correct manner. However, sometimes assumptions about material or mechanical behaviour had to be made. When this is the case, it will be highlighted as such.

D.1. BENDING STIFFNESS OF THE TOP SLAB

The computation of the bending stiffness of the top part of the intermediate slabs is a fairly straightforward calculation. It is important, however, to decide what parts of the cross-section will be taken into account when determining the stiffness. The cross-section that will be considered is displayed in figure D.1. The components of the cross-section that will be assumed to contribute to the bending stiffness are.

1. The uncracked concrete
2. The cracked concrete (if applicable)
3. The top reinforcement mesh
4. The bottom reinforcement mesh

The top flange of the profiled steel deck is assumed not to contribute to the bending stiffness. This is due to the geometry cross-section of the COMFLOR210, which is taken as a modelling subject in this thesis. The embossment made in both corners of the top flange, see figure D.2a and D.2b, secure a larger effective steel area when the steel profiled deck is loaded by a bending moment, by stiffening this corner to prevent local buckling. This embossment continues over the full length of the steel deck and when is loaded in transverse bending the top flange might not be stiff enough to contribute to the bending stiffness because of this embossment. Another factor that makes the contribution of the top flange uncertain is the fact that the top part of the composite deck can be loaded by both a positive and a negative bending moment between two ribs. This would respectively cause a tension stress and compressive stress in the steel top flange. Because of these uncertainties the contribution of the top flange of steel profiled deck to the bending stiffness is neglected.

D.1.1. CRACKING BENDING MOMENT AND THE BENDING STIFFNESS OF THE UNCRACKED CROSS-SECTION

First of all the height of the bending moment at which the concrete starts to crack has to be determined. Before this happens the concrete in the extreme fibres has not yet reached a tension stress at which it starts to crack. It is assumed that until this happens the concrete in the cross-section is the only contributor to the bending stiffness, because there has not yet been enough deformation for the steel reinforcement meshes to become active.
Assuming that only the concrete in the cross-section is active, results in the examination of a simple rectangular area. The height of the neutral axis is therefore at half of the concrete height $0.5h_c$. The section modulus

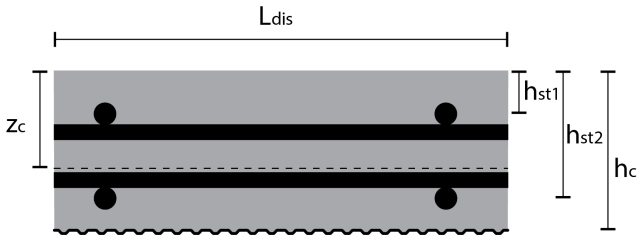

Figure D.1: The cross-section of the top slab in the traverse direction, with the used dimensions assigned. In this figure z_c is the height of the neutral axis.

(a) The cross-section of a single plate of the COMFLOR210 steel profiled deck.

(b) A close-up of the top corner of the cross-section.

Figure D.2: The embossment made in this top corner provides more effective steel surface area in bending, but it does not provide anchorage for the top flange in transverse bending of the top slab.

of the uncracked top slab $W_{ts,uc}$ can then be computed via equation D.1 and then the cracking moment is determined in equation D.2, where f_{ctm} is determined according to Eurocode 2 [2].

$$W_{ts,uc} = \frac{1}{6} L_{eff} h_c^2 \tag{D.1}$$

$$M_{cr,ts} = \frac{W_{ts,uc}}{f_{ctm}} \tag{D.2}$$

By using the values shown in table D.1 the section modulus is then calculated in equation D.1. It has to be noted that the distributive length L_{dis} is assumed to be 200 mm for now. But this value is actually a variable in the modelling.

Table D.1: The parameters used to compute the section modulus of the uncracked top slab of the composite slab.

Parameters	Values
Concrete class	$C20/25$
L_{dis}	200 $[mm]$
f_{ctm}	2.2 $[N/mm^2]$
h_c	70 $[mm]$
E_{concr}	30000 $[N/mm^2]$

The section modulus and the cracking moment are now computed in equation D.3 and D.4 respectively.

$$W_{ts,uc} = \frac{1}{6} \times 200 \times 70^2 = 1.63 \times 10^5 mm^3 \tag{D.3}$$

$$M_{cr,ts} = \frac{1.63 \times 10^5}{2.2} = 3.61 \times 10^5 Nmm \tag{D.4}$$

The next step is to calculate the bending stiffness of the uncracked cross-section. This is done by using equation D.5.

$$EI_{ts,uc} = E_{concr} \times I_{ts,uc} = E_{concr} \times \frac{1}{12} \times L_{dis} \times h_c^3 = 30000 \times \frac{1}{12} \times 200 \times 70^3 = 1.72 \times 10^{11} Nmm^2 \quad \text{(D.5)}$$

Because the cross-section is not yet cracked and thus acts exactly the same when loaded by a positive bending moment or a negative bending moment, the direction of the acting moment does not yet matter. This only becomes an important issue after cracking of the concrete occurs.

D.1.2. BENDING STIFFNESS OF THE CRACKED CROSS-SECTION

After cracking of the concrete occurs because the tension stress becomes too large, a new equilibrium is established. The reinforcement meshes will act in tension to resist and act in unison with the compression stresses in the concrete compression zone. It is not that the direction of the of the acting bending moments starts being an important issue. This is because of the asymmetrical nature of the cross-section along the horizontal axis. This asymmetry is caused by the unequal cover heights of the reinforcement meshes at the top and the bottom of the top slab. The parameters that will be used in this section additional to the parameters already introduced in the previous section are displayed in table D.2.

Table D.2: Addition parameters used to compute the bending stiffness of the cracked top slab of the composite slab. It has to be noted that the surface area of the reinforcement meshes is related to the length L_{dis} that is chosen, since it concerns a 8-150 mesh.

Parameters	Values	Units
h_{st1}	19	mm
h_{st2}	56	mm
E_{concr}	30000	N/mm^2
A_{s1}	67	mm^2
A_{s2}	67	mm^2
E_{s1}	210000	N/mm^2
E_{s2}	210000	N/mm^2

First of all the newly established equilibrium needs to be computed in order to learn which parts of the cross-section are cracked and which are not. The equilibrium that is created after the concrete cracks is governed by three equations.

- The horizontal equilibrium of the cross-section $\sum F_x = 0$
- The similarity of the strain diagrams of the concrete and the tensile reinforcement
- The moment equilibrium of the cross-section $\sum M_{cs} = 0$

There are several situations that need to be checked however. The composite slab can be reinforced by two reinforcement meshes or only one reinforcement mesh at the top. And the direction of the acting bending moment also matters because of the horizontal asymmetry of cross-section. Therefore there are four different situations that can be identified. The corresponding stress-strain diagrams are drawn in figure D.3.

1. A positive bending moment acts on the cross-section with only the top reinforcement mesh
2. A positive bending moment acts on the cross-section with both the top and the bottom reinforcement meshes
3. A negative bending moment acts on the cross-section with only the top reinforcement mesh
4. A negative bending moment acts on the cross-section with both the top and the bottom reinforcement meshes

In figure D.3 the total height of the cross-section is indicated by h_c and the heights of the top reinforcement mesh and the bottom reinforcement mesh are h_{st1} and h_{st1} respectively. The stresses of the top and bottom reinforcement meshes and the concrete are respectively ϵ_{s1}, ϵ_{s2} and ϵ_c and the imaginary concentrated loads

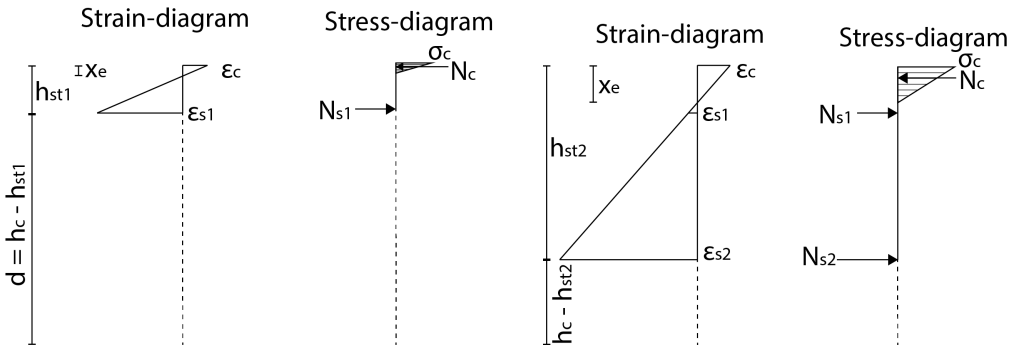

(a) The stress and strain diagram resulting from a positive bending moment on a cross-section with only the top reinforcement mesh.

(b) The stress and strain diagram resulting from a positive bending moment on a cross-section with both the top and the bottom reinforcement meshes.

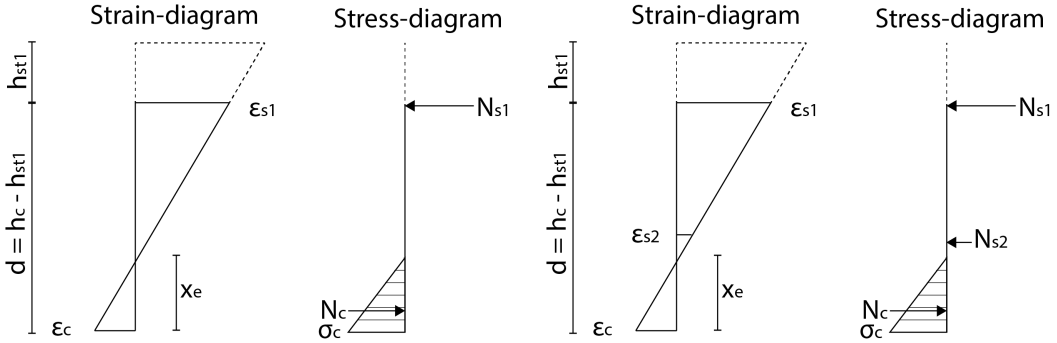

(c) The stress and strain diagram resulting from a negative bending moment on a cross-section with only the top reinforcement mesh.

(d) The stress and strain diagram resulting from a negative bending moment on a cross-section with both the top and the bottom reinforcement meshes.

Figure D.3: Both stress and strain diagrams resulting from a positive and negative bending moments acting on the cross-section of the top part of the composite slab.

acting on the cross-section as a result of the stresses caused by those strains are N_{s1}, N_{s2} and N_c. The height of the compression zone is x_e. The four situations described above will be elaborated upon separately below and at the end of this section they will be compared in a table to give a good overview the effect of the direction of the bending moment and the presence bottom reinforcement mesh have on the bending moment stiffness.

A POSITIVE BENDING MOMENT ACTING ON A CROSS-SECTION WITH ONLY A TOP REINFORCEMENT MESH

The three equations governing the new equilibrium, see figure D.3a, are implemented in equations D.6, D.7 and D.8 respectively, while doing this it is assumed that the neutral axis of the cross-section is situated above the position of the top reinforcement mesh. This will be checked at a later stage of course.

$$\sum F_x = 0 \rightarrow \frac{1}{2} \times L_{dis} \times x_e \times \epsilon_c \times E_{concr} = \epsilon_{s1} \times A_{s1} \times E_{s1} \tag{D.6}$$

$$\frac{\epsilon_c}{\epsilon_{s1}} = \frac{x_e}{h_{st1} - x_e} \tag{D.7}$$

$$\sum M_{cs} = 0 \rightarrow \epsilon_{s1} \times A_{s1} \times E_{s1} \times \left(h_{st1} - \frac{x_e}{3}\right) = M_{cr} \tag{D.8}$$

When the values from table D.2, in addition to the values introduced previously, are used the equations from above result in equations D.9, D.10 and D.11.

$$\sum F_x = 0 \rightarrow \frac{1}{2} \times 200 \times x_e \times \epsilon_c \times 30000 = \epsilon_{s1} \times 67 \times 210000 \tag{D.9}$$

$$\frac{\epsilon_c}{\epsilon_{s1}} = \frac{x_e}{19 - x_e} \tag{D.10}$$

$$\sum M_{cs} = 0 \rightarrow \epsilon_{s1} \times 67 \times 210000 \times \left(67 - \frac{x_e}{3}\right) = 3.61 \times 10^5 \tag{D.11}$$

The three equations above can be solved for the four unknown factors ϵ_c, ϵ_{s1} and x_e. With the height of the compression zone just after cracking of the concrete occurs now known, it can be checked whether the initial assumption about the position of the top reinforcement was correct. The values resulting from the calculations are shown in table D.3.

Table D.3: The values of the unknowns found trough solving the equilibrium equations for the cross-section.

Parameters	**Values**	**Unit**
x_e	7.381	mm
ϵ_c	1.551×10^{-3}	–
ϵ_{s1}	0.986×10^{-3}	–

The height of the compressive zone is indeed smaller than the height at which the top reinforcement mesh is located. Now that the stress and strain diagrams are completely known. The next step is to calculate the height of the neutral axis of the cross-section. This is done by implementing the formula shown in equation D.12.

$$z_c = \frac{\sum \left(y_{C,i} \times E_i \times A_i\right)}{\sum \left(E_i \times A_i\right)} \tag{D.12}$$

This is done for all components of the cross-section in table D.4.

Table D.4: This table displays the computation of the height of the centre of gravity of the cross-section.

Component	**Young's modulus E** $[N/mm^2]$	**Width b** $[mm]$	**Height h** $[mm]$	**Surface area A** $[mm^2]$	**Height centre of gravity** y_c $[mm]$	$y_c \times E \times A$ $[Nmm]$	$E \times A[N]$	$\frac{y_c \times E \times A}{\sum E \times A}$ $[mm]$
Concrete	3.0×10^4	200	7.381	1476	3.690	1.634×10^8	4.428×10^7	0.89
Cracked concrete	1.0×10^4	200	62.620	12524.0	38.690	1.652×10^9	1.252×10^8	9.00
Top reinforcement mesh	2.1×10^5	–	–	67	19	2.674×10^8	1.407×10^7	1.46
Sum						7.373×10^9	8.159×10^8	
Height centre of gravity z_c								11.34

With the height of the neutral axis known, the bending stiffness of the cross-section can now be calculated according to formula D.13.

$$EI_{ts} = \sum \left(E_i \times (I_{eigen,i} + I_{steiner,i})\right) \tag{D.13}$$

This is done for all components of the cross-section in table D.5.
With this the bending stiffness of the top slab under a positive bending moment only the top mesh is now known.

Table D.5: This table displays all the components used for the computation of the bending stiffness of the cross-section.

Component	**Young's modulus E** $[N/mm^2]$	I_{eigen} $[mm^4]$	$I_{steiner}$ $[mm^4]$	I_{tot} $[mm^4]$	$E \times I$ $[Nmm^2]$	**Percentage [%]**
Concrete	3.0×10^4	6.699×10^3	8.647×10^4	9.317×10^4	2.795×10^9	6
Cracked concrete	3.0×10^4	4.092×10^6	3.836×10^5	4.476×10^6	4.476×10^{10}	91
Top reinforcement mesh	2.1×10^5	3.217×10^3	3.928×10^3	7.145×10^3	1.500×10^9	3
Positive bending stiffness with only top mesh $EI_{ts,pos,1}$ $[N/mm^2]$					4.906×10^{10}	100

A POSITIVE BENDING MOMENT ACTING ON A CROSS-SECTION WITH BOTH A TOP AND A BOTTOM REINFORCEMENT MESH

The three equations governing the equilibrium from the previous section are now split into four equations because the similarity of the strain diagrams is expanded by another triangle, that of the added reinforcement mesh. The situation that is considered can be seen in figure D.3b. The four equilibrium equations are implemented in equations D.14, D.15, D.16 and D.17 respectively, while doing this it is assumed that the neutral axis of the cross-section is situated above the position of the top reinforcement mesh. This will be checked at a later stage of course.

$$\sum F_x = 0 \rightarrow \frac{1}{2} \times L_{dis} \times x_e \times \epsilon_c \times E_{concr} = \epsilon_{s1} \times A_{s1} \times E_{s1} + \epsilon_{s2} \times A_{s2} \times E_{s2} \tag{D.14}$$

$$\frac{\epsilon_c}{\epsilon_{s2}} = \frac{x_e}{h_{st2} - x_e} \tag{D.15}$$

$$\frac{\epsilon_{s1}}{\epsilon_{s2}} = \frac{h_{st1} - x_e}{h_{st2} - x_e} \tag{D.16}$$

$$\sum M_{cs} = 0 \rightarrow \epsilon_{s1} \times A_{s1} \times E_{s1} \times h_{st1} + \epsilon_{s2} \times A_{s2} \times E_{s2} \times h_{st2} - \frac{1}{2} \times \frac{L_{dis} \times \epsilon_c \times x_e^2 \times E_{concr}}{3} = M_{cr} \tag{D.17}$$

When the values from table D.2, in addition to the values introduced previously, are used the equations from above result in equations D.18, D.19, D.20 and D.21.

$$\sum F_x = 0 \rightarrow \frac{1}{2} \times 200 \times x_e \times \epsilon_c \times 30000 = \epsilon_{s1} \times 67 \times 210000 + \epsilon_{s2} \times 67 \times 210000 \tag{D.18}$$

$$\frac{\epsilon_c}{\epsilon_{s2}} = \frac{x_e}{56 - x_e} \tag{D.19}$$

$$\frac{\epsilon_{s1}}{\epsilon_{s2}} = \frac{19 - x_e}{56 - x_e} \tag{D.20}$$

$$\sum M_{cs} = 0 \rightarrow \epsilon_{s1} \times 67 \times 210000 \times 19 + \epsilon_{s2} \times 67 \times 210000 \times 56 - \frac{1}{2} \times \frac{200 \times \epsilon_c \times x_e^2 \times 30000}{3} = 3.61 \times 10^5 \tag{D.21}$$

The four equations above can be solved for the four unknown factors ϵ_c, ϵ_{s1}, ϵ_{s2} and x_e. With the height of the compression zone just after cracking of the concrete occurs now known, it can be checked whether the initial assumption about the position of the top reinforcement was correct. The values resulting from the calculations are shown in table D.6.

The height of the compressive zone is indeed smaller than the height at which the top reinforcement mesh is located. Now that the stress and strain diagrams are completely known. The next step is to calculate the

Table D.6: The values of the unknowns found trough solving the equilibrium equations for the cross-section.

Parameters	Values	Unit
x_e	14.643	mm
ϵ_c	0.173×10^{-3}	–
ϵ_{s1}	0.051×10^{-3}	–
ϵ_{s2}	0.488×10^{-3}	–

height of the neutral axis of the cross-section. This is done by implementing the formula shown in equation D.22.

$$z_c = \frac{\sum \left(y_{C,i} \times E_i \times A_i\right)}{\sum \left(E_i \times A_i\right)} \tag{D.22}$$

This is done for all components of the cross-section in table D.7.

Table D.7: This table displays the computation of the height of the centre of gravity of the cross-section.

Component	**Young's modulus E** $[N/mm^2]$	**Width b** $[mm]$	**Height h** $[mm]$	**Surface area A** $[mm^2]$	**Height centre of gravity** y_c $[mm]$	$y_c \times E \times A$ $[Nmm]$	$E \times A[N]$	$\frac{y_c \times E \times A}{\sum E \times A}$ $[mm]$
Concrete	3.0×10^4	200	14.643	2928.0	7.320	6.430×10^8	8.784×10^7	5.52
Cracked concrete	3.0×10^4	200	55.360	11072.0	42.320	3.065×10^9	5.536×10^5	26.30
Top reinforcement mesh	2.1×10^5	–	–	67	19	2.674×10^8	1.407×10^7	2.29
Bottom reinforcement mesh	2.1×10^5	–	–	67	56	7.882×10^8	1.407×10^7	6.76
Sum						4.763×10^9	1.165×10^8	
Height centre of gravity z_c								40.87

With the height of the neutral axis known, the bending stiffness of the cross-section can now be calculated according to formula D.23.

$$EI_{ts} = \sum \left(E_i \times (I_{eigen,i} + I_{steiner,i})\right) \tag{D.23}$$

This is done for all components of the cross-section in table D.8.
With this the bending stiffness of the top slab under a positive bending moment both the top mesh and the bottom mesh is now known.

Table D.8: This table displays all the components used for the computation of the bending stiffness of the cross-section.

Component	**Young's modulus E** $[N/mm^2]$	I_{eigen} $[mm^4]$	$I_{steiner}$ $[mm^4]$	I_{tot} $[mm^4]$	$E \times I$ $[Nmm^2]$	**Percentage [%]**
Concrete	3.0×10^4	5.230×10^4	3.296×10^6	3.384×10^6	1.005×10^{11}	66
Cracked concrete	3.0×10^4	1.179×10^6	3.373×10^6	4.552×10^6	4.552×10^{10}	30
Top reinforcement mesh	2.1×10^5	3.217×10^3	7.094×10^3	1.031×10^4	2.165×10^9	1
Bottom reinforcement mesh	2.1×10^5	3.217×10^3	1.534×10^4	1.856×10^4	3.897×10^9	3
Positive bending stiffness with top and bottom meshes $EI_{ts,pos,1}$ $[N/mm^2]$					1.520×10^{11}	100

A NEGATIVE BENDING MOMENT ACTING ON A CROSS-SECTION WITH ONLY A TOP REINFORCEMENT MESH

The three equations governing the new equilibrium, see figure D.3c, are implemented in equations D.24, D.25 and D.26 respectively, while doing this it is assumed that the neutral axis of the cross-section is situated below the position of the bottom reinforcement mesh. This will be checked at a later stage of course.

$$\sum F_x = 0 \rightarrow \frac{1}{2} \times L_{dis} \times x_e \times \epsilon_c \times E_{concr} = \epsilon_{s1} \times A_{s1} \times E_{s1} \tag{D.24}$$

$$\frac{\epsilon_c}{\epsilon_{s1}} = \frac{x_e}{d - x_e} \tag{D.25}$$

$$\sum M_{cs} = 0 \rightarrow \epsilon_{s1} \times A_{s1} \times E_{s1} \times d - \frac{1}{2} \times \frac{L_{dis} \times x_e^2 \times \epsilon_c \times E_{concr}}{3} = M_{cr} \tag{D.26}$$

When the values from table D.2, in addition to the values introduced previously, are used the equations from above result in equations D.27, D.28 and D.29.

$$\sum F_x = 0 \rightarrow \frac{1}{2} \times 200 \times x_e \times \epsilon_c \times 30000 = \epsilon_{s1} \times 67 \times 210000 \tag{D.27}$$

$$\frac{\epsilon_c}{\epsilon_{s1}} = \frac{x_e}{51 - x_e} \tag{D.28}$$

$$\sum M_{cs} = 0 \rightarrow \epsilon_{s1} \times 67 \times 210000 \times 51 - \frac{1}{2} \times \frac{200 \times x_e^2 \times \epsilon_c \times 30000}{3} = 3.61 \times 10^5 \tag{D.29}$$

The three equations above can be solved for the four unknown factors ϵ_c, ϵ_{s1} and x_e. With the height of the compression zone just after cracking of the concrete occurs now known, it can be checked whether the initial assumption about the position of the top reinforcement was correct. The values resulting from the calculations are shown in table D.9.

Table D.9: The values of the unknowns found trough solving the equilibrium equations for the cross-section.

Parameters	**Values**	**Unit**
x_e	13.29	mm
ϵ_c	0.194×10^{-3}	–
ϵ_{s1}	0.550×10^{-3}	–

The height of the compressive zone is indeed smaller than the height at which the top reinforcement mesh is located. Now that the stress and strain diagrams are completely known. The next step is to calculate the height of the neutral axis of the cross-section. This is done by implementing the formula shown in equation D.30.

$$z_c = \frac{\sum \left(y_{C,i} \times E_i \times A_i\right)}{\sum \left(E_i \times A_i\right)} \tag{D.30}$$

This is done for all components of the cross-section in table D.10.

Table D.10: This table displays the computation of the height of the centre of gravity of the cross-section.

Component	**Young's modulus E** $[N/mm^2]$	**Width b** $[mm]$	**Height h** $[mm]$	**Surface area A** $[mm^2]$	**Height centre of gravity** y_c $[mm]$	$y_c \times E \times A$ $[Nmm]$	$E \times A[N]$	$\frac{y_c \times E \times A}{\sum E \times A}$ $[mm]$
Concrete	3.0×10^4	200	13.29	2658.0	63.355	5.052×10^9	7.974×10^7	24.38
Cracked concrete	3.0×10^4	200	56.71	11342.0	28.355	3.216×10^9	1.134×10^8	15.52
Top reinforcement mesh	2.1×10^5	–	–	67	19	2.674×10^8	1.407×10^7	1.29
Sum						8.535×10^9	2.072×10^8	
Height centre of gravity z_c								41.19

With the height of the neutral axis known, the bending stiffness of the cross-section can now be calculated according to formula D.31.

$$EI_{ts} = \sum \left(E_i \times (I_{eigen,i} + I_{steiner,i})\right) \tag{D.31}$$

This is done for all components of the cross-section in table D.11.

Table D.11: This table displays all the components used for the computation of the bending stiffness of the cross-section.

Component	**Young's modulus E** $[N/mm^2]$	I_{eigen} $[mm^4]$	$I_{steiner}$ $[mm^4]$	I_{tot} $[mm^4]$	$E \times I$ $[Nmm^2]$	**Percentage [%]**
Concrete	3.0×10^4	3.912×10^4	3.171×10^6	$^3.211 \times 10^6$	9.632×10^{10}	61
Cracked concrete	3.0×10^4	3.040×10^6	1.868×10^6	4.907×10^6	4.907×10^{10}	31
Top reinforcement mesh	2.1×10^5	3.217×10^3	5.754×10^4	6.076×10^4	1.276×10^{10}	8
Positive bending stiffness with only top mesh $EI_{ts,pos,1}$ $[N/mm^2]$					1.581×10^{11}	100

With this the bending stiffness of the top slab under a negative bending moment only the top mesh is now known.

A NEGATIVE BENDING MOMENT ACTING ON A CROSS-SECTION WITH BOTH A TOP AND A BOTTOM REINFORCEMENT MESH

The three equations governing the equilibrium from the previous section are now split into four equations because the similarity of the strain diagrams is expanded by another triangle, that of the added reinforcement

mesh. The situation that is considered can be seen in figure D.3d. The four equilibrium equations are implemented in equations D.32, D.33, D.34 and D.35 respectively, while doing this it is assumed that the neutral axis of the cross-section is situated above the position of the top reinforcement mesh. This will be checked at a later stage of course.

$$\sum F_x = 0 \rightarrow \frac{1}{2} \times L_{dis} \times x_e \times \epsilon_c \times E_{concr} = \epsilon_{s1} \times A_{s1} \times E_{s1} + \epsilon_{s2} \times A_{s2} \times E_{s2} \tag{D.32}$$

$$\frac{\epsilon_c}{\epsilon_{s2}} = \frac{x_e}{d - x_e} \tag{D.33}$$

$$\frac{\epsilon_{s2}}{\epsilon_{s1}} = \frac{(d - x_e) - (h_{st2} - h_{st1})}{d - x_e} \tag{D.34}$$

$$\sum M_{cs} = 0 \rightarrow \epsilon_{s1} \times A_{s1} \times E_{s1} \times d + \epsilon_{s2} \times A_{s2} \times E_{s2} \times (d - (h_{st2} - h_{st1})) - \frac{1}{2} \times \frac{L_{dis} \times \epsilon_c \times x_e^2 \times E_{concr}}{3} = M_{cr} \tag{D.35}$$

When the values from table D.2, in addition to the values introduced previously, are used the equations from above result in equations D.36, D.37, D.38 and D.39.

$$\sum F_x = 0 \rightarrow \frac{1}{2} \times 200 \times x_e \times \epsilon_c \times 30000 = \epsilon_{s1} \times 67 \times 210000 + \epsilon_{s2} \times 67 \times 210000 \tag{D.36}$$

$$\frac{\epsilon_c}{\epsilon_{s2}} = \frac{x_e}{51 - x_e} \tag{D.37}$$

$$\frac{\epsilon_{s2}}{\epsilon_{s1}} = \frac{(51 - x_e) - (56 - 19)}{51 - x_e} \tag{D.38}$$

$$\sum M_{cs} = 0 \rightarrow \epsilon_{s1} \times 67 \times 210000 \times 51 + \epsilon_{s2} \times 67 \times 210000 \times (51 - (56 - 19)) - \frac{1}{2} \times \frac{200 \times \epsilon_c \times x_e^2 \times 30000}{3} = 3.61 \times 10^5 \tag{D.39}$$

The four equations above can be solved for the four unknown factors ϵ_c, ϵ_{s1}, ϵ_{s2} and x_e. With the height of the compression zone just after cracking of the concrete occurs now known, it can be checked whether the initial assumption about the position of the top reinforcement was correct. The values resulting from the calculations are shown in table D.12.

Table D.12: The values of the unknowns found trough solving the equilibrium equations for the cross-section.

Parameters	Values	Unit
x_e	13.389	mm
ϵ_c	0.196×10^{-3}	–
ϵ_{s1}	0.550×10^{-3}	–
ϵ_{s2}	0.009×10^{-3}	–

The height of the compressive zone is indeed smaller than the height at which the top reinforcement mesh is located. Now that the stress and strain diagrams are completely known. The next step is to calculate the height of the neutral axis of the cross-section. This is done by implementing the formula shown in equation D.40.

$$z_c = \frac{\sum \left(y_{C,i} \times E_i \times A_i \right)}{\sum \left(E_i \times A_i \right)} \tag{D.40}$$

This is done for all components of the cross-section in table D.7.
With the height of the neutral axis known, the bending stiffness of the cross-section can now be calculated according to formula D.41.

Table D.13: This table displays the computation of the height of the centre of gravity of the cross-section.

Component	**Young's modulus E** $[N/mm^2]$	**Width b** $[mm]$	**Height h** $[mm]$	**Surface area A** $[mm^2]$	**Height centre of gravity** y_c $[mm]$	$y_c \times E \times A$ $[Nmm]$	$E \times A[N]$	$\frac{y_c \times E \times A}{\sum E \times A}$ $[mm]$
Concrete	3.0×10^4	200	13.38	2676.0	63.31	5.083×10^9	8.028×10^7	24.48
Cracked concrete	3.0×10^4	200	56.620	11324.0	28.31	3.206×10^9	1.132×10^8	15.44
Top reinforcement mesh	2.1×10^5	–	–	67	19	2.674×10^8	1.407×10^7	1.29
Bottom reinforcement mesh	2.1×10^5	–	–	67	56	7.882×10^8	1.407×10^7	3.80
Sum						9.344×10^9	2.076×10^8	
Height centre of gravity z_c								41.21

$$EI_{ts} = \sum \left(E_i \times (I_{eigen,i} + I_{steiner,i}) \right) \tag{D.41}$$

This is done for all components of the cross-section in table D.14.
With this the bending stiffness of the top slab under a negative bending moment both the top mesh and the bottom mesh is now known.

Table D.14: This table displays all the components used for the computation of the bending stiffness of the cross-section.

Component	**Young's modulus E** $[N/mm^2]$	I_{eigen} $[mm^4]$	$I_{steiner}$ $[mm^4]$	I_{tot} $[mm^4]$	$E \times I$ $[Nmm^2]$	**Percentage [%]**
Concrete	3.0×10^4	3.992×10^4	3.190×10^6	3.229×10^6	9.688×10^{10}	77
Cracked concrete	3.0×10^4	8.874×10^5	9.268×10^5	1.814×10^6	1.814×10^{10}	14
Top reinforcement mesh	2.1×10^5	3.217×10^3	3.307×10^4	3.629×10^4	7.621×10^9	6
Bottom reinforcement mesh	2.1×10^5	3.217×10^3	1.465×10^4	1.787×10^4	3.753×10^9	3
Positive bending stiffness with top and bottom meshes $EI_{ts,pos,1}$ $[N/mm^2]$					1.264×10^{11}	100

D.1.3. COMPARRISON OF BENDING STIFFNESSES

Now that the bending stiffness of the top part of the composite slab is computed for all four situations they can be used in the analytical model. To give a convenient overview, they have been placed in table D.15.

Table D.15: This table displays the bending stiffness of the top part of the composite slab in all four of the scenarios of load and reinforcement geometry.

Situation	**Bending stiffness** EI_{ts} $[Nmm^2]$
Positive bending moment + only top mesh	4.906×10^{10}
Positive bending moment + top and bottom mesh	1.520×10^{11}
Negative bending moment + only top mesh	1.581×10^{11}
Negative bending moment + top and bottom mesh	1.264×10^{11}

D.1.4. PLASTIC BENDING BEHAVIOUR OF THE TOP SLAB

As already discussed in chapter 5 the top slab has a certain bending stiffness, but when the end of the linear elastic zone is reached the behaviour changes. It is assumed that the bending moment will remain constant and that the bending stiffness decreases to accommodate the increasing rotation of the cross-section. By using the same method as done before and assuming yielding in the reinforcement bars the elastic moment capacity of top slab can be calculated. This process is very similar to the calculations done in the previous section therefore only the results are shown in table D.16. Then using equation D.42, the rotation of the cross-section at that point can be found.

The next step is to determine at what point failure will occur in the top slab. It is assumed that failure will occur when the concrete in the compression zone reaches the ultimate compressive strain of 3.5×10^{-3}. Since the relation with the strains of the reinforcement is known, the rotation of the cross-section can be found from this assumption. The moment is still assumed to be constant and the ultimate rotation κ_u is also known and by again using equation D.42 the corresponding ultimate bending stiffness can be obtained. Both the ultimate rotation and the corresponding bending stiffness are shown in table D.16. This is done for both directions. It is noted that the unreinforced top slab only reaches the cracking moment capacity of the concrete and fails immediately after that since there is no reinforcement present which could bear the force. The values showed in the table below have been visualized in the graph in figure D.4. The bending stiffness of the points in between the elastic phase and the ultimate rotation can be determined with equation D.42 again. Now the behaviour of the bending stiffness of the top slab from elastic phase until failure is known.

Type of top slab (L_{dis} = $200mm$)	**0 meshes**	**1 mesh**	**2 meshes**
Positive elastic moment capacity M_e+	0.46×10^{6}	0.22×10^{6}	1.92×10^{6}
Positive elastic rotation limit κ_e	2.67×10^{-6}	4.47×10^{-6}	1.26×10^{-5}
Positive ultimate rotation limit κ_u	–	4.47×10^{-6}	1.26×10^{-5}
Positive bending stiffness at ultimate rotation EI_{u+}	–	5.70×10^{8}	8.28×10^{9}
Relative remaining bending stiffness at ultimate limit $EI_{\%+}$	–	1.2	5.4
Negative elastic moment capacity M_e-	0.46×10^{6}	1.69×10^{6}	1.69×10^{6}
Negative elastic rotation limit κ_e	2.67×10^{-6}	1.07×10^{-5}	1.33×10^{-5}
Negative ultimate rotation limit κ_u	–	2.63×10^{-4}	2.64×10^{-4}
Negative bending stiffness at ultimate rotation EI_{u-}	–	6.41×10^{9}	6.38×10^{9}
Relative remaining bending stiffness at ultimate limit $EI_{\%-}$	–	4.1	5.1

Table D.16: The values used for the M-κ-diagram of the top slab.

$$M = EI \times \kappa \tag{D.42}$$

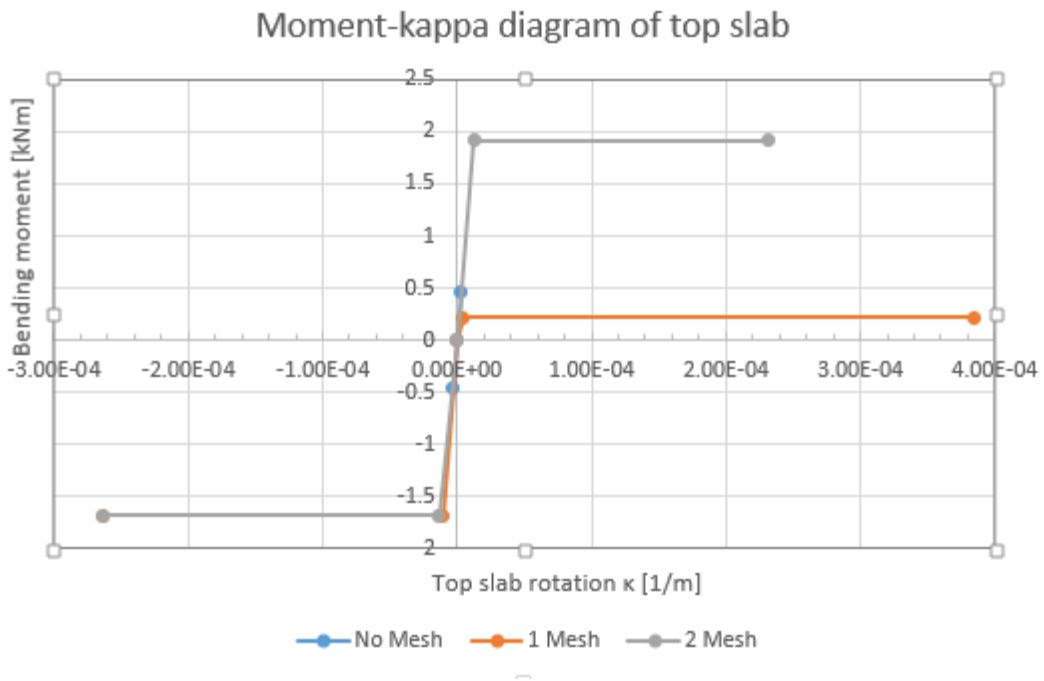

Figure D.4: The bending moment-κ relationship for each of the top slab types. The bending stiffness can be determined with this graph.

D.2. BENDING STIFFNESS OF THE RIB

The bending stiffness of the ribs influences both the overall deflection of the composite slab and the horizontal distribution of the concentrated load. It's correct determination is therefore of importance. As with the top part of the composite slab the ribs have a bending stiffness before any load is applied and before the concrete has started cracking. After the acting bending moment becomes to large, non-compressive zone parts of the cross-section will crack and will reduce the bending moment of the rib. The same steps will be taken as for the top part of the composite slab: the uncracked bending moment will be computed, then the cracking moment of ribs is determined and at finally the bending moment of the cracked ribs is calculated. The cross-section of the rib that is used to analyse the bending stiffness is shown in figure D.5.
The values belonging to the variables that will be used in this section are all displayed in table D.17.
Before the bending stiffness can be calculated, the height of the neutral axis needs to be determined first. Then the bending stiffness of the rib sections can be computed. On both of these computations the presence or absence of the reinforcement meshes will have an influence. The influence will be quite small, but it cannot be neglected until the size of their influence is known. Therefore three situations are considered.

1. No reinforcement meshes present
2. Only top reinforcement mesh is present
3. Both top and bottom reinforcement meshes are present

Parameters	Values	Units
Reinforcement meshes (top and bottom)	$\varnothing 8-150$	mm
h_{sl1}	27	mm
h_{sl2}	48	mm
$h_{s,ab}$	50	mm
h_c	70	mm
h_a	210	mm
B_{bot}	56	mm
B_{rib}	175	mm
B_{tot}	600	mm
$E_{concr,uc}$	30000	N/mm^2
$E_{concr,cr}$	10000	N/mm^2
A_{s1}	67	mm^2
A_{s2}	67	mm^2
E_{s1}	210000	N/mm^2
E_{s2}	210000	N/mm^2
$E_{s,ab}$	210000	N/mm^2
$A_{a,eff}$	572.10	mm^2
E_a	210000	N/mm^2
Height neutral axis of steel profile to top flange $z_{a,eff}$	141.5	mm
Height centre of gravity of trough area from bottom flange	123.0	mm
$I_{a,eff}$	4.20×10^6	mm^4

Table D.17: The values of the parameters used to calculate the bending stiffness of the ribs.

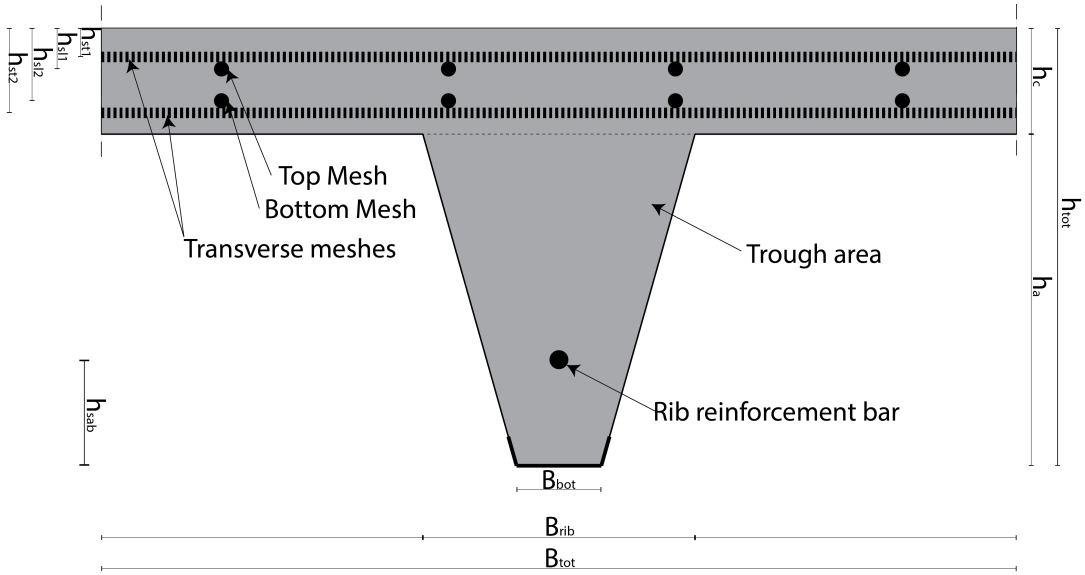

Figure D.5: The cross-section of a single rib

D.2.1. BENDING STIFFNESS OF THE UNCRACKED RIB

The height of the neutral axis needs to be determined first. This is done by implementing equation D.43. The results of this computations for all scenarios are shown in tables D.18, D.19 and D.20 respectively.

$$z_{c,r} = \frac{\sum \left(y_{C,i} \times E_i \times A_i \right)}{\sum \left(E_i \times A_i \right)} \tag{D.43}$$

The tables above show that the height ot the centre of gravity is slightly influenced by the presence of the reinforcement meshes, although not by much. The bending stiffnesses correlating those centres of gravity are computed in tables D.21, D.22 and D.23.

The computed bending moments from tables D.21, D.22 and D.23 are summarized in table D.24. The difference between the bending stiffnesses with or without reinforcement meshes are also displayed. The difference caused by the presence or absence of the reinforcement meshes is not very large, yet it is not small is enough to be classified as negligible.

Table D.18: This table displays the computation of the height of the centre of gravity of the uncracked cross-section without reinforcement meshes.

Uncracked and no reinforcement meshes in the top slab								
Component	**Young's modulus E** $[N/mm^2]$	**Width b** $[mm]$	**Height h** $[mm]$	**Surface area A** $[mm^2]$	**Height centre of gravity** y_c $[mm]$	$y_c \times E \times A$ $[Nmm]$	$E \times A[N]$	$\frac{y_c \times E \times A}{\sum E \times A}$ $[mm]$
Concrete of the top slab	3.0×10^4	600	70	42000	35	4.410×10^{10}	1.260×10^9	20.69
Concrete in the trough of the rib	3.0×10^4	56&175	210	24255	157	1.142×10^{11}	7.277×10^8	53.59
Top reinforcement mesh	2.1×10^5	–	–	–	–	–	–	–
Bottom reinforcement mesh	2.1×10^5	–	–	–	–	–	–	–
Rib reinforcement bar	2.1×10^5	–	–	113.1	230	5.463×10^9	2.375×10^7	2.56
steel profiled deck	2.1×10^5	–	–	572.1	211.5	2.541×10^{10}	1.201×10^8	11.92
Sum						1.892×10^{11}	2.132×10^9	
Height centre of gravity z_c								86.76

Table D.19: This table displays the computation of the height of the centre of gravity of the uncracked cross-section with only the top reinforcement mesh.

Uncracked and only top reinforcement mesh in the top slab								
Component	**Young's modulus E** $[N/mm^2]$	**Width b** $[mm]$	**Height h** $[mm]$	**Surface area A** $[mm^2]$	**Height centre of gravity** y_c $[mm]$	$y_c \times E \times A$ $[Nmm]$	$E \times A[N]$	$\frac{y_c \times E \times A}{\sum E \times A}$ $[mm]$
Concrete of the top slab	3.0×10^4	600	70	42000	35	4.410×10^{10}	1.260×10^9	20.29
Concrete in the trough of the rib	3.0×10^4	56&175	210	24255	157	1.142×10^{11}	7.277×10^8	52.54
Top reinforcement mesh	2.1×10^5	–	–	201.1	27	1.140×10^9	4.222×10^7	0.52
Bottom reinforcement mesh	2.1×10^5	–	–	–	–	–	–	–
Rib reinforcement bar	2.1×10^5	–	–	113.1	230	5.463×10^9	2.375×10^7	2.51
steel profiled deck	2.1×10^5	–	–	572.1	211.5	2.541×10^{10}	1.201×10^8	11.69
Sum						1.903×10^{11}	2.174×10^9	
Height centre of gravity z_c								87.56

Table D.20: This table displays the computation of the height of the centre of gravity of the uncracked cross-section with both reinforcement meshes.

Uncracked and both reinforcement meshes in the top slab								
Component	**Young's modulus E** $[N/mm^2]$	**Width b** $[mm]$	**Height h** $[mm]$	**Surface area A** $[mm^2]$	**Height centre of gravity** y_c $[mm]$	$y_c \times E \times A$ $[Nmm]$	$E \times A[N]$	$\frac{y_c \times E \times A}{\sum E \times A}$ $[mm]$
Concrete of the top slab	3.0×10^4	600	70	42000	35	4.410×10^{10}	1.260×10^9	19.90
Concrete in the trough of the rib	3.0×10^4	56&175	210	24255	157	1.142×10^{11}	7.277×10^8	51.54
Top reinforcement mesh	2.1×10^5	–	–	201.1	27	1.140×10^9	4.222×10^7	0.51
Bottom reinforcement mesh	2.1×10^5	–	–	67	56	1.140×10^9	4.222×10^7	0.91
Rib reinforcement bar	2.1×10^5	–	–	113.1	230	5.463×10^9	2.375×10^7	2.47
steel profiled deck	2.1×10^5	–	–	572.1	211.5	2.541×10^{10}	1.201×10^8	11.46
Sum						1.924×10^{11}	2.216×10^9	
Height centre of gravity z_c								86.80

Table D.21: This table displays all the components used for the computation of the bending stiffness of the uncracked cross-section without reinforcement meshes.

Component	**Young's modulus E** $[N/mm^2]$	I_{eigen} $[mm^4]$	$I_{steiner}$ $[mm^4]$	I_{tot} $[mm^4]$	$E \times I$ $[Nmm^2]$	**Percentage [%]**
Concrete of the top slab	3.0×10^4	1.715×10^7	1.214×10^8	1.385×10^8	4.156×10^{12}	31.6
Concrete in the trough of the rib	3.0×10^4	8.125×10^7	1.129×10^8	1.941×10^8	5.823×10^{12}	44.3
Top reinforcement mesh	2.1×10^5	–	–	–	–	0.0
Bottom reinforcement mesh	2.1×10^5	–	–	–	–	0.0
Rib reinforcement bar	2.1×10^5	1.629×10^4	2.256×10^6	2.273×10^6	4.772×10^{11}	3.6
Steel profiled deck	2.1×10^5	4.918×10^6	8.615×10^6	1.281×10^7	2.691×10^{12}	20.5
Positive bending stiffness without meshes $EI_{rib,uc,1}$ $[N/mm^2]$					1.315×10^{13}	100

Table D.22: This table displays all the components used for the computation of the bending stiffness of the uncracked cross-section with only the top reinforcement mesh.

Component	**Young's modulus E** $[N/mm^2]$	I_{eigen} $[mm^4]$	$I_{steiner}$ $[mm^4]$	I_{tot} $[mm^4]$	$E \times I$ $[Nmm^2]$	**Percentage [%]**
Concrete of the top slab	3.0×10^4	1.715×10^7	1.160×10^8	1.332×10^8	3.995×10^{12}	30.0
Concrete in the trough of the rib	3.0×10^4	8.125×10^7	1.169×10^8	1.981×10^8	5.944×10^{12}	44.7
Top reinforcement mesh	2.1×10^5	3.217×10^3	7.373×10^5	7.405×10^5	1.555×10^{12}	1.2
Bottom reinforcement mesh	2.1×10^5	–	–	–	–	0.0
Rib reinforcement bar	2.1×10^5	1.629×10^4	2.295×10^6	2.311×10^6	4.853×10^{11}	3.6
Steel profiled deck	2.1×10^5	4.918×10^6	8.784×10^6	1.298×10^7	2.726×10^{12}	20.5
Positive bending stiffness with top meshes $EI_{rib,uc,2}$ $[N/mm^2]$					1.331×10^{13}	100

Table D.23: This table displays all the components used for the computation of the bending stiffness of the uncracked cross-section with both reinforcement meshes.

Component	**Young's modulus E** $[N/mm^2]$	I_{eigen} $[mm^4]$	$I_{steiner}$ $[mm^4]$	I_{tot} $[mm^4]$	$E \times I$ $[Nmm^2]$	**Percentage [%]**
Concrete of the top slab	3.0×10^4	1.715×10^7	1.127×10^8	1.299×10^8	3.896×10^{12}	29.1
Concrete in the trough of the rib	3.0×10^4	8.125×10^7	1.194×10^8	2.007×10^8	6.020×10^{12}	45.0
Top reinforcement mesh	2.1×10^5	3.217×10^3	7.191×10^5	7.223×10^5	1.517×10^{12}	1.1
Bottom reinforcement mesh	2.1×10^5	3.217×10^3	3.027×10^5	3.059×10^5	6.425×10^{10}	0.5
Rib reinforcement bar	2.1×10^5	1.629×10^4	2.319×10^6	2.335×10^6	4.904×10^{11}	3.7
Steel profiled deck	2.1×10^5	4.918×10^6	8.891×10^6	1.309×10^7	2.749×10^{12}	20.6
Positive bending stiffness with top and bottom meshes $EI_{rib,uc,3}$ $[N/mm^2]$					1.337×10^{13}	100

Table D.24: This table displays an overview of the bending stiffness of the uncracked ribs with or without the presence of the reinforcement meshes in the top part of the cross-section.

Situation	**Bending stiffness** $EI_{r,uc}$ $[Nmm^2]$	**Difference [%]**
Both top and bottom reinforcement mesh	1.337×10^{13}	0.0
Only top reinforcement mesh	1.331×10^{13}	0.45
No top or bottom mesh	1.315×10^{13}	1.65

D.2.2. CRACKING BENDING MOMENT OF THE RIB

The bending stiffness of the ribs before cracking occurs is now known. The following step is to calculate the cracking moment of the ribs. Again only the concrete of the cross-section will be taken into account for this calculation, because it is assumed that the steel profiled deck and the steel reinforcement meshes are not yet active.

First of all the height of the neutral axis has to be determined again. In this calculation the surface area of the concrete in the top part of the composite slab and the concrete in the trough area are the only factors. The calculation is done in equations D.44, D.45 and D.46, which calculate the surface of are of the trough A_{trough}, the distance of the centre of gravity of the trough from the bottom flange $z_{c,trough}$ and the height of the centre of gravity of the total cross-section $z_{c,rib,cr}$ respectively. In this calculation the Young's modulus of the concrete is omitted because this variable is constant in both concrete areas, since no cracking has occurred yet. The cross-section that is considered is depicted in figure D.6.

$$\begin{aligned} A_{trough} = h_a \times \frac{B_{bot} + B_{rib}}{2} = \\ 210 \times \frac{56 + 175}{2} = \\ 24255.0 mm^2 \end{aligned} \tag{D.44}$$

$$\begin{aligned} z_{c,trough} = \frac{1}{3} \times \frac{0.5 \times B_{bot} + B_{rib}}{0.5 \times B_{bot} + 0.5 \times B_{rib}} = \\ \frac{1}{3} \times \frac{0.5 \times 56 + 175}{0.5 \times 56 + 0.5 \times 175} = \\ 123.0 mm \end{aligned} \tag{D.45}$$

$$\begin{aligned} z_{c,rib,cr} = \frac{\sum \left(y_{C,i} \times A_i \right)}{\sum A_i} = \\ \frac{h_c \times 0.5 \times h_c \times B_{tot} + A_{trough} \times (h_{tot} - z_{c,trough})}{B_{tot} \times h_c + A_{trough}} = \\ \frac{210 \times 0.5 \times 210 \times 600 + 24255 \times (280 - 123)}{600 \times 70 + 24255} = \\ 79.65 mm \end{aligned} \tag{D.46}$$

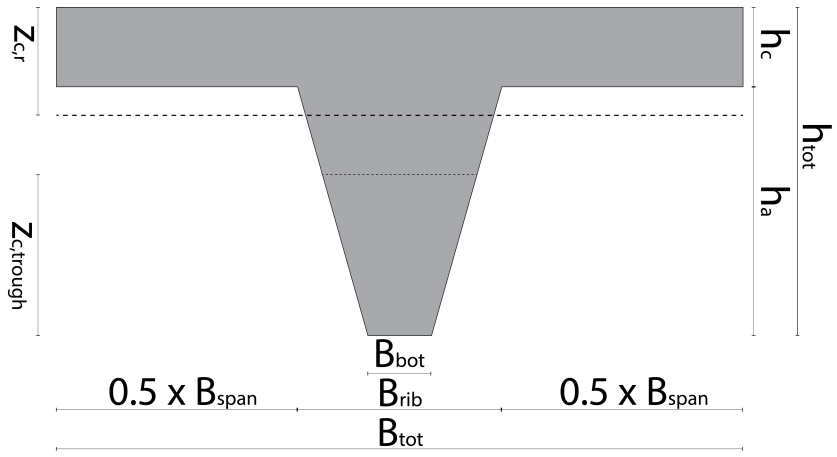

Figure D.6: The cross-section of the rib analysed during the calculation of the cracking moment of the rib.

With the height of the centre of gravity known, the following step is to compute the section modulus of the cross-section with regards to the stress in the bottom fibres of the cross-section. The bottom fibres are chosen here since the goal is after all the determine when the concrete will start to crack due to an excessive tensile stress. This section modulus for the bottom is computed in equation D.48 and the inertia of the trough that is used there is calculated in equation D.47.

$$I_{trough} = \frac{B_{bot}^2 \times 4 \times B_{bot} \times B_{rib} + B_{rib}^2}{36 \times (B_{bot} + B_{rib})} \times h_a^3 = \frac{56^2 \times 4 \times 56 \times 175 + 175^2}{36 \times (56 + 175)} \times 210^3 = 8.125 \times 10^7 mm^4 \tag{D.47}$$

$$W_{rib} = \frac{I_{rib}}{h_{tot} - z_{c,rib,cr}} = \frac{\frac{1}{12} \times B_{tot} \times h_c^3 + B_{tot} \times h_c \times (z_{c,rib,cr} - 0.5 \times h_c)^2 + I_{trough} + A_{trough} \times (h_{tot} - z_{c,trough} - z_{c,rib,cr})^2}{h_{tot} - z_{c,rib,cr}} = \frac{\frac{1}{12} \times 600 \times 70^3 + 600 \times 70 \times (79.65 - 0.5 \times 70)^2 + 8.125 \times 10^7 + 24255 \times (280 - 123 - 79.65)^2}{280 - 79.65} = 3.271 \times 10^8 mm^3 \tag{D.48}$$

The final step to be taken is to calculate the bending moment $M_{rib,cr}$ at which the concrete in the ribs will start to crack. This value depends not only on the geometry of the cross-section but of course also on the tensile strength of the concrete class that will be used in the composite slab. The computation is done in equation D.49.

$$M_{rib,cr} = W_{rib} \times f_{ctm} = 3.271 \times 10^8 \times 2.2 = 3.61 \times 10^6 nmm^2 \tag{D.49}$$

D.2.3. BENDING STIFFNESS OF THE CRACKED RIB

After the concrete in the rib has cracked there will be a new equilibrium between the compression zone and the cracked concrete on one side and the steel reinforcement and steel profiled deck on the other. The cracked concrete is assumed to have approximately a third of the stiffness of that of the uncracked concrete. With this information the steps of section D.2.1 can be repeated but now the concrete in the trough of the rib is cracked and a new bending stiffness can be computed.
The height of the neutral axis needs to be determined first. This is done by implementing equation D.50. The results of this computations for all scenarios are shown in tables D.25, D.26 and D.27 respectively.

$$z_{c,r} = \frac{\sum \left(y_{C,i} \times E_i \times A_i \right)}{\sum \left(E_i \times A_i \right)} \tag{D.50}$$

The tables above show that the height ot the centre of gravity is slightly influenced by the presence of the reinforcement meshes, although not by much. The bending stiffnesses correlating those centres of gravity are computed in tables D.28, D.29 and D.30.
The computed bending moments from tables D.21, D.22 and D.23 are summarized in table D.31. The difference between the bending stiffnesses with or without reinforcement meshes are also displayed. The difference caused by the presence or absence of the reinforcement meshes is not very large, yet it is not small is enough to be classified as negligible. The bending stiffnesses of both the cracked and uncracked ribs and the difference in percentage are shown in table D.32.

Table D.25: This table displays the computation of the height of the centre of gravity of the cracked cross-section without reinforcement meshes.

Uncracked and no reinforcement meshes in the top slab								
Component	**Young's modulus E** $[N/mm^2]$	**Width b** $[mm]$	**Height h** $[mm]$	**Surface area A** $[mm^2]$	**Height centre of gravity** y_c $[mm]$	$y_c \times E \times A$ $[Nmm]$	$E \times A[N]$	$\frac{y_c \times E \times A}{\sum E \times A}$ $[mm]$
Concrete of the top slab	3.0×10^4	600	70	42000	35	4.410×10^{10}	1.260×10^9	26.79
Concrete in the trough of the rib	1.0×10^4	56&175	210	24255	157	3.807×10^{10}	2.426×10^8	23.12
Top reinforcement mesh	2.1×10^5	–	–	–	–	–	–	–
Bottom reinforcement mesh	2.1×10^5	–	–	–	–	–	–	–
Rib reinforcement bar	2.1×10^5	–	–	113.1	230	5.463×10^9	2.375×10^7	3.32
steel profiled deck	2.1×10^5	–	–	572.1	211.5	2.541×10^{10}	1.201×10^8	15.43
Sum						1.130×10^{11}	1.646×10^9	
Height centre of gravity z_c								68.66

Table D.26: This table displays the computation of the height of the centre of gravity of the cracked cross-section with only the top reinforcement mesh.

Uncracked and only top reinforcement mesh in the top slab								
Component	**Young's modulus E** $[N/mm^2]$	**Width b** $[mm]$	**Height h** $[mm]$	**Surface area A** $[mm^2]$	**Height centre of gravity** y_c $[mm]$	$y_c \times E \times A$ $[Nmm]$	$E \times A[N]$	$\frac{y_c \times E \times A}{\sum E \times A}$ $[mm]$
Concrete of the top slab	3.0×10^4	600	70	42000	35	4.410×10^{10}	1.260×10^9	26.12
Concrete in the trough of the rib	1.0×10^4	56&175	210	24255	157	3.807×10^{10}	2.426×10^8	22.55
Top reinforcement mesh	2.1×10^5	–	–	201.1	27	1.140×10^9	4.222×10^7	0.68
Bottom reinforcement mesh	2.1×10^5	–	–	–	–	–	–	–
Rib reinforcement bar	2.1×10^5	–	–	113.1	230	5.463×10^9	2.375×10^7	3.23
steel profiled deck	2.1×10^5	–	–	572.1	211.5	2.541×10^{10}	1.201×10^8	15.04
Sum						1.142×10^{11}	1.689×10^9	
Height centre of gravity z_c								67.62

Table D.27: This table displays the computation of the height of the centre of gravity of the cracked cross-section with both reinforcement meshes.

Uncracked and both reinforcement meshes in the top slab							
Component	**Young's modulus E** $[N/mm^2]$	**Width b** $[mm]$	**Height h** $[mm]$	**Surface area A** $[mm^2]$	**Height centre of gravity** y_c $[mm]$	$y_c \times E \times A$ $[Nmm]$	$E \times A[N]$	$\frac{y_c \times E \times A}{\sum E \times A}$ $[mm]$
Concrete of the top slab	3.0×10^4	600	70	42000	35	4.410×10^{10}	1.260×10^9	25.48
Concrete in the trough of the rib	1.0×10^4	56&175	210	24255	157	3.807×10^{10}	2.426×10^8	22.00
Top reinforcement mesh	2.1×10^5	–	–	201.1	27	1.140×10^9	4.222×10^7	0.66
Bottom reinforcement mesh	2.1×10^5	–	–	67	56	1.140×10^9	4.222×10^7	1.17
Rib reinforcement bar	2.1×10^5	–	–	113.1	230	5.463×10^9	2.375×10^7	3.16
steel profiled deck	2.1×10^5	–	–	572.1	211.5	2.541×10^{10}	1.201×10^8	14.68
Sum						1.162×10^{11}	1.731×10^9	
Height centre of gravity z_c								67.14

Table D.28: This table displays all the components used for the computation of the bending stiffness of the cracked cross-section without reinforcement meshes.

Component	**Young's modulus E** $[N/mm^2]$	I_{eigen} $[mm^4]$	$I_{steiner}$ $[mm^4]$	I_{tot} $[mm^4]$	$E \times I$ $[Nmm^2]$	**Percentage [%]**
Concrete of the top slab	3.0×10^4	1.715×10^7	4.758×10^7	6.473×10^7	1.942×10^{12}	22.6
Concrete in the trough of the rib	1.0×10^4	8.125×10^7	1.892×10^8	2.704×10^8	2.704×10^{12}	31.4
Top reinforcement mesh	2.1×10^5	–	–	–	–	0.0
Bottom reinforcement mesh	2.1×10^5	–	–	–	–	0.0
Rib reinforcement bar	2.1×10^5	1.629×10^4	2.944×10^6	2.960×10^6	6.217×10^{11}	7.2
Steel profiled deck	2.1×10^5	4.918×10^6	1.167×10^7	1.587×10^7	3.332×10^{12}	38.7
Positive bending stiffness without meshes $EI_{rib,cr,1}$ $[N/mm^2]$					8.600×10^{12}	100

Table D.29: This table displays all the components used for the computation of the bending stiffness of the cracked cross-section with only the top reinforcement mesh.

Component	**Young's modulus E** $[N/mm^2]$	I_{eigen} $[mm^4]$	$I_{steiner}$ $[mm^4]$	I_{tot} $[mm^4]$	$E \times I$ $[Nmm^2]$	**Percentage [%]**
Concrete of the top slab	3.0×10^4	1.715×10^7	4.468×10^7	6.183×10^7	1.855×10^{12}	21.4
Concrete in the trough of the rib	1.0×10^4	8.125×10^7	1.937×10^8	2.749×10^8	2.749×10^{12}	31.7
Top reinforcement mesh	2.1×10^5	3.217×10^3	3.317×10^5	3.349×10^5	7.033×10^{10}	0.8
Bottom reinforcement mesh	2.1×10^5	–	–	–	–	0.0
Rib reinforcement bar	2.1×10^5	1.629×10^4	2.982×10^6	2.998×10^6	6.297×10^{11}	7.3
Steel profiled deck	2.1×10^5	4.918×10^6	1.184×10^7	1.604×10^7	3.368×10^{12}	38.8
Positive bending stiffness with top meshes $EI_{rib,cr,2}$ $[N/mm^2]$					8.672×10^{13}	100

Table D.30: This table displays all the components used for the computation of the bending stiffness of the cracked cross-section with both reinforcement meshes.

Component	**Young's modulus E** $[N/mm^2]$	I_{eigen} $[mm^4]$	$I_{steiner}$ $[mm^4]$	I_{tot} $[mm^4]$	$E \times I$ $[Nmm^2]$	**Percentage [%]**
Concrete of the top slab	3.0×10^4	1.715×10^7	4.338×10^7	6.053×10^7	1.816×10^{12}	20.9
Concrete in the trough of the rib	1.0×10^4	8.125×10^7	1.957×10^8	2.770×10^8	2.770×10^{12}	31.9
Top reinforcement mesh	2.1×10^5	3.217×10^3	3.239×10^5	3.271×10^5	6.870×10^{10}	0.8
Bottom reinforcement mesh	2.1×10^5	3.217×10^3	7.364×10^4	7.686×10^4	1.614×10^{10}	0.2
Rib reinforcement bar	2.1×10^5	1.629×10^4	3.000×10^6	3.016×10^6	6.334×10^{11}	7.3
Steel profiled deck	2.1×10^5	4.918×10^6	1.192×10^7	1.612×10^7	3.384×10^{12}	39.0
Positive bending stiffness with top and bottom meshes $EI_{rib,cr,3}$ $[N/mm^2]$					8.688×10^{13}	100

Table D.31: This table displays an overview of the bending stiffness of the cracked ribs with or without the presence of the reinforcement meshes in the top part of the cross-section.

Situation	**Bending stiffness** $EI_{r,uc}$ $[Nmm^2]$	**Difference [%]**
Both top and bottom reinforcement mesh	8.688×10^{12}	0.0
Only top reinforcement mesh	8.672×10^{12}	0.18
No top or bottom mesh	8.600×10^{12}	1.01

Table D.32: This table displays an overview of the bending stiffness of the cracked ribs with or without the presence of the reinforcement meshes in the top part of the cross-section.

Situation	**Uncracked bending stiffness** $EI_{rib,uc}$ $[Nmm^2]$	**Cracked bending stiffness** $EI_{rib,cr}$ $[Nmm^2]$	$\frac{EI_{rib,cr}}{EI_{rib,uc}} \times 100$ **[%]**
Both top and bottom reinforcement mesh	1.337×10^{13}	8.688×10^{12}	64.98
Only top reinforcement mesh	1.331×10^{13}	8.688×10^{12}	65.15
No top or bottom mesh	1.315×10^{13}	8.688×10^{12}	65.40

E

FEM MODELLING RESULTS

F

MATERIAL TESTING

F.1. TEST SET UP

The Dowty-Rotel test set-up is used to perform the tension tests on the steel members in the Stevin II laboratory at the University of Technology in Delft. This test set up is shown in Figure F.1a The maximum load capacity of this set up is 250 kN. The Dowty-Rotel test set up is used to perform the tests on the reinforcement bars and the steel deck test pieces. The concrete tests are performed in a different set up, this set up is shown in Figure F.1b. The concrete cubes are loaded in compression and tension to obtain the required material data. The same test set up is used for both tests. The maximum capacity for this set up is 5000 kN.

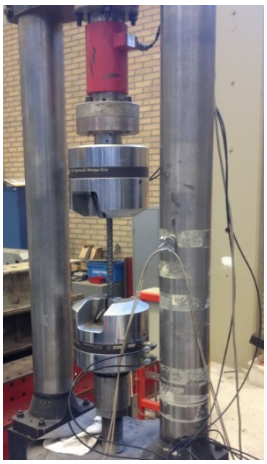

(a) The Dowty-Rotel test set-up

(b) Test set-up for the concrete cubes

Figure F.1: The test set-ups for the material tests

F.1.1. STEEL TESTS

The different steel members are loaded in the Dowty-Rotel test set-up. Steel deck test pieces are cut out of a part of the steel deck. Reinforcement bars Ø8-150 and Ø20 of about 35 centimeter are tested as well.

The force applied to the test specimen and the displacement of the cylinder is measured during the steel tests. This displacement is not the exact displacement of the specimen; slip inside the clamps and other phenomena restrain the possibility to calculate the strain from this data. An extensiometer is used to measure the displacement in the specimen only over a specific length. This device is attached to the test piece and stretches during loading. This displacement removes the contribution of slip in the clamps and follows the displacement of the test specimen to obtain a more reliable displacement pattern, but also has some disadvantages.

The Extensiometer is not capable in following the displacement path very accurately. This device generates friction during the test and results are therefore not very accurate, especially in the elastic part of the σ-ϵ-diagram. The elastic part is furthermore also influenced by other effects, such as warping effects and so on. The elastic part of the diagram is however not the main objective of the tension test.

The objectives of the material tests is to obtain force characteristics of the used material. Especially the yield stress of the different materials is an important aspect. The displacement characteristics are less important; the expectation is that the concrete will crack and will be governing during the laboratory test on the ComFlor210 specimens.

F.1.2. CONCRETE TESTS

Concrete cubes with dimensions 150x150x150 mm are cast at the same moment as the ComFlor210 test specimens were cast. The concrete specifications of the cubes are thus the same as the concrete in the floors. In total 36 test cubes were cast, which will be tested in four series:

1. The 28 days concrete tests
2. Test series performed at the day of the first ComFlor210 test
3. Test series performed at the day of the second ComFlor210 test
4. Test series performed at the day of the third ComFlor210 test

The tests at the day of the experiments makes sure that the analyses can be performed with the actual concrete strength. The 28 day test is executed to verify the strength class of the concrete that the concrete factory provided.

Every test series consists of nine tests: three compression tests and six split tests. The expectation beforehand was that the scatter in the test results of the split tests are greater than the compression tests. The compression test provides the cubic compression strength and the split tests the tension strength of the concrete.

Further details of the tests are considered in section F.4. The steel tests are discussed first, starting with the steel deck tests and followed by the tension tests on the reinforcement. The concrete test are discussed hereafter.

F.2. STEEL DECK TESTS

The first material that will be discussed is the steel deck of the composite floor. Test pieces are cut out of the effective area of the thin steel plate; at the topside of the ribs. This is depicted in figures F.2a and F.2b. The dimensions of the "dog-bone" model are according the Dutch codes [17]. The most important matter in determining the geometric properties is that there is enough difference in the width between the middle and end parts of the test pieces. This makes sure that the stress at the middle part will be governing and failure will occur in this part.

The small cross section will fail due to the increasing load. The extensiometer is used to measure the relative displacement in the middle part of the test pieces. A σ-ϵ-diagram can be constructed if this measuring device is used properly. The "dog-bone" test pieces reduce the length of possible governing cross sections and promote the usage of the extensiometer. This advantage is not the case with the reinforcement test pieces. This will be discussed in the next section. A unbroken and broken test piece is shown in figure F.2c. Eight test specimens are made with equal dimensions.

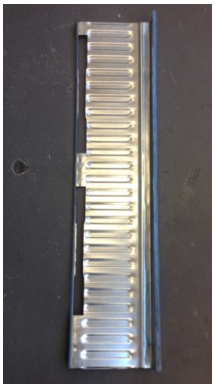

(a) Location close up

(b) Location overview

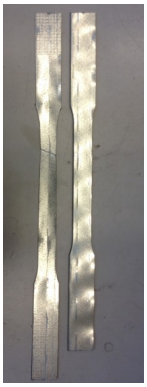

(c) Two (un)broken test pieces

Figure F.2: The test pieces to obtain the material data from the steel deck. The location where they are cut out is also shown.

.

The dimensions of these tension test pieces are shown in table F.1. The steel decks are cold formed to create the desired shape. The test pieces are cut out of the effective area of the steel deck and are therefore influenced by the cold forming process, resulting in dents and slight warping. An accurate thickness could therefore not be measured. The nominal thickness of 1,25 mm is therefore taken for every test piece.

The width of the necking area is measured three times for every specimen. The measuring length is the length that is covered by the extensiometer; this is the initial length of the extensiometer and is used to calculate the strain. Special tubes are made to keep these values constant and to avoid any deviations between the four attachments. A deviation will introduce measuring errors. Figure F.3a and F.3b show an overview and a close-up of the test piece in the test set-up with the extensiometer attached to the middle part of the specimen. Figure F.3c shows four broken test pieces.

Table F.1: The geometric characteristics of the necking area of the steel deck test pieces.

Bar	Thickness [mm]	Width [mm]	Surface [mm^2]	Measuring length [mm]
1	1.25	19.92	24.90	50.1
2	1.25	20.17	25.21	50.1
3	1.25	20.03	25.04	50.1
4	1.25	20.4	25.50	50.1
5	1.25	20.22	25.27	50.1
6	1.25	20.1	25.13	50.1
7	1.25	19.93	24.92	50.1
8	1.25	19.98	24.98	50.1

(a) Overview of the test set-up

(b) Close up of the test set-up

(c) Broken test pieces

Figure F.3: The tension test set-up to obtain the material data from the steel deck

The tests are displacement controlled with two different speeds. A low speed of 0,01 mm/s is required for the elastic part, according to [17]. This speed is kept constant until the hardening starts, the speed is then increased to 0,06 mm/s. The output of the tests is used to create the σ-ϵ diagrams. The force is divided by the initial cross section of the middle part. This results in the engineering stress/strain relation, whereby the cross section is kept constant. The actual cross section reduces however, resulting in a stress that does not show a decrease in the necking phase; this is the true stress/strain relation. This relation is not considered here.

The extensiometer measures the relative displacements at both sides of the test specimen. The average value is divided by the measuring length (as shown in table F.1) to obtain the strain. The σ-ϵ diagrams are constructed and shown in figure F.5. In section F.1 it is already stated that especially the elastic part of this diagram is not very accurate. The objective however of the tests of the steel deck test specimens is to obtain the yield stress. The diagrams indicate a clear yield plateau, so the average stress value of this plateau is the desired yield stress. The inaccurate displacement characteristics are not required to find the yield stress. This will not be the case with the reinforcement meshes with a diameter of 8 mm, as discussed in the next section.

The separate diagrams of figure F.5 are all put together in figure F.4 to compare the results with each other. Tests 1,3 and 7 do not have a necking phase in the σ-ϵ diagram. The governing cross section lies outside the measuring area of the extensiometer. So the necking phase is not found in these tests as is clearly visible in F.4. Figure F.6 illustrates this as well, whereby the left picture shows necking inside the extensiometer and figure F.6b shows necking outside the extensiometer.

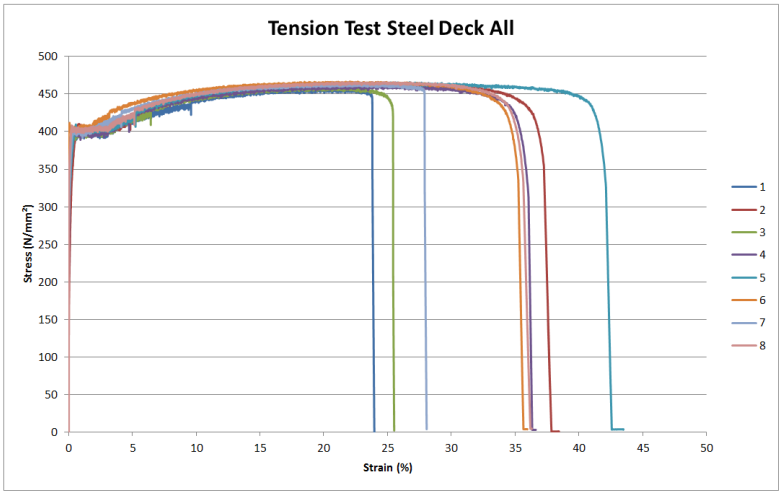

Figure F.4: The eight tensile test on the steel deck test pieces together to make a comparison

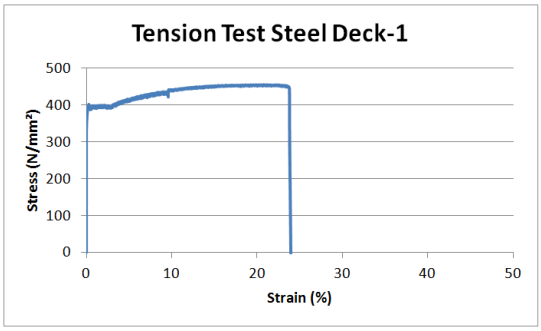

(a) First test

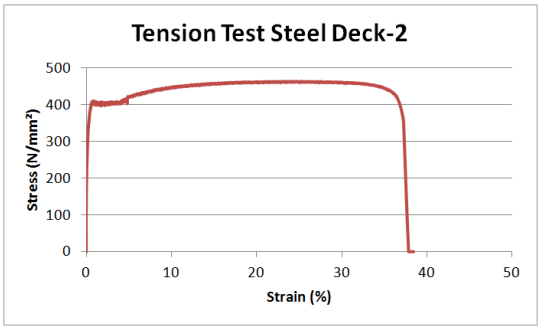

(b) Second test

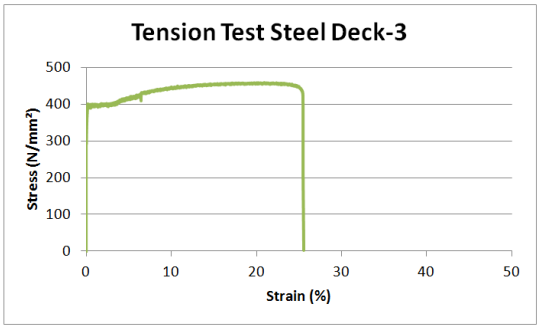

(c) Third test

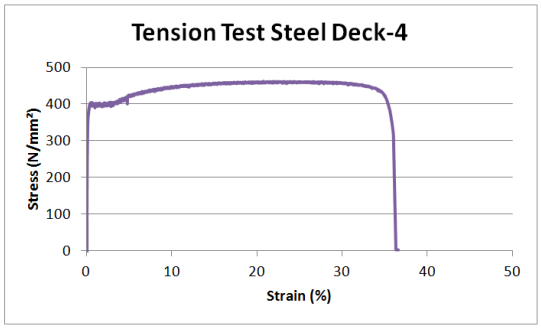

(d) Fourth test

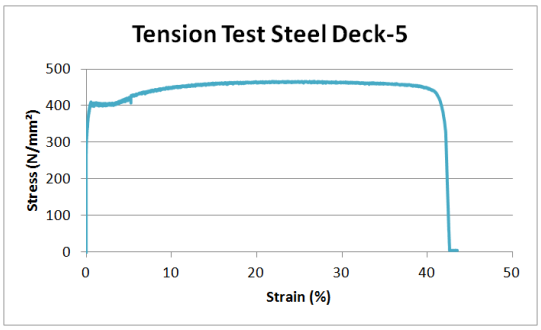

(e) Fifth test

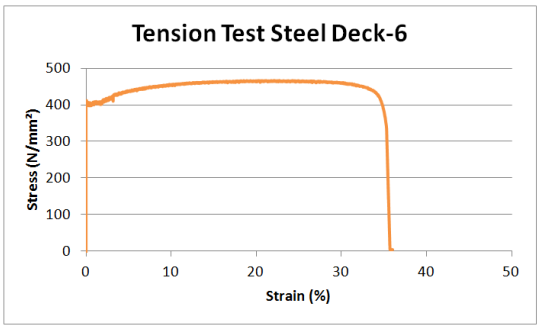

(f) Sixt test

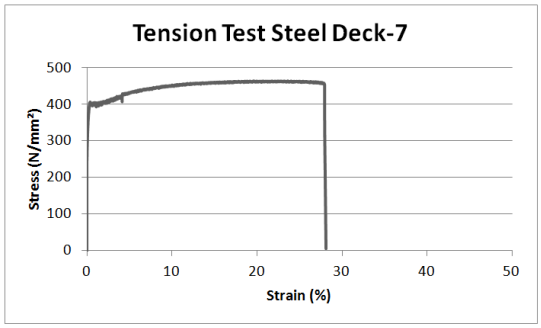

(g) Seventh test

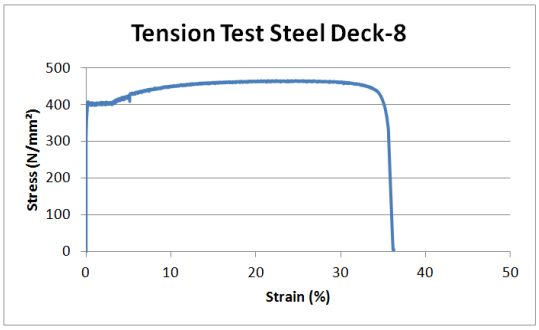

(h) Sixt test

Figure F.5: The tension tests performed on the steel deck test pieces

The σ-ϵ diagrams show a clear yield plateau and a rupture strain that could be expected at normal hot rolled steel, despite the fact that the test pieces are constructed in the cold deformed area of the steel deck. It can be noticed that the cold formed process has (barely) influenced the stress/strain characteristics.

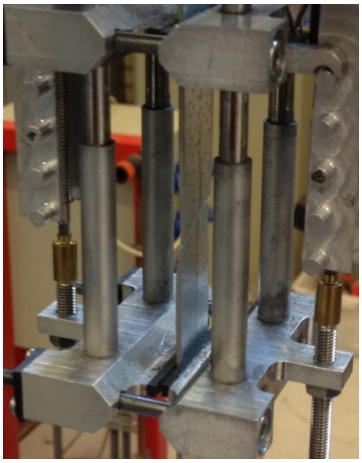

(a) Necking inside extensiometer

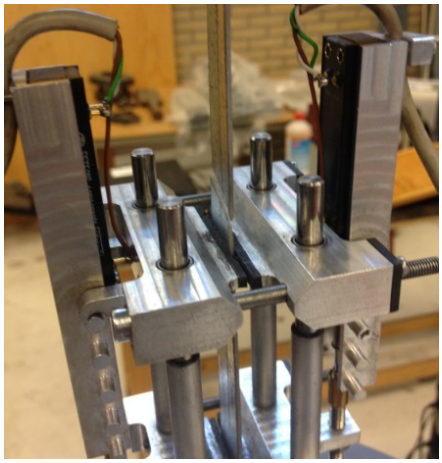

(b) Necking outside extensiometer

Figure F.6: Necking inside and outside the Extensiometer

.

The force characteristics are shown in table F.2. The yield and ultimate stresses are shown and also the fraction between them. The scatter between these values is small. The average value is shown at the bottom of the table, these values are used in the numerical and analytical modelling of the ComFlor210.

Table F.2: The yield and ultimate stress of the steel deck

Bar	Yield stress [MPa]	Ultimate stress [MPa]	Fraction f_u/f_y
1	395.164	456.126	1.154
2	403.274	463.379	1.156
3	396.761	458.649	1.156
4	398.078	461.371	1.159
5	402.414	465.846	1.158
6	404.041	466.823	1.155
7	400.139	463.180	1.158
8	403.322	466.113	1.157
Average	400,399	462,686	1,156

F.3. REINFORCEMENT TESTS

This section will discuss the preparation and test progress of the two types of reinforcement used in the composite floor.

F.3.1. REINFORCEMENT MESH Ø8-150

The reinforcement meshes Ø8-150 are used in two of the three test pieces as discussed in 7. Four test pieces were cut out of a mesh with a length of about 35 centimetre. The welding details remained inside the test pieces, this is clearly visible in figure F.7a. These welds did not influence the test results. Figure F.7b shows a broken and an unbroken test piece.

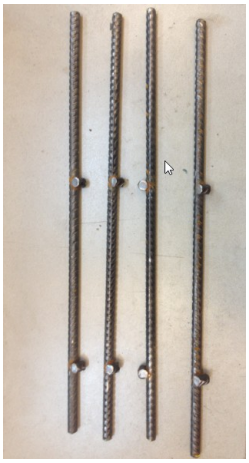

(a) The four test pieces

(b) Two test pieces; broken and unbroken

Figure F.7: Bars of the reinforcement mesh used to perform the tension tests to obtain the material data

.

The exact dimensions should be obtained, just as in the previous section. The ridges on the bars create a non homogeneous diameter. Three test pieces, different ones than the specimens used for the tension tests, were weighed and measured with great care to overcome this problem. The density of steel (7850 $\frac{kg}{m^3}$) is then used to calculate the volume of these reinforcement pieces. A homogeneous cylindrical shape was assumed to calculate a homogeneous diameter for these reinforcement bars. This procedure is illustrated in table F.3. A homogeneous diameter of 7.88 mm was obtained by using this procedure. This value is used to calculate the stresses in the members during testing. It is remarkable that the calculated diameter is smaller than the nominal diameter of 8 mm.

Table F.3: The calculation of the homogeneous reinforcement diameter Ø8.

Bar	Length (mm)	Weight (g)	Volume (mm^3)	Diameter (mm)
1	133.61	50.91	6485.35	7.86
2	132.00	50.86	6478.98	7.91
3	130.88	49.95	6363.06	7.87
Average				7.88

The same test set-up was used as was used with the steel deck test series. A displacement controlled test was executed with a constant speed of 0,01 mm/s. The first force-displacement diagram, shown in figure F.8a, does not contain a clear yield plateau. This force-displacement diagram indicates that the reinforcement bar is cold formed or experienced other treatments to obtain the desired shape and dimensions. The stress at which a permanent strain of 0,2% is reached is the yield stress in this case. The Extensiometer was used on the other three tests to obtain the displacement characteristic of the specimen and the yield stress. The yield stress can not be obtained with the results of the first test; the required displacement characteristics were not sufficiently accurate to calculate the 0,2% proof stress. Figure F.8 shows all four force-displacement diagrams.

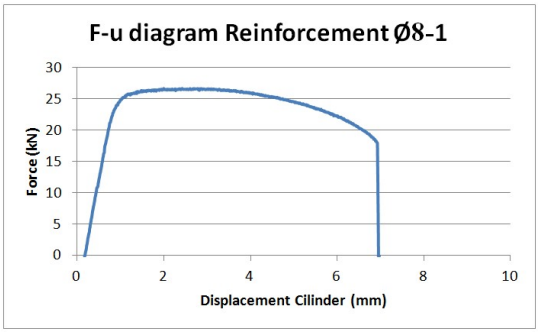

(a) First test

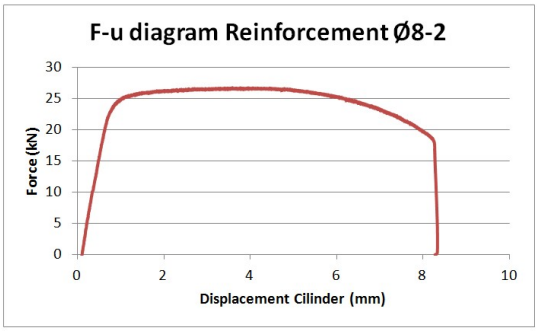

(b) Second test

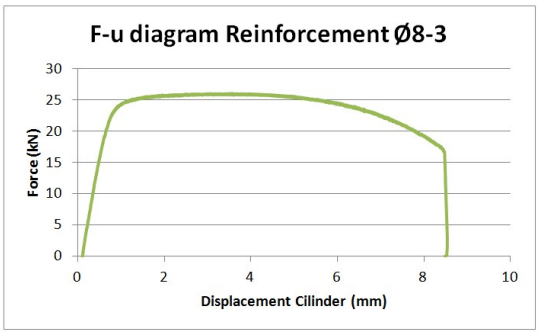

(c) Third test

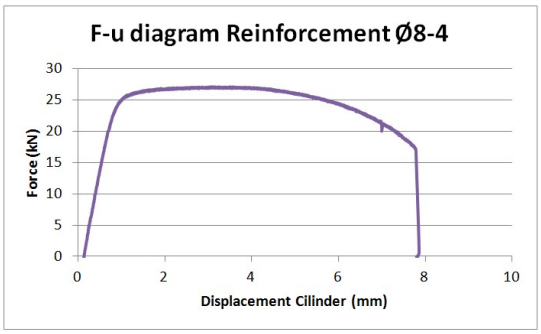

(d) Fourth test

Figure F.8: The F-u-diagram of the tension tests performed on the reinforcement with a diameter of 8 mm

Figure F.9 presents all four force-displacement diagrams in one figure. The stress level is almost the same for all tests, the only significant difference is the scatter in deformation capacity. The reinforcement meshes will not be loaded up to this level; the concrete will crush before these deformation values are reached in the reinforcement. The locations containing weld zones were not governing in all four tests. The heat input did not change the material properties that significantly apparently. The diagrams show a pattern that clearly belongs to steel that experienced some cold deformation or other treatment to obtain the desired shape and dimensions. The welding procedure changes the material properties in a mostly disadvantageous manner, so it is quite remarkable that these zones were not governing.

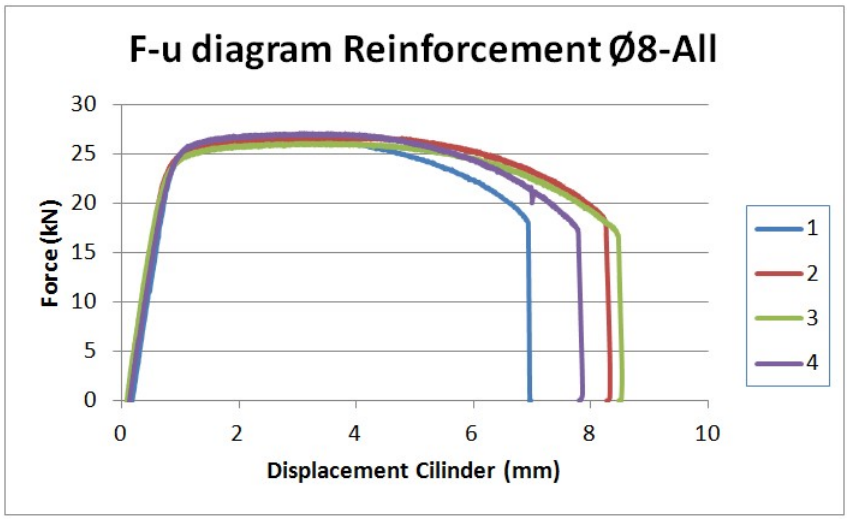

Figure F.9: The four F-u-diagrams of the tensile tests (Ø8) shown together to compare the tests with each other

The extensiometer is used in the same manner as discussed in the previous section on the other three tests.

The only problem is that the reinforcement test specimens have constant cross sectional dimensions along the length of the bars. The governing cross section is therefore harder to find since the extensiometer can monitor only a part of the bar. The chance of failure outside the range of the extensiometer is therefore higher. Necking of the second test specimen occurred in the centre of the test specimen, but the governing cross section was located outside the range of the extensiometer with test three and four. Figure F.10 and F.11 show the different tests to obtain the required material data. The necking in- and outside the range of the extensiometer is clearly visible.

(a) The first test

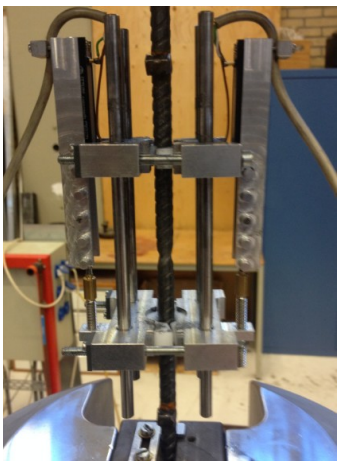

(b) The second test, necking inside extensiometer

Figure F.10: The tension test with and without the extensiometer. Test 1 and 2 respectively

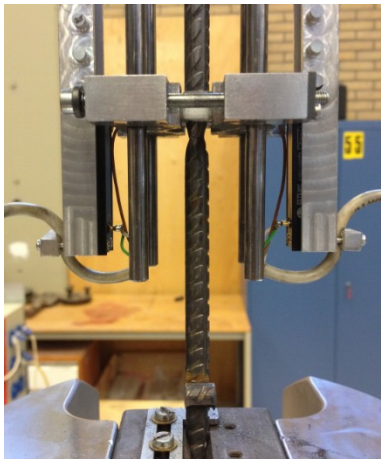

(a) The third test

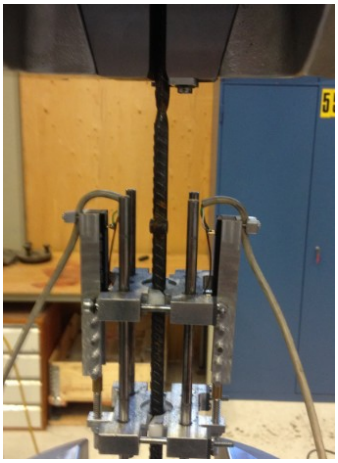

(b) The fourth test

Figure F.11: The third and fourth tension test on the reinforcement bar Ø8, necking outside the extensiometer

Figure F.12 presents the σ-ϵ-diagrams of the reinforcement bars, the engineering stress/strain relation is shown again. The stress levels are obtained by using a constant cross section. The force is divided by the actual cross section with diameter of 7.88 mm to obtain the stress levels. The strain is obtained with the output that the exteniometer generated; the relative displacements were divided by the initial length. Figure F.12b and F.12c clearly show as well that necking took place outside the range of the extensiometer. Figure F.13 shows this even better, whereby all three σ-ϵ-diagrams are put into one graph. The yield stress can still be obtained however as will be discussed next.

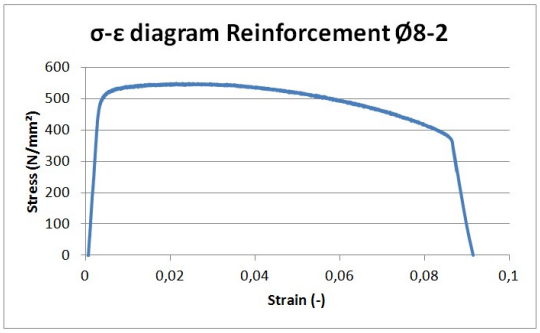

(a) Second test

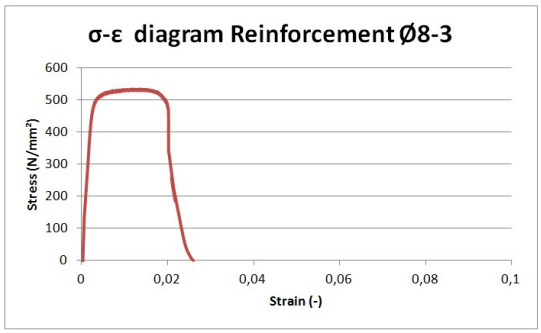

(b) Third test

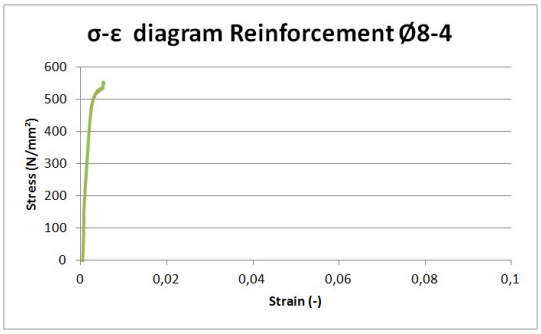

(c) Fourth test

Figure F.12: The σ-ϵ-diagrams of the tension tests performed on the reinforcement with a diameter of 8 mm

.

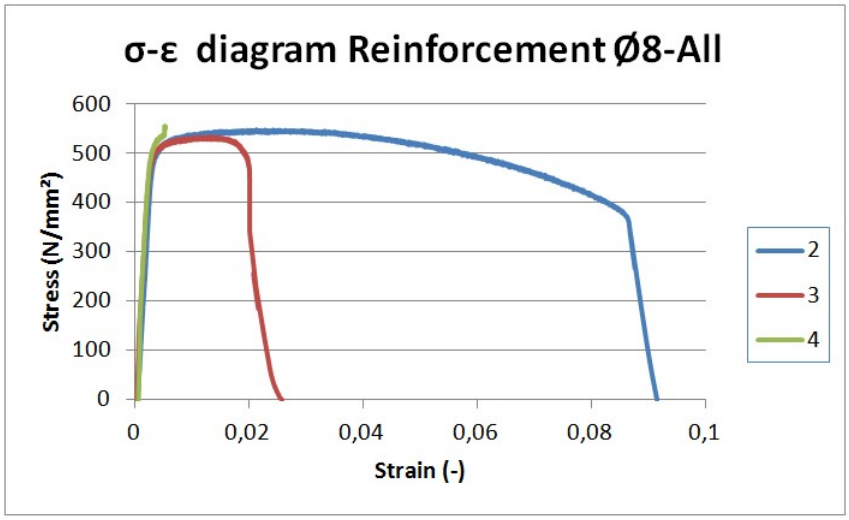

Figure F.13: The three σ-ϵ-diagrams of the tensile tests (Ø8) together to compare the tests with each other

Several problems with the measuring equipment that was used prevent the accurate calculation of the elastic part of the σ-ϵ-diagram, and then especially the modulus of elasticity. Friction inside the extensiometer and performing the tests on the bars under a small angle results in unrealistic values for the modulus of elasticity. Is is assumed therefore that the modulus of elasticity is, despite the actual performed tests, 200000 MPa. The σ-ϵ-diagrams are reconsidered with this new value and the slope of elastic line is changed. The stress level that belongs to a permanent strain of 0.2% is obtained; this is the yield stress of the reinforcement bars with a diameter of 8 mm. This value is obtained at all three tests that were performed with a extensiometer. The ultimate stress level is only obtained at test two and three. This results in the following table:

Table F.4: The yield and ultimate stress of the reinforcement mesh Ø8

Bar	Yield stress (MPa)	Ultimate stress (MPa)	Fraction f_u/f_y
1	-	547.714	-
2	508.935	549.028	1.079
3	514.468	534.177	1.038
4	530.717	-	-
Average	518.040	541.603	1.054

The value for the yield stress, that is used in the numerical and analytical modelling, is thus 518.040 MPa. This value however is obtained by making some assumptions and by adjusting the actual obtained data from the tension tests.

F.3.2. REINFORCEMENT IN RIB Ø20

This part briefly discusses the tension tests on the reinforcement test specimen of the steel reinforcement located at the bottom of every rib with a diameter of 20 mm. All details are already treated in previous sections. The Dowty-Rotel test set-up was used again. The tests were displacement controlled, with a speed of 0,01 until the hardening phase starts. The speed was then increased up to 0,06 mm/s. The test pieces had an initial length of about 35 cm. Six tests were executed in total. Figure F.14a shows a broken and a unbroken test piece. The tests were performed without an extensiometer, as discussed next. The test is shown in figure F.14b.

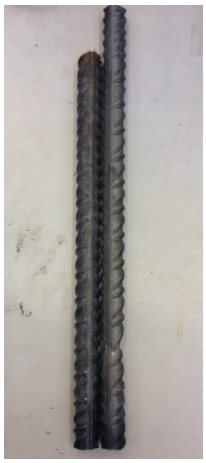

(a) Two (un)broken test pieces

(b) Test overview tension test Ø20

Figure F.14: Test pieces and test overview of the tension test to obtain the material data of the reinforcement bar Ø20

The same procedure, regarding the calculation of the homogeneous diameter as discussed in the previous section, is used for these test pieces as well. Other samples are measured and weighted to eventually obtain a diameter of 20,06 mm. The procedure is visualized in Table F.5. This diameter is used to calculate the cross sectional area and the stresses in the members during testing. This diameter is larger than the nominal value of 20 mm.

Table F.5: The calculation of the homogeneous reinforcement diameter Ø20.

Bar	Length (mm)	Weight (g)	Volume (mm^3)	Diameter (mm)
1	96.43	237.56	30456.41	20.05
2	97.66	240.77	30867.95	20.06
3	104.42	257.56	33020.51	20.07
Average				20.06

The ridges on the bar initiate slip during the tests. This slip occurs in the clamps of the test set-up, as shown in figure F.16a. The slip results in sudden changes in the continuous force-displacement diagram, this will not have an influence on the results. Figure F.16b presents an image of a test piece that is almost failing; the necking process is clearly visible. The six tests were executed, resulting in the six force-displacement diagrams, shown in Figure F.15. Finally, all six test results are shown in Figure F.17.

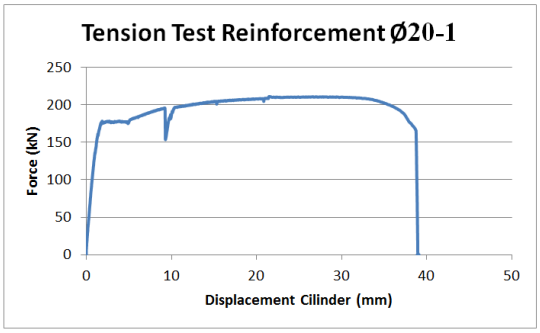

(a) First test

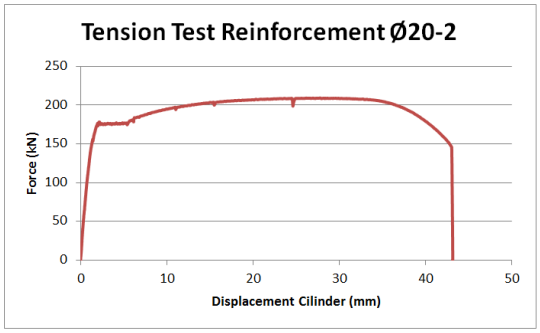

(b) Second test

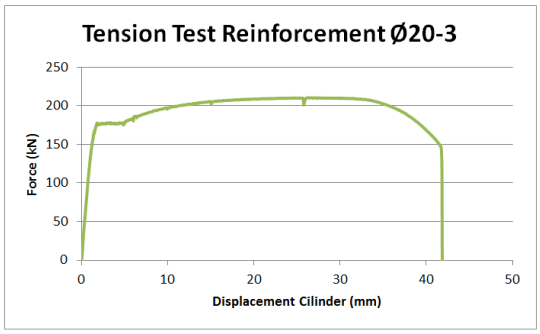

(c) Third test

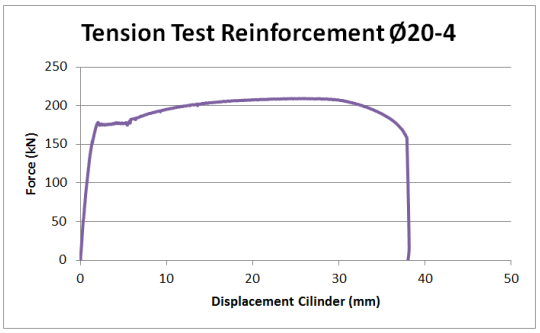

(d) Fourth test

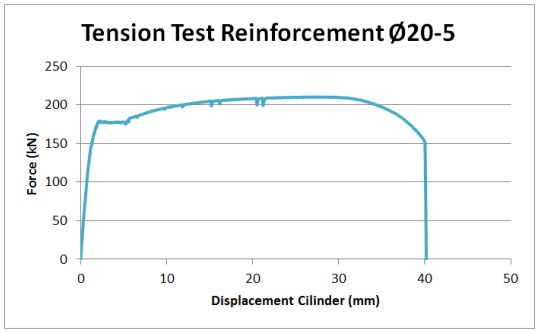

(e) Fifth test

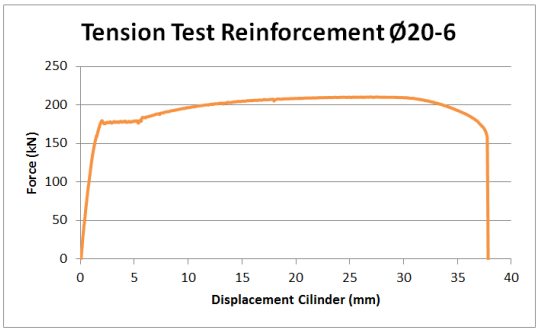

(f) Sixt test

Figure F.15: The tension tests performed on the reinforcement with a diameter of 20 mm

.

(a) The clambs of the test set up

(b) Necking of a test piece

Figure F.16: Details of the tension tests performed on the reinforcement bar with a diameter of 20 mm.

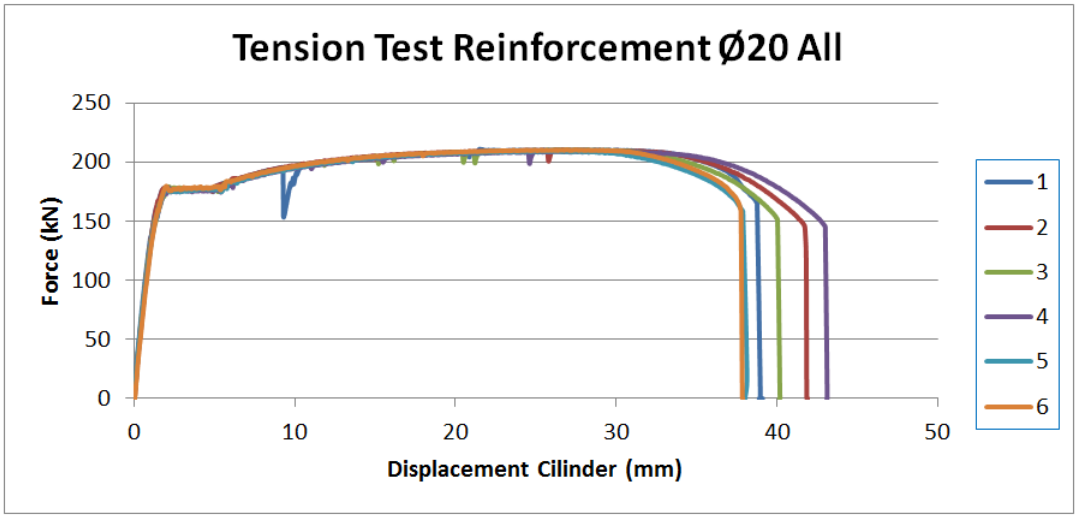

Figure F.17: The six F-u diagrams of the tensile tests (Ø20) together to compare the tests with each other

The test results shows some slip, especially in the first force-displacement diagram around a displacement of the cylinder of 10 mm. The only difference between the different tests is the deformation capacity, the other quantities are almost equal. The curve shows a clear yield plateau. The yield stress can be obtained without the use of an extensiometer, as discussed in the tests with the reinforcement bar Ø8. The average stress level in this plateau results in the yield stress. The ultimate stress is the highest stress level reached in the test. The different values are presented in table F.6.

Table F.6: The yield and ultimate stress of the reinforcement bars Ø20

Bar	Yield stress (MPa)	Ultimate stress (MPa)	Fraction f_u/f_y
1	560.519	668.215	1.192
2	559.772	666.222	1.190
3	561.325	665.996	1.186
4	556.893	661.967	1.187
5	558.499	663.102	1.187
6	563.202	666.306	1.183
Average	560.035	665.302	1.188

F.4. CONCRETE TESTS

Two different tests are performed to obtain the required material data of the concrete: compression tests and split tests. The concrete tests are much easier to perform compared to the steel tests. In total 36 concrete cubes were created. Every test series comprises nine tests: six split tests and three compression tests. The scatter in test results of the compression tests is expected to be lower than the split tests. More split tests are therefore executed. One batch of concrete cubes is depicted in figure F.18. The dimensions of the concrete cubes are 150 x 150 x 150 mm. The two different tests are discussed separately. The test set-up shown in figure F.1b is used for both tests.

Figure F.18: One batch of concrete cubes, packed in styrofoam

F.4.1. COMPRESSION TESTS

The concrete cubes are placed inside the test set-up one by one. The test is load controlled, with a loading speed of 13,5 kN/s. The result of the compression tests is the actual cubic compression strength. No additional material is allowed to be placed between the steel plate and the concrete cube. The pressure (in MPa) is measured during the tests and the test is finished when the concrete is crushed.

(a) The compression test

(b) A concrete cube, failed in compression

Figure F.19: The test set-up of the compression test and a test piece that has failed on compression.

The results of the different series are shown in the following tables. The concrete factory provided concrete class C20/25, the characteristic cubic compressions strength should be at least 25 MPa. Three tests were executed for each test series.

Table F.7: The cubic concrete compression strength of the 28 days test series

Cube	Force [kN]	Compression strength [MPa]
1	637.8	28.35
2	534.5	23.76
3	600.9	26.71
Average	591.07	26.27

Table F.8: The actual cubic concrete compression strength of the concrete at the first lab experiment of the ComFlor210 test specimen

Cube	Force [kN]	Compression strength [MPa]
1	734.0	32.62
2	572.5	25.44
3	681.0	30,27
Average	662.50	29.44

Table F.9: The actual cubic concrete compression strength of the concrete at the second lab experiment of the ComFlor210 test specimen

Cube	Force [kN]	Compression strength [MPa]
1	740.7	32.92
2	740.9	32.93
3	734.2	32.63
Average	738.6	32.83

Table F.10: The actual cubic concrete compression strength of the concrete at the third lab experiment of the ComFlor210 test specimen

Cube	Force [kN]	Compression strength [MPa]
1	682.1	30.32
2	753.7	33.50
3	818.6	36.38
Average	751.47	33.40

F.4.2. SPLIT TESTS

The same test set up is used for the split tests as used for the compression tests. The only difference is the usage of a small piece of plywood. This sample is placed between the concrete and the steel compression cylinder. This piece of material changes the internal stresses inside the concrete completely. Tensile stresses are now introduced in the middle of the concrete instead of compression stresses. The tensile strength of the concrete will be governing in this tests. The result of this test is the actual tensile strength of the concrete.

Six tests were executed for each test series. These tests are load controlled as well, with a loading speed of 1.1 kN/s. Figure F.20 shows a concrete cube in the split test set-up.

(a) The split test set-up

(b) A failed concrete cube

Figure F.20: The test set up of the split test and a test piece that has failed on tension.

The following tables present the results of the different concrete split test series. Six tests were performed for each series.

Table F.11: The tensile strength of the 28 days test series

Cube	Force [kN]	Tensile strength [MPa]
1	112.3	3.18
2	104.9	2.97
3	81.4	2.30
4	114.5	3.24
5	104.3	2.95
6	88.8	2.51
Average	101.0	2.86

Table F.12: The actual tensile strength of the concrete at the first lab experiment of the ComFlor210 test specimen

Cube	Force [kN]	Tensile strength [MPa]
1	105.1	2.97
2	126.4	3.58
3	119.0	3.37
4	106.7	3.02
5	126.0	3.57
6	88.1	2.50
Average	111.88	3.17

Table F.13: The actual tensile strength of the concrete at the second lab experiment of the ComFlor210 test specimen

Cube	Force [kN]	Tensile strength [MPa]
1	122.6	3.47
2	106.5	3.01
3	135.6	3.84
4	145.0	4.10
5	126.4	3.58
6	117.4	3.32
Average	125.58	3.55

Table F.14: The actual tensile strength of the concrete at the third lab experiment of the ComFlor210 test specimen

Cube	Force [kN]	Tensile strength [MPa]
1	100.2	2.84
2	103.4	2.94
3	134.5	3.81
4	133.6	3.78
5	111.9	3.17
6	116.5	3.30
Average	116.68	3.31

Finally the results of both the compression and tension test of the concrete are shown displayed against time in figure F.21. In this graph it can be seen that the concrete compressive strength increases a little over time and shows a steep climb towards the end, while the tensile strength climbs only slightly and remains quite constant over time.

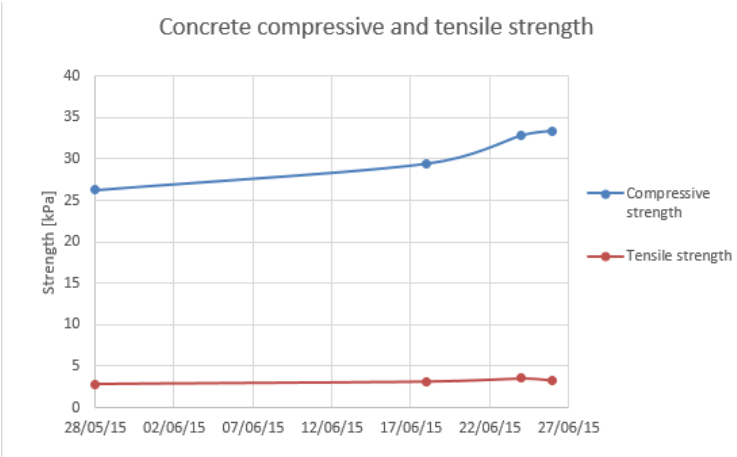

Figure F.21: The compressive and tensile strength of the concrete displayed over time

G

LABORATORY TEST RESULTS

This chapter will show the measurement results that were obtained from the experiment performed in the test laboratory of the TU Delft and that were not shown in the main report. The test results will be shown divided by test type. First the test results from loading the slabs at a quarter of the span length and secondly the results from the test at half the span length.

G.1. TEST AT A QUARTER OF THE SPAN LENGTH

The results of the test at a quarter of the span length which were not shown in the main report are shown in this section.

G.1.1. TEST SPECIMEN WITH 2 REINFORCEMENT MESHES

The results of the slab with two reinforcement meshes are shown in this section.

Table G.1: This table shows initial values of the load cells before commencement of the experiment.

Load cell number	Initial load [kN]
RO1	4.2
RO2	5.7
RO3	5.4
RO4	5.8
RO5	4.7
RO6	4.9
RO7	6.0
RO8	5.7
RO9	5.0
RO10	4.7

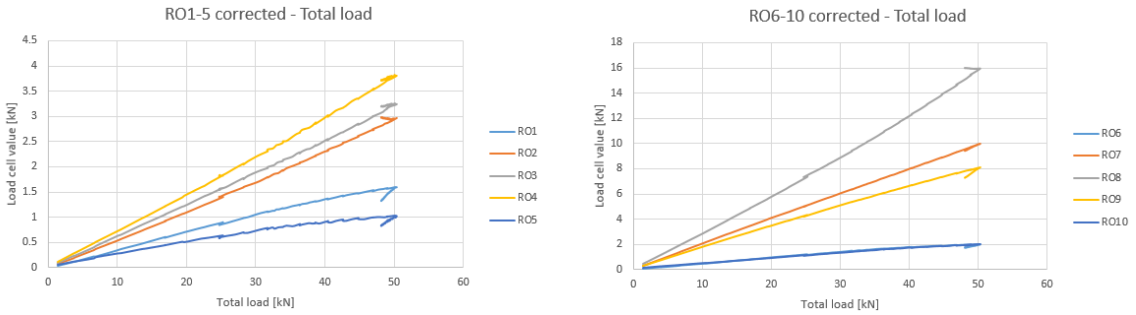

(a) The absolute and corrected values for RO1 to RO5

(b) The absolute and corrected values for RO6 to RO10

Figure G.1: Two graphs depicting the distribution for R01 to R05 and R06 to R010 respectively of the slab with 2 reinforcement meshes.

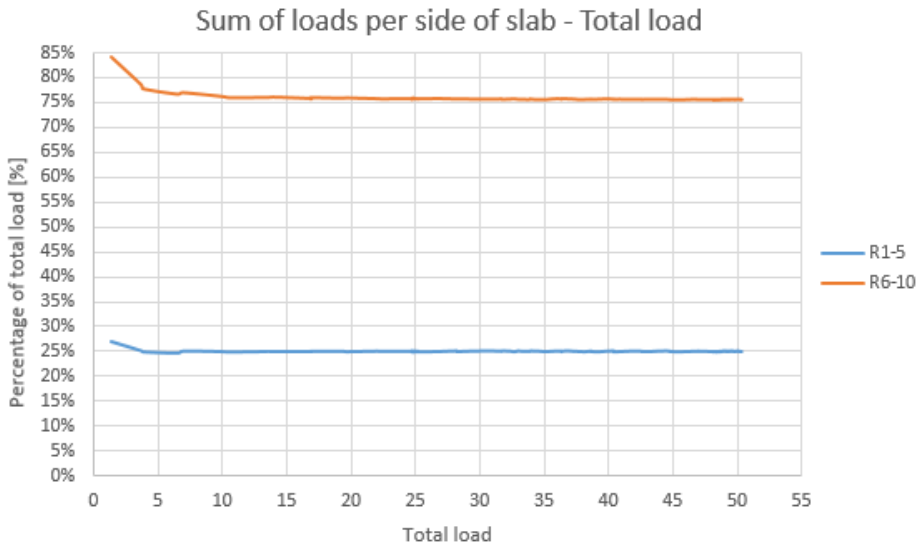

Figure G.2: A graph showing the percentage of the total applied load the sum of all the load cells on each of the test specimen contribute.

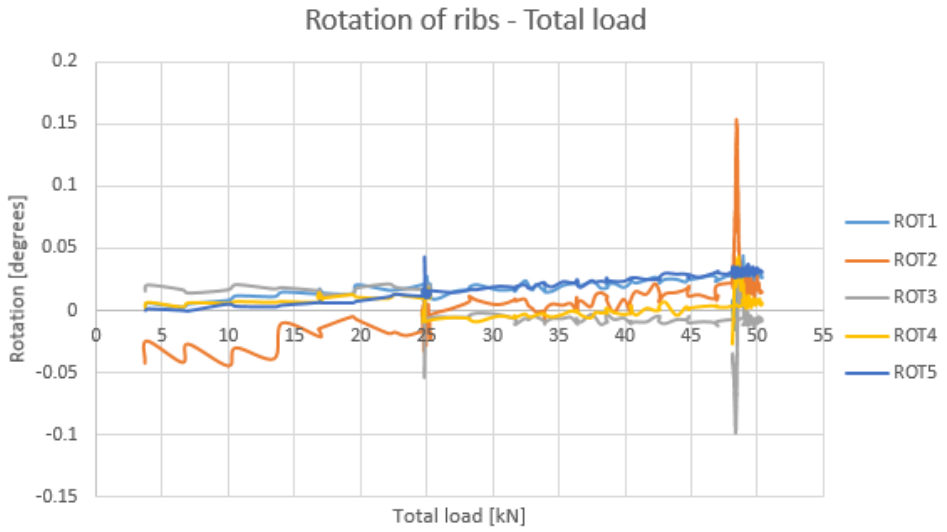

Figure G.3: A graph showing the rotation of each of the ribs set against the total load.

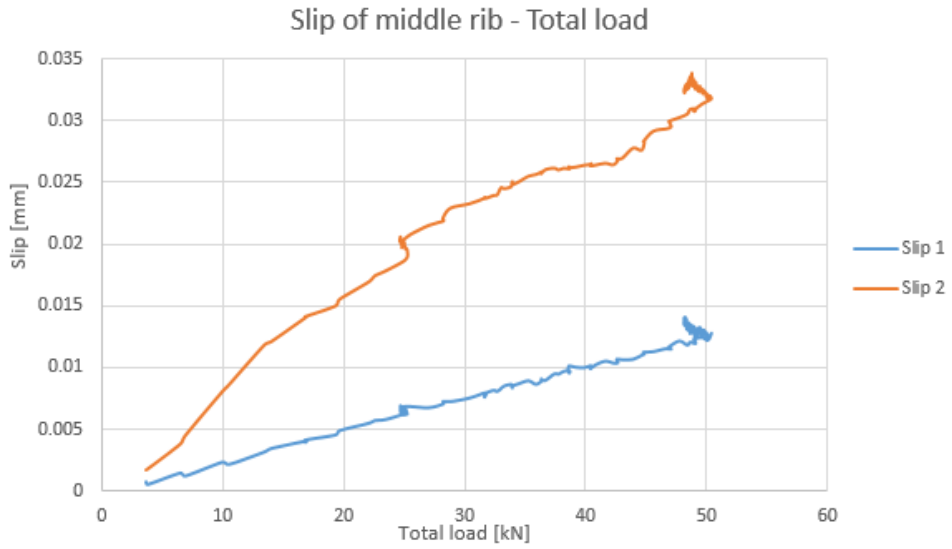

Figure G.4: A graph showing the slip on either side of the middle rib set against the total load.

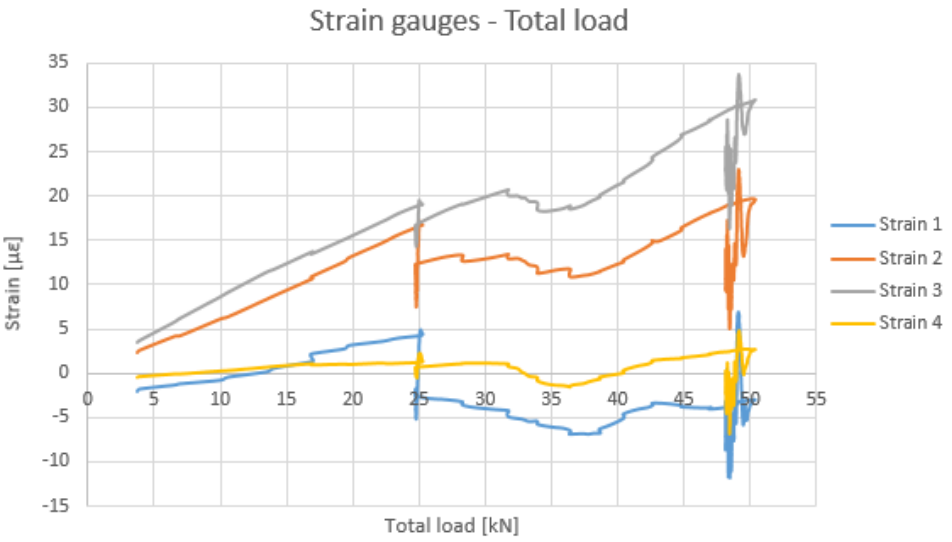

Figure G.5: A graph showing the strain in the strain gauges set against the total load.

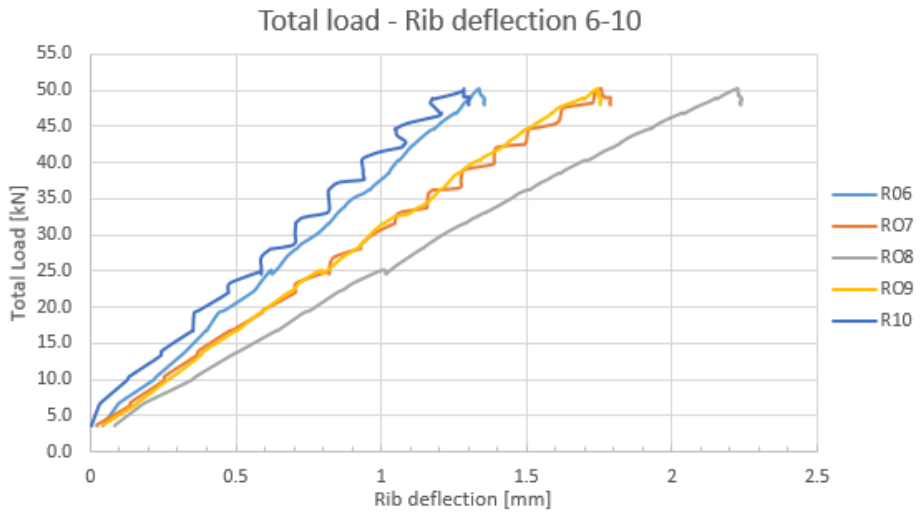

Figure G.6: A graph showing the deflection of each of the ribs at a quarter of the span set against the total load.

G.1.2. TEST SPECIMEN WITH 1 REINFORCEMENT MESH

The results of the slab with one reinforcement mesh are shown in this section.

Table G.2: This table shows initial values of the load cells before commencement of the experiment.

Load cell number	Initial load [kN]
RO1	4.8
RO2	5.1
RO3	5.9
RO4	5.5
RO5	4.9
RO6	5.1
RO7	6.1
RO8	6.0
RO9	5.2
RO10	4.7

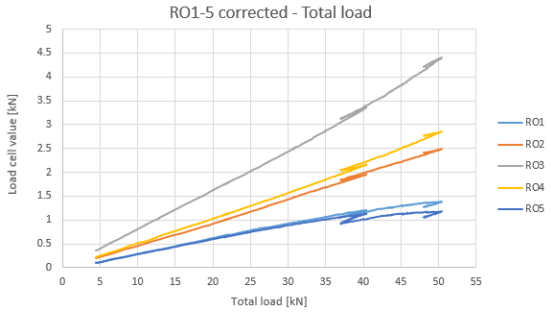

(a) The absolute and corrected values for RO1 to RO5

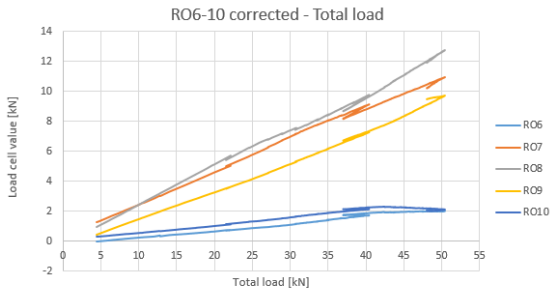

(b) The absolute and corrected values for RO6 to RO10

Figure G.7: Two graphs depicting the distribution for R01 to R05 and R06 to R010 respectively of the slab with 2 reinforcement meshes.

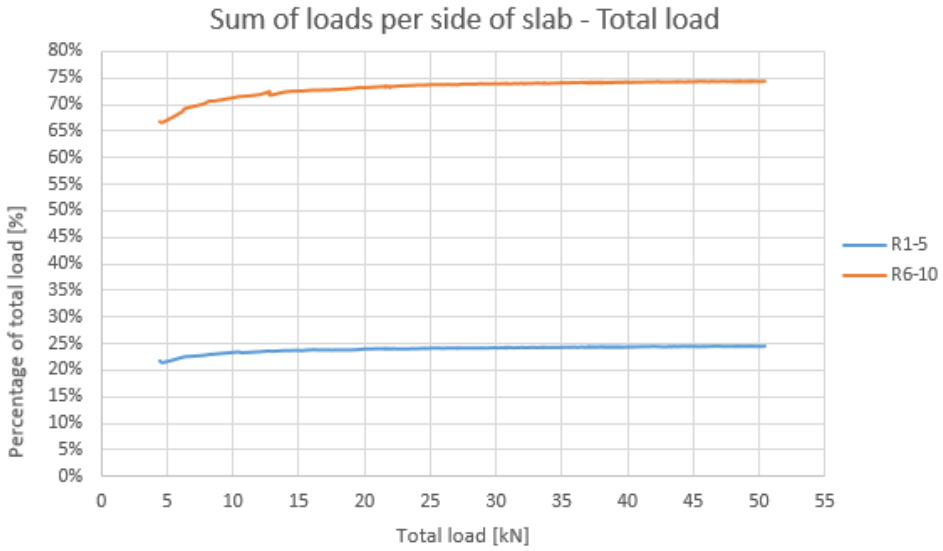

Figure G.8: A graph showing the percentage of the total applied load the sum of all the load cells on each of the test specimen contribute.

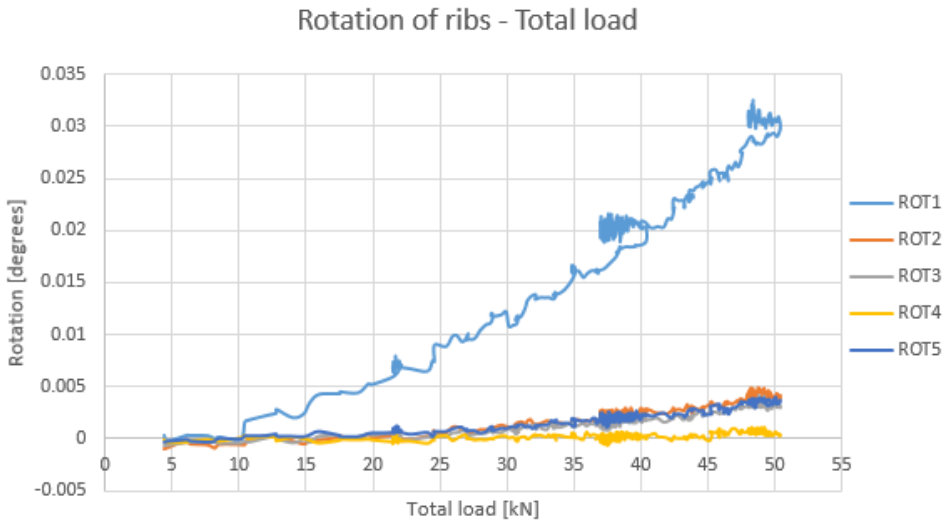

Figure G.9: A graph showing the rotation of each of the ribs set against the total load.

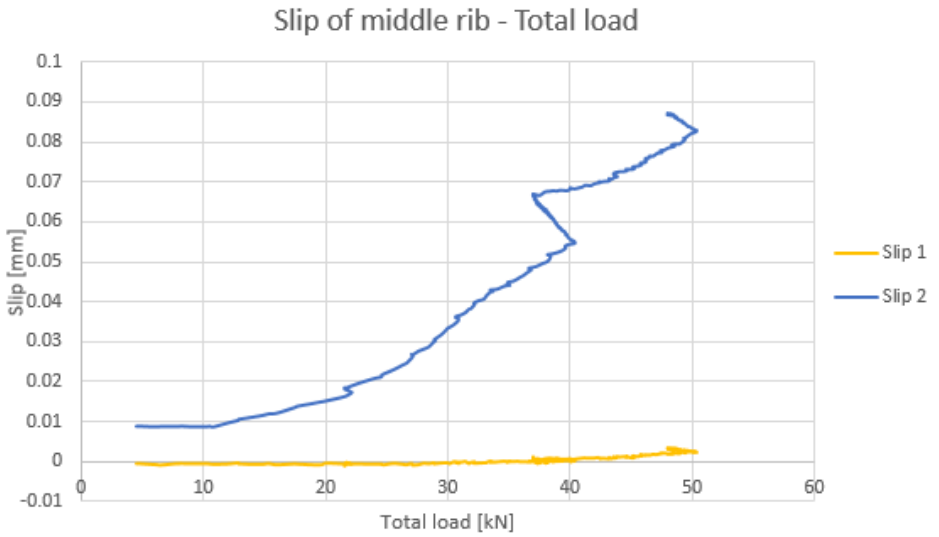

Figure G.10: A graph showing the slip on either side of the middle rib set against the total load.

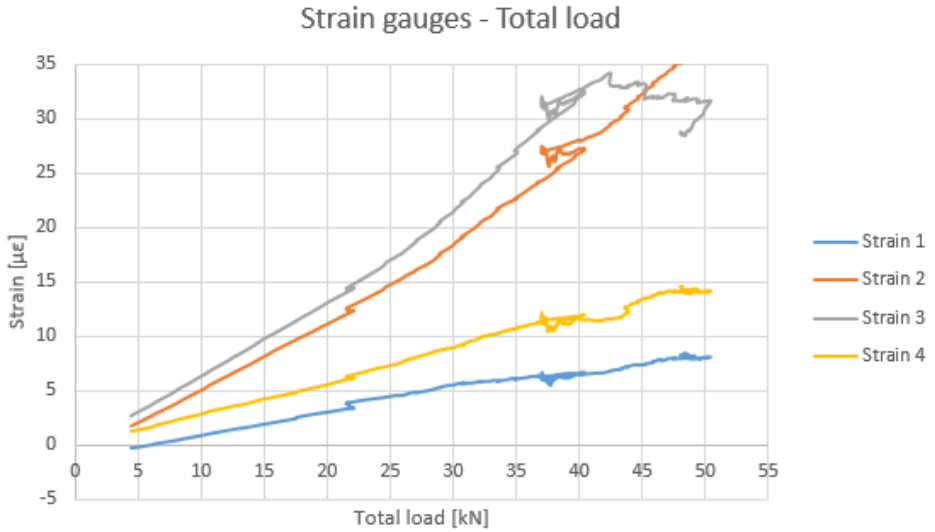

Figure G.11: A graph showing the strain in the strain gauges set against the total load.

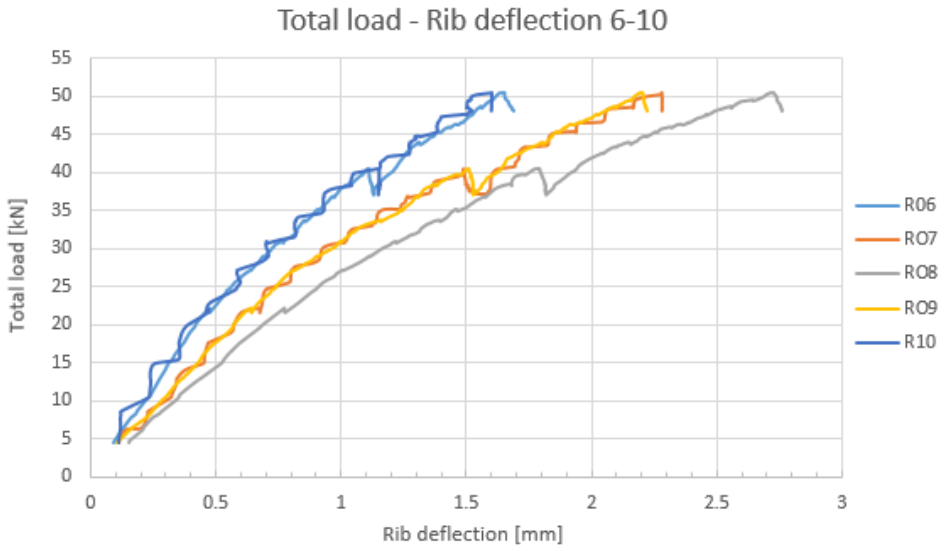

Figure G.12: A graph showing the deflection of each of the ribs at a quarter of the span set against the total load.

G.1.3. TEST SPECIMEN WITHOUT REINFORCEMENT MESH

The results of the slab without any reinforcement meshes are shown in this section.

Table G.3: This table shows initial values of the load cells before commencement of the experiment.

Load cell number	Initial load [kN]
RO1	5.1
RO2	6.6
RO3	5.3
RO4	5.1
RO5	4.3
RO6	4.9
RO7	4.3
RO8	5.2
RO9	6.8
RO10	5.0

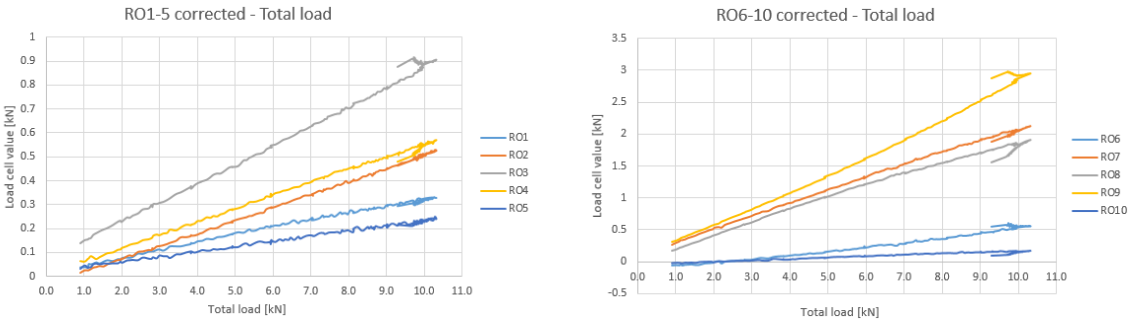

(a) The absolute and corrected values for RO1 to RO5

(b) The absolute and corrected values for RO6 to RO10

Figure G.13: Two graphs depicting the distribution for R01 to R05 and R06 to R010 respectively of the slab with 2 reinforcement meshes.

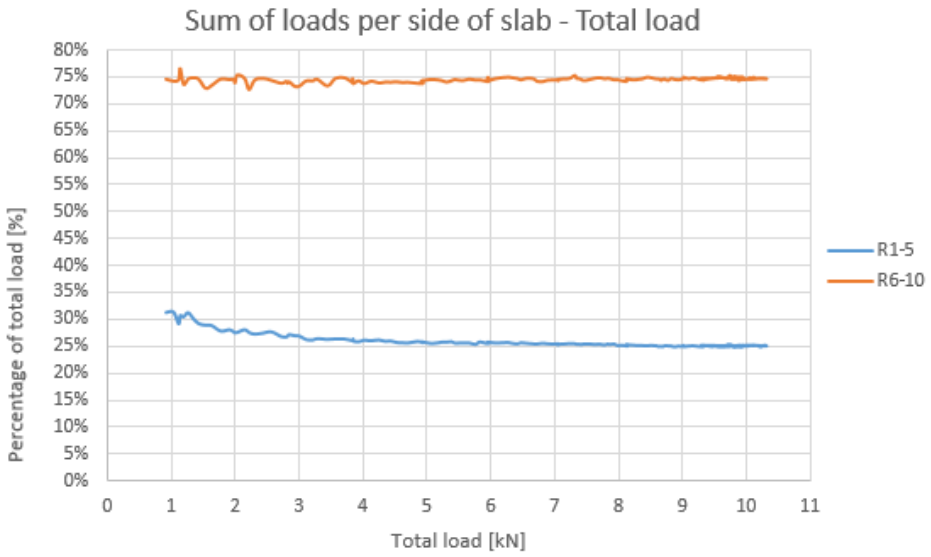

Figure G.14: A graph showing the percentage of the total applied load the sum of all the load cells on each of the test specimen contribute.

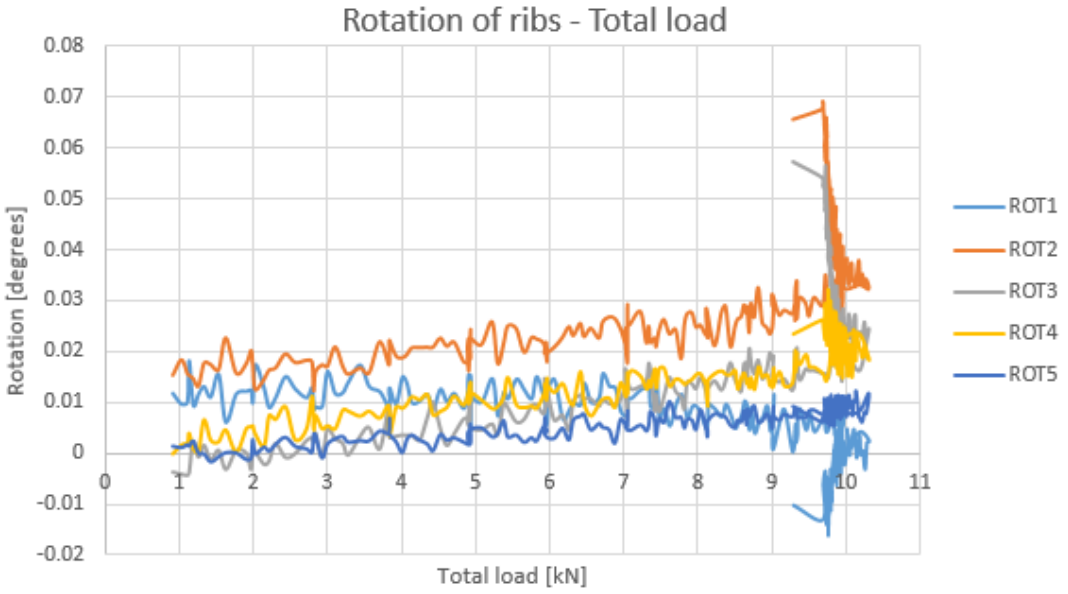

Figure G.15: A graph showing the rotation of each of the ribs set against the total load.

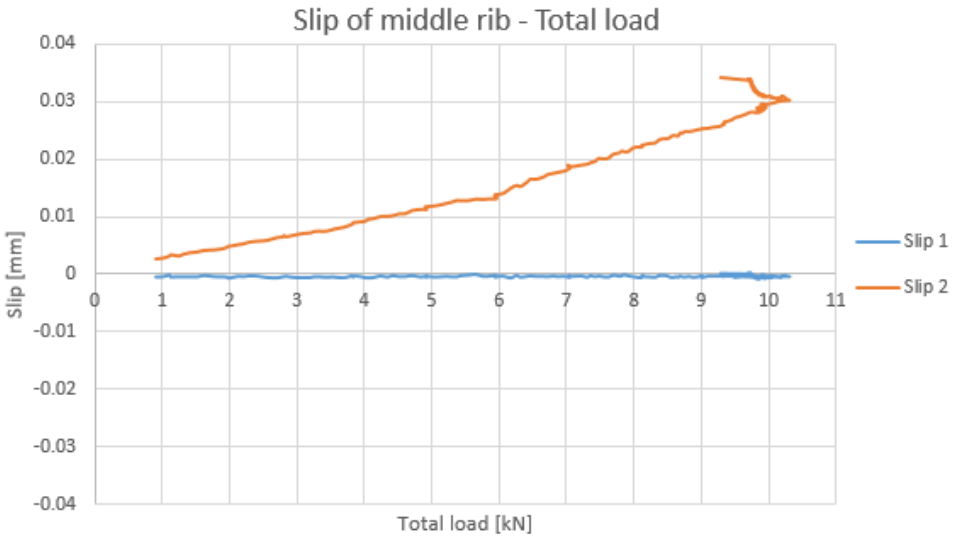

Figure G.16: A graph showing the slip on either side of the middle rib set against the total load.

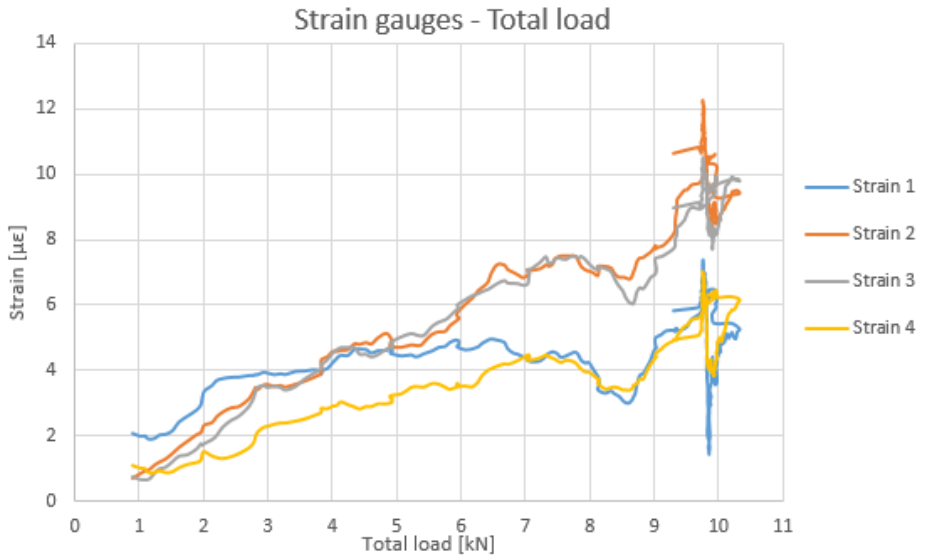

Figure G.17: A graph showing the strain in the strain gauges set against the total load.

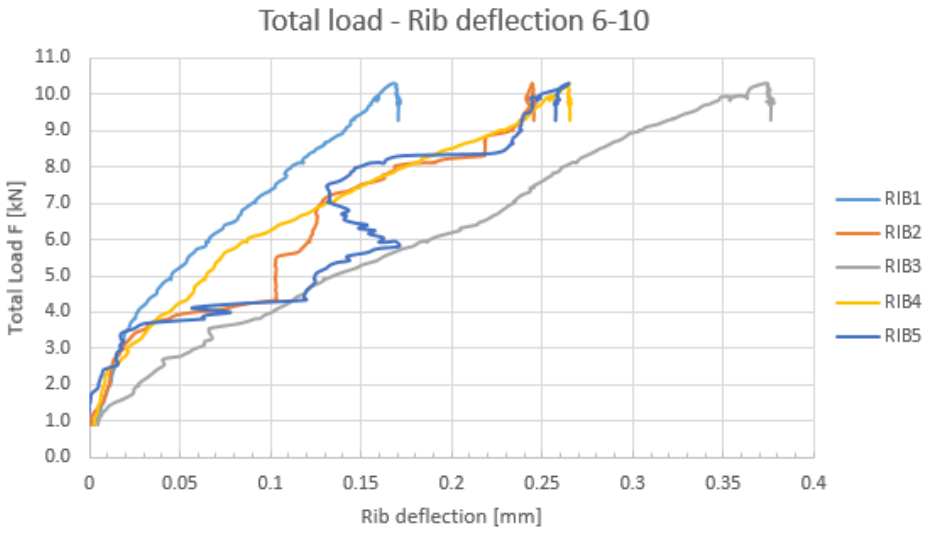

Figure G.18: A graph showing the deflection of each of the ribs at a quarter of the span set against the total load.

G.2. TEST AT HALF OF THE SPAN LENGTH

The results of the test at half of the span length which were not shown in the main report are shown in this section.

G.2.1. TEST SPECIMEN WITH 2 REINFORCEMENT MESHES

The results of the slab with two reinforcement meshes are shown in this section.

Table G.4: This table shows initial values of the load cells before commencement of the experiment.

Load cell number	Initial load [kN]
RO1	2.3
RO2	7.2
RO3	6.5
RO4	6.7
RO5	2.9
RO6	3.4
RO7	7.5
RO8	7.6
RO9	4.6
RO10	3.1

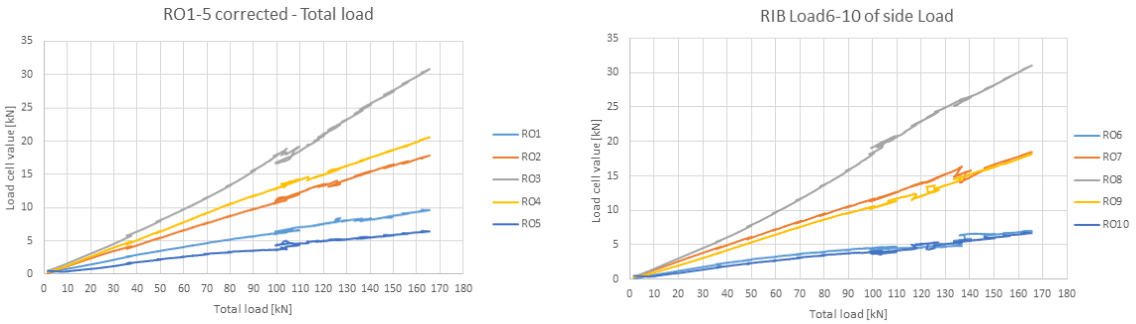

(a) The absolute and corrected values for RO1 to RO5

(b) The absolute and corrected values for RO6 to RO10

Figure G.19: Two graphs depicting the distribution for R01 to R05 and R06 to R010 respectively of the slab with 2 reinforcement meshes.

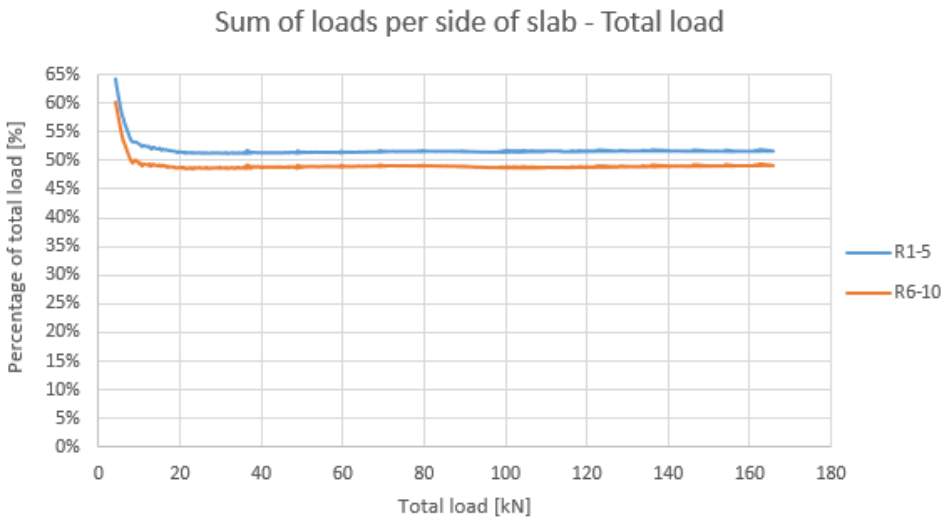

Figure G.20: A graph showing the percentage of the total applied load the sum of all the load cells on each of the test specimen contribute.

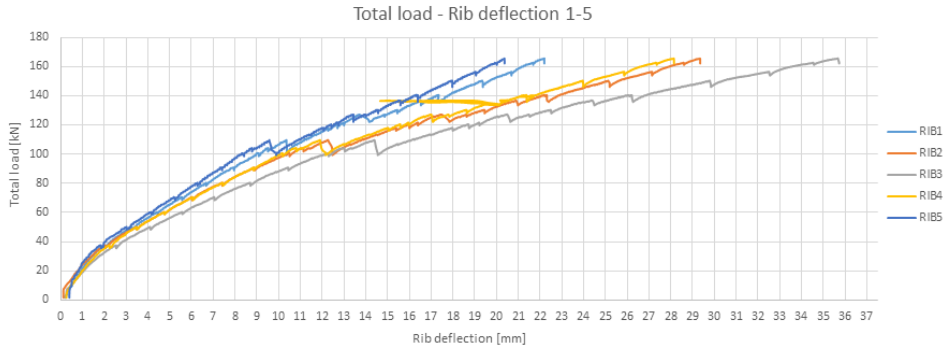

Figure G.21: A graph showing the deflection of each of the ribs at half of the span set against the total load.

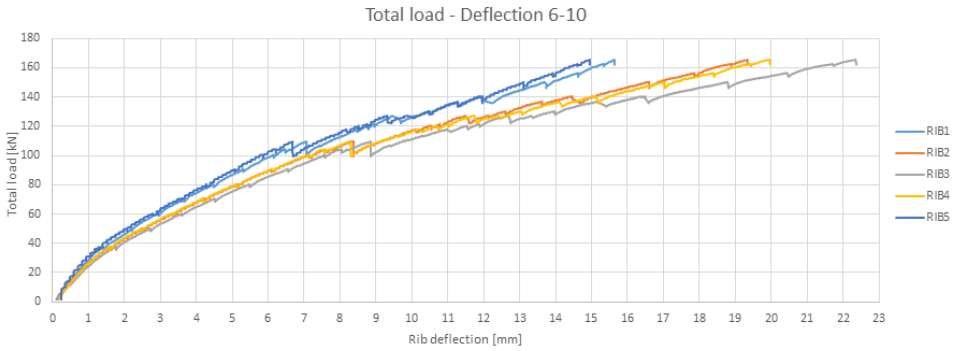

Figure G.22: A graph showing the deflection of each of the ribs at a quarter of the span set against the total load.

G.2.2. TEST SPECIMEN WITH 1 REINFORCEMENT MESH

The results of the slab with one reinforcement mesh are shown in this section.

Table G.5: This table shows initial values of the load cells before commencement of the experiment.

Load cell number	Initial load [kN]
RO1	4.7
RO2	5.3
RO3	5.9
RO4	5.8
RO5	4.5
RO6	5.1
RO7	6.5
RO8	4.8
RO9	5.3
RO10	4.9

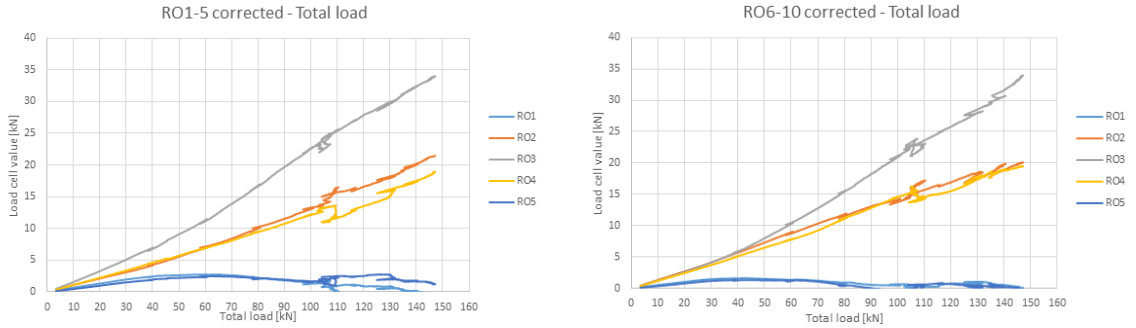

(a) The absolute and corrected values for RO1 to RO5

(b) The absolute and corrected values for RO6 to RO10

Figure G.23: Two graphs depicting the distribution for R01 to R05 and R06 to R010 respectively of the slab with 2 reinforcement meshes.

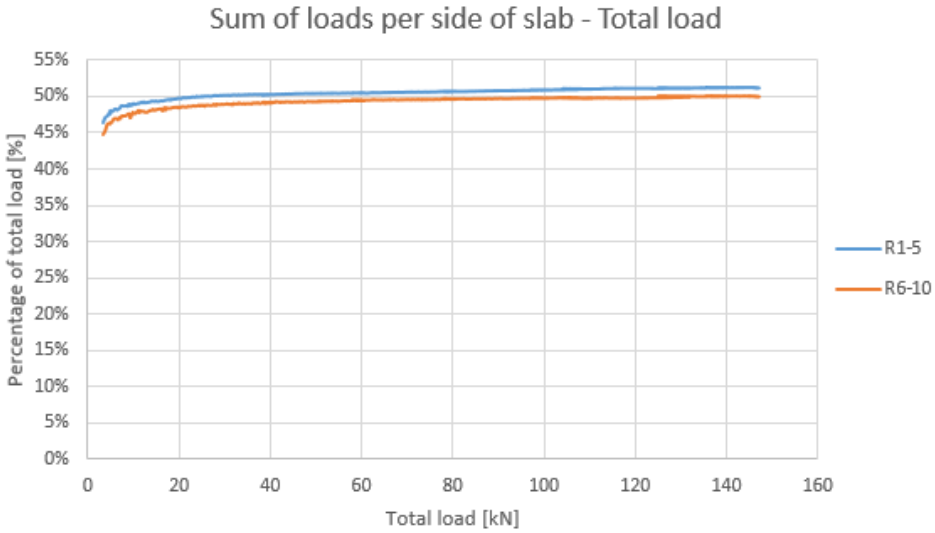

Figure G.24: A graph showing the percentage of the total applied load the sum of all the load cells on each of the test specimen contribute.

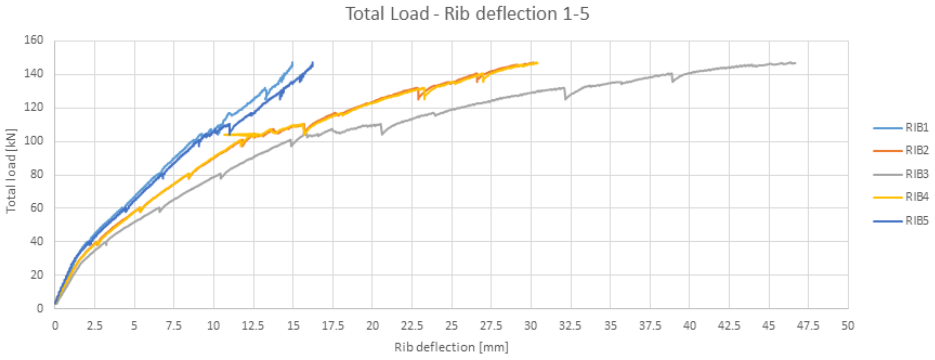

Figure G.25: A graph showing the deflection of each of the ribs at half of the span set against the total load.

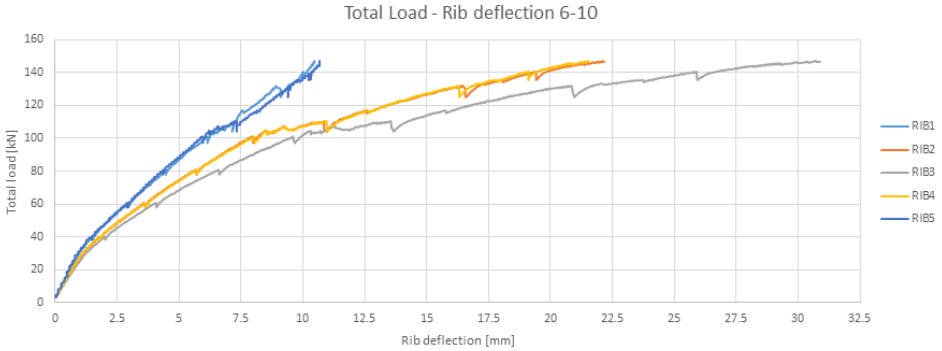

Figure G.26: A graph showing the deflection of each of the ribs at a quarter of the span set against the total load.

G.2.3. TEST SPECIMEN WITHOUT REINFORCEMENT MESH

The results of the slab without any reinforcement meshes are shown in this section.

Table G.6: This table shows initial values of the load cells before commencement of the experiment.

Load cell number	Initial load [kN]
RO1	5.0
RO2	6.4
RO3	6.0
RO4	6.1
RO5	3.7
RO6	5.1
RO7	3.9
RO8	4.4
RO9	9.3
RO10	4.1

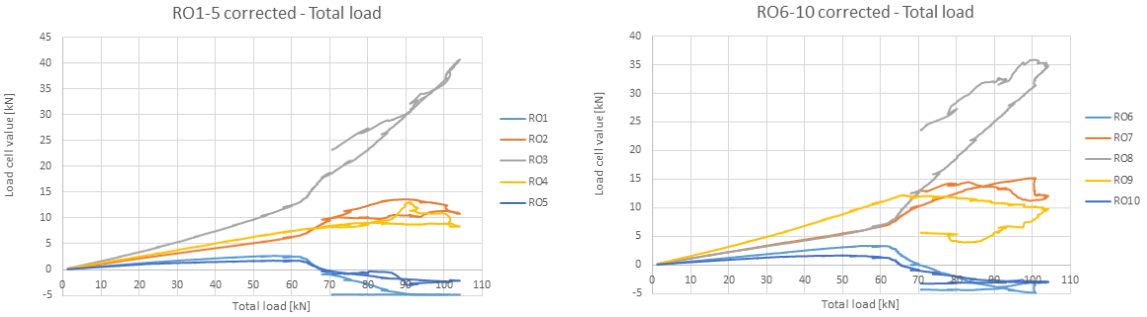

(a) The absolute and corrected values for RO1 to RO5

(b) The absolute and corrected values for RO6 to RO10

Figure G.27: Two graphs depicting the distribution for R01 to R05 and R06 to R010 respectively of the slab with 2 reinforcement meshes.

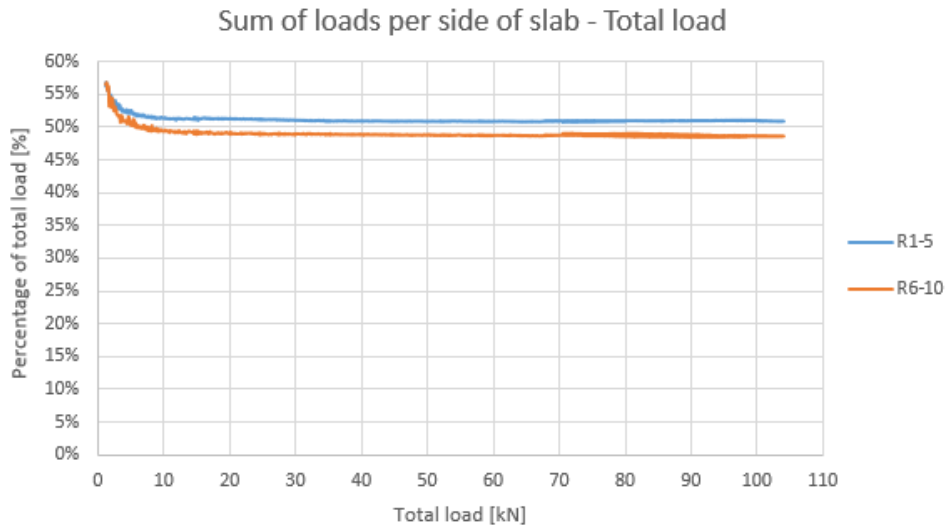

Figure G.28: A graph showing the percentage of the total applied load the sum of all the load cells on each of the test specimen contribute.

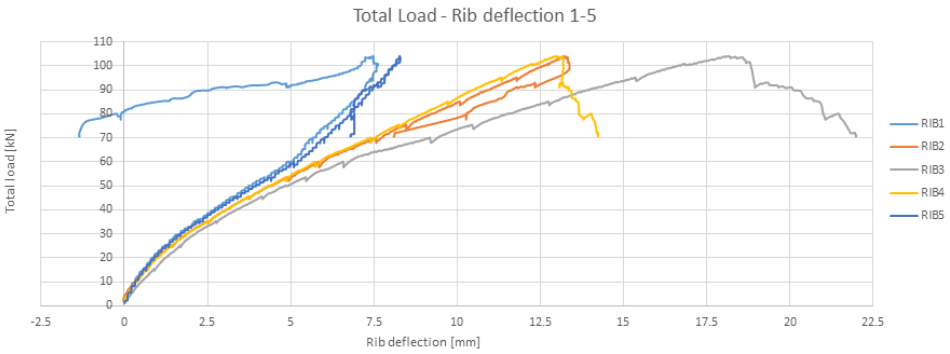

Figure G.29: A graph showing the deflection of each of the ribs at half of the span set against the total load.

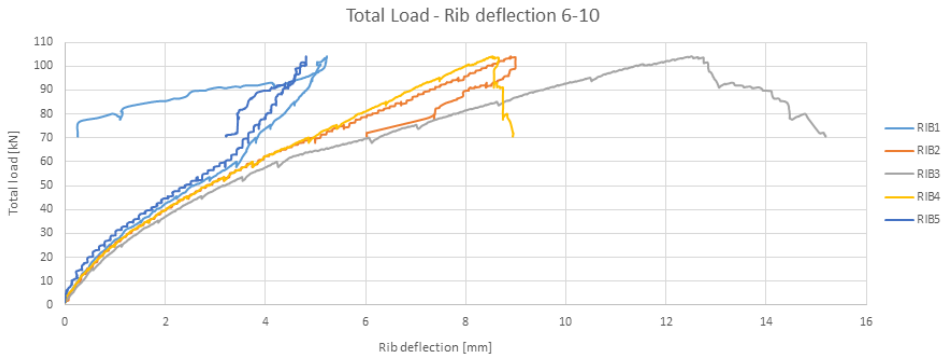

Figure G.30: A graph showing the deflection of each of the ribs at a quarter of the span set against the total load.

H

COMPARISON RESULTS

The results of the comparison between the fine-tuned analytical model and the test results are shown in this chapter.

H.1. RESULTS OF TEST AT QUARTER SPAN LENGTH

For the non-destructive tests at a quarter of the span length only the results of the load cells which were close to the load will be examined. This means that only the distribution of load cells RO6-RO10 will be reproduced. These results are the most important and that is what the analytical model is calibrated for.

H.1.1. 2 MESH

The change in distribution in the 2 mesh slab from 0 kN to the final load of 50 kN is minimal. Therefore only the initial and final distribution will be examined. The values that are used to fine-tune the analytical model are shown in table H.1. The resulting parameter values and the corresponding moment and deflection diagram are shown below.

Table H.1: The distribution and deflection values used to adjust the analytical model for the 2 mesh slab in the non-destructive test.

	load 10 kN		Load 50 kN	
Rib number	**Contribution [%]**	**Deflection [mm]**	**Contribution [%]**	**Deflection [mm]**
1	5.5	0.18	5	1.3
2	25.5	0.25	24	1.75
3	38.0	0.45	42	2.25
4	25.5	0.25	24	1.75
5	5.5	0.18	5	1.3

Table H.2: The distribution and deflection resulting from the fine-tuned analytical model in the 2 mesh slab and the non-destructive test.

Load [kN]	Rib number	Load [%]	Stiffness [kN/mm]	Deflection [mm]
10	1	5.0	2.0	0.26
	2	26.3	7.0	0.38
	3	37.2	8.5	0.44
	4	26.3	7.0	0.38
	5	5.0	2.0	0.26
50	1	4.1	2.0	1.03
	2	25.9	7.0	1.85
	3	40.0	8.5	2.37
	4	25.9	7.0	1.85
	5	4.1	1.9	1.03

Table H.3: The bending stiffness values of the top slab and the found value of the distributive length in the 2 mesh slab in the non-destructive test.

		Load 10 kN	Load 50 kN
Parameter	**Symbol**	**Value**	**Value**
Distributive length [mm]	L_{dis}	1800	1300
Positive top slab bending stiffness $[Nmm^2]per200mm$	$EI_{TS,+}$	8.71×10^{10}	idem
Negative top slab bending stiffness $[Nmm^2]per200mm$	$EI_{TS,-}$	1.06×10^{11}	idem
Uncracked top slab bending stiffness $[Nmm^2]per200mm$	$EI_{TS,uc}$	1.72×10^{11}	idem

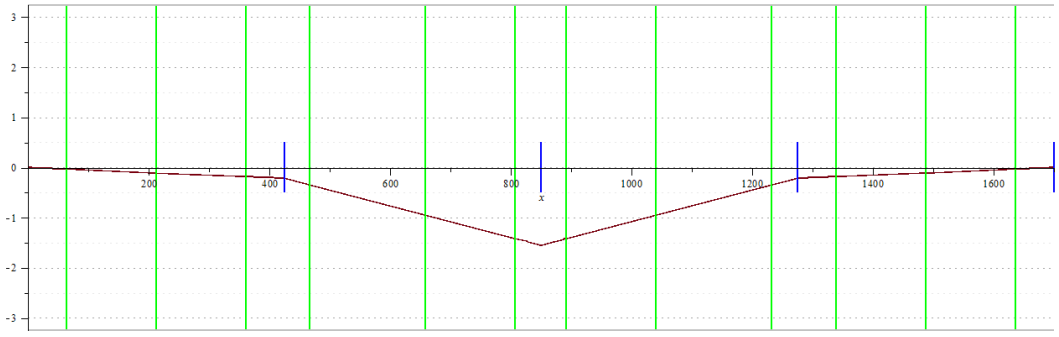

Figure H.1: A figure showing the moment diagram of the fine-tuned analytical model of the 2 mesh slab in the non-destructive test at 10 kN.

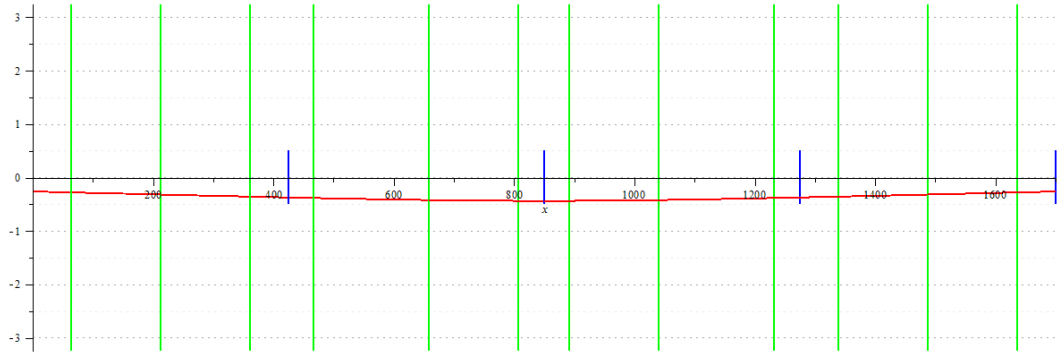

Figure H.2: A figure showing the deflection diagram of the fine-tuned analytical model of the 2 mesh slab in the non-destructive test at 10 kN.

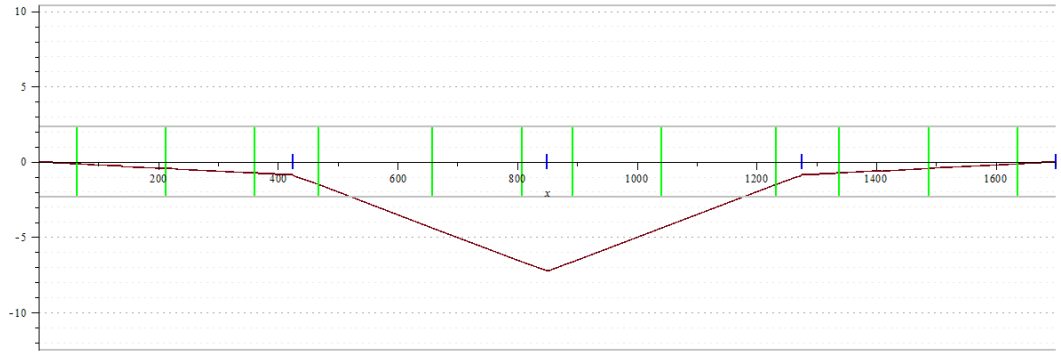

Figure H.3: A figure showing the moment diagram of the fine-tuned analytical model of the 2 mesh slab in the non-destructive test at 50 kN.

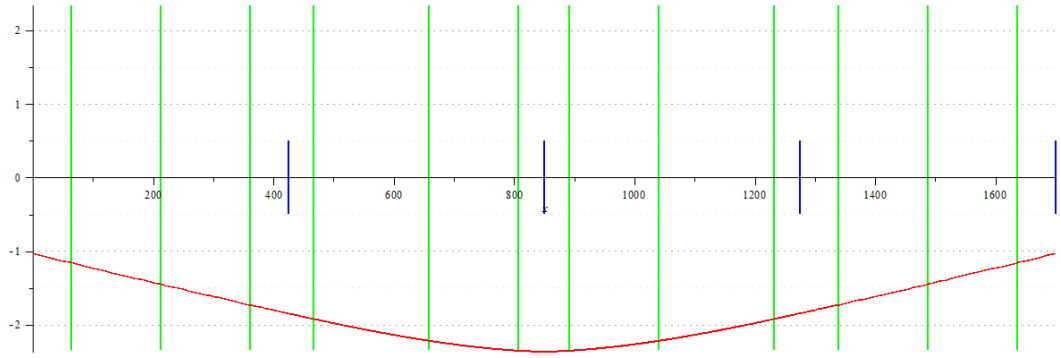

Figure H.4: A figure showing the deflection diagram of the fine-tuned analytical model of the 2 mesh slab in the non-destructive test at 50 kN.

H.1.2. 1 MESH

The 1 mesh slab has more variation between the symmetrical ribs in the results than the 2 mesh slab did. But the overall change of the distribution is not very large. Therefore only the initial load of 10 kN and the final load of 50 kN are taken into account. The values that are used to fine-tune the analytical model are shown in table H.4.

Table H.4: The distribution and deflection values used to adjust the analytical model for the 1 mesh slab in the non-destructive test.

	load 10 kN		Load 50 kN	
Rib number	**Contribution [%]**	**Deflection [mm]**	**Contribution [%]**	**Deflection [mm]**
1	6.0	0.20	5.5	1.6
2	27.0	0.45	27.5	2.25
3	34.0	0.55	34.0	2.7
4	27.0	0.45	27.5	2.25
5	6.0	0.20	5.5	1.6

Table H.5: The distribution and deflection resulting from the fine-tuned analytical model in the 1 mesh slab and the non-destructive test.

Load [kN]	**Rib number**	**Load [%]**	**Stiffness [kN/mm]**	**Deflection [mm]**
10	1	6.8	3.1	0.22
	2	25.4	7.5	0.34
	3	35.5	8.8	0.44
	4	25.4	7.5	0.34
	5	6.8	3.1	0.22
50	1	5.9	2.1	1.40
	2	26.3	5.8	2.27
	3	35.7	6.2	2.88
	4	26.3	5.8	2.27
	5	5.9	2.1	1.40

Table H.6: The bending stiffness values of the top slab and the found value of the distributive length in the 1 mesh slab in the non-destructive test.

		Load 10 kN	Load 50 kN
Parameter	**Symbol**	**Value**	**Value**
Distributive length [mm]	L_{dis}	1900	3000
Positive top slab bending stiffness $[Nmm^2]per200mm$	$EI_{TS,+}$	4.91×10^{10}	idem
Negative top slab bending stiffness $[Nmm^2]per200mm$	$EI_{TS,-}$	9.70×10^{10}	idem
Uncracked top slab bending stiffness $[Nmm^2]per200mm$	$EI_{TS,uc}$	1.72×10^{11}	idem

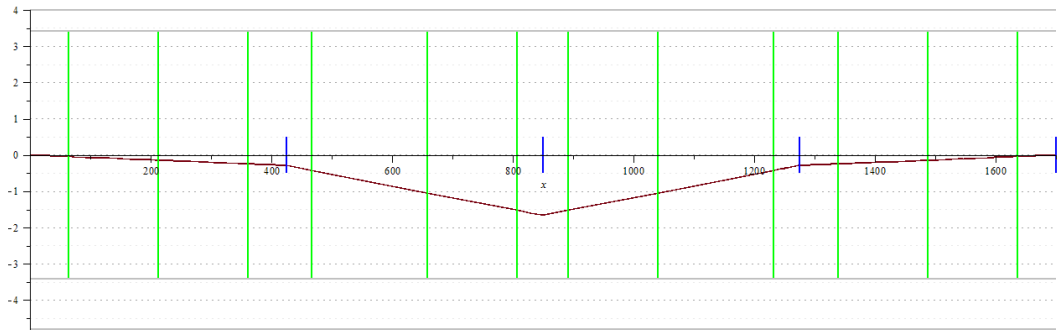

Figure H.5: A figure showing the moment diagram of the fine-tuned analytical model of the 1 mesh slab in the non-destructive test at 10 kN.

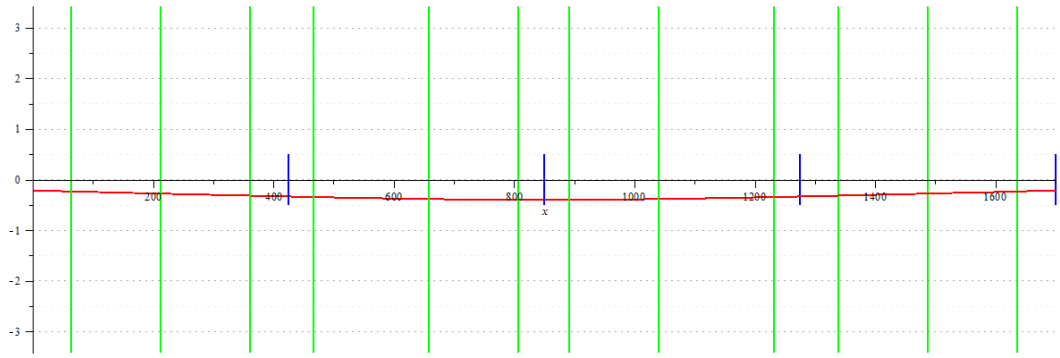

Figure H.6: A figure showing the deflection diagram of the fine-tuned analytical model of the 1 mesh slab in the non-destructive test at 10 kN.

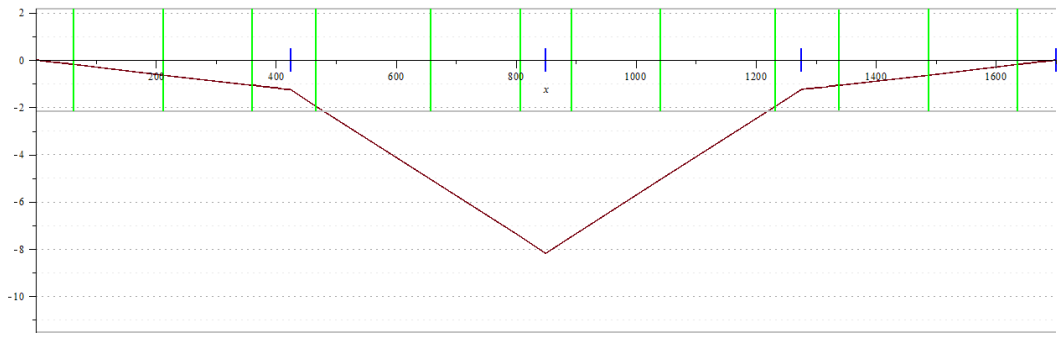

Figure H.7: A figure showing the moment diagram of the fine-tuned analytical model of the 1 mesh slab in the non-destructive test at 50 kN.

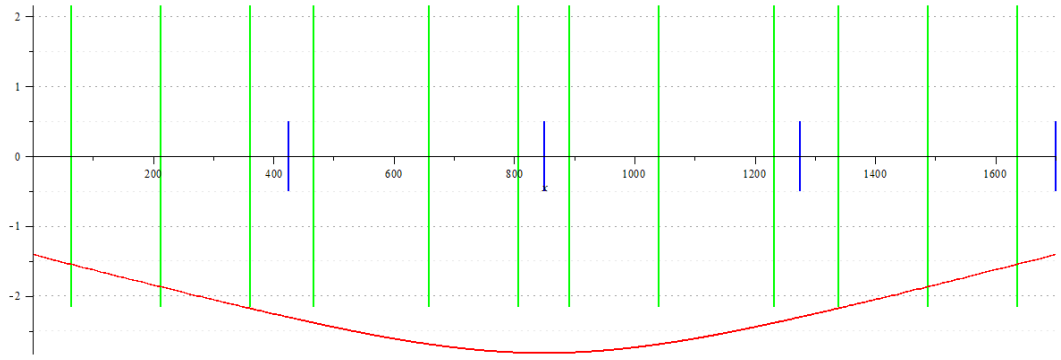

Figure H.8: A figure showing the deflection diagram of the fine-tuned analytical model of the 1 mesh slab in the non-destructive test at 50 kN.

H.1.3. 0 MESH

For the slab without reinforcement the non-destructive test was only loaded until 10 kN.

Table H.7: The distribution and deflection values used to adjust the analytical model for the 0 mesh slab in the non-destructive test.

	load 10 kN	
Rib number	**Contribution [%]**	**Deflection [mm]**
1	4.5	0.22
2	33.0	0.25
3	24.0	0.37
4	33.0	0.25
5	4.5	0.22

Table H.8: The distribution and deflection resulting from the fine-tuned analytical model in the 0 mesh slab and the non-destructive test.

Load [kN]	**Rib number**	**Load [%]**	**Stiffness [kN/mm]**	**Deflection [mm]**
10	1	4.6	3.3	0.14
	2	32.4	12.0	0.27
	3	26.0	7.5	0.35
	4	32.4	12.0	0.27
	5	4.6	3.3	0.14

Table H.9: The bending stiffness values of the top slab and the found value of the distributive length in the 0 mesh slab in the non-destructive test.

		Load 10 kN
Parameter	**Symbol**	**Value**
Distributive length [mm]	L_{dis}	1700
Uncracked top slab bending stiffness $[Nmm^2]per200mm$	$EI_{TS,uc}$	1.72×10^{11}

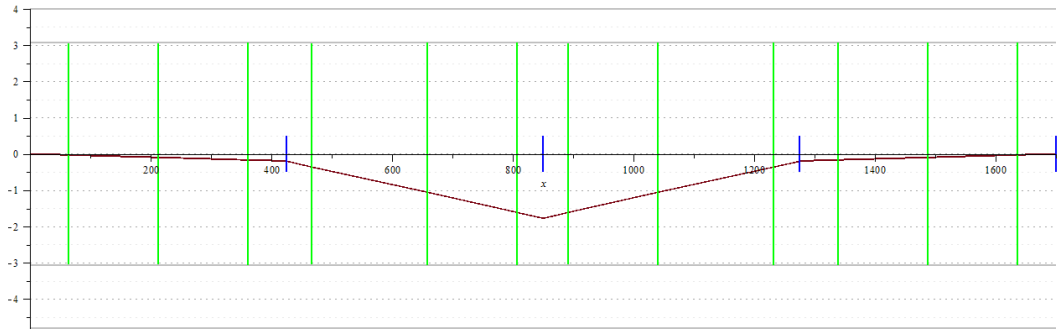

Figure H.9: A figure showing the moment diagram of the fine-tuned analytical model of the 0 mesh slab in the non-destructive test at 10 kN.

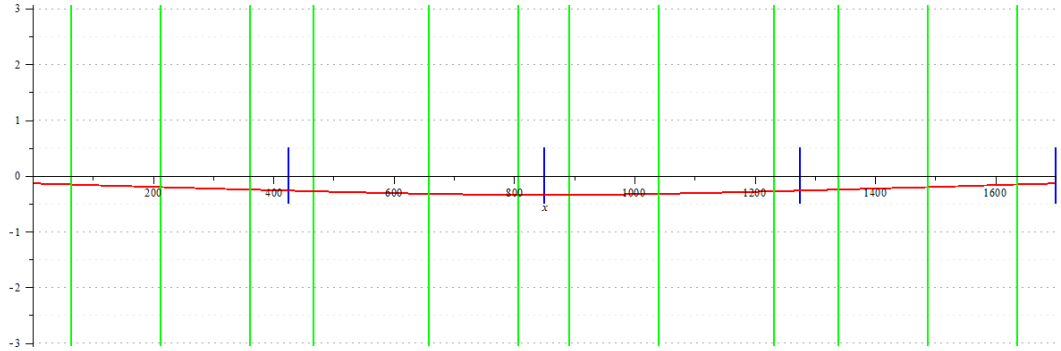

Figure H.10: A figure showing the deflection diagram of the fine-tuned analytical model of the 0 mesh slab in the non-destructive test at 10 kN.

H.2. RESULTS OF TEST AT HALF SPAN LENGTH

For the destructive tests at a quarter of the span length only the results of the load cells on the side of the slab which was not previously loaded will be examined. This is to prevent previous loading from influencing these results.

H.2.1. 2 MESH SLAB

Table H.10: The distribution and deflection values used to adjust the analytical model for the 2 mesh slab in the destructive test.

	load 10 kN		Load 60 kN		Load 165 kN	
Rib number	**Contribution [%]**	**Deflection [mm]**	**Contribution [%]**	**Deflection [mm]**	**Contribution [%]**	**Deflection [mm]**
1	11.5	0.50	10.5	4.30	9.5	20.50
2	23.0	0.50	23.0	4.80	22.5	28.67
3	31.0	0.50	32.0	5.60	36.0	36.60
4	23.0	0.50	23.0	4.80	22.5	28.67
5	11.5	0.50	10.5	4.30	9.5	20.50

Table H.11: The distribution and deflection resulting from the fine-tuned analytical model in the 2 mesh slab and the destructive test.

Load [kN]	Rib number	Load [%]	Stiffness [kN/mm]	Deflection [mm]
10	1	11.5	2.9	0.40
	2	23.1	5.1	0.45
	3	30.8	6.4	0.48
	4	23.1	5.1	0.45
	5	11.5	2.9	0.40
60	1	10.2	1.5	4.08
	2	23.9	2.9	4.93
	3	31.9	3.5	5.46
	4	23.9	2.9	4.93
	5	10.2	1.5	4.08
165	1	9.5	0.7	22.49
	2	22.8	1.3	30.12
	3	35.3	1.7	34.23
	4	22.8	1.3	30.12
	5	9.5	0.7	22.49

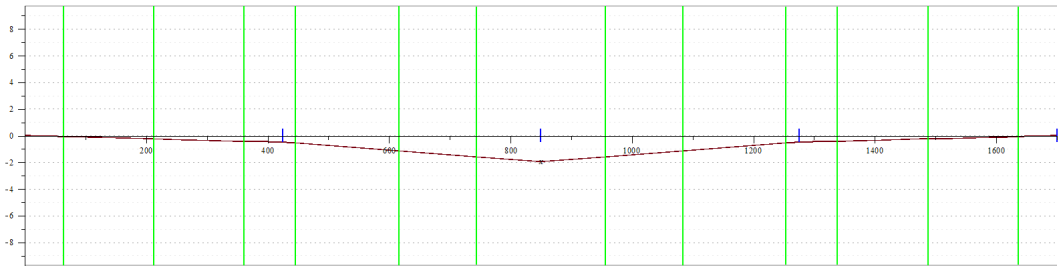

Figure H.11: A figure showing the moment diagram of the fine-tuned analytical model of the 2 mesh slab in the destructive test at 10 kN.

Table H.12: The bending stiffness values of the top slab and the found value of the distributive length in the 2 mesh slab in the destructive test.

		Load 10 kN	Load 60 kN	Load 165 kN
Parameter	**Symbol**	**Value**	**Value**	**Value**
Distributive length [mm]	L_{dis}	5400	3100	1100
Positive top slab bending stiffness $[Nmm^2]per200mm$	$EI_{TS,+}$	8.71×10^{10}	idem	idem
Negative top slab bending stiffness $[Nmm^2]per200mm$	$EI_{TS,-}$	1.06×10^{11}	idem	idem
Uncracked top slab bending stiffness $[Nmm^2]per200mm$	$EI_{TS,uc}$	1.72×10^{11}	idem	idem

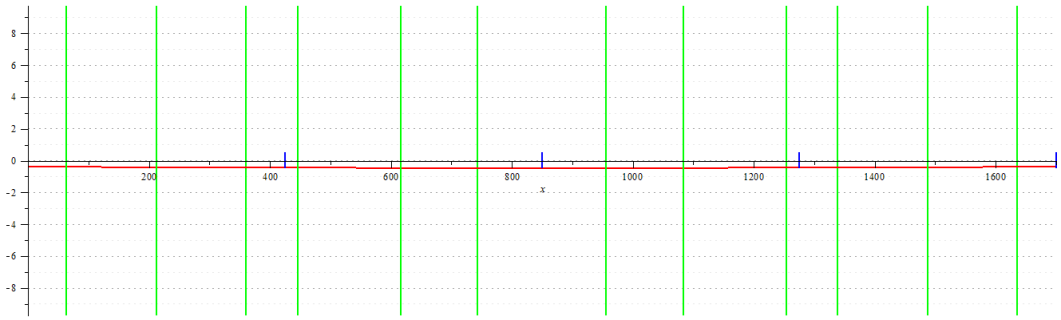

Figure H.12: A figure showing the deflection diagram of the fine-tuned analytical model of the 2 mesh slab in the destructive test at 10 kN.

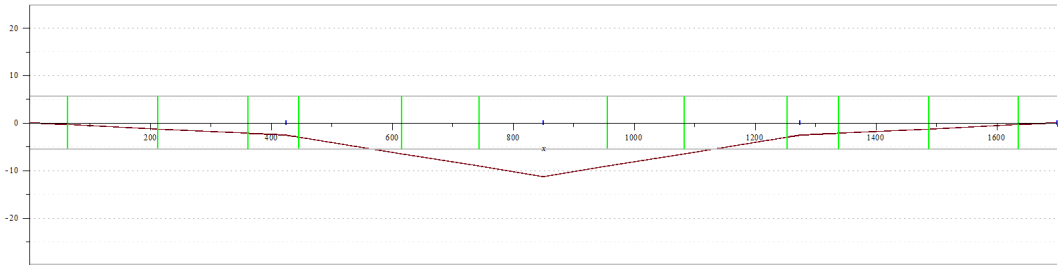

Figure H.13: A figure showing the moment diagram of the fine-tuned analytical model of the 2 mesh slab in the destructive test at 60 kN.

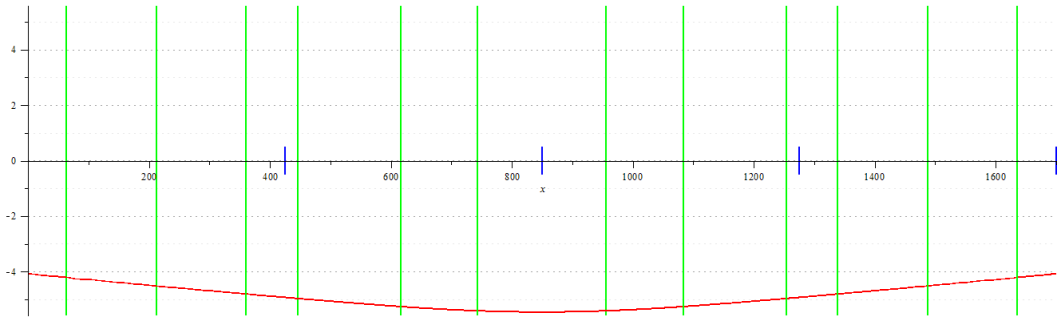

Figure H.14: A figure showing the deflection diagram of the fine-tuned analytical model of the 2 mesh slab in the destructive test at 60 kN.

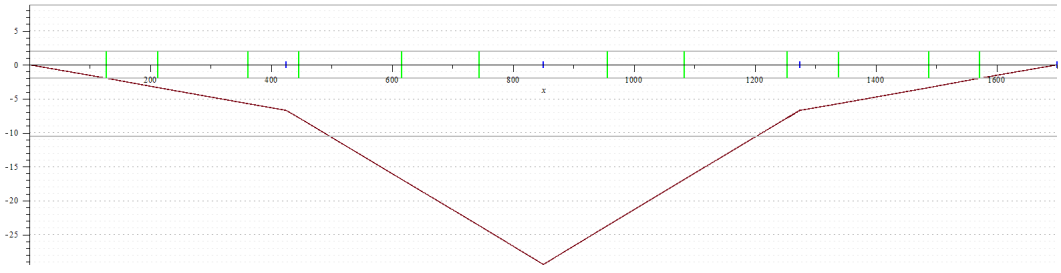

Figure H.15: A figure showing the moment diagram of the fine-tuned analytical model of the 2 mesh slab in the destructive test at 165 kN.

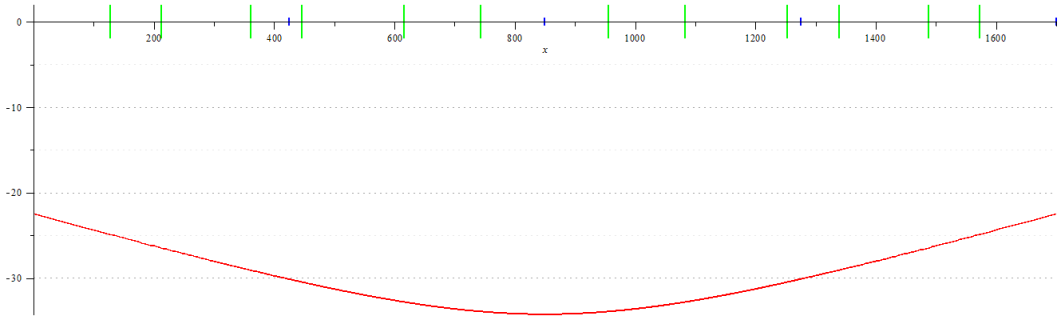

Figure H.16: A figure showing the deflection diagram of the fine-tuned analytical model of the 2 mesh slab in the destructive test at 165 kN.

H.2.2. 1 MESH SLAB

Table H.13: The distribution and deflection values used to adjust the analytical model for the 1 mesh slab in the destructive test.

	load 10 kN		Load 60 kN		Load 145 kN	
Rib number	**Contribution [%]**	**Deflection [mm]**	**Contribution [%]**	**Deflection [mm]**	**Contribution [%]**	**Deflection [mm]**
1	11.5	0.32	8.5	4.50	1.0	15.50
2	22.5	0.36	23.5	5.50	27.0	30.00
3	32.0	0.52	37.0	6.50	45.0	46.50
4	22.5	0.36	23.5	5.50	27.0	30.00
5	11.5	0.32	8.5	4.50	1.0	15.50

Table H.14: The distribution and deflection resulting from the fine-tuned analytical model in the 1 mesh slab and the destructive test.

Load [kN]	**Rib number**	**Load [%]**	**Stiffness [kN/mm]**	**Deflection [mm]**
10	1	10.3	3.2	0.32
	2	24.9	6.0	0.41
	3	29.7	6.4	0.46
	4	24.9	6.0	0.41
	5	10.3	3.2	0.32
60	1	7.3	0.8	4.38
	2	24.3	2.8	5.82
	3	36.9	3.3	6.71
	4	24.3	2.8	5.82
	5	7.3	0.8	4.38
145	1	0.6	0.06	14.20
	2	27.4	1.3	30.55
	3	44.0	1.5	42.57
	4	27.4	1.3	30.55
	5	0.6	0.06	14.20

Table H.15: The bending stiffness values of the top slab and the found value of the distributive length in the 1 mesh slab in the destructive test.

		Load 10 kN	Load 60 kN	Load 165 kN
Parameter	**Symbol**	**Value**	**Value**	**Value**
Distributive length [mm]	L_{dis}	3000	3000	1100
Positive top slab bending stiffness $[Nmm^2]per200mm$	$EI_{TS,+}$	4.91×10^{10}	idem	idem
Positive plastic top slab bending stiffness $[Nmm^2]per200mm$	$EI_{TS,+}$	1.47×10^{10}	idem	idem
Negative top slab bending stiffness $[Nmm^2]per200mm$	$EI_{TS,-}$	9.70×10^{10}	idem	idem
Uncracked top slab bending stiffness $[Nmm^2]per200mm$	$EI_{TS,uc}$	1.72×10^{11}	idem	idem

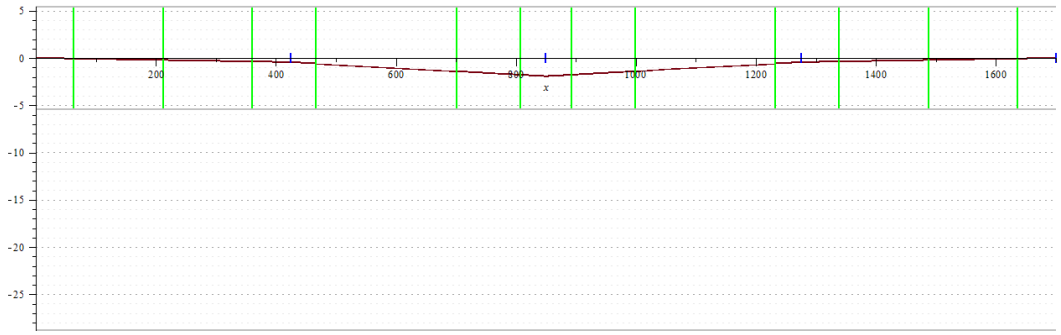

Figure H.17: A figure showing the moment diagram of the fine-tuned analytical model of the 1 mesh slab in the destructive test at 10 kN.

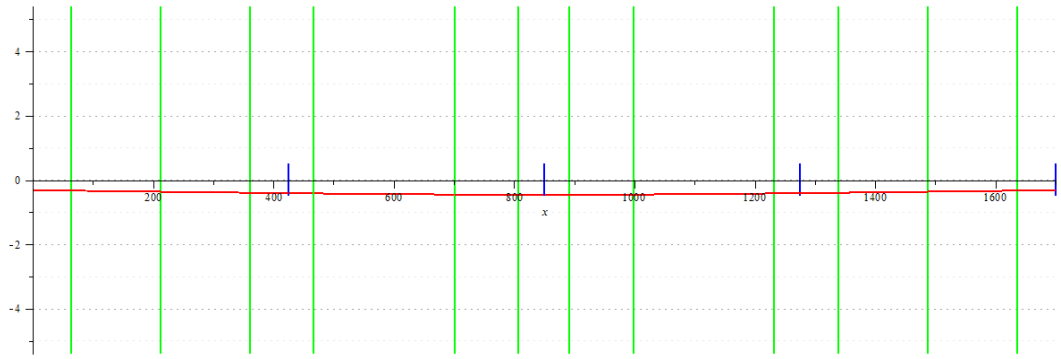

Figure H.18: A figure showing the deflection diagram of the fine-tuned analytical model of the 1 mesh slab in the destructive test at 10 kN.

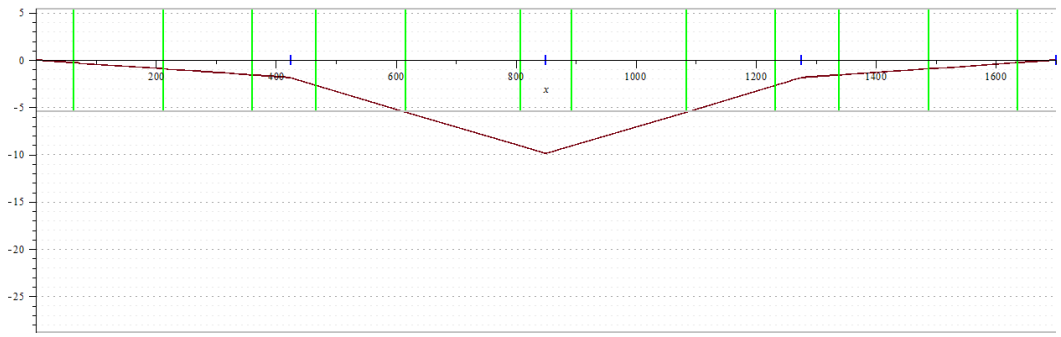

Figure H.19: A figure showing the moment diagram of the fine-tuned analytical model of the 1 mesh slab in the destructive test at 60 kN.

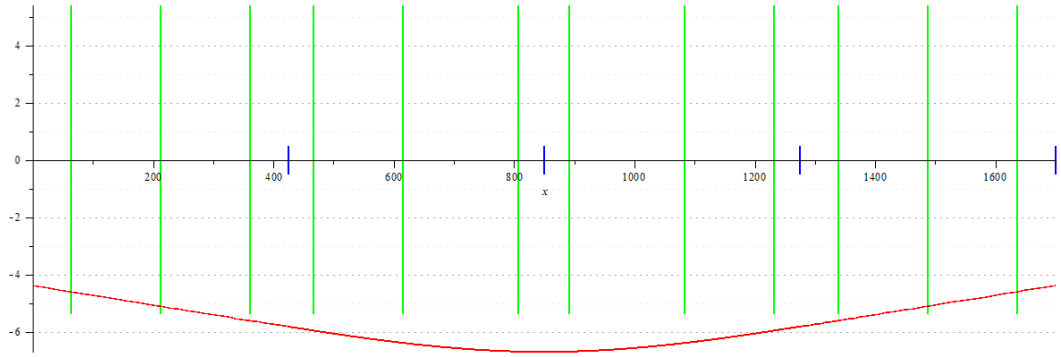

Figure H.20: A figure showing the deflection diagram of the fine-tuned analytical model of the 1 mesh slab in the destructive test at 60 kN.

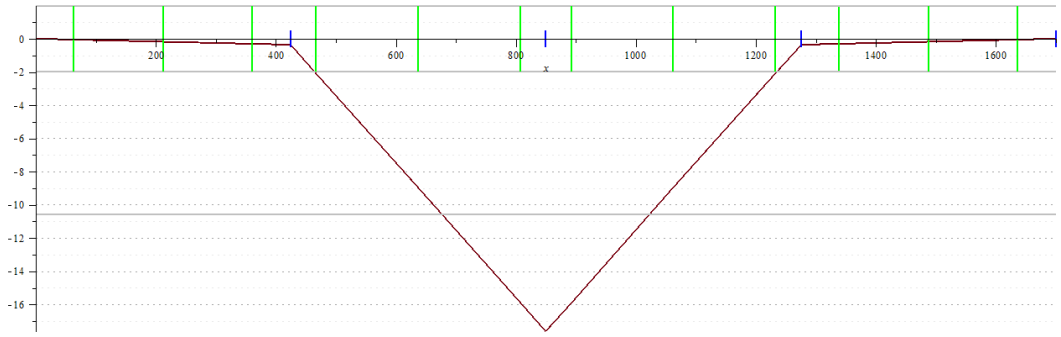

Figure H.21: A figure showing the moment diagram of the fine-tuned analytical model of the 1 mesh slab in the destructive test at 145 kN.

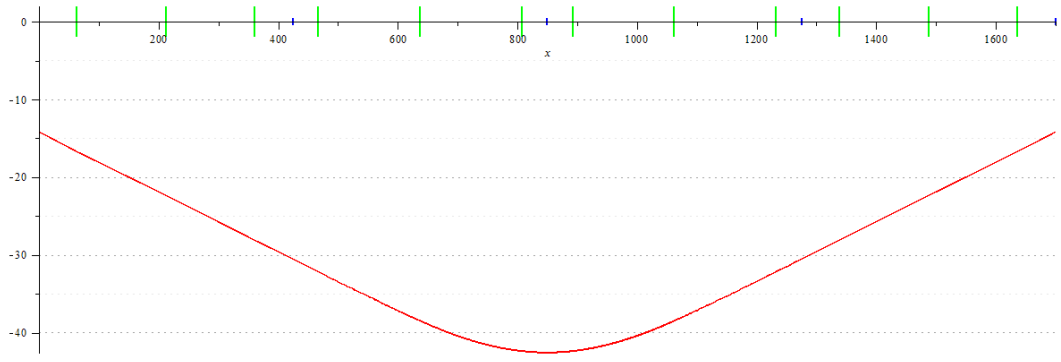

Figure H.22: A figure showing the deflection diagram of the fine-tuned analytical model of the 1 mesh slab in the destructive test at 145 kN.

H.2.3. 0 MESH SLAB

Table H.16: The distribution and deflection values used to adjust the analytical model for the 0 mesh slab in the destructive test.

	load 10 kN		Load 60 kN	
Rib number	**Contribution [%]**	**Deflection [mm]**	**Contribution [%]**	**Deflection [mm]**
1	11.0	0.33	7.0	5.00
2	23.0	0.34	23.0	5.80
3	32.0	0.51	31.0	6.50
4	23.0	0.34	23.0	5.80
5	11.0	0.33	7.0	5.00

Table H.17: The distribution and deflection resulting from the fine-tuned analytical model in the 0 mesh slab and the destructive test.

Load [kN]	**Rib number**	**Load [%]**	**Stiffness [kN/mm]**	**Deflection [mm]**
10	1	10.1	3.3	0.31
	2	24.4	6.5	0.38
	3	30.9	7.5	0.41
	4	24.4	6.5	0.38
	5	10.1	3.3	0.31
60	1	8.1	0.9	5.39
	2	26.5	2.7	5.89
	3	30.8	3.0	6.17
	4	26.5	2.7	5.89
	5	10.1	0.9	5.39

Table H.18: The bending stiffness values of the top slab and the found value of the distributive length in the 0 mesh slab in the destructive test.

		Load 10 kN	Load 50 kN
Parameter	**Symbol**	**Value**	**Value**
Distributive length [mm]	L_{dis}	4000	3000
Uncracked top slab bending stiffness $[Nmm^2]per200mm$	$EI_{TS,uc}$	1.72×10^{11}	idem

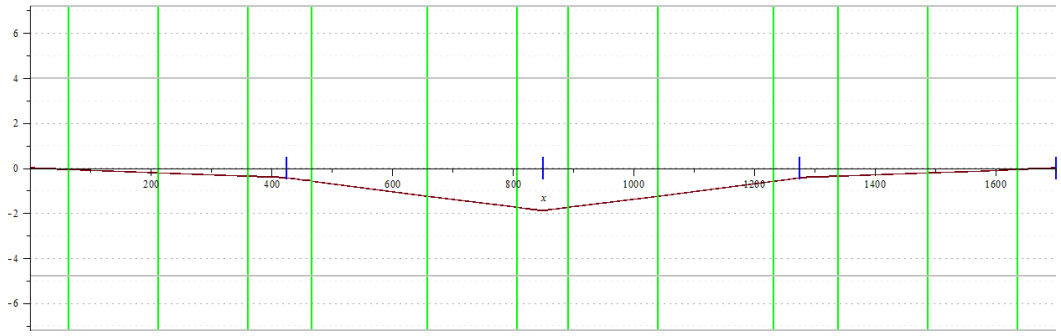

Figure H.23: A figure showing the moment diagram of the fine-tuned analytical model of the 0 mesh slab in the destructive test at 10 kN.

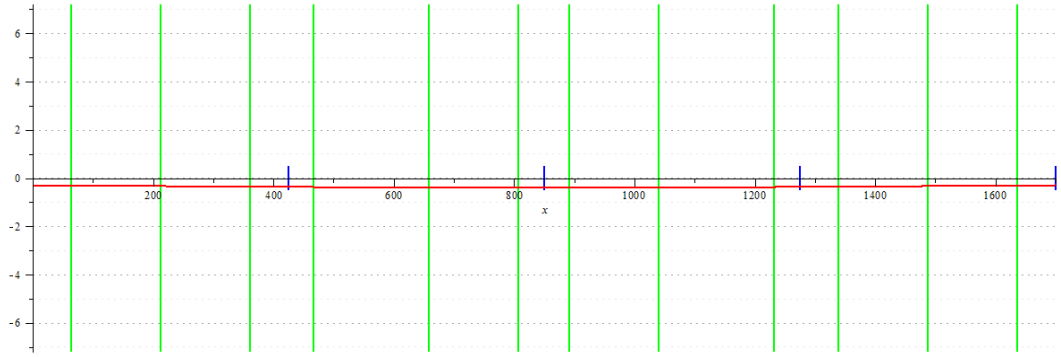

Figure H.24: A figure showing the deflection diagram of the fine-tuned analytical model of the 0 mesh slab in the destructive test at 10 kN.

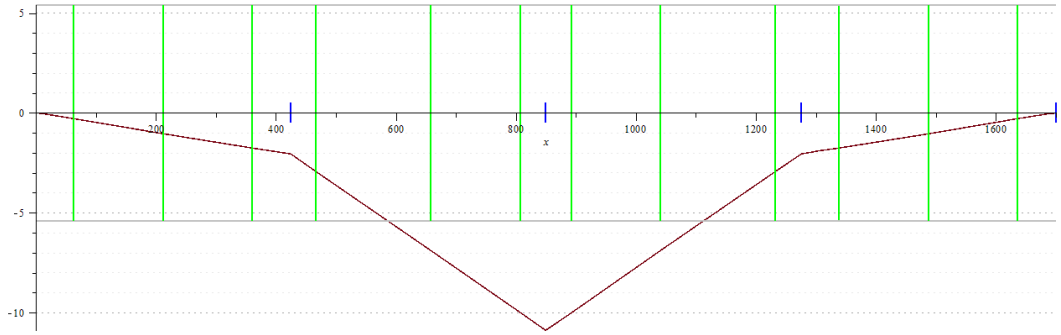

Figure H.25: A figure showing the moment diagram of the fine-tuned analytical model of the 0 mesh slab in the destructive test at 60 kN.

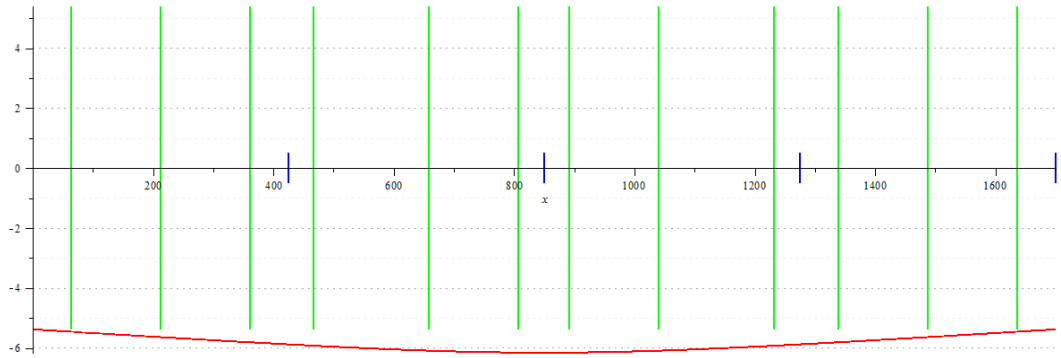

Figure H.26: A figure showing the deflection diagram of the fine-tuned analytical model of the 0 mesh slab in the destructive test at 60 kN.

H.3. FEM COMPARISON

In this section the strains in the concrete at several levels of loading in the finite element modelling are shown. Also the stresses and strains in the steel deck and reinforcement are given in tables.

H.3.1. 2 MESH SLAB

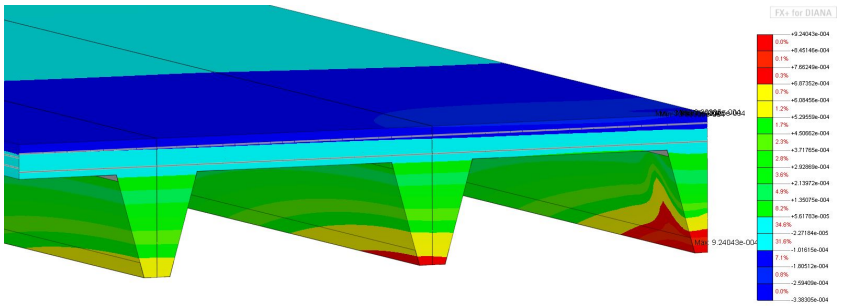

Figure H.27: The strain in the finite element model of the 2 mesh slab at 36 kN.

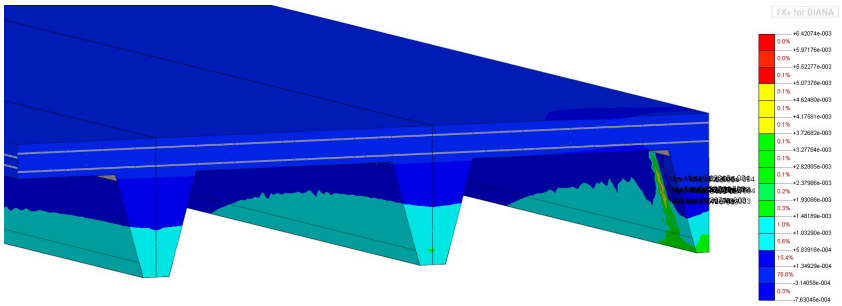

Figure H.28: The strain in the finite element model of the 2 mesh slab at 49 kN.

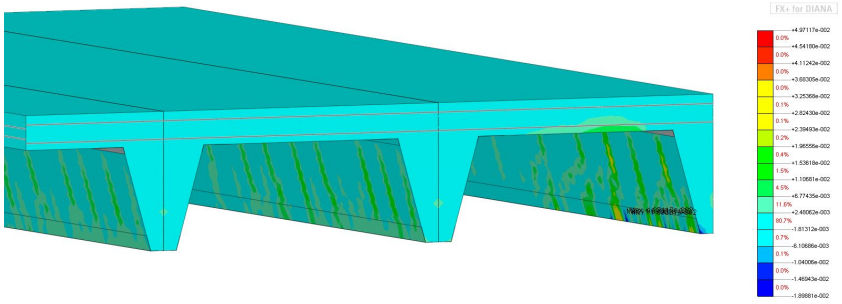

Figure H.29: The strain in the finite element model of the 2 mesh slab at 104 kN.

Table H.19: This table shows the stresses in the steel reinforcement in the 2 mesh slab at different loading situations.

Position	Load				
	0	36	49	76	104
Bottom steel flange rib 1	27	150	200	400	400
Bottom steel flange rib 2	27	160	250	400	400
Bottom steel flange rib 3	27	227	377	400	400
Top steel flange rib 1	-2.5	-4.9	-5.9	50	110
Top steel flange rib 2	-2.5	-4.9	-5.9	100	150
Top steel flange rib 3	-2.5	-4.9	-5.9	133	380

Table H.20: This table shows the strains in the steel reinforcement in the 2 mesh slab at different loading situations.

Position	Load				
	0	36	49	76	104
Bottom steel flange rib 1	0.1	0.7	1.0	1.9	4.0
Bottom steel flange rib 2	0.1	0.8	1.2	2.0	6.5
Bottom steel flange rib 3	0.1	1.1	1.8	4.7	8.0
Top steel flange rib 1	0.0	0.0	0.0	0.2	0.5
Top steel flange rib 2	0.0	0.0	0.0	0.5	0.7
Top steel flange rib 3	0.0	0.0	0.0	0.6	1.8

Table H.21: This table shows the strains in the steel reinforcement in the 2 mesh slab at different loading situations.

Position	Load				
	0	36	49	76	104
Top mesh x rib 3 direction	-7	-27	-30	-45	-80
Top mesh y rib 3 direction	20	50	120	195	250
Bottom mesh x rib 3 direction	-5	16	40	85	120
Bottom mesh y rib 3 direction	15	16	40	180	250
Rib reinforcement bar 1	16	90	130	280	500
Rib reinforcement bar 2	16	90	130	280	500
Rib reinforcement bar 3	16	140	240	540	540

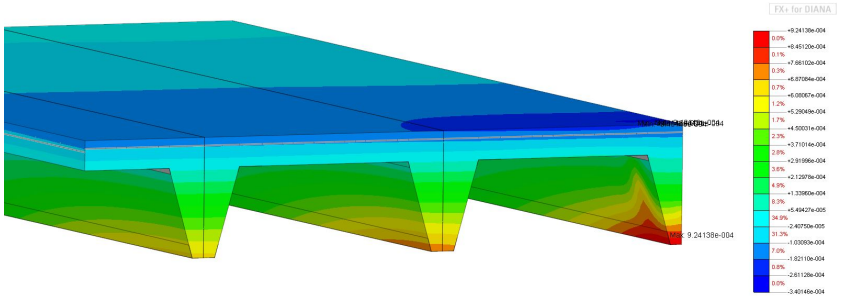

Figure H.30: The strain in the finite element model of the 2 mesh slab at 32 kN.

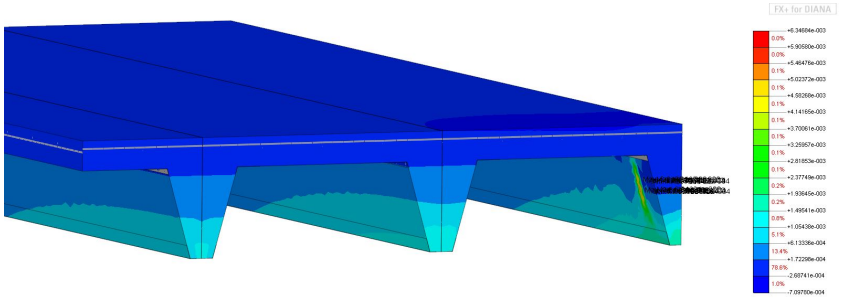

Figure H.31: The strain in the finite element model of the 2 mesh slab at 49 kN.

H.3.2. 1 MESH SLAB

Table H.22: This table shows the stresses in the steel reinforcement in the 1 mesh slab at different loading situations.

Position	Load				
	0	36	49	76	104
Bottom steel flange rib 1	20	140	150	350	400
Bottom steel flange rib 2	20	160	230	400	400
Bottom steel flange rib 3	20	210	350	400	400
Top steel flange rib 1	0	-5	0	50	70
Top steel flange rib 2	0	0	0	100	150
Top steel flange rib 3	0	20	50	133	200

Table H.23: This table shows the strains in the steel reinforcement in the 1 mesh slab at different loading situations.

Position	Load				
	0	36	49	76	104
Bottom steel flange rib 1	0.1	0.7	0.7	1.7	2.5
Bottom steel flange rib 2	0.1	0.8	1.1	2.0	4.5
Bottom steel flange rib 3	0.1	1.0	1.7	4.0	6.0
Top steel flange rib 1	0.0	0.0	0.0	0.1	0.3
Top steel flange rib 2	0.0	0.0	0.0	0.2	0.7
Top steel flange rib 3	0.0	0.1	0.2	0.5	1.0

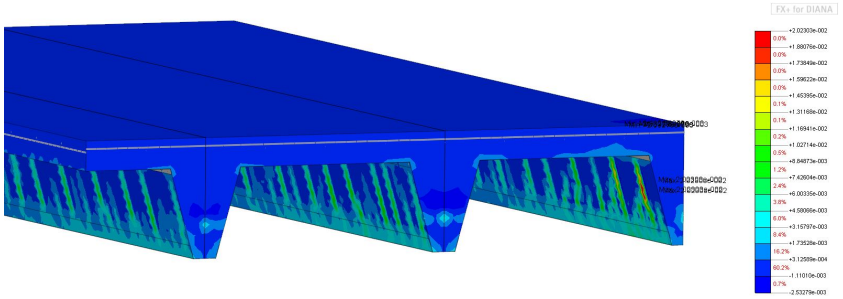

Figure H.32: The strain in the finite element model of the 2 mesh slab at 84 kN.

Table H.24: This table shows the strains in the steel reinforcement in the 1 mesh slab at different loading situations.

Position	Load				
	0	36	49	76	104
Top mesh x rib 3 direction	-7	-30	-31	-50	-70
Top mesh y rib 3 direction	20	50	120	195	250
Rib reinforcement bar 1	16	95	100	250	350
Rib reinforcement bar 2	16	120	170	300	400
Rib reinforcement bar 3	16	140	230	400	540

H.3.3. 0 MESH SLAB

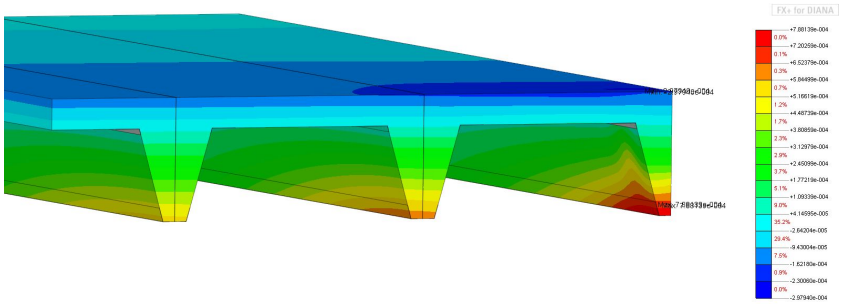

Figure H.33: The strain in the finite element model of the 0 mesh slab at 29 kN.

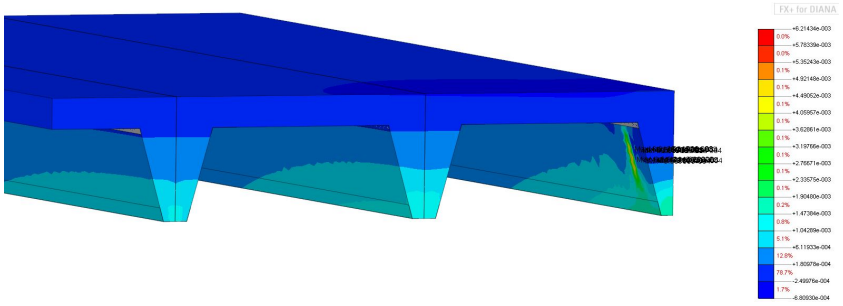

Figure H.34: The strain in the finite element model of the 0 mesh slab at 49 kN.

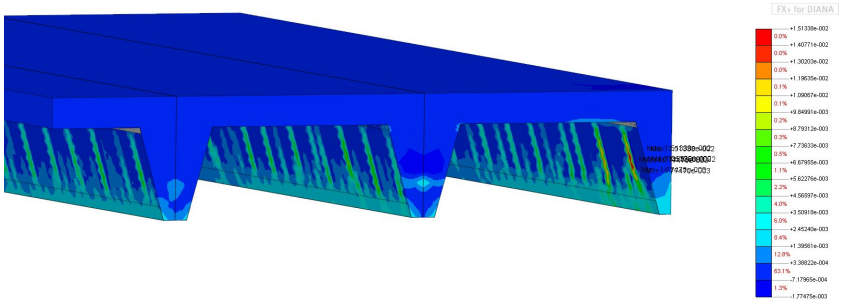

Figure H.35: The strain in the finite element model of the 0 mesh slab at 71 kN.

Table H.25: This table shows the stresses in the steel reinforcement in the 0 mesh slab at different loading situations.

Position	Load				
	0	36	49	76	104
Bottom steel flange rib 1	25	140	180	350	380
Bottom steel flange rib 2	25	150	240	400	450
Bottom steel flange rib 3	25	200	350	450	450
Top steel flange rib 1	-2	-5	-5	50	70
Top steel flange rib 2	-2	0	20	60	100
Top steel flange rib 3	-2	20	60	100	130

Table H.26: This table shows the strains in the steel reinforcement in the 0 mesh slab at different loading situations.

Position	Load				
	0	36	49	76	104
Bottom steel flange rib 1	0.1	0.7	0.9	1.7	1.8
Bottom steel flange rib 2	0.1	0.7	1.1	1.9	2.0
Bottom steel flange rib 3	0.1	1.0	1.7	2.1	2.1
Top steel flange rib 1	0.0	0.0	0.0	0.2	0.3
Top steel flange rib 2	0.0	0.0	0.1	0.3	0.5
Top steel flange rib 3	0.0	0.1	0.3	0.5	0.6

Table H.27: This table shows the strains in the steel reinforcement in the 0 mesh slab at different loading situations.

Position	Load				
	0	36	49	76	104
Rib reinforcement bar 1	16	90	100	180	200
Rib reinforcement bar 2	16	110	160	300	340
Rib reinforcement bar 3	16	140	230	420	450

BIBLIOGRAPHY

[1] *Eurocode 4: design of steel structures (part 1-1: general rules for buildings),* (2004).

[2] *Eurocode 2: Design of concrete structures (part 1-1: general rules for buildings),* (2004).

[3] I. E. H. Shobaki, *The behaviour of profiled steel seet/concrete composite slabs*, Ph.D. thesis, Salford School of Environment & Life Sciences Division of Civil & Environmental Engineering University of Salford (2000).

[4] M. Crisinel, *Working group no. 10 lecture no. 7 - in composite slabs - european steel design education programme,* (1991), switzerland.

[5] J. Stark and R. Stark, *Vertical shear resistance of composite floors with ComFlor 60*, Tech. Rep. (Dutch Engineering, Zoeterwoude, 2012).

[6] J. Stark and R. Stark, *Staal-beton* (Bouwen met Staal, Zoetermeer, 2009).

[7] R. Schuurman, *The Physical Behaviour of Shear Connections in Composite Slabs* (DUP science, 2001).

[8] J. Brekelmans, B. Daniels, B. van Hove, and H. Koukkari, *Analysis of the combined vertical and horizontal shear tests on deep deck composite slabs*, Tech. Rep. (TNO, Delft, 1995).

[9] H. Bode and T. Däuwel, *Ergänzungen zum Gutachten über das Tragverhalten von COMFLOR210 - Verbunddecken*, Tech. Rep. (Universität Kaiserlautern, Kaiserlautern, 1999).

[10] *Eurocode 1: Actions on structures (part 1-1: general actions - densities, self-weight, imposed loads for buildings),* (2004).

[11] NEN6725, *[Dutch] Vrijdragende systeemvloeren van vooraf vervaardigd beton*, Tech. Rep. (TGB 1990, 1995).

[12] NEN6720, *[Dutch] Voorschriften beton - constructieve eisen en rekenmethoden (withdrawn)*, Tech. Rep. (TGB 1990, 1995) withdrawn.

[13] T. Arrajarusit, *Ribbed slabs under concentrated loads*, Tech. Rep. (University of Illinois, Urbana, Illinois, 1973).

[14] H. Bode and T. Däuwel, *Gutachten zum Tragverhalten von COMFLOR210 - Verbunddecken*, Tech. Rep. (Universität Kaiserlautern, Kaiserlautern, 1997).

[15] M. van Infrastructuur en Milieu, *Guidelines for Nonlinear Finite Element Analysis of Concrete Structures*, Tech. Rep. (Rijkswaterstaat, 2012).

[16] J. Stark and R. Abspoel, *Steel Structures 3 Reader - Part 1: composite constructions* (Delft University of Technology, Delft, 2010).

[17] NEN6892-1, *Metallic materials-Tensile testing-part-1*, Tech. Rep. (TGB 1990, 2009).